

Bottom-Up Synthesis of Graphene Nanoribbons and Nanographene Molecules with New Types of Periphery

Dissertation

zur Erlangung des Grades

“Doktor der Naturwissenschaften”

im Fachbereich Chemie, Pharmazie, und Geowissenschaften der Johannes
Gutenberg-Universität Mainz und in Kooperation mit dem Max-Planck-
Institut für Polymerforschung Mainz

Vorgelegt von

Bo Yang

geboren in Ningxia Province / P. R. China

Mainz, 2015

Dekan: Prof. Dr. [REDACTED]

1. Berichterstatter: Prof. Dr. [REDACTED]

2. Berichterstatter: Priv. Doz. Dr. [REDACTED]

Tag der mündlichen Prüfung: 30.03.2016

Die vorliegende Arbeit wurde in der Zeit von April 2011 bis Mai 2015 im Max-Planck-Institut für Polymerforschung in Mainz unter Anleitung von Herrn Prof. Dr. [REDACTED] ausgeführt.

Ich danke Herrn Prof. Dr. [REDACTED] für seine wissenschaftliche und persönliche Unterstützung sowie für sein ständige Diskussionsbereitscha

Table of Contents

Abbreviations	V
Chapter 1. Introduction	1
1.1 Polycyclic aromatic hydrocarbons (PAHs)	1
1.2 Graphene	2
1.3 Nanographene molecules (NGs)	7
1.3.1 Classification of nanographene molecules (NGs)	8
1.3.2 Methods of synthesizing NGs	18
1.4 Graphene nanoribbons (GNRs)	21
1.4.1 Classification of GNRs	22
1.4.2 Fabrication of GNRs via “top-down” approach	23
1.4.3 Fabrication of GNRs via “bottom-up” approach	26
1.5 Motivation and objectives	37
1.5.1 Bottom-up synthesis of novel GNRs with zigzag edge structures	37
1.5.2 Attempts of synthesizing novel NGs with zigzag edge structures	39
1.5.3 Chemical functionalization of NGs	40
1.6 References	42
Chapter 2. Bottom-Up Synthesis of GNRs with Zigzag Edge Structures: Surface-Assisted Synthesis	52
2.1 Introduction	52
2.2 Surface-assisted synthesis of GNRs with zigzag edge	54
2.2.1 Synthetic strategy	54
2.2.2 Synthesis of monomers based on photochemistry	56
2.2.3 Synthesis of monomers based on Pyrylium chemistry	61
2.2.4 Surface synthesis of GNR with partial zigzag edge	70
2.2.5 Synthesis of novel monomer based on Pt catalyzed cyclization	75
2.2.6 Surface synthesis of GNR with perfect zigzag edge	83

2.2.7 Edge state characterization of 6-ZGNR (f) and 6-ZGNR plus (f')	86
2.3 Summary	90
2.4 References	92
Chapter 3. Bottom-up synthesis of GNR with zigzag edges in solution	96
3.1 Introduction	96
3.2 Synthetic strategy	96
3.2.1 Synthesis of monomers (building blocks).....	97
3.2.2 Synthesis of model compounds 3-15 , 3-17 , and 3-19	99
3.2.3 AA-type Yamamoto polymerization.....	108
3.2.4 MALDI-TOF MS analysis of polymer precursors 3-2a~c	109
3.2.5 Fractionation and SEC analysis of precursor 3-2c	111
3.2.6 Graphitization towards GNR.....	114
3.3 Characterization and analysis	116
3.3.1 UV-vis and PL analysis (model compounds and GNR).....	116
3.3.2 Electronic properties analysis and DFT calculation.....	119
3.3.3 Raman and FTIR spectroscopy	121
3.3.4 Solid-state NMR analysis.....	132
3.3.5 AFM and STM visualization	136
3.4. Summary	141
3.5 References	142
Chapter 4. Design and synthesis of nanographene molecules (NGs) with zigzag edges	144
4.1 Introduction	144
4.2 Target molecules and synthetic strategy	147
4.2.1 Design and synthetic attempt toward full-zigzag HBC (4-5).....	149
4.2.2 Design and synthesis of tetra zigzag molecule (4-4).....	156
4.3. Summary	164
4.4 References	165

Chapter 5. Chemical functionalization of nanographene molecules	167
5.1 Introduction	167
5.2 Edge chlorination of NGs	168
5.2.1 Synthetic strategy	168
5.2.2 Characterization and analysis of chlorinated nanographenes	170
5.2.3 Optical and electronic properties of chlorinated nanographene	174
5.3 Attempts on hydrogenation	176
5.4 Summary	182
5.5 References	183
Chapter 6. Conclusion and Outlook	185
6.1 Conclusion	185
6.2 Outlook	187
Chapter 7. Experiment part	191
7.1 General information	191
7.1.1 Materials	191
7.1.2 Methods	191
7.2 Analytical techniques	191
7.2.1 NMR spectroscopy	191
7.2.2 Mass spectrometry	192
7.2.3 UV-vis absorption spectroscopy	193
7.2.4 Photoluminescence spectroscopy	193
7.2.5 FTIR spectroscopy	193
7.2.6 Raman spectroscopy	194
7.2.7 Size-exclusion chromatography analysis	194
7.2.8 STM visualization	194
7.2.9 AFM visualization	195
7.2.10 DFT calculation	195
7.3 Synthetic procedures	196

<i>7.3.1 Synthesis of monomer precursor for fabricating GNRs on surface</i>	196
<i>7.3.2 Synthesis of monomer precursor 3-1 for solution-mediated fabrication of GNR 3-3c in solution</i>	214
<i>7.3.3 Synthesis of polymer precursor 3-2(a, b, and c) in solution</i>	218
<i>7.3.4 Synthesis of GNR 3-3c in solution</i>	220
<i>7.3.5 Synthesis of model compounds 3-15, 3-17, and 3-19</i>	221
<i>7.3.6 Synthesis of NGs with zigzag edges</i>	226
<i>7.3.7 Chemical functionalization of NGs</i>	233
7.4 References	239
List of Publications	241
Curriculum Vitae	242
Acknowledgements	245

Abbreviations

2D	two-dimensional
AFM	atomic force microscopy
AGNR	armchair-type graphene nanoribbons
APPI	atmospheric pressure photoionization
CNT	carbon nanotube
COSY	correlation spectroscopy (NMR)
CV	cyclic voltammetry
CVD	chemical vapor deposition
d	doublet (NMR)
D-A	Diels-Alder
DBU	1,8-diazabicycloundec-7-ene
DDQ	2,3-dichloro-5,6-dicyano-1,4-benzoquinone
DFT	density functional theory
DME	dimethoxyethane
DMF	<i>N,N</i> -dimethylformamide
DMSO	dimethyl sulfoxide
DQ	double quantum
E_g	energy bandgap
ESI	electrospray ionization
F-C	Friedel-Craft
FD MS	field-desorption mass spectrometry
FET	field-effect transistor
FTIR	Fourier transform infrared (spectroscopy)
GNRs	graphene nanoribbons
GO	graphene oxide
GODs	graphene quantum dots
H ₂ SO ₄	sulfuric acid
HBC	hexa- <i>peri</i> -hexabenocoronene
HOMO	highest occupied molecular orbital
HOPG	highly oriented pyrolytic graphite
HPB	hexaphenylbenzene
KMnO ₄	potassium permanganate
LED	light-emitting diodes
LUMO	lowest unoccupied molecular orbital
m	multiplet (NMR)
MALDI	matrix-assisted laser desorption/ionization
MAS	magic-angle-spinning (solid-state NMR)
M_n	number-average molecular weight
M_p	melting point
MS	mass spectrometry
M_w	weight-average molecular weight
MWCNTs	multiwalled carbon nanotubes
nc	non-contact
NGs	nanographene molecules
NMP	<i>N</i> -methyl-pyrrolidone
NMR	nuclear magnetic resonance

Abbreviations

NOESY	nuclear Overhauser enhancement spectroscopy
OLED	organic light-emitting diodes
OLED	organic light-emitting diodes
<i>opla</i>	out-of-plane
PAH	polycyclic aromatic hydrocarbons
Pd/C	palladium on active carbon
PDI	polydispersity index
PL	photoluminescence
PMMA	poly(methylmethacrylate)
PPP	poly(<i>para</i> -phenylene)
PS	poly(styrene)
PSD	power spectrum density
REPT-HSQC	recoupled polarization heteronuclear single quantum correlation
rGO	reduced graphene oxide
s	singlet (NMR)
SEC	size exclusion chromatography
SiC	silicon carbide
SPM	scanning probe microscopy
SQ	single quantum
STM	scanning tunneling microscopy
SWNTs	single-walled carbon nanotubes
t	triplet (NMR)
TBA	tetrabutylammonium hydroxide
TBAF	tetra- <i>n</i> -butylammonium fluoride
TCNQ	tetracyanoquinodimethane
Tf ₂ O	trifluoromethanesulfonic anhydride
TFA	trifluoroacetic acid
THF	tetrahydrofuran
THz	terahertz
TIPS	triisopropylsilyl
TLC	thin-layer chromatography
TMS	trimethylsilyl
TOF	time of flight
TTBS	tri- <i>tert</i> -butylsilyl
UHV	ultrahigh vacuum
UV-vis	ultraviolet-visible (absorption spectroscopy)
ZGNR	zigzag-type graphene nanoribbons

Chapter 1. Introduction

1.1 Polycyclic aromatic hydrocarbons (PAHs)

PAHs are neutral, nonpolar molecules. They were first found in coal tar and fossil fuels (coal and curd oil) in the 19th century. Generally, the PAHs are produced when insufficient oxygen or other factors result in incomplete combustion of organic matter. PAHs are abundant in the environment, such as in engines and incinerators, in biomass burnt in forest fires, and even in some cooked foods, e.g., in meat cooked at high temperatures over flame.

PAHs have become one of the most widely investigated compounds due to their enormous diversity and potential applications in medical sciences, biology, physics, organic chemistry and material sciences in recent decades.¹⁻⁶ PAHs, which are constituted by the periodical annelation of benzene rings, often lead to extended aromaticity and constitute an extraordinarily large and diverse class of organic molecules. An amazing fact is that 20600 possible structures of PAHs can be constructed from four to ten benzene rings through different permutations. Series of PAHs examples that are constructed by annelation of four benzene rings are shown below (Fig. 1-1) in order to more clearly display the enormous structure diversity. There are seven possible structures can be given as result, which are named: a) tetracene, b) pyrene, c) triphenylene, d) crysene, e) tetraphene, f) benzo[*d,e*]anthracene, and g) benzo[*c*]phenanthrene.

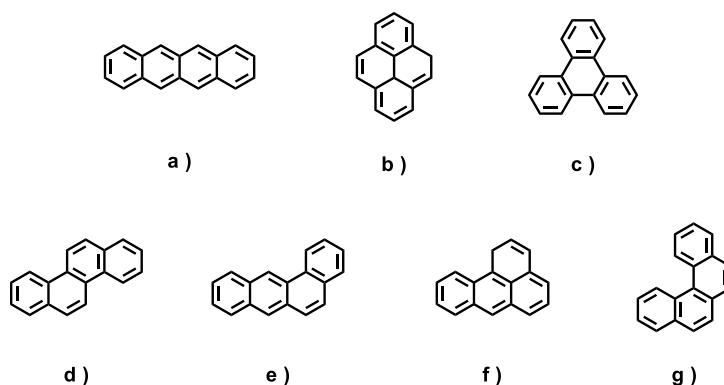


Figure 1-1. The structural diversity of PAH as exemplified by annelation of four benzene rings

On the other hand, with the interesting electronic and optical properties, which are induced by the electron delocalization along the aromatic structures, PAHs are continuously attracting organic chemists' and material scientists' attention. Especially after the discovery of conducting and semiconducting organic polymers in 1970's and discotic liquid crystals by Chandrasekhar in 1977,⁷⁻⁹ a new important field dealing with the application of PAHs began to emerge. In combination with

their tendency to self-assemble (PAHs bearing flexible peripheral alky chains can form stable a columnar mesophase), the excellent intrinsic electronic properties of PAHs make them promising semiconducting materials and widely used in organic electronic devices, such as light-emitting diodes (LED), photo- and electroluminescent devices,¹⁰⁻¹² field-effect transistors,^{10,13-16} as well as solar cells and liquid crystal display.^{10,17-20}

1.2 Graphene

Looking back at the history, the word “Graphene” was first coined by Hanns-Peter Boehm, as a combination of graphite and the suffix –ene, to describe single-layer carbon foils in 1962.^{21,22} Following that, the term “Graphene” was also used in early descriptions of carbon nanotubes and epitaxial graphene.^{23,24} Nowadays, Graphene is usually defined as an individual two-dimensional allotrope of carbon, and atomically thick sheet of graphite (one layer) composed of a hexagonal network of sp^2 -hybridized carbon atoms. It can also be seen as an “infinite alternant” (only six-member carbon ring) PAH.

Although the conception of “Graphene” had been described and theoretically studied for more than 60 years, the free-standing graphene was never really prepared. The reason can be partially attributed to the fact that graphene was presumed not to exist in the free-standing state, and believed to be thermodynamically unstable compared to other curved structures such as fullerenes and nanotubes. Basically, it was considered as an “academic” material²⁵ until the pioneering experiments done by Geim and Novoselov et al. in 2004, who prepared the stable single- to few-layer graphene for the first time.²⁶⁻²⁸ After that, studies of graphene have quickly become a hot research topic both in physics and chemistry. The excellent work of Geim and Novoselov as well as their Manchester team, which boosted the research activities in the graphene field, and were recognized with the Nobel Prize in physics in 2010.²⁹

Graphene is a basic 2D building block for all other graphitic materials (Fig.1-2). It can be wrapped up into 0D fullerenes, rolled into 1D nanotubes, or stacked into 3D graphite. Besides, its flexible network structure and possibilities in fabricating other dimensional carbon materials, the extraordinary electronic, thermal, and mechanical properties attracted lots of attention and intensive studies.

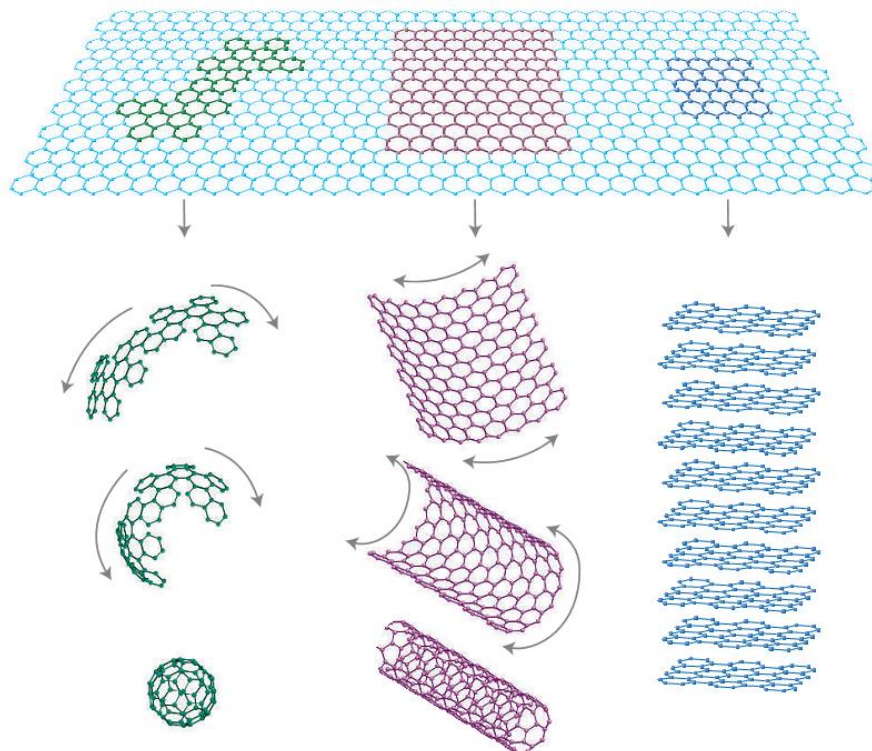


Figure 1-2. Mother of all graphitic forms. Graphene is a 2D building block for other carbon materials of all dimensionalities. Reprinted with permission from Ref. [29]; copyright: 2007, Nature publishing group.

Thanks to the simple but efficient preparation method by Geim and Novoselov, who peeled off highly oriented pyrolytic graphite (HOPG) with a regular adhesive tape (namely mechanical exfoliation), a high-quality graphene can be easily obtained without a need of expensive and complicated setups. And the feasibility and reliability of the method allowed other researchers to follow up this procedure for further investigation of graphene's properties (Fig. 1-3). The subsequent numerous studies showed that the isolated single-layer graphene not only theoretically, but also experimentally exhibits series of favorable properties, such as quantum Hall effect at room temperature,^{30,31} high carrier mobilities ($> 200\,000\text{ cm}^2\text{V}^{-1}\text{s}^{-1}$ at electron densities of $2 \times 10^{11}\text{ cm}^{-2}$),³² exceptional Young modulus values ($> 0.5\sim 1\text{ TPa}$), and large spring constants ($1\sim 5\text{ N m}^{-1}$).³³⁻³⁵ Moreover, graphene also revealed unique morphological properties, such as high specific surface areas (theoretically predicted $> 2500\text{ m}^2\text{g}^{-1}$ and experimentally measured as $400\text{-}700\text{ m}^2\text{g}^{-1}$)³⁶⁻³⁹. All of above mentioned properties make graphene a promising candidate for practical applications in electronics,⁴⁰⁻⁴² sensing,^{43,44} catalysis,^{45,46} gas and energy storage,^{47,48} conversion,³⁹ as well as micro- and optoelectronics.^{2,49-52}

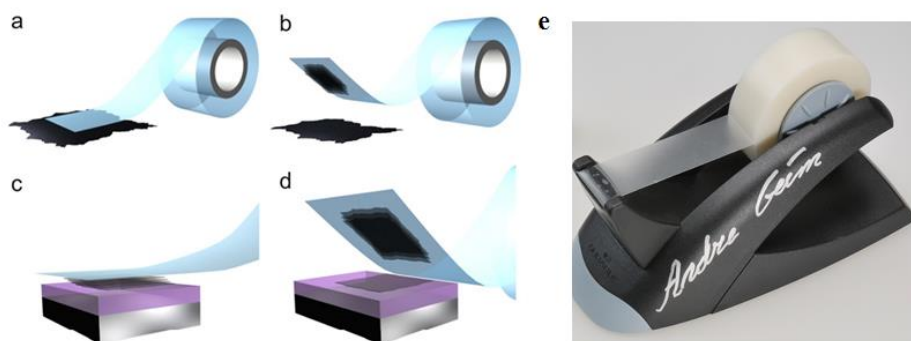


Figure 1-3. Micromechanical exfoliation of HOPG. a) Adhesive tape is pressed against a HOPG crystal so that the top few layers are attached to the tape; b) c) The tape with layered material is pressed against a substrate's surface. d) Upon peeling off, the bottom layer is left on the substrate. f) Typically used adhesive tape for exfoliation. Ref. [26]; Copyright 2012, the Royal Swedish Academy of Sciences.

With all these distinguished properties and promising applications, mass production methods of graphene became one of most important research directions. Actually, producing methods of graphene were indeed developed very fast since Geim and Novoselov first isolated graphene from graphite. Nowadays, tens of graphene manufacturing companies have sprung up all over the world, which produce not only small graphene sheets but also large-area, high-quality graphene films on an industrial scale (Fig 1-4).⁵³

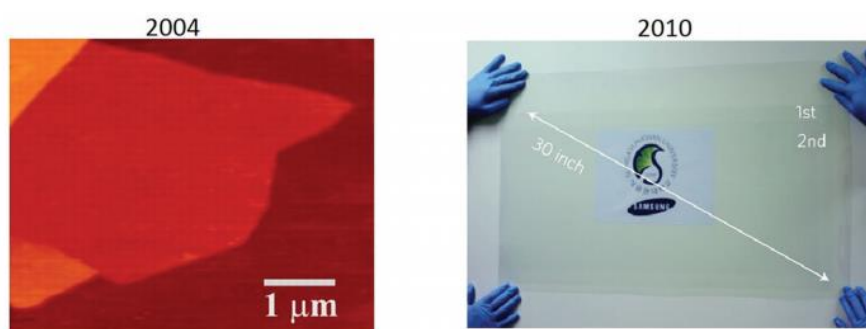


Figure 1-4. Rapid evolution of graphene production: from microscale flakes to roll-to-roll processing.

Ref. [53]; Copyright: the Royal Society of Chemistry 2015

The mechanical exfoliation indeed provides high-quality graphene and enough quantity for laboratory use, yet this method is incapable of mass production, especially in industrial preparation at a large-scale. Today there are several alternative ways to overcome the above obstacle (Fig. 1-5). One of these methods is liquid-phase exfoliation of graphene, which allows production of defect-free graphene sheets in a range of organic solvents such as *N*-methyl-pyrrolidone (NMP) and *N,N*-

dimethylformamide (DMF).^{54,55} The reason for the successful exfoliation can be explained by the strong interaction between the solvent and graphitic basal planes, which minimizes the energetic barrier for the exfoliation and subsequent dispersion. Graphene can also be prepared by sonicating tetrabutylammonium hydroxide (TBA) and oleum-intercalated graphite in DMF to provide high-quality graphene sheets. It was also reported that graphene dispersions can be produced in the presence of 1-pyrenecarboxylic acid⁵⁶ in relatively high yields. The good processability of these methods allows the deposition on insulating substrates and preparation of transparent electrodes by standard methods such as drop-casting, spin-coating, as well as inkjet printing.⁵⁷⁻⁵⁹ All of the liquid-phase methods mentioned so far use ultrasonic energy to drive the exfoliation. However, ultrasonication led to decrease of the size of produced graphene flakes, in particular when long sonication processes were required. Besides exfoliation using sonication as driven force, several other approaches have been reported as well, such as one driven by negatively charged complexes in polycarbonate electrolytes,⁶⁰ and electrochemical exfoliation of HOPG crystals in sulfuric acid to produce single and few layer graphene.

Apart from the solution exfoliation of graphite, another way to prepare graphene is through the formation of graphene oxide (GO). The preparation of GO was first reported in 1859 by Brodie through treatment of graphite with strong acids (sulfuric and nitric acids), as well as oxidants, such as KClO_3 .⁶¹ This method was modified and optimized afterwards by Hummers et al. in 1958, who used sulfuric acid, sodium nitrate, and potassium permanganate.⁶² This Hummers' method became the most frequently used protocol for the preparation of GO since then. Resulting GO can be easily dispersed in water or other organic solvents, and subsequently reduced chemically or thermally to furnish reduced graphene oxide (rGO). The facile preparation and high solution processability of GO provide possibilities to fabricate devices on a variety of substrates and over large areas.⁶³ Nevertheless, GO is intrinsically insulating and rGO also contains considerable structural defects generated during the chemical oxidation reaction, i.e., usually covalently bonded oxygen-containing groups such as hydroxyl and epoxide, which disrupt the electronic structure of graphene. Although rGO shows good electrical properties, it is not comparable with the pristine graphene, and complete reduction of GO to perfect graphene has not been achieved so far.^{64,65}

Chemical vapor deposition (CVD) is another important way of preparing high-quality graphene, especially toward preparing large-area uniform polycrystalline graphene films (Fig. 1-5). The CVD technique has proven efficient for producing large-area graphene layers on transition-metal surfaces such as platinum,⁶⁶ nickel,⁶⁷ and copper.⁶⁸ One remarkable progress of the CVD graphene synthesis was achieved by Bae et al., who reported growth of a monolayer graphene extending over 30 inches

in size on a copper foil (Fig. 1-4, right).⁵³ Despite the successful preparation of CVD graphene on a copper foil in large scale, subsequent device fabrication requires transfer of the CVD graphene from the copper support to a dielectric surface or another substrate of interest. At present, the mass application of CVD process is obstructed by its high cost, owing to large energy consumption and the need to remove the underlying metal support layer. Another disadvantage of CVD graphene is the formation of structural defects especially in the grain boundaries and the presence of few layer regions, which lead to lower mobilities compared to that of mechanically exfoliated graphene.⁶⁹⁻⁷¹

Another frequently used method for the fabrication of graphene is epitaxial growth by using silicon carbide (SiC). It has been reported that graphitic layers can be grown either on the silicon or carbon faces of a SiC wafer by sublimating Si atoms, thus leaving a graphitized surface.^{23,52,72-75} The resulting graphene can show very high quality, with crystallites approaching hundreds of micrometers in size.⁷⁶ Interestingly, the electronic properties of the resulting graphene starkly depend on the face used for the growth.^{69,77} The multi-layer graphene grown on the carbon face has higher mobility compared with those grown on silicon face.^{73,77} Furthermore, the number of graphene layers can be easily controlled on the silicon face, which makes the graphene grown on silicon faces more compatible for application in electronics.^{78,79} However, this method suffers from two drawbacks, which are the high cost of SiC wafers and high temperatures used ($> 1,000$ °C).

Besides all above-mentioned remarkable methods, another emerging method for fabricating graphene structures is surface-assisted or solution-mediated coupling of molecular precursors into linear or 2D polyphenylenes with subsequent cyclodehydrogenation. By using this method, high-quality sub-structures of graphene such as graphene nanoribbons (GNRs) and nanographene molecules (NGs) can be obtained through a chemistry-driven bottom-up approach. These graphene nanostructures have significant meaning not only because they can be considered as graphene fragments and model compounds, which lead to deeper understanding of graphene, but also because of their unique electronic properties compared to pristine graphene. Even though graphene has a series of extraordinary properties, it is actually a zero-bandgap material, which means that the conduction of graphene cannot be switched off. The zero-bandgap nature of graphene definitely hinders its further application in FET devices. However, the theoretical study predicted that the 2D quantum confinement of infinite graphene into NGs or GNRs can open up a bandgap, and in the case of GNRs the energy gap scales inversely proportional to the width.^{90,91} Therefore, cutting the graphene into nanometer-wide small pieces (NGs) or strips (GNRs) seems to be the most straightforward manner to fabricate graphene structures with tailorable bandgaps.

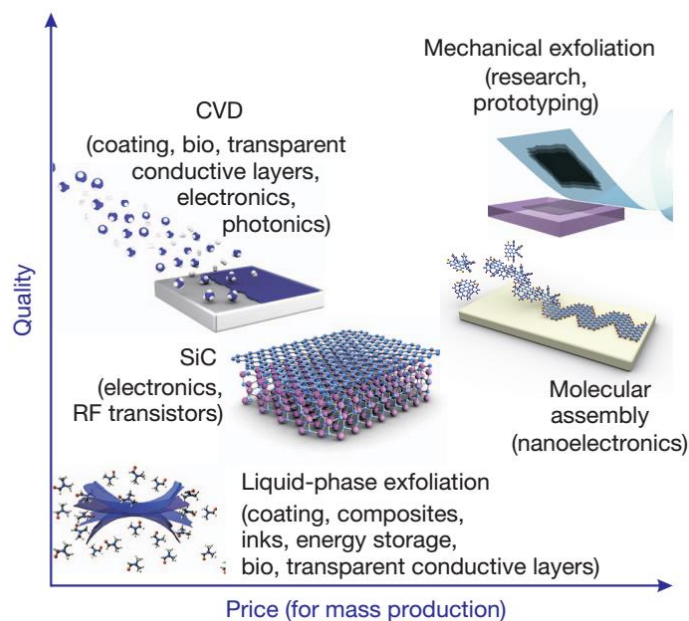


Figure 1-5. Several methods of mass-production of graphene, which allow a wide choice in terms of size, quality and price for any particular application. Ref. [29]; Copyright: 2012, Nature publishing group.

1.3 Nanographene molecules (NGs)

Nanographene can be defined as a graphene fragment which has a sizes span from 1 to 100 nm from top-down point of view. And from bottom-up perspective, NGs could be seen as big PAH molecules, which are sub-structures of graphene with defined shapes and sizes. The NGs can also be defined as expanded 2D polymers of arene networks.

NGs or larger PAHs have significant meaning as model compounds of infinite graphene, and in the studies of their self-assembling behavior, and electronic properties in organic devices. Usually there are two methods to prepare NGs including top-down approach and bottom-up approach. In the early times, small NGs, namely PAHs with sizes less than 2 nm such as pyrene, naphthalene, usually could be obtained from distillation of mixtures of coal tar^{80,81} and side-products of the catalytic hydrocracking of petroleum.⁸²⁻⁸⁴ Even some PAHs only exist in minor amounts in the crude material could be obtained in reasonable amounts due to the industrial scale of process. A single layer nanographene sheets with a size of approximately 10 nm were prepared in 2001 through heat-induced conversion of nanodiamond particles on HOPG.⁸⁵ More recently, production of geometrically well-defined graphene quantum dots (GODs), which have perfect hexagonal shapes and sizes (5 nm in size), were also realized in 30% yield based on the cage opening of C₆₀ on a

ruthenium surface.⁸⁶ In this process, the strong C₆₀-ruthenium interaction induced the formation of surface vacancies in the ruthenium single crystal and a subsequent embedding of C₆₀ molecules on the surface. At elevated temperatures, the embedded C₆₀ molecules produced carbon clusters that underwent diffusion and aggregation to form GODs. Moreover, graphene oxide and graphite have also been used to generate small graphene fragments, such as nanographene oxide and graphene dots. These nanostructures displayed wavelength-dependent emission behavior, which allowed their application in photovoltaic devices, cellular imaging, and drug delivery.⁸⁷ However, further applications and electronic property study of these nanographene species are hindered by their poorly defined structures.

On the contrary, the bottom-up approach could offer NGs with defined size and shape through the versatile organic chemistry. In the early 20th century, pioneering studies were carried out by Scholl, Clar, and Zander,⁸⁸⁻⁹³ who addressed a number of bottom-up methodologies for the direct synthesis and characterization of PAHs, which could further be extended to NG molecules. The earliest synthetic methods to NG molecules used relatively vigorous reaction conditions such as high temperature and pressure. However, modern organic synthesis enables preparation of NG molecules through much milder methods, which also offer better selectivity and higher yields.

1.3.1 Classification of nanographene molecules (NGs)

Like graphene, NGs generated from either top-down or bottom-up approaches have two kinds of distinct edge structures - armchair and zigzag edge. The NGs could be further classified into three types according to their edge structures, i.e., NGs with only zigzag edges, ones with only armchair edges, and ones with hybrid edges of armchair and zigzag (Fig. 1-6).

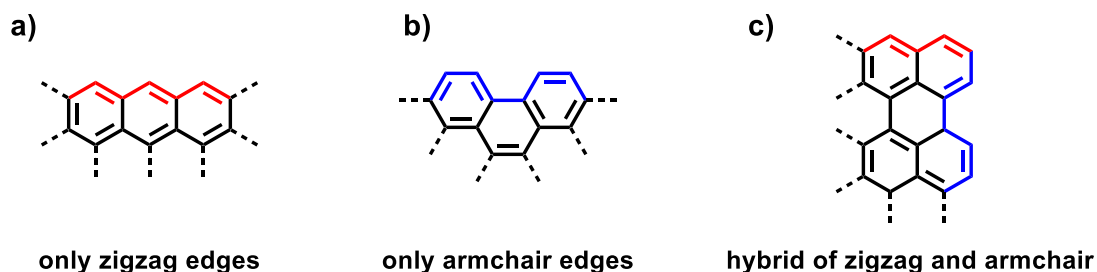


Figure 1-6. Representative edges structures of NGs with only zigzag edges (a), with only armchair edges (b), and with both zigzag and armchair edges (c)

1.3.1.1 NGs with only zigzag edges

NGs with only zigzag edges could be seen as cutout of graphene with a zigzag motif, or series of benzene rings fused in a triangular manner. Because of the special shape and edge structure, this sort of NGs are usually claimed to have a non-Kekulé structure or open-shell structure, which inevitably results in one or more unpaired electrons within the molecule. One of classic and smallest members in this family is phenalenyl radical **1-1**, which is composed of three benzene rings fused in triangular manner. It possesses one unpaired electron and spin multiplicity $2S + 1 = 2$. Extension of π -conjugation of **1-1** in triangular manner results in compound **1-2**, which have two unpaired electrons and a triplet ground state. Further extension leads to compound **1-3** with three unpaired electrons and higher spin state (Fig. 1-7). Moreover, it's worth noting that these systems have a large delocalization of spin densities over the entire molecule. But the largest coefficient still resides on the periphery of the molecule, which means that the edges are still more exposed than the core.

The unique electronic and spin characteristic of these zigzag NGs offers the promising potentialities in the field of electronics and spintronic devices.⁹⁴ However, synthesis of NGs with only zigzag edges is highly challenging. The intrinsic nature of “open-shell” systems, such as the low stability or high reactivity, obstructs their synthesis, isolation and application. Generally the decomposition of these systems is ascribed to the side reaction of generated radicals species, including dimerization, hydrogen abstraction, and oxidation. Thanks to the deeper understanding of the decomposition mechanism and development of the modern organic chemistry, many methods have been conceived to stabilize these systems, such as protection with steric bulky groups, employment of heteroatoms in the aromatic system, and fusion with other aromatic skeletons.

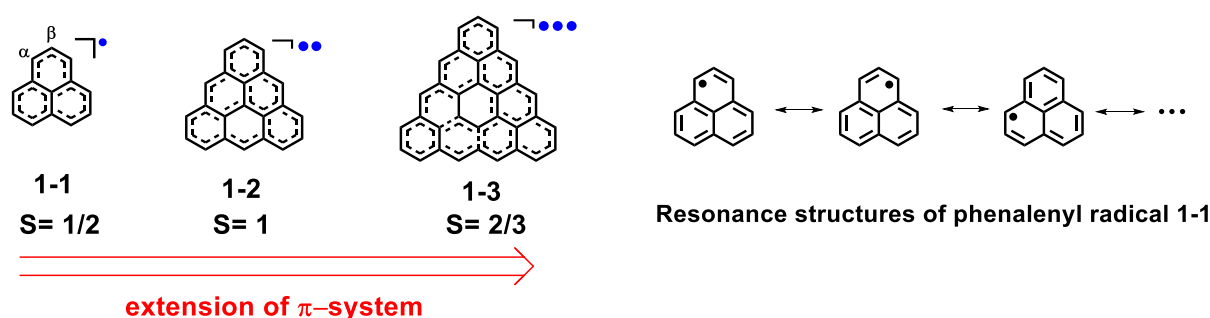


Figure 1-7. Phenalenyl radical **1-1** and its resonance structures; Extension of the π -conjugated system offers compound **1-2** and **1-3** with higher spin states.

The phenalenyl radical **1-1** is the representation of the most fundamental and widely investigated member in phenalenyl-based monoradicals' family. As shown in Fig. 1-6, the radical **1-1** has a planar, rigid structure with a spin spread over the whole molecular skeleton. Its resonance structures also show that the spin density is predominantly at its α position, while the spin density at the β position is much smaller. The reason can be explained by the spin polarization effect. Compound **1-1** displays high amphoteric redox ability with thermodynamically stable cation, neutral radical, and anion species. The first study of **1-1** in 1950s revealed that it can only be handled in solution under inert conditions due to its high reactivity.⁹⁵ Because of its kinetic instability caused by immediate intermolecular σ -bond formation and oxidation by air, preparation of phenalenyl radical species has mainly been performed in degassed solutions and sealed conditions over the past 50 years.

The first isolation of a phenalenyl radical in the solid state in air was accomplished in 1999, when Nakasuji et al. synthesized compound **1-4** (Fig. 1-8a), installing three *tert*-butyl groups on the β positions. Obtained as a deep blue needle, **1-4** showed high stability when exposed to air. Nevertheless, it decomposed gradually after 1 week by changing into phenalanone and other byproducts.⁹⁶ Based on the same principle, phenalenyl radical derivatives with other substituents at the β position, such as alkoxy,⁹⁷ hydroxyl, amino,^{98,99} and N-S-N groups,¹⁰⁰ have also been synthesized and studied. One interesting case among them was perchlorophenalenyl radical **1-5** with full chlorination at the edges, which was prepared by Haddon et al. in 1987¹⁰¹ and the X-ray crystal structure was obtained in 2001.¹⁰² Radical **1-5** also shows a high stability in air. The thiolation is another alternate way to stabilize phenalenyl radical species. As shown in Fig. 1-8a, dithiophenalenyl **1-6** was first prepared in 1978 and it can survive in the solid state in air for 1 day but decomposed quickly in solution.¹⁰³ Apart from modification around the periphery of phenalenyl, introduction of heteroatoms within the phenalenyl moiety has also been proven as an effective way to stabilize phenalenyl radical. A typical example is compound **1-7** which was obtained in 2002 as a green crystal and showed increased stability in air due to heteroatomic modification.¹⁰⁴ All above mentioned species possess similar electronic structures with phenalenyl radicals which exhibit stronger positive spin densities at α positions. Additionally, introduction of two oxygen atoms leads to a new series of radicals termed "oxophenalenoxyls". The two oxygen atoms could be introduced at " α - α " or " α - β " positions. Compound **1-8** shown in Fig. 1-8 is one example of these kinds of oxophenalenoxyls, which has enough kinetic stability to be handled in air.^{105,106}

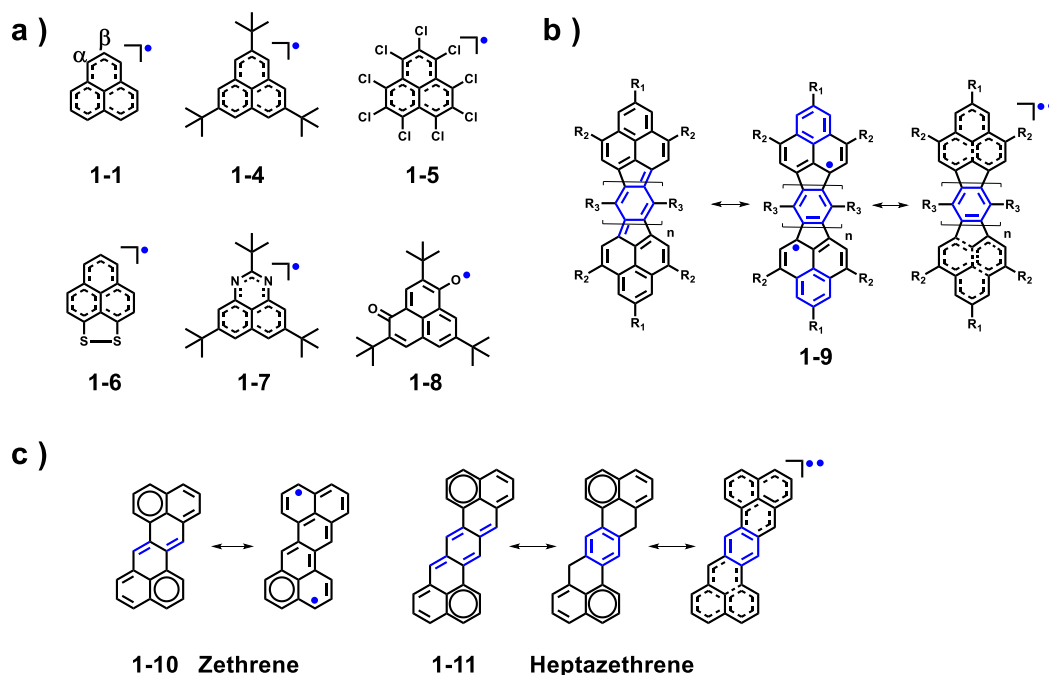


Figure 1-8. Typical stable phenalenyl radical and its derivatives

Extension of a π -conjugated system is an alternative way towards stable phenalenyl radicals, including linking of two phenalenyl moieties with an aromatic bridge to reduce singlet biradical character with Kekulé structural resonance (Fig. 1-8b), and “head-to-head” fusion of two phenalenyl moieties to give a series of NGs that are named “zethrenes” for their unique Z-shaped skeleton (Fig. 1-8c, left). Extending fused benzene rings in a similar Z-shape manner, longitudinal homologues of zethrene can be obtained, which are named as heptazethrene (Fig. 1-8c, right). All these novel type of phenalenyl species have been investigated widely by Kubo’s,¹⁰⁷ Tobe’s,¹⁰⁸ and Wu’s groups¹⁰⁹. These “zethrene” homologues also displayed reasonable stability and intrinsic spin characters.

The NGs with only zigzag edges have suffered from their low stability and lack of efficient synthetic methods for a long time. However, as the emergence of novel efficient synthetic methods such as employing bulky protecting groups to stabilize whole system, more and more breakthroughs have been achieved.

1.3.1.2 NGs with only armchair edges

Cutting graphene into defined fragments with fully armchair edge gives NGs, which often have a “close-shell” character. Because their chemical structures can be depicted in an all-benzenoid manner without additional isolated double bonds, they usually exhibit high stability and relatively large band gaps. Furthermore, they also display intriguing self-assembly behavior. For example, triphenylene homologues bearing flexible substituents can form a hexagonal columnar mesophase, and they are one of the most extensively investigated classes of columnar liquid crystals.¹⁰ All these characteristics render them as potential candidates in electronic applications and boost the field of synthesizing all-benzenoid NG systems in last decades.

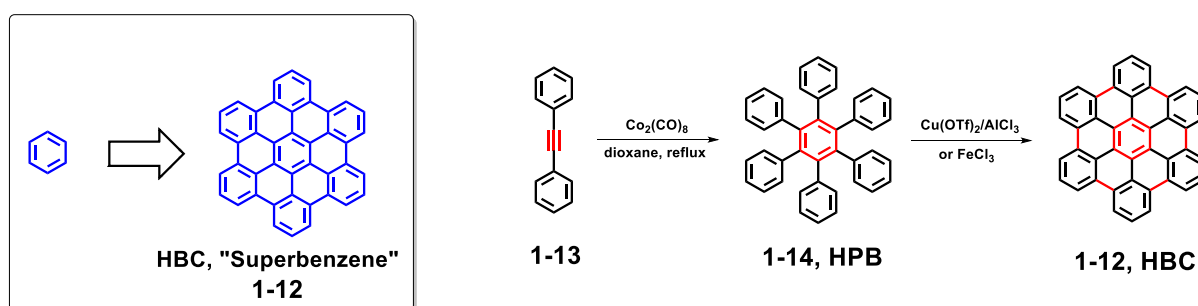


Figure 1-9. Chemical structure of HBC molecule and synthetic route developed by Prof. Müllen’s group.¹²⁶

Hexa-*peri*-hexabenzocoronene, often abbreviated HBC, is the most famous and widely investigated case among this class of NGs. HBC has D_{6h} symmetry and can be depicted as fusion of seven benzene rings in structure, which can also be viewed as “superbenzene” (Fig.1-9). The synthesis of HBC has been achieved for the first time in 1958 by Clar et al.^{110,111} and Halleux et al.¹¹², and later in 1986 by Schmidt et al.¹¹³ However, all synthetic methods used by above-mentioned groups to obtain HBC suffered from requirement of harsh reaction conditions, low overall yield as well as complicated experimental workup procedures. Later in 1995, a milder and highly efficient synthesis procedure towards HBC (Fig. 1-9) was developed by Müllen et al. which was based on oxidative cyclodehydrogenation of hexaphenylbenzene (HPB) as a precursor.¹¹⁴ This remarkable work led to a golden age of HBC and its derivatives as well as other all-benzenoid NGs synthesis and applications.

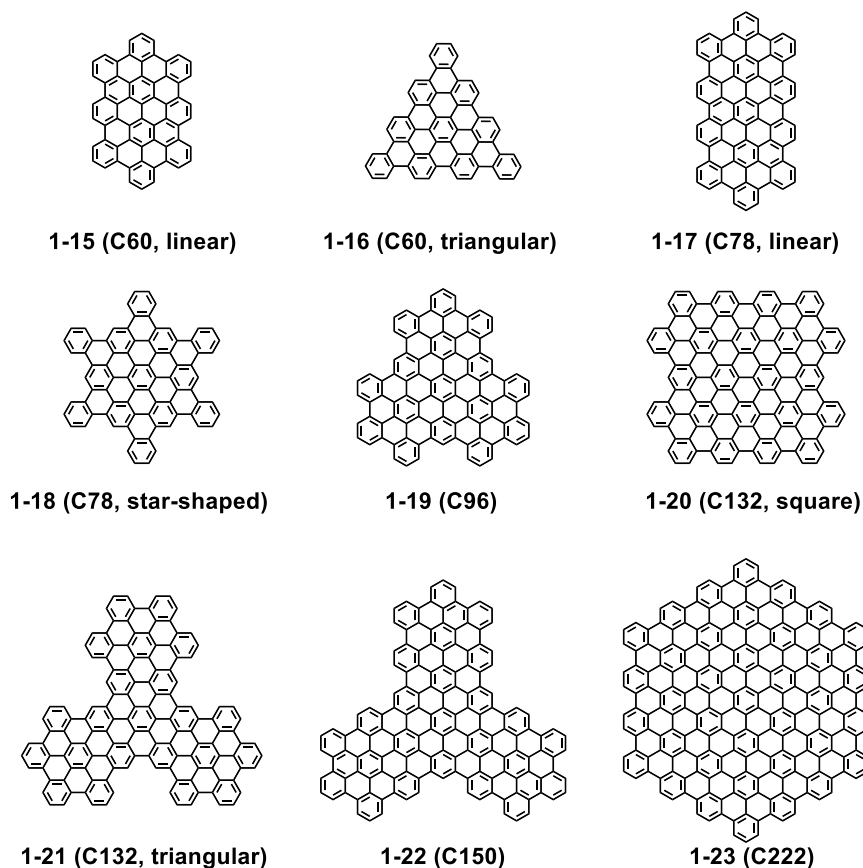


Figure 1-10. Chemical structures of representative π -conjugate extended NGs

By using FeCl_3 and $\text{Cu}(\text{OTf})_2\text{-AlCl}_3$ mediated oxidative cyclodehydrogenation reaction (also known as Scholl reaction), series of larger all-benzenoid NGs with variable shapes and sizes have been synthesized, including C60 with linear (**1-15**)¹¹⁵ and triangular (**1-16**)¹¹⁶ structures, C78 with linear (**1-17**)¹¹⁷ and star-shaped (**1-18**)¹¹⁸ structures, C96 (**1-19**)^{119,120}, C132 with square (**1-20**)^{121,122} and triangular (**1-21**)¹¹⁹ structures, C150 (**1-22**)¹²⁰, and C222 (**1-23**)¹²³. The numbers displayed in above abbreviations of NGs, which span from 60 to 222, indicate the number of carbon atoms in the aromatic core (Fig.1-10). As the extension of the size of aromatic core, the π - π intermolecular interaction should be enhanced as well due to the larger overlap of the π -surface, which can be essential for the organic electronic device studies. However, the stronger π - π intermolecular interactions can also decrease the solubility of NGs, which will further lead to difficulties in obtaining reliable structural characterization in the solution as well as processing methods for applications.

1.3.1.3 NGs with hybrid of zigzag and armchair edges

Cutting graphene into a rectangular fragment results novel NG structures accompanied by both zigzag and armchair edges. Compared to the NGs with only zigzag edges and only armchair, this new type of NG can all be depicted as a typical Kekulé structures. Furthermore, the NGs in this category benefit from hybrid of zigzag and armchair edges. The armchair edge provides enhanced stability and the zigzag edges can lead to a narrowed bandgap.

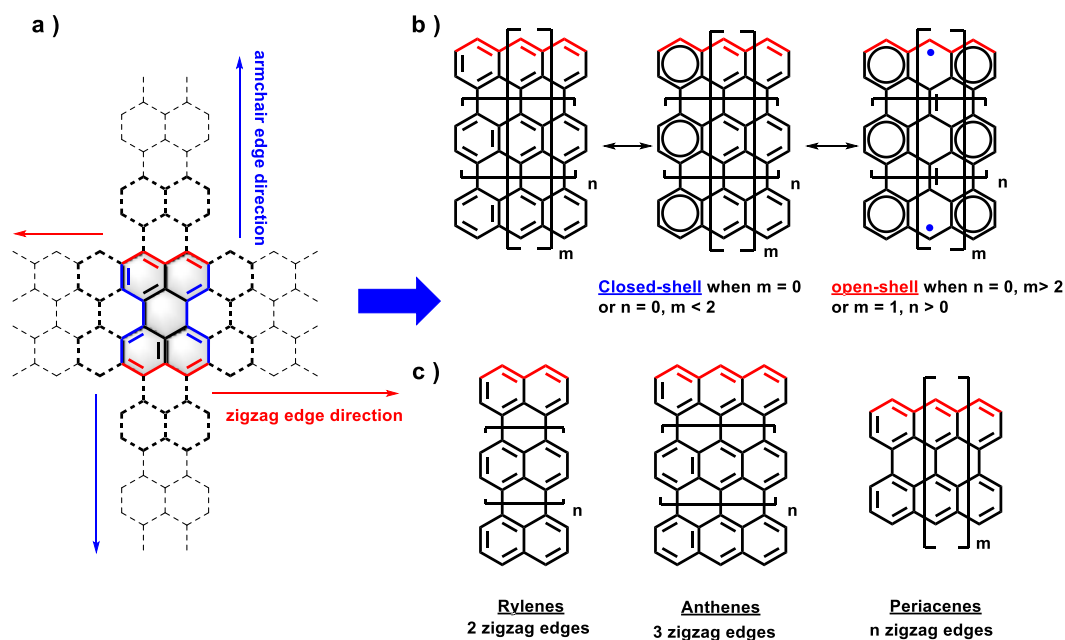


Figure 1-11. Chemical structures of NGs with both zigzag and armchair edges and general classifications.

As displayed in Fig.1-11a, rylene can be seen as basic unit of this class of NG. The π -conjugated system can be extended along the armchair direction, zigzag direction or both directions. Generally these rylene-based novel NGs with a hybrid of armchair and zigzag edges can be classified into three types (Fig.1-11c), including: 1) rylenes, namely *peri*-fused naphthalenes, which preserve two zigzag edges and extended conjugation along the armchair edges direction; 2) anthenes, namely *peri*-fused anthracenes, which preserve three zigzag edges and extended armchair edges; 3) periacenes which preserve two armchair edges and extended zigzag edges. The stability of rylene homologues can be predicted according to Clar's aromatic sextet rule, by counting the number of sextet rings for a given system as shown in Fig 1-10b which show their resonance structures. Usually more sextet rings lead to a more stable system. Moreover, an open-shell biradical character will be generated under particular conditions such as extension of the conjugation ($n = 0, m > 2$ or $m = 1, n > 0$). These open-shell NGs have a narrower bandgap and extra stability compared to NGs with only zigzag edges, which can be ascribed to more Clar's sextet rings in the biradical form.

Based on the numbers of fused naphthalenes, rylenes could be named as perylene, terrylene, and so on. Rylenes have been attracting lots of attention as promising candidates in dye chemistry for their high stability and extinction coefficients and long-wavelength absorption/emission. However, there are two main obstacles that hinder the preparation of high-order rylenes ($n \geq 1$). One is that high-order rylenes are too electron-rich to be stable upon exposure to air. The other is that the rigid molecular skeleton will lead to a high tendency of aggregation in solution and poor solubility. To solve the problems mentioned above, mild reaction conditions and reasonable substituents are needed to be investigated and employed.

In 1990, Müllen et al. synthesized series of rylenes from **1-24a** to **1-24c**, which were functionalized with four *tert*-butyl groups to enhance the solubility.^{124,125} However, although the *tert*-butyl group works well in improving solubility of rylenes **1-24a** and **1-24b**, the solubility of quaterrylene **1-24c** is too low to show resolved peaks in ¹H-NMR characterization. In 2010, a remarkable breakthrough has been achieved to further improve the solubility and stability of rylenes, which is introduction of the dicarboxylic imide functional groups (Fig. 1-12, top). The imide group is an electron-withdrawing group, and thus it could help stabilize the electron-rich rylene cores by reducing the electron density. Additionally, the introduction of bulky R₁ substituents such as diisopropylphenyl or other long alkyl chains on the imide could prevent aggregation. Besides, the solubility can be further improved by introducing substitution R₂ in the bay region of rylene cores. Thanks to the enhanced stability and solubility with the imide groups, high-order rylene bisimides could be obtained, such as pentarylene bisimide (**1-25d**) and hexarylene bisimide (**1-25e**) as well as heptarylene bisimide and octarylene bisimide, which were all synthesized by Müllen et al.¹²⁶ High-order rylene bisimides are expected to exhibit a larger π -conjugation and concomitant better light-harvesting property, so they are promising in the field of organic solar cells and field-effect transistors (FETs) as semiconducting materials.¹²⁷ Moreover, Bao's group recently developed a scalable synthesis of quaterrylene bisimides **1-27** and **1-28**, which can be processed from solution thanks to swallow-tailed chains, namely branched alkyl groups, attached to nitrogen atoms of bisimides. This method opens up a new route to fabricate crystalline thin films based on solution processed higher rylene bisimides.¹²⁸

Another case is anthenes. When two anthracene units are fused together by three single bonds between neighboring anthryls, it is named as bisanthene (Fig.1-12, down-left, $n = 0$, **1-29**), and extended homologues are named as teranthene (**1-30**) and quateranthene (**1-31**).

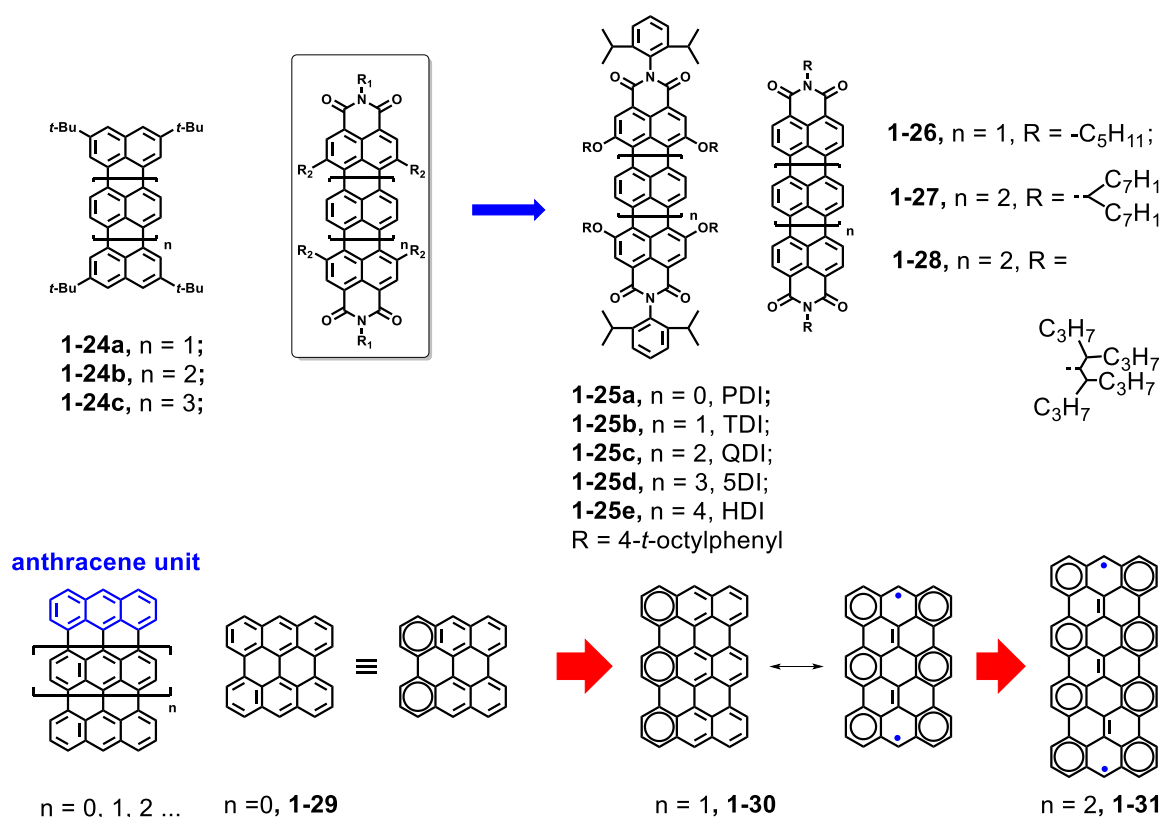


Figure 1-12. Chemical structures of rylenes and anthenes.

Compared with the rylenes, the anthenes exhibit even lower bandgaps and stability with the presence of more zigzag edges and extended π -conjugation. In particular, higher anthenes from teranthene ($n = 1$, **1-30**) display a large singlet biradical character in the ground state. The reason can be ascribed to the narrowed HOMO-LUMO gaps and recovery of more sextet benzenoid rings, i.e., two resonance structures of teranthene (Fig.1-12, down-right), having three sextet benzenoid rings on the left compared to six sextet benzenoid rings with biradical on the right.

The most representative member of this family is bisanthene, which was firstly reported by Clar and improved by Scott's¹²⁹ and Wu's¹³⁰ group. Actually, the parent bisanthene is unstable due to its high-lying HOMO energy level, and the most reactive sites are the *meso*-positions of the zigzag edges. It is easily oxidized when exposed to air. Therefore, it is necessary to introduce protecting groups on the zigzag edges to stabilize bisanthene core as well as improve the solubility to enable further characterizations and applications. Similar to rylenes, electron-withdrawing imide groups can be employed on the zigzag edges, which can effectively stabilize the bisanthene aromatic core. As shown in Fig.1-13a, compound **1-32** synthesized by Wu et al. has been proven to have good stability and is promising candidate for NIR absorbing materials.¹³¹ An alternative way was also developed

by Wu's group, which protected the *meso*-position of zigzag edges with bulky aryl or alkyl groups. The *meso*-substituted compounds **1-33a** – **1-33c** (Fig.1-13a) were synthesized successfully with enhanced stability and solubility as well as absorption/emission in the NIR region.¹³²

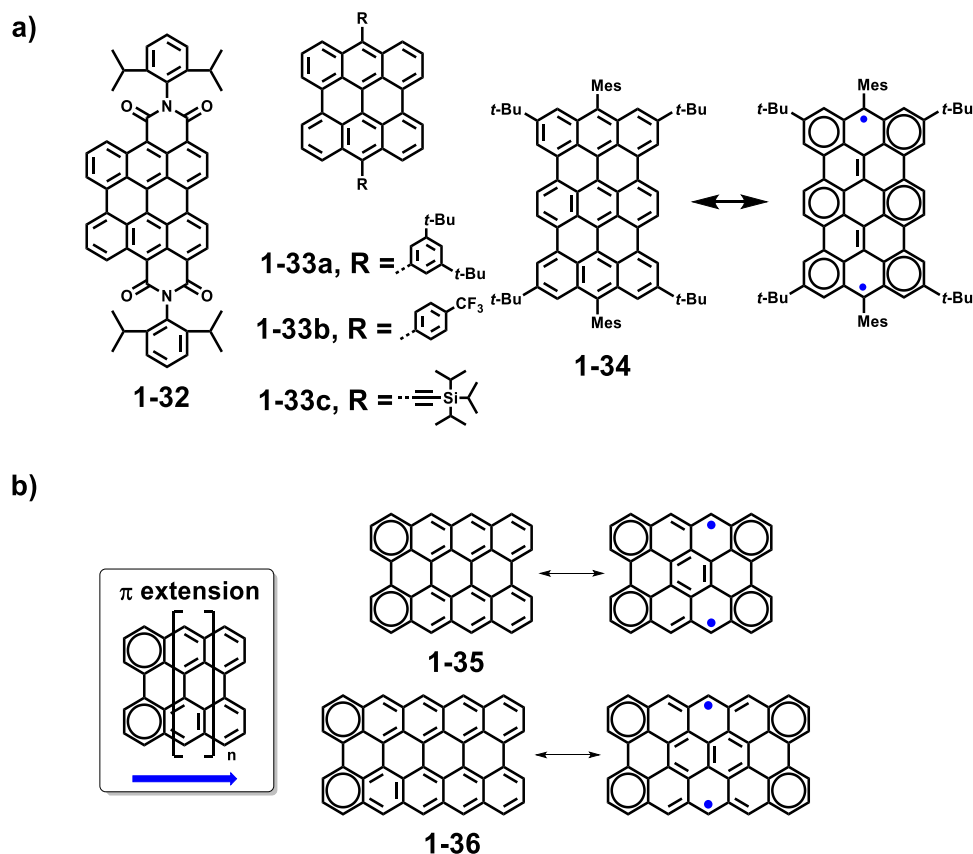


Figure 1-13. Typical examples of a) bisanthene and b) anthenes.

Besides bisanthene, synthesis of stable teranthene is a big challenge. The first teranthene derivative **1-34** has been reported by Kubo's group recently.¹³³ With the resonance structures shown in Fig.1-13b, compound **1-34** exhibits moderate stability in solution with a half-life of around 3 days upon exposure to air at room temperature.

The last class of NGs with both armchair and zigzag edges is called periacenes, which can be defined as NGs with constant armchair edges and extending zigzag edges. Typical examples are peritetracene (**1-35**) and peripentacene (**1-36**), which are displayed in Fig. 1-13b. However, the extremely low stability of these periacenes compared to rylenes and anthenes impedes the synthesis. Even the simplest member of this family: peritetracene **1-35** has not been achieved yet.

1.3.2 Methods of synthesizing NGs

In the early times, smaller NGs (or PAHs) such as naphthalene and anthracene were often isolated from mixtures of coal tar or side products from the catalytic hydrocracking of petroleum. However, it is impossible to obtain all smaller NGs via above procedure. The reason can be ascribed to two main aspects: 1) some small NGs only exist in small amounts in nature, e.g., in crude materials such as oil shale; 2) big NGs or complex NGs can only be produced by synthetic procedure to give a reasonable amount. Generally, the idea of synthesizing NGs usually involves preparation of appropriate small PAH skeletons and/or branched oligophenylenes by various reactions such as carbon-carbon coupling reaction, cyclotrimerization, and Diels-Alder reaction, followed by oxidative cyclodehydrogenation to fuse and planarize the rotating benzene rings.

1.3.2.1 Friedel-Crafts Condensation

One of the representative cases is the synthetic procedure towards phenanthrene by using *Friedel-Crafts* condensation, which was developed by Haworth's group.¹³⁴⁻¹³⁷ As displayed in Fig. 1-14, the condensation of naphthalene **1-37** with succinic anhydrides **1-38** gives keto-acid product **1-39**, and then following reduction and intramolecular *Friedel-Crafts* acylation yield ketone **1-41**. The final reduction and aromatization gives desired product phenanthrene **1-43**.

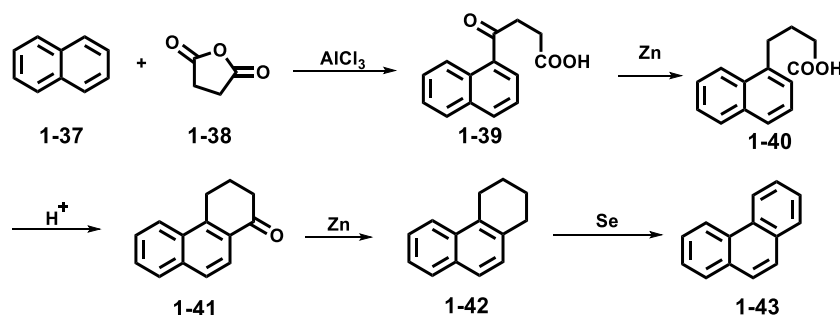


Figure 1-14. Haworth's method towards phenanthrene synthesis.

1.3.2.2 Diels-Alder Cycloaddition and Cyclotrimerization

Diels-Alder reaction is a reaction between a conjugated diene and a substituted alkene to form a substituted cyclohexene system. This reaction is often used to extend conjugated systems and build desired aromatic skeletons. One typical example is the Diels-Alder cycloaddition reaction between perylene (**1-44**) and maleic anhydride (**1-45**) to yield coronene (**1-49**), which was developed by E. Clar and M. Zander (Fig. 1-15).¹³⁸

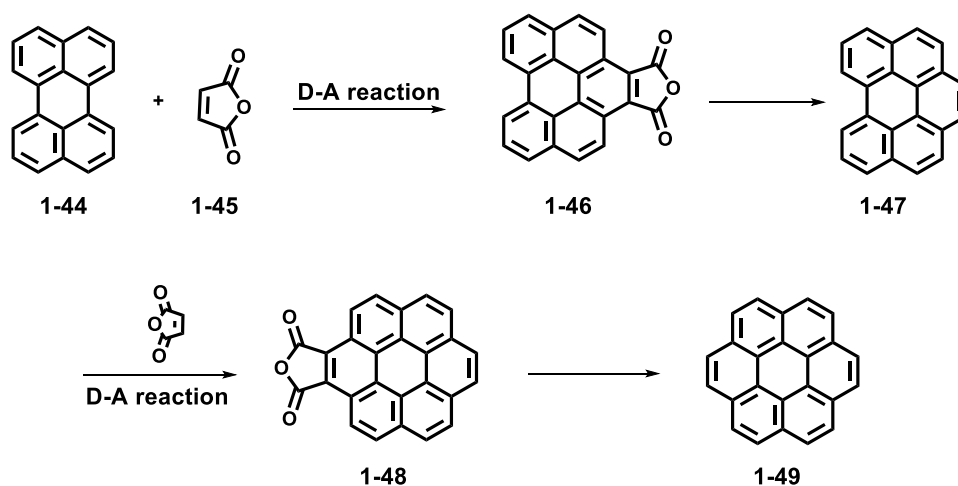


Figure 1-15. Diels-Alder cycloaddition towards coronene.

Another classical example is the synthesis of hexa-*peri*-hexabenzocoronene (HBC). As displayed in Fig. 1-16, a synthetic route including Diels-Alder cycloaddition between tetraphenylcyclopentadienone (1-50) and diphenylacetylene (1-51) gives cycloaddition product 1-52, and subsequent oxidative cyclodehydrogenation yield final HBC molecule.^{139,140}

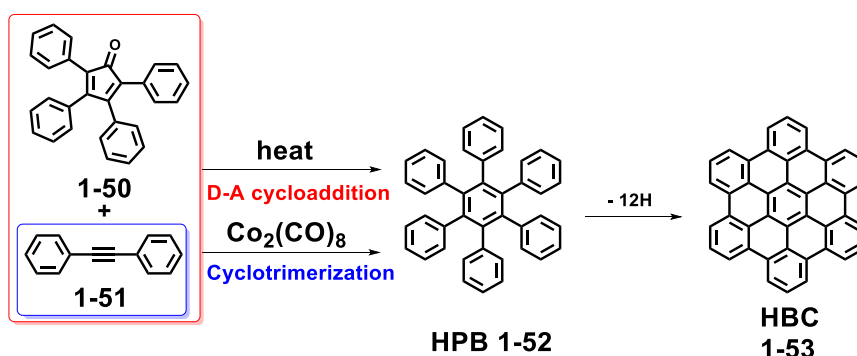


Figure 1-16. Synthetic route toward HBC via Diels-Alder cycloaddition.

Cyclotrimerization is an alternative synthetic method to build a benzene core and has been used by Müllen's group to prepare HBC and its derivatives (Fig.1-16).^{114,141,142} The starting material diphenylacetylene 1-51 can be cyclotrimerized by cobalt catalyst to form HPB 1-52; the final cyclodehydrogenation reaction gives desired HBC product. The above mentioned two methods have been already successfully and widely used in synthesizing series of HBC derivatives as well as other larger NGs span from C60 and C78 to C222.

1.3.2.3 Photocyclization

There was a long history of utilizing photo-induced cyclization in the synthesis of small NGs. One of the classical cases is the synthesis of phenanthrene **1-43** from stilbene **1-54**. The procedure was developed by Mallory et al. in 1964.¹⁴³ Based on the same synthetic procedure, triphenylene **1-56** can be synthesized as well from its precursor **1-55**. This photocyclization method can also be employed in the synthesis of NGs with larger conjugated systems, such as star-shaped NG molecule **1-57**, starting from the precursor molecule **1-56** (Fig. 1-17).¹⁴⁴

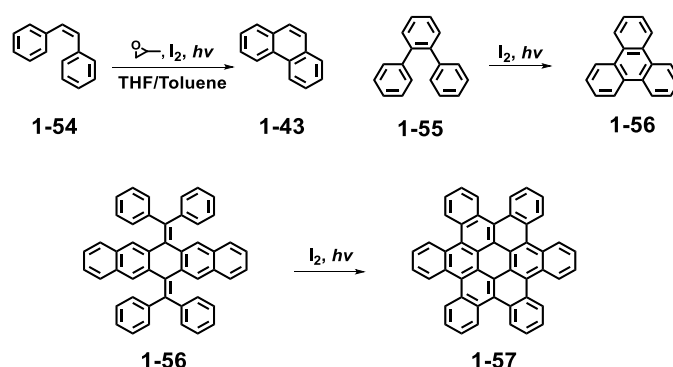


Figure 1-17. Photocyclization reactions used in synthesis of NGs.

1.3.2.4 Oxidative Cyclodehydrogenation

In 1995, Müllen's group developed a powerful method to fuse appropriate oligophenylene precursors, which led to the formation of various planar all benzenoid NG molecules by using the combination of oxidant and Lewis acid catalysts.¹⁴² This method is usually termed as oxidative cyclodehydrogenation. The HPB precursor can be further cyclodehydrogenated via different catalytic conditions, such as 1) CuCl₂-AlCl₃ condition; 2) Cu(OTf)₂-AlCl₃ condition; 3) FeCl₃ condition. For the former two conditions, copper salt act as an oxidant and aluminum salt act as Lewis acid catalyst. For the latter condition, the iron (III) chloride acts as both oxidant and Lewis acid catalyst.

1.3.2.5 Surface-assisted Cyclodehydrogenation

In 2010, Müllen and Fasel et al. claimed a feasible method of synthesizing triangular NG molecule **1-59** via a surface-assisted intramolecular cyclodehydrogenation.¹⁴⁵ The reaction was performed on a Cu(111) surface with vacuum-sublimed cyclic polyphenylene: cyclohexa-*o-p-o-p-o-p*-phenylene (CHP, **1-58**). Then the substrate was annealed to 230 °C to give a planarized product **1-59** (Fig. 1-18, left). The structurally defined NG molecule **1-59** can be visualized by *in-situ* scanning tunneling microscopy (STM) (Fig. 1-18, right)

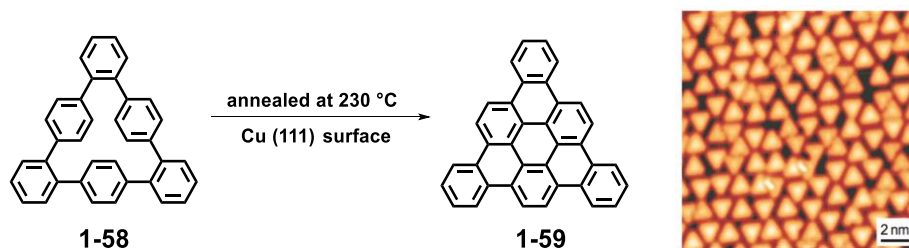


Figure 1-18. Surface-assisted synthesis of triangular NG **1-59** and the STM image of **1-59** on Cu (111) surface by annealing at 230 °C. Ref. [145]; Copyright 2011, Nature publishing group.

1.3.2.6 Other synthetic methods

There are also other synthetic methods useful for the synthesis of NG molecules, including flash vacuum pyrolysis,^{146,147} extrusion of heteroatoms,¹⁴⁸⁻¹⁵⁰ and electrophilic cyclization.¹⁵¹⁻¹⁵³ These synthetic methods open up new horizon in designing and synthesizing novel NG molecules. Besides, some new facile and efficient route emerged as well. For example, a self-sorting assemble strategy has been developed (Fig. 1-19) to give a new way in synthesizing 3-fold symmetrical and highly substituted hexa-*cata*-hexabenzocoronenes (*c*-HBCs).¹⁵⁴

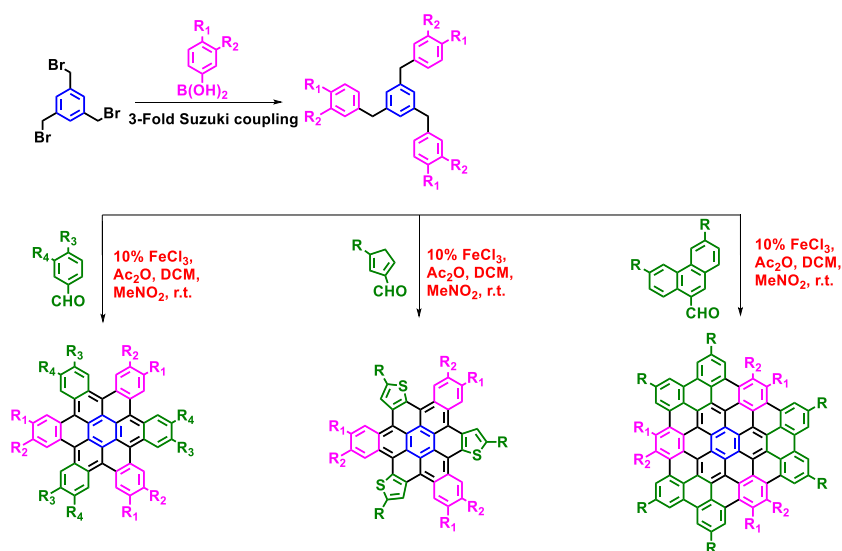


Figure 1-19. Synthetic routes to 3-fold symmetrical and highly substituted hexa-*cata*-hexabenzocoronenes (*c*-HBCs). Ref. [154]; Copyright: 2014, ACS publishing group.

1.4 Graphene nanoribbons (GNRs)

Graphene nanoribbons, abbreviated GNRs, are usually defined as strips cut from pristine graphene with a width below 50 nm. As mentioned above, GNRs preserve tunable bandgaps in

contrast to infinite graphene that exhibits zero-bandgap character. The definition of GNRs was first introduced by Mitsutaka Fujita et al. as a theoretical model to study edge and nanoscale size effect in graphene.¹⁵⁵⁻¹⁵⁷

1.4.1 Classification of GNRs

The GNRs' electronic properties are governed by their edge structures and widths. The GNRs are conventionally classified into two types, namely armchair type and zigzag type, according to their edge structures (Fig.1-20a). The widths of the armchair and zigzag GNRs are depicted as the numbers “ N_a ” and “ N_z ”, respectively. The N_a equals the number shown in figure 1-20a across the armchair type GNRs, and the N_z equals the number of zigzag chains across the zigzag type GNRs. Many theoretical studies have been made to investigate the electronic properties of GNRs. It has been predicted that armchair type GNRs exhibit semiconducting behaviors with a direct bandgaps when especially narrower than 10 nm,^{156,158} and zigzag type GNRs preserve half-metallic properties with zero bandgap (based on the tight banding theory) as well as strongly localized edge state along the zigzag edge.^{156,159}



Figure 1-20. a) Structures of armchair type and zigzag type GNRs. b) Structures of GNRs with “Gulf” and “Cove” edges and hybrid of armchair and zigzag edges.

Additionally, the GNRs can be further classified into more types due to the variety of edge structures besides armchair and zigzag, such as “gulf” and “cove” edge structures, and also hybrids of armchair and zigzag edge structures (Fig. 1-20b). The GNRs with “gulf” and “cove” edge structures are predicted to show semiconducting behaviors with open bandgaps. For the GNRs with hybrids of armchair and zigzag edges, they display no or limited localized states and also behave as semiconductors with open bandgaps.

Similar to the synthesis of NGs, GNRs can also be fabricated through either “top-down” or “bottom-up” approaches. The former approach is fabrication of GNRs from other carbon materials such as pristine graphene, graphite, and carbon nanotube (CNT). The latter approach starts from small units or so-called building blocks. These building blocks are usually small NG molecules with functional groups allowing further longitudinal extension of conjugate system.

1.4.2 Fabrication of GNRs via “top-down” approach

For the “top-down” approach, series of methods have been developed to prepare GNRs, and these methods can be generally divided into two strategies, i.e. 1) cutting or etching of graphene or graphite precursors into one dimensional graphene stripes; 2) unzipping of CNT along the longitudinal direction to corresponding GNRs.

Among the first strategy, cutting of graphene was performed in 2007 by using electron-beam lithographical patterning and subsequent oxygen plasma etching to make GNRs with various widths span from 15 to 500 nm.^{160,161} The following study of these GNRs revealed that their bandgap changes inversely with the lateral width, which is in agreement with the theoretical predictions.^{159,161} The additional investigation of their FETs’ performance showed a high variability which can be ascribed to the defects and undefined edge structure. This approach was further optimized in 2009 by employing chemically synthesized nanowires as the physical protection mask in oxygen plasma etching (Fig. 1-21) to give GNRs with widths down to 6 nm.¹⁶²

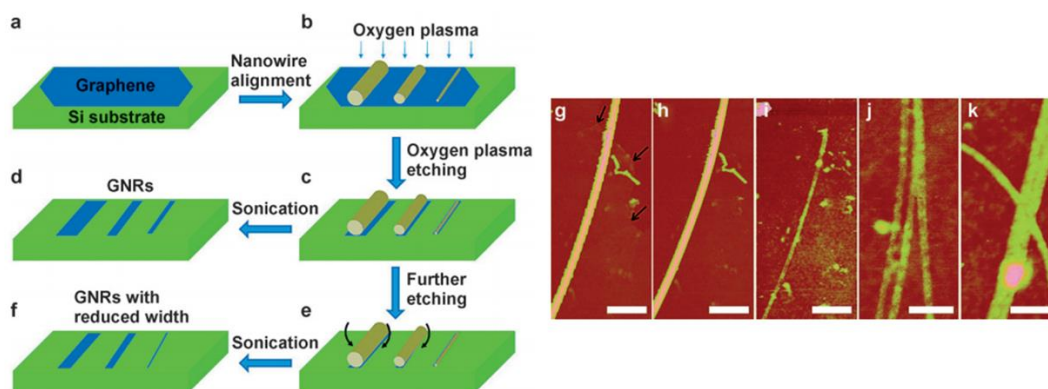


Figure 1-21. a-f) Fabrication process to obtain GNRs by an oxygen plasma etch with a nanowire as protection mask. g, h) AFM images of a nanowire etch mask before (g) and after (h) oxygen plasma etch. i) AFM images of the resulting GNR after sonication. j, k) Branched and crossed graphene nanostructures from merged and crossed nanowire masks. Ref. [162]; Copyright: 2009, American Chemical Society.

An alternative approach was carried out in solution to produce GNRs with widths down to 10 nm from bulk graphite in 2008 by Dai et al.¹⁶³ At the beginning, expanded graphite was prepared by intercalation with sulfuric and nitric acids and subsequent heat treatment at 1000 °C in H₂/Ar

produced a few layered graphene sheets. Afterwards, the sonication of this precursor accompanied with poly(*m*-phenylene-vinylene-2,5-dioctoxy-*p*-phenylenevinylene) (PmPV) resulted a stable dispersion of GNRs. As shown in Fig. 1-22, various widths of GNRs were achieved through this approach. The narrowest GNR with a width of 10 nm had a bandgap (E_g) of approximately 0.4 eV and a remarkable FET performance with high I_{on}/I_{off} ratio of up to 10^6 as well as an estimated hole mobility of ca. 50-200 $\text{cm}^2/\text{V s}$. All these distinguished properties indicated the high quality of GNRs.

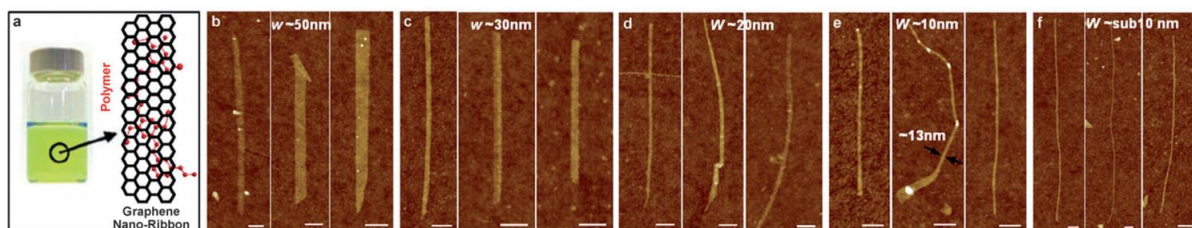


Figure 1-22. a) A stable dispersion of PmPV polymer with suspended GNRs. b-f) AFM images of GNRs with different widths. Ref. [163]; Copyright 2008, American Association for the Advancement of Science.

Another “top-down” approach is based on the cutting of CNTs (Fig.1-23a), which was first claimed in 2009 by Tour et al.^{172,164,165} and Dai et al.¹⁶⁶ They used different methods to realize the fabrication of GNRs from CNTs, i.e., unzipping of CNTs via an oxidative process and via plasma etching process. The oxidative process started from the treatment of multiwalled carbon nanotubes (MWCNTs) (diameter: 40-80 nm) with strong oxidative mixtures of concentrated sulfuric acid (H_2SO_4) and potassium permanganate (KMnO_4) (Fig. 1-23b). As the results of this chemical unwrapping process, oxidized GNRs with length of up to 4 μm and width of 100-500 nm were obtained in high yields of approximately 100%. However, similar to the synthesis of GO, the structural defects with oxygen-containing groups cannot be avoided because of the strong oxidative process, and the further chemical or thermal reduction could not fully recover the expected electronic properties of the resulting GNRs.¹⁶⁵ Another disadvantage of this method is that the width of final fabricated GNRs is too large to open up the bandgap.

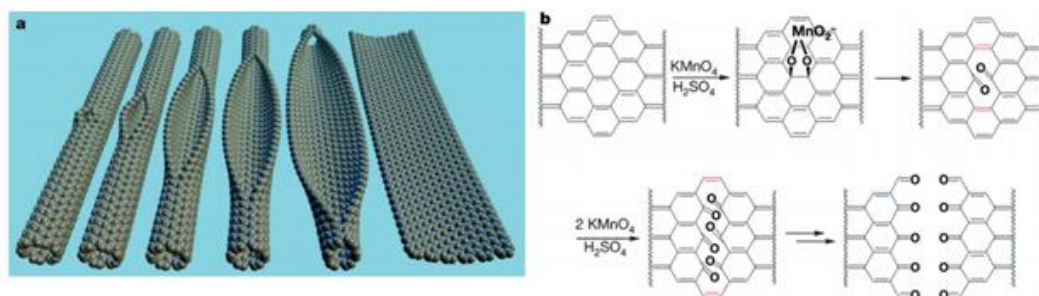


Figure 1-23. a) Representation of fabrication of GNRs through unzipping of CNTs. b) The proposed chemical mechanism of CNT unzipping. Ref. [164]; Copyright 2009, Nature publishing group.

In contrast to the oxidative process, much narrower GNRs (10-20 nm wide) with less defects could be achieved through the unzipping of highly crystalline MWCNTs with an Ar plasma etching (Fig. 1-24).¹⁶⁶ In Dai's work, MWCNTs were dispersed on a silicon substrate and partly embedded in an etching mask layer which was made of poly(methyl methacrylate) (PMMA), and then subsequent Ar plasma treatment could lead to the unzipping of the MWCNTs. The unmasked areas of CNTs were etched faster than the areas protected by PMMA, leading to the formation of unzipped GNRs. At the end, the PMMA film was removed by exposing the system to acetone vapor. FET device investigations based on these GNRs indicated that an $I_{\text{on}}/I_{\text{off}}$ ratio of up to 10^3 could be achieved.

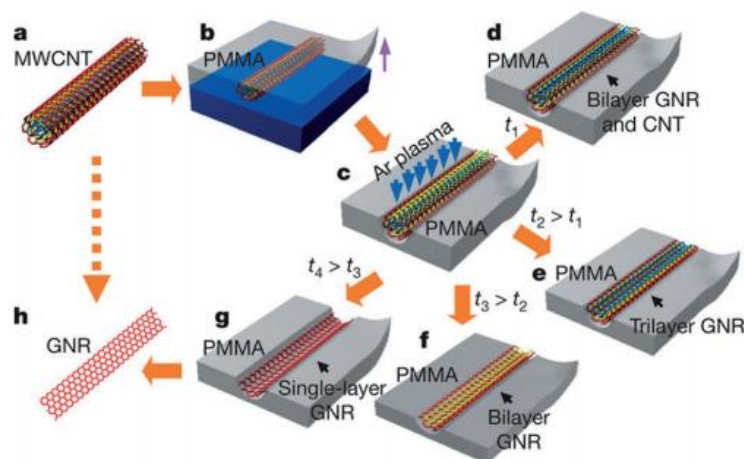


Figure 1-24. Schematic illustration of fabricating GNRs from CNTs. a) MWCNT was used as starting material. b) The MWCNT was deposited on silicon substrate and coated with a PMMA film. c) The PMMA-MWCNT film was peeled from the Si substrate, turned over, and then exposed to Ar plasma. d-g) Several possible products generated as time passing. h) Removing PMMA to give GNR. Ref. [166]; Copyright 2009, Nature publishing group.

Some of the above mentioned “top-down” fabricated GNRs indeed exhibit semiconducting properties with high on-off ratio and mobility. Nevertheless, all these GNRs suffered from low yields and lack of reliable control over the width and edge structures, which further affected their electronic properties.^{156,158,167} These drawbacks hinder the practical applications of “top-down” fabricated GNRs in electronic devices. Besides, “top-down” approach is incapable in fabricating GNRs with widths below 5 nm which are expected to provide sufficient bandgaps for FET devices.

1.4.3 Fabrication of GNRs via “bottom-up” approach

As mentioned above, the “bottom-up” approach is an alternative way for the fabrication of GNRs. Compared to the “top-down” method, the “bottom-up” fabrication has several advantages, such as the capabilities of fabricating GNRs with well-defined structure, narrow width (< 5 nm), and improved electronic properties. Moreover, tailorable bandgaps can be obtained depending on various designs of GNRs’ structures. Similar to the synthesis of NGs, the “bottom-up” fabrication can also be realized through protocols, which are solution-mediated and surface-assisted protocols.

1.4.3.1 Solution-mediated protocol

Solution-mediated organic chemistry is a well-known powerful tool and established protocol for the synthesis of numerous new organic compounds. In modern organic chemistry, a large number of reactions such as Diels-Alder, Friedel-Craft, and metal-catalyzed coupling reactions have been developed, which serve as efficient methods in fabrication of carbon-rich PAHs, polymers, and GNRs. From a chemical point of view, the simplest GNR following a bottom-up synthetic concept is fusion of benzene rings into a one-dimensional linear polymer as displayed in Fig. 1-25. This simple linear conjugated system is usually called poly(acenes) (**1-60**).^{168,169} If the benzene rings are fused in a chevron shape, the resulting structure is named as “angular polyacene” (**1-61**).

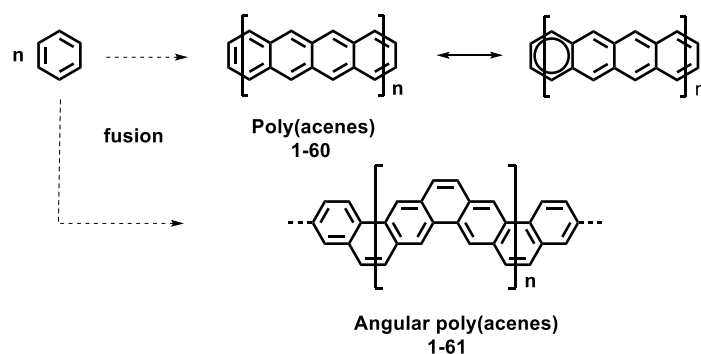


Figure 1-25. Schematic illustration of how benzene rings fused into poly(acenes) and angular poly(acenes).

However, similar to zigzag type NGs, the chemical structures of high order acenes can be depicted with only one sextet according to Clar’s rule. Thus they are highly unstable and acting as a challenging target in organic and polymer chemistry. Facing the above situation, lots of methods have been developed to overcome the stability issue, including employment of stabilizing substituents¹⁷⁰⁻¹⁷² and interruption of the conjugation.^{168,169} Typical examples of the stabilization of acenes by introducing substituents are syntheses of hexacene and heptacene, which are the longest characterized acenes at the moment (Fig. 1-26). In 2005, Anthony et al.¹⁷³ reported an efficient way forward functionalized hexacene (**1-62**) and heptacene (**1-63**, **1-64**) from acenequinone precursors. In their work, bulky protection groups such as triisopropylsilyl (TIPS) and tri-*tert*-butylsilyl (TTBS)

were employed and the X-ray crystal structures of them were obtained as well. Another work on the synthesis of heptacene and its derivatives has been done by Zade et al.¹⁷² in 2010, who also provided a feasible way to build stable acenes. The parent heptacene and hexacene have also been synthesized in 2006¹⁷⁴ and 2012¹⁷⁵, respectively. However, the former was obtained in a polymer matrix and latter was synthesized via a thermal treatment or irradiation process. Both two parent acenes decomposed when exposed to the atmosphere.

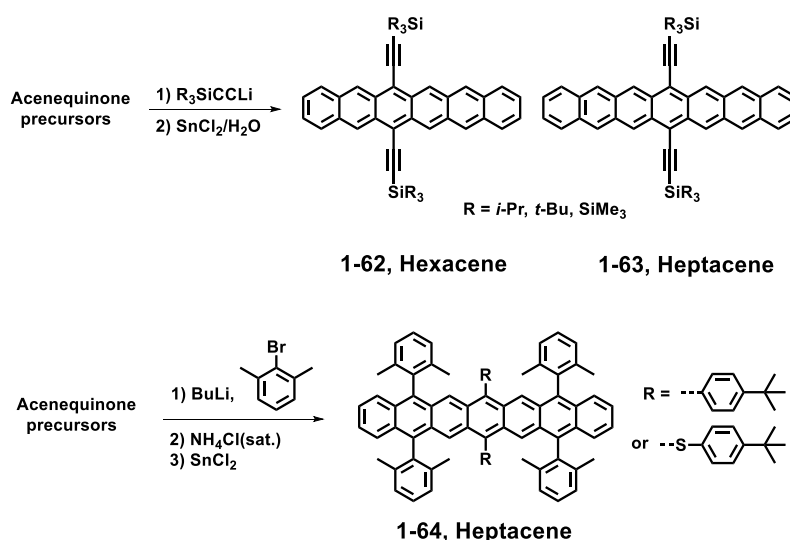


Figure 1-26. Schemes of synthetic routes toward stable hexacenes and heptacenes.

Some early works forward heteroatom-containing ladder-type polymers in 1960's can also be seen as fabrication of GNRs. Typical examples (Fig. 1-27) include linear polymers like **1-65** and **1-66** synthesized via polycondensation reactions by Stille¹⁷⁶ and Marvel¹⁷⁷, respectively. On the other hand, ladder-type polymer **1-67a** was synthesized by *AB*-type Diels-Alder polymerization, but its low solubility due to the strong π - π stacking interaction, limiting further characterization and applications of such structures.¹⁷⁸ In 1994, Schlüter et al. dealt with the solubility problem of **1-67b** by introducing flexible alkyl chain groups on monomer.¹⁷⁸ Following studies by Scherf and Müllen in 1991 demonstrated the fabrication of soluble polyaromatic polymers **1-68** through intramolecular Friedel-Craft alkylation.^{179,180} The successful synthesis of ladder-type polymer **1-69a**, also called angular polyacene, had been achieved by Chmil and Scherf in 1993^{181,182} via a carbonyl olefination reaction. One year later, its homologue **1-69b** with the same skeleton was synthesized by Swager et al.¹⁸³ via intramolecular electrophilic substitution (Fig. 1-27).

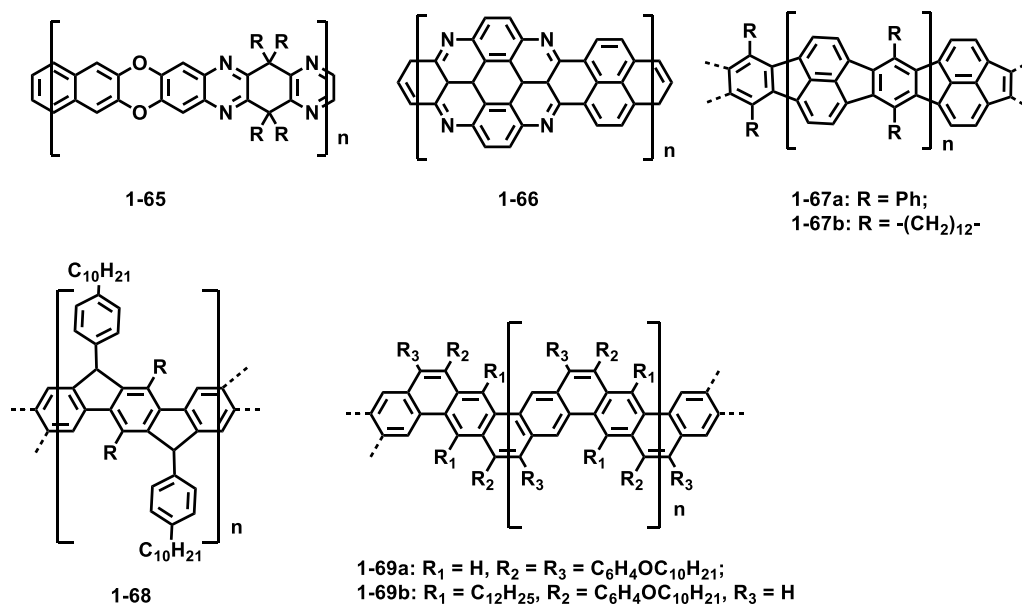


Figure 1-27. Chemical structures of conjugated ladder-type polymers which can be considered as narrowest GNRs.

The first attempt at synthesizing more extended GNRs was carried out in 2000 through an oxidative cyclodehydrogenation of polyphenylene precursor **1-73**, which was synthesized from *A*₂*B*₂-type Diels-Alder polymerization of 1,4-bis(2,4,5-triphenylcyclopentadienone-3-yl)benzene (**1-71**) and 1,4-diethynylbenzene (**1-70**) (Fig. 1-28).¹⁸⁴ The following size exclusion chromatography (SEC) analysis against polystyrene (PS) standard of polymer **1-73** indicated that its weight-average molecular weight (*M_w*) ranged from 12,000 to 120,000 g/mol. However, its final cyclodehydrogenation product **1-75** was insoluble in common organic solvents, which hindered its further characterizations, except for Raman and FTIR spectroscopic analyses that could be done in the solid state. Moreover, GNR **1-75** and its precursor **1-73** were irregular in their structures, which can be ascribed to the unsymmetrical structures of **1-71**. The random mixtures of three regioisomeric repeating units led to structural isomerization of **1-73** and **1-75**, and GNR **1-75** had even more regioisomers due to the free rotation of **1-73** within the main polyphenylene chains during the cyclodehydrogenation. In 2003, an additional work has been achieved by using 1,4-diethynyl-2,5-di(4'-tert-butylphenyl)benzene (**1-72**) instead of **1-70** as the bisdienophile.¹⁸⁵ Compared to the aforementioned GNR **1-75**, the improvement of this work was introduction of two extra phenyl rings to fill the lateral “gaps”, which generated a GNR **1-76** with regular lateral width and armchair edge structure (Fig. 1-28). Nevertheless, this new GNR structure still contained a mixture of non-straight, irregularly kinked structures.

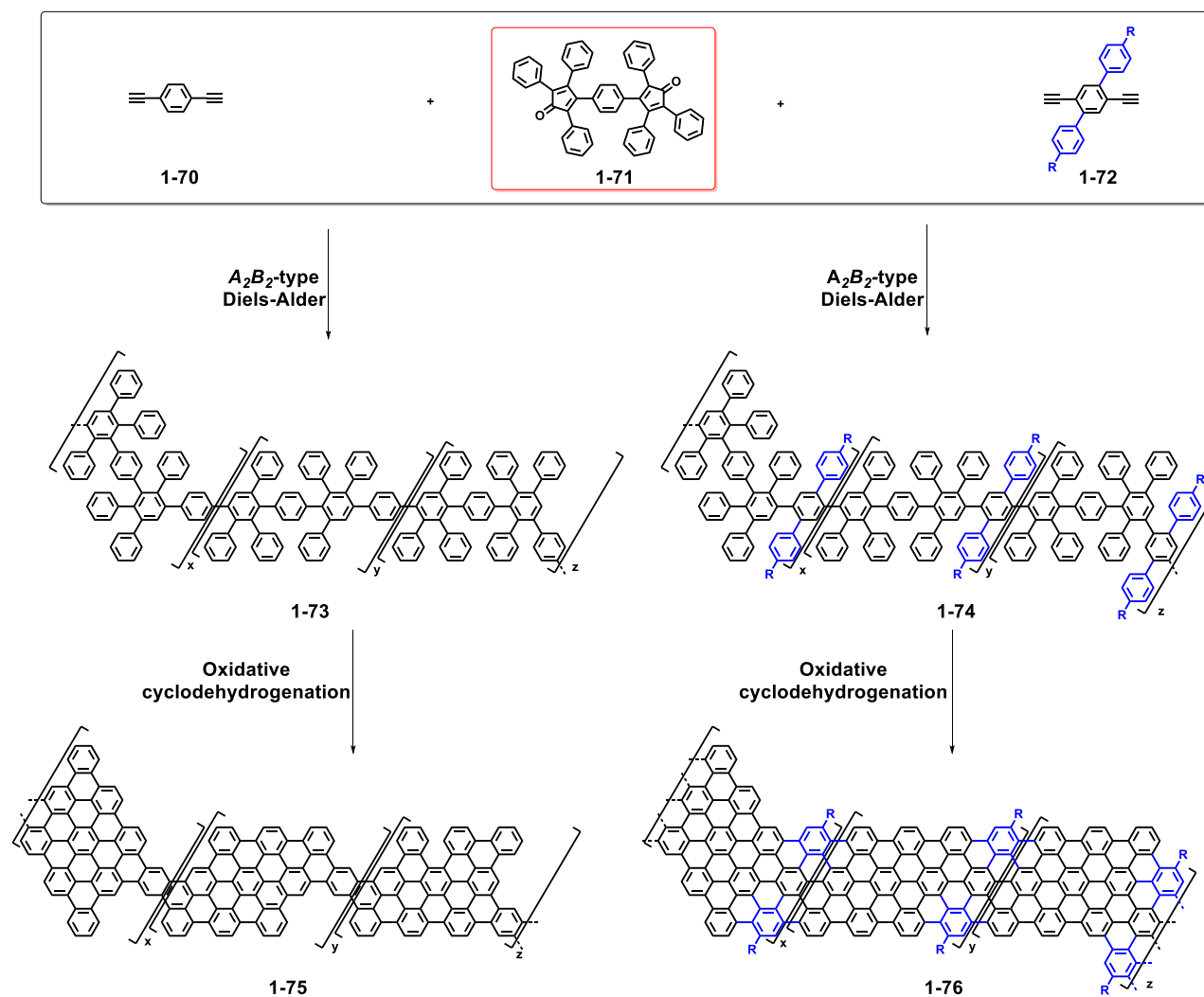


Figure 1-28. "Bottom-up" synthesis of GNRs with armchair edge structures.

In 2009, another breakthrough of synthesizing GNRs with "gulf-type" edge structures by Diels-Alder cycloaddition has been developed¹⁸⁶ as shown in Fig. 1-29. In this work, 2,2'-diethynylbiphenyl (**1-77**), diene **1-78**, and 1,2,3,4-tetra-(4-dodecylphenyl)-5-(2'-ethynylbiphen-2-yl) (**1-79**) were used for cycloaddition to yield corresponding oligophenylenes. However, only oligomeric precursors **1-80** were obtained and their corresponding ribbon-type NGs of up to C373 ($n = 5$) could be produced by cyclodehydrogenation. The cyclodehydrogenation products of larger oligomers were insoluble in common organic solvents, except for the smallest NG **1-81** that could be comprehensively characterized. Recently, a remarkable synthesis of a long "gulf type" GNR **1-84**, through "graphitization" of polyphenylene precursor **1-83**, has been accomplished by Müllen et al.¹⁸⁷ In this work, a monomeric building block **1-82**, consisting of a cyclopentadienone as the conjugated diene and an ethynyl groups as dienophile, was designed and used as precursor for the AB -type Diels-Alder polymerization to give **1-83** in high yield.

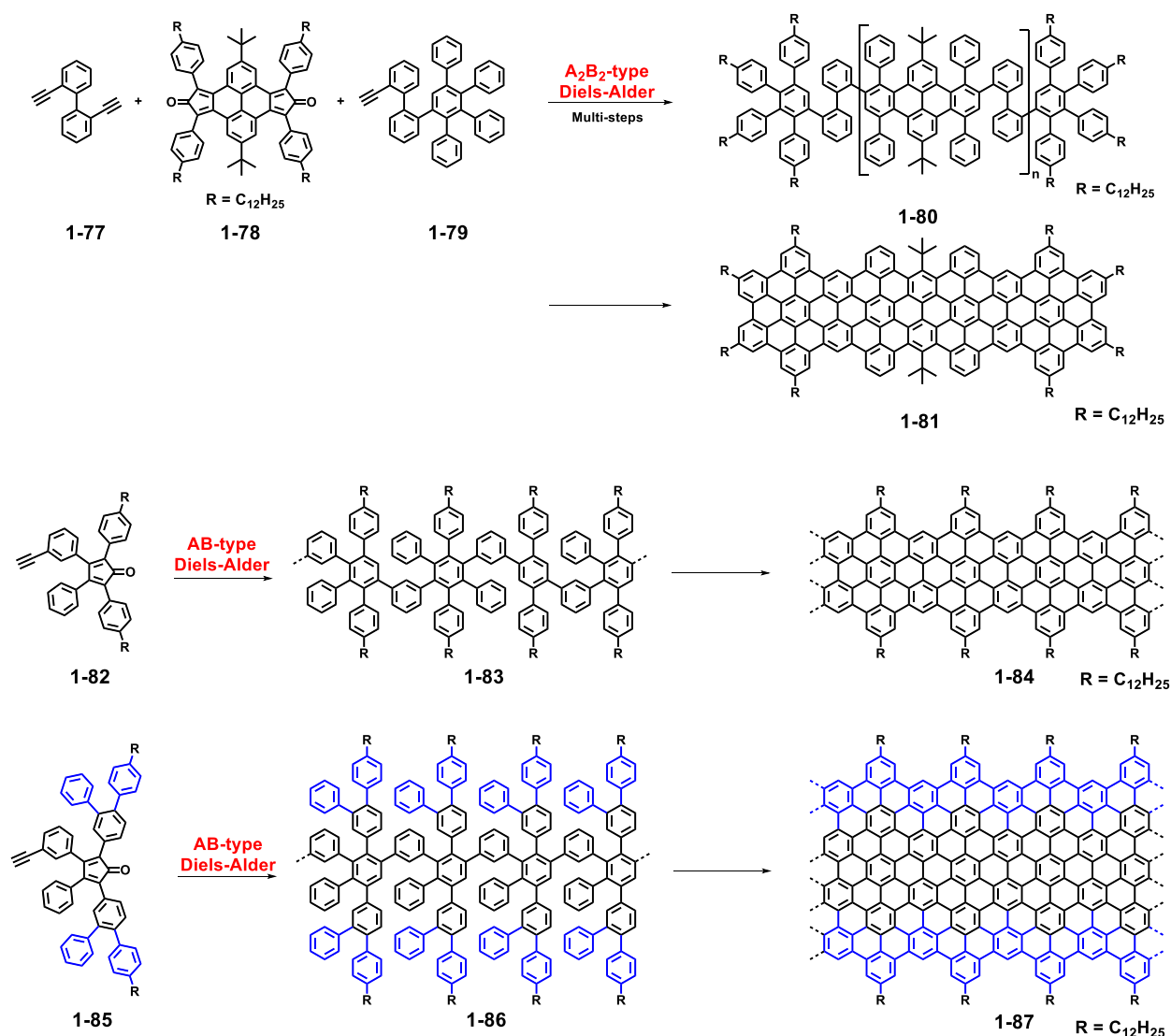


Figure 1-29. Schemes of “bottom-up” synthesis of GNRs **1-81**, **1-84** and **1-87** via Diels-Alder polymerization.

Thanks to good solubility derived from the intensely installed dodecyl chains on the periphery, polymer **1-83** could be subjected to SEC analysis. Its M_w was estimated based on PPP and PS standards to be 270,000 g/mol and 640,000 g/mol, respectively. The final cyclodehydrogenation yielded a liquid-phase-processable and longitudinally well-extended GNR **1-84** (>600 nm), which exhibited a large optical bandgap of 1.88 eV. This GNR is the longest solution-mediated synthesized GNR structures to date. In the same year, a laterally extended GNR **1-87** with a width of ~2 nm and length exceeding 100 nm was reported.¹⁸⁸ Comparing to the synthesis of GNR **1-84**, the same synthetic strategy was employed (Fig. 1-30), but the resulting GNR **1-87** demonstrated a lower, well-defined bandgap of ~1.2 eV and a broad optical absorption which extended into the near infrared (NIR) region.

Besides the aforementioned methods for the synthesis of GNRs via Diels-Alder polymerization, transition metal catalyzed coupling reactions are an alternative way in fabricating novel GNRs with high efficiency. In 2008, the synthesis of straight, armchair-type GNR **1-91** was reported by

Müllen's group by employing A_2B_2 -type Suzuki polymerization of 1,4-diiodo-2,3,5,6-tetraphenylbenzene (**1-88**) and bis-boronic ester (**1-89**) (Fig. 1-30a).¹⁸⁹ However, the polyphenylene polymer **1-90** obtained from Suzuki polymerization only had an estimated number average molecular weight (M_n) of 14,000 g/mol against PS standards, which corresponded to very short GNR **1-91** after cyclodehydrogenation. The following STM analysis also indicated that GNRs **1-91** were only up to about 12 nm in length. The reason of such short GNR in length can be explained by the high steric hindrance during the Suzuki polymerization and the rigid polyphenylene backbone of **1-90**. Another example of using an A_2B_2 -type Suzuki polymerization to fabricate GNR structure was reported by Müllen et al.¹⁹⁰ as displayed in Fig. 1-30a. A kinked polyphenylene **1-94** with dodecyl substituents was synthesized by microwave-assisted Suzuki polymerization between *o*-dibromobenzene **1-92** and benzene-1,4-diboronic ester (**1-93**). The SEC analysis indicated that the M_n of polyphenylene **1-94** against PS standard was 9,900 g/mol, corresponding to the average longitudinal length of ca. 25 nm for GNR **1-95**.

Another feasible method of transition metal catalyzed polymerization applied in the synthesis of GNRs is *AA*-type *Yamamoto* polymerization (Fig. 1-30b). Comparing to the intrinsic sensitivity of aforementioned A_2B_2 -type polymerization including Diels-Alder and Suzuki coupling reactions to stoichiometry, the *AA*-type *Yamamoto* polymerization which can circumvent this drawback is believed to be more efficient and can yield high molecular weight precursors. In 2012, Müllen et al.¹⁹¹ reported fabrication of GNR **1-98** with a low optical bandgap (1.12 eV) from polyphenylene precursor **1-97**, which was synthesized via the *AA*-type *Yamamoto* polymerization of monomer **1-96**. The SEC analysis of precursor **1-97** showed M_w of 52,000 g/mol with PDI of 1.2 against a PS standard. This result indeed highlights the superiority of the *AA*-type *Yamamoto* polymerization for the preparation of high molecular weight precursors compared to the A_2B_2 -type Suzuki polymerization. In 2014, another GNR structure (**1-101**) was reported,¹⁹² which was synthesized from its polyphenylene precursor **1-100** via the *AA*-type *Yamamoto* polymerization (Fig. 1-30b). The following characterization of this chevron-shaped GNR **1-101** indicated that it had width of ~ 1 nm and lengths of >100 nm as well as a large electronic bandgap of ~1.6 eV.

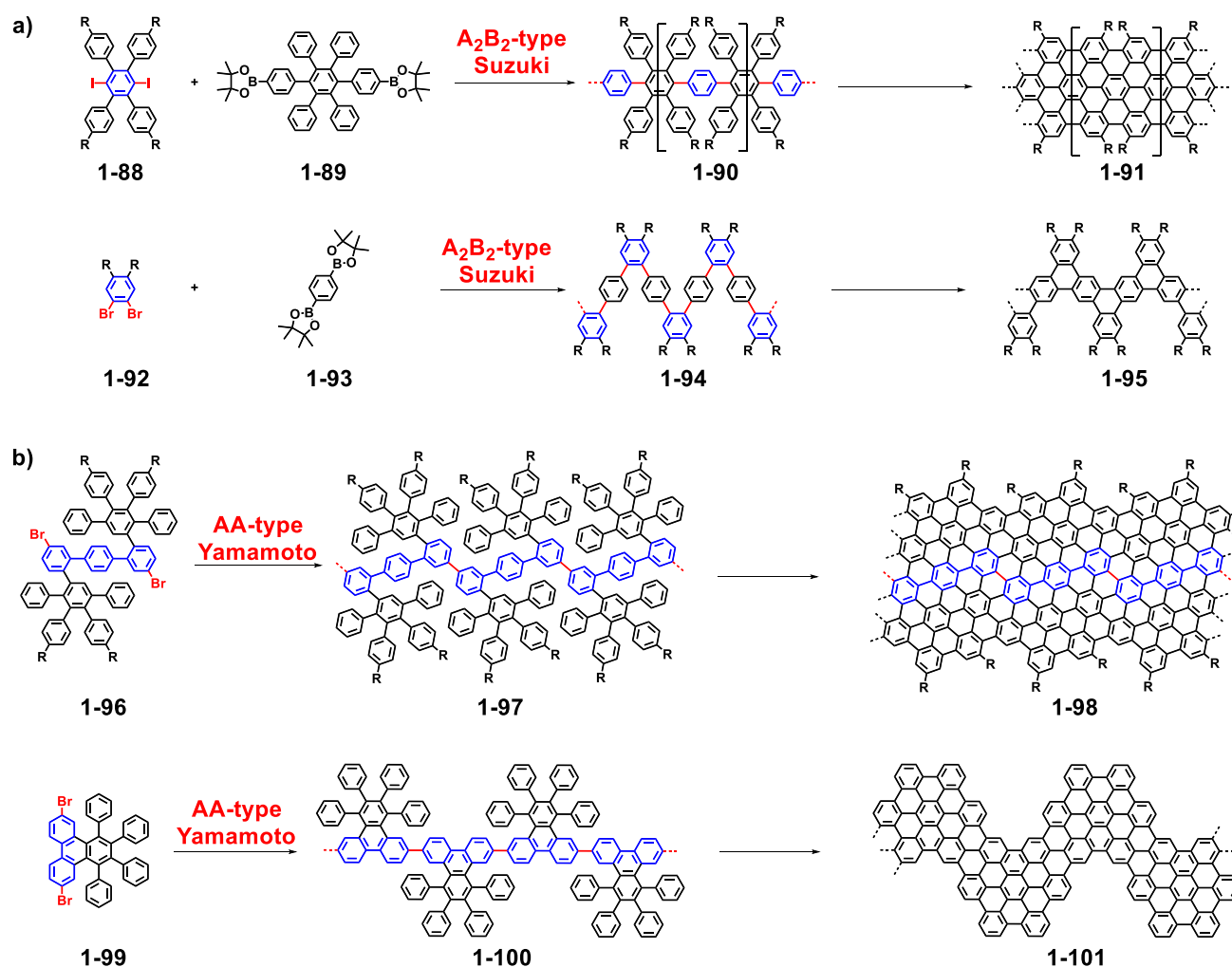


Figure 1-30. a) Schemes of synthesis of GNRs via A_2B_2 -type Suzuki polymerization; b) Schemes of synthesis of GNRs via AA-type *Yamamoto* polymerization.

1.4.3.2 Surface-assisted protocol

Besides the solution-mediated protocol, an alternative way of synthesizing GNRs is a surface-assisted synthesis. Both way of synthesis have their advantages and drawbacks, for example, the solution-mediated protocol enables synthesis of GNRs with reasonable processability and larger amount but suffer from short longitudinal length, side reactions, and possible defects during the oxidative cyclodehydrogenation, which cannot be properly characterized. On the contrary, surface-assisted synthesis has advantages in synthesis of GNRs with perfect architecture that can be directly visualized by the STM, however, its disadvantages are the extremely low yields and difficulty in transferring the resulting GNRs from the metal surfaces to other substrates.

The first preparation of GNRs via the surface-assisted synthesis was reported by Müllen and Fasel et al. in 2010 (Fig. 1-31a, b).¹⁹³ In this work, they demonstrated a feasible method combing the on-surface coupling reactions of aryl halides with the surface-assisted cyclodehydrogenation to obtain

GNRs. This synthetic protocol can generally be divided into three steps, i.e. 1) vacuum sublimation of monomers with two halogen functions on a metal surface; 2) polymerization of biradical intermediates which are generated by dehalogenation of monomers; 3) surface-assisted cyclodehydrogenation upon annealing (Fig. 1-31). Notably, by using different monomers 10,10'-dibromo-9,9'-bianthryl (**1-102**) and 6,11-dibromo-1,2,3,4-tetraphenyltriphenylene (**1-105**), $N = 7$ armchair-type GNR **1-104** and chevron-type GNR **1-107** can be efficiently synthesized with atomic precision, respectively. The subsequent in-situ STM visualization also provided strong evidence for the successful synthesis of the GNRs.^{193,194} Following studies of their electronic properties indicated that GNRs **1-104** and **107** exhibited a same bandgap of ~ 1.6 eV based on density functional theory (DFT) calculation. Moreover, covalent colligations of GNR **1-104** in parallel was observed as well, leading to the formation of $N = 14$ and 21 armchair GNRs.

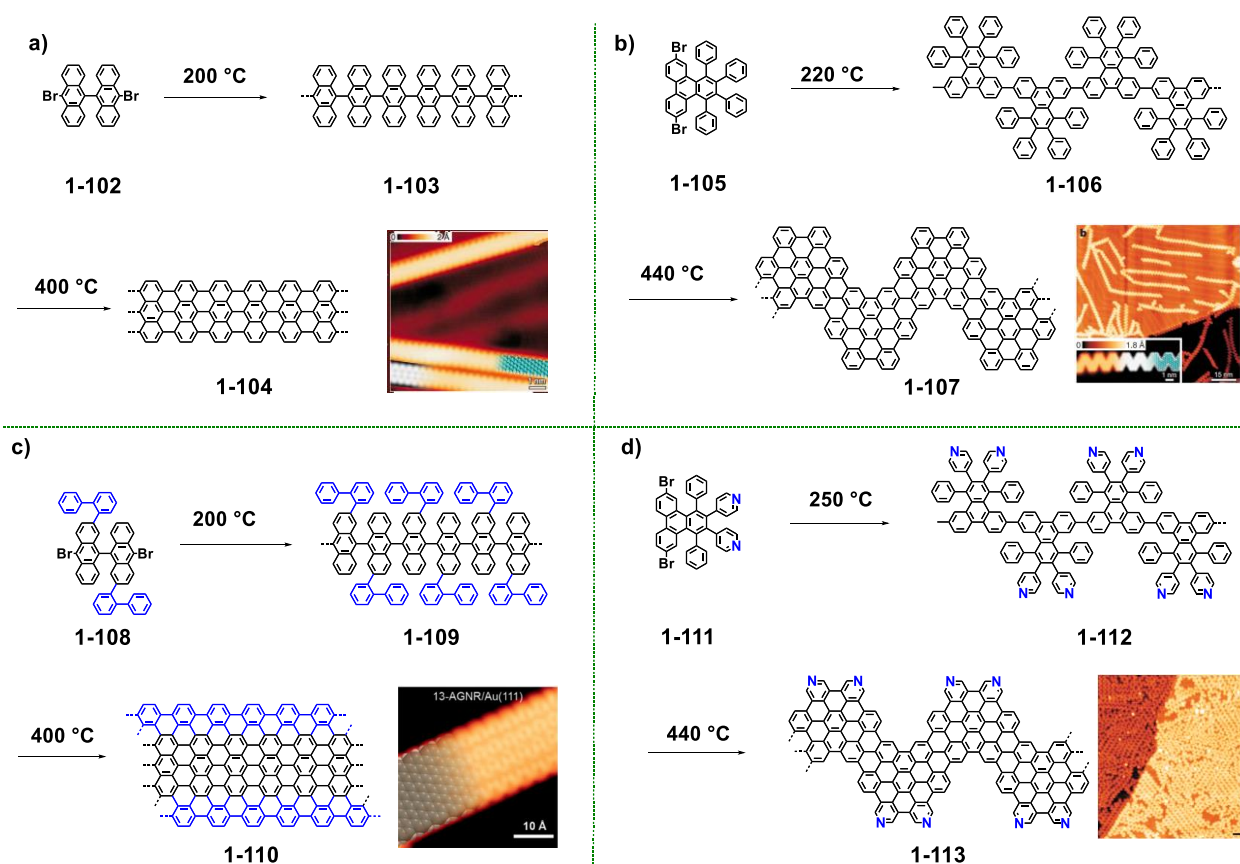


Figure 1-31. a, b) Surface-assisted synthesis of GNRs **1-104** and **1-107** as well as their STM images. c,d) Surface-assisted synthesis of lateral extended GNR **1-110** and nitrogen doped GNR **1-113**. Ref. [193-196]; Copyright 2010, Nature publishing group.

Furthermore, this surface-assisted strategy was also applied to fabricate extended or heteroatom-doped GNRs by employing different monomer precursors. As displayed in Fig. 1-31b and c, by using extended dibromobianthryl **1-108** and 6,11-dibromo-1,4-diphenyl-2,3-di(4-pyridyl)triphenylene (**1-111**) as monomer precursors, laterally extended $N = 13$ GNR **1-110**¹⁹⁵ and N-doped chevron-type

GNR **1-113**¹⁹⁶ could be synthesized with atomic precision, respectively. Notably, N-doping can lead to lowering of the energy levels without affecting the bandgap energy. The bandgap of laterally extended N = 13 GNR **1-110** was elucidated to be ca. 1.4 eV based on DFT calculation, which is about 1 eV lower than the value of N = 7 GNR **1-104**.¹⁹⁷⁻¹⁹⁹

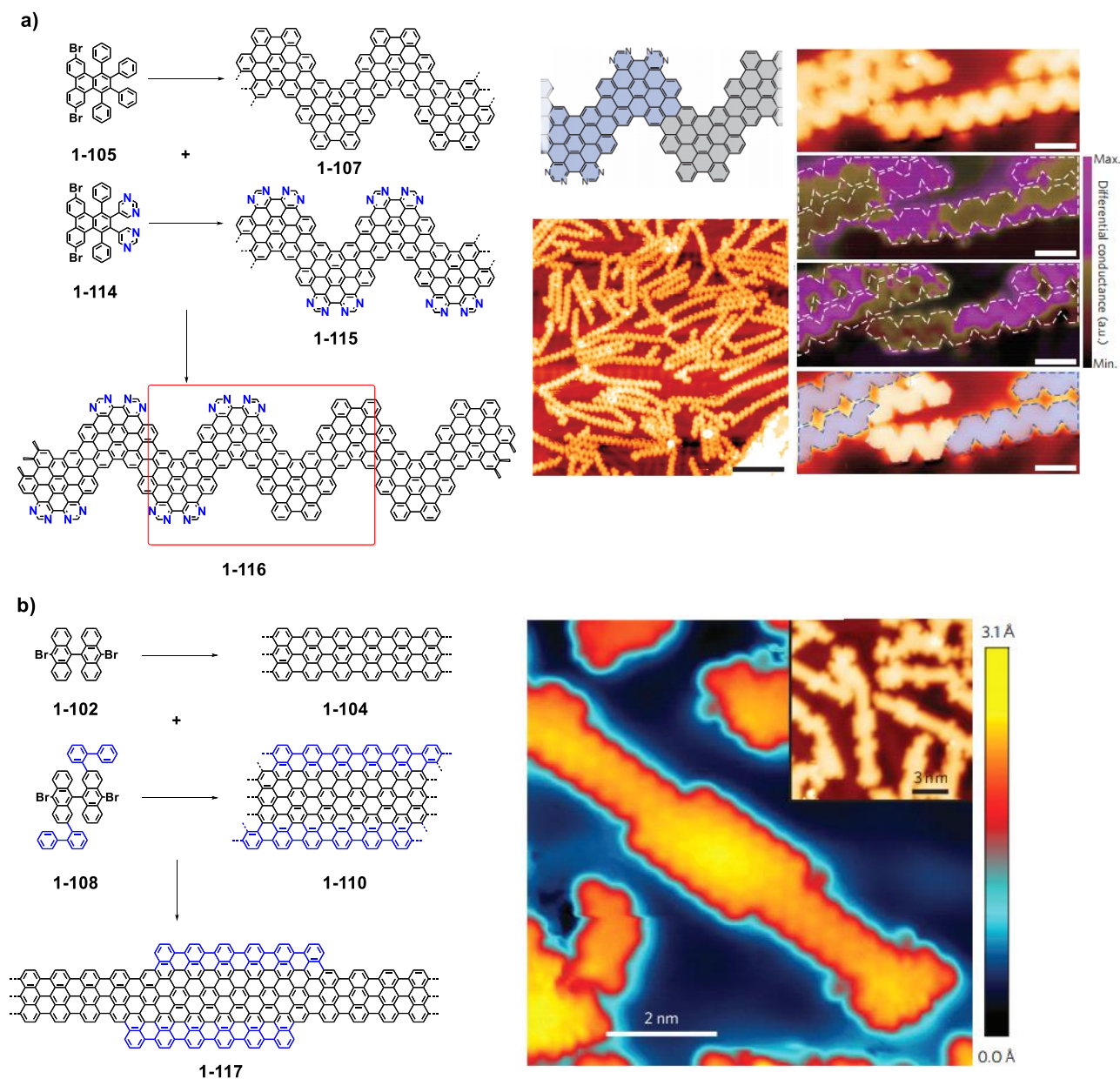


Figure 1-32. a) Surface-assisted synthetic schemes of heterojunction **1-116** (left) and STM images as well as corresponding differential conductance dI/dV maps at different bias voltages (right); b) Surface-assisted synthetic schemes of heterojunction **1-117** (left) and its STM images. Inset: Large-scale STM image of multiple GNR heterojunctions, showing a variety of segment lengths (right). Ref. [200, 201]; Copyright 2014 and 2015, Nature publishing groups.

Besides the aforementioned GNRs, the GNR heterojunctions, which can be defined as GNR heterostructures obtained by fusing segments made from two different molecular precursors, have also been investigated for the purpose of bandgap engineering. Two typical GNR heterojunctions have been reported by Müllen and Fasel et al. in 2014²⁰⁰ and Crommie et al. in 2015²⁰¹. As shown in Fig. 1-32a, by combination of the monomer precursors **1-105** and 5,5'-(6,11-dibromo-1,4-diphenyltriphenylene-2,3-diyl)dipyrimidine (**1-114**), GNR heterojunction **1-116** could be obtained through the same surface-assisted protocol as GNR **1-107**. The synthesized GNR heterojunction **1-116** consisted of combined segments of GNR **1-107** and **1-115**, which can also be depicted as combination of pristine (undoped) graphene nanoribbons (p-GNRs) (grey) and nitrogen-doped graphene nanoribbons (N-GNRs) (blue) (Fig. 1-32a, right). The corresponding differential conductance dI/dV maps allowed a clear distinction of two chemically different ribbon segments (Fig. 1-32a, right: violet/green).

On the other hand, the use of monomer precursors **1-102** and **1-108** in the same surface-assisted protocol led to the formation of GNR heterojunction **1-117**²⁰¹, which consisted of segments of $N = 7$ GNR **1-104** and $N = 13$ GNR **1-110**. The GNR heterojunction structure was identified by high-resolution STM topographic image of a representative sample, which clearly revealed the 7-13 GNR heterojunctions with shapes resembling the sketch in Fig. 1-32b. The narrower segments in these heterojunctions are 1.3 ± 0.1 nm in width in STM image and are composed of covalently bonded monomers of **1-102**. The wider segments measure 1.9 ± 0.2 nm in apparent width and consist of fused monomer **1-108**. The STM image also showed that heterojunction **1-117** contained a variety of $N = 7$ and $N = 13$ segment lengths, which can be ascribed to the monomer precursors mixed and fused in a random sequence during the initial step-growth polymerization.

While the aforementioned examples were all based on monomeric precursors with di-halogen functional groups that could further generate biradical intermediates for polymerization, other monomeric precursors can be useful in the surface-assisted synthesis of GNRs. Recently, two precursors were reported as building blocks in surface-assisted Bergman cyclization to yield polyphenylenes and conjugated polymers^{202,203}. As exhibited in Fig. 1-33, in 2013, 1,6-di-2-naphthylhex-3-ene-1,5-diyne (**1-118**) was used as a monomeric precursor in the Bergman cyclization on Cu(110) surface, and the following thermal treatment triggered the formation of diradical intermediate **1-119**, which then grew into a linear polyphenylene **1-120** through radical polymerization²⁰³. Further cyclodehydrogenation of polyphenylene **1-120** would lead to $N = 13$ GNR. Although it was not included in this work, this synthesis of **1-120** still enlightens an alternative pathway to synthesize GNR on a surface via Bergman cyclization. Another case of the surface-assisted Bergman cyclization was reported in 2014 by Crommie, who used enediyne 1,2-bis(2-ethynylphenyl)ethyne (**1-121**) as monomeric precursor. Thermal annealing of **1-121** at 160 °C on an

Au(111) surface induced two intramolecular radical cyclizations as well as intermolecular carbon-carbon coupling reactions between monomer units to give conjugated polymer **1-123**²⁰². However, only oligomer chains were generated in this work, which were mostly composed of 5-10 monomer units (sometimes exceeded 20). Same as the fabrication of **1-120**, this process on surface also provides a new possibility toward fully conjugated polymer or GNR structures.

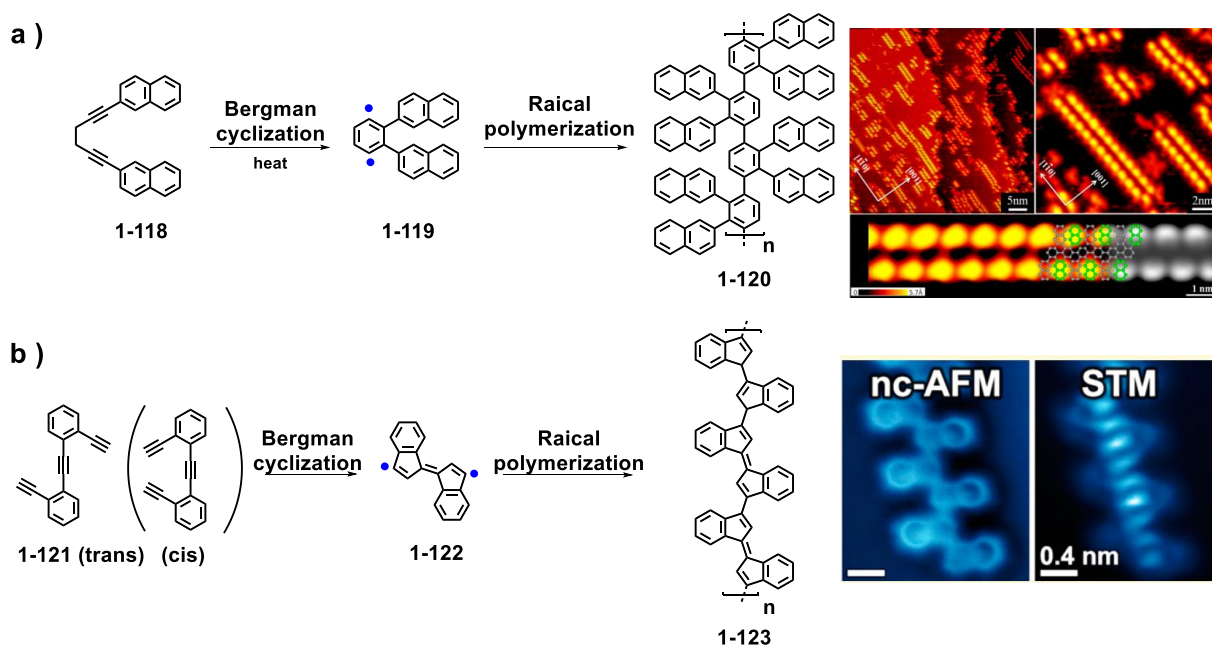


Figure 1-33. a) Surface-assisted synthetic scheme of linear polyphenylene **1-120** via Bergman cyclization (left) and its STM images (right); b) Surface-assisted synthetic scheme of conjugate polymer **1-123** via Bergman cyclization (left) and its nc-AFM and STM images (right). Ref. [202]; Copyright 2013, 2014 ACS publishing group.

Furthermore, it is worth noting that although a variety of GNRs with different edge structures and widths can be synthesized with atomic precision via surface-assisted approach, a further transfer process is still needed: separation of synthesized GNRs from metal surfaces onto dielectric substrates is required for the further studies on their electronic properties as well as practical application in electronic devices. In 2010, successfully transferred the intact GNRs from gold films onto a SiO₂ substrate by using a mechanical contact method, namely “chip-to-chip press” method was reported.¹⁹³ Later in 2013, a more reliable method of full layer transfer procedure by using poly-methyl methacrylate (PMMA) was developed. The isolated GNRs were used to fabricate field-effect transistors (FET), and a strong environmental sensitivity and unique transport behaviors were observed.²⁰⁴ Recently, a PMMA free method to transfer their surface synthesized GNRs from Au/mica surface to non-conductive target substrates such as Al₂O₃, CaF₂, or SiO₂ was claimed.²⁰⁰

1.5 Motivation and objectives

As described in the previous sections (1.3 and 1.4), two kinds of synthetic strategies including “top-down” and “bottom-up” in the fabrication of NGs and GNRs as well as classification of NGs and GNRs have been introduced. Nowadays, plenty of NGs and GNRs with armchair edge structures have been reported based on surface-assisted and solution-mediated protocols. However, NGs and GNRs with zigzag edge structures have thus far remained elusive. Based on tight-binding theory, zigzag-type NGs and GNRs are predicted to show spin polarized edge states as well as half-metallic properties with zero bandgap, which render them as promising materials in spintronics. Moreover, GNRs with a hybrid of zigzag edge and other types of edge structures such as “gulf-type” or “cove-type” (see section 1.4), are promising targets as well, because they have never been reported before, and are also predicted to show relatively low bandgaps. Therefore, as one of the main aspects of our objectives and motivations, synthesis of novel NGs and GNRs with zigzag edge structures plays a significant role in this dissertation.

In addition to tuning the electronic properties of structurally defined NGs and GNRs through modulation of their edge structures which can be pre-designed by using modern synthetic chemistry, another pathway is through chemical functionalization. By employing various substituent groups, i.e., electron-withdrawing or electron-donating groups, or destroying the π -conjugated system of parent NGs/GNRs by chemical reduction, it is possible to tune their optoelectronic properties.

1.5.1 Bottom-up synthesis of novel GNRs with zigzag edge structures

In order to fabricate structurally well-defined GNRs with zigzag edge structures and various widths based on the “bottom-up” strategy, two different approaches, “surface-assisted” and “solution-mediated” methods are conceivable. To realize a chemically precise fabrication of the novel GNRs with zigzag edges, the key idea is chemically designing and synthesizing suitable monomers. As displayed in Fig. 1-34, we have designed compound **1-123** with 2,12-dihalogenated (X)-7-phenyl-14-phenylbenzo[*m*]tetraphene as the backbone, or termed as the “U-shaped” building block, as the key monomer. The aryl-aryl coupling could allow for the polymerization that leads to corresponding snake-like polymers **1-124**.

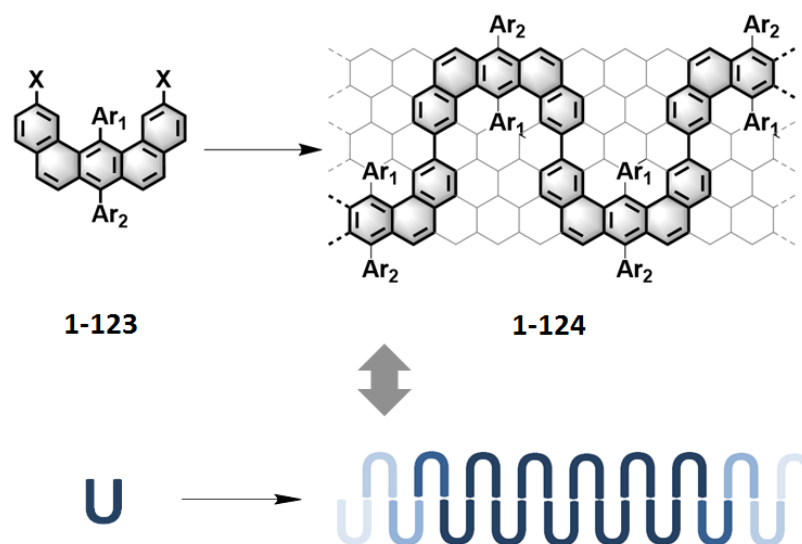


Figure 1-34. “U-shaped” monomer **1-123** and corresponding polymer **1-124**.

By choosing the substituted groups Ar₁ and Ar₂ on monomers, four different polymers can thus be formed. A “graphitization” or “cyclodehydrogenation” reaction of polymer precursors affords the desired GNR structures with zigzag periphery. Four different GNRs with different edge structures can be finally formed. As showed in Fig 1-35a, the first monomer **1-123a** (Ar₁ = Ar₂ = phenyl group) can be polymerized to yield corresponding snake-like polymer **1-124a**, the subsequent cyclodehydrogenation leads to final GNR with a partial zigzag-type and gulf-type edge structure. Similarly, the second monomer **1-123b** (Ar₁ = biphenyl group, Ar₂ = phenyl group) can generate GNR with a hybrid of zigzag-type and cove-type edge structure (Fig. 1-35b). Theoretically, both the third monomer **1-123c** (Ar₁ = 1,3-dimethylbiphenyl group, Ar₂ = phenyl group) and the fourth monomer **1-123d** (Ar₁ = 1,3-dimethylbiphenyl group, Ar₂ = H) can lead to GNRs with full zigzag-type edge structures, except that the third GNR possesses additional phenyl groups along its edge peripheries (Fig. 1-35c and d). Moreover, both surface-assisted and solution-mediated approaches are applicable for the fabrication of desired GNRs with zigzag edges. For the surface-assisted synthesis of GNRs, we collaborated with Roman Fasel’s group (EMPA, Switzerland) and all four monomers were favorable for the surface-assisted protocol. For the solution-mediated synthesis, we initially focus on the synthesis of the first monomer **1-123a** and its corresponding GNR.

Furthermore, the surface-assisted fabrication of full-zigzag GNRs is more favorable than solution-mediated fabrication. The reason can be ascribed to the relatively unstable nature of zigzag edge structures, especially under oxidative environment of solution-mediated approach.

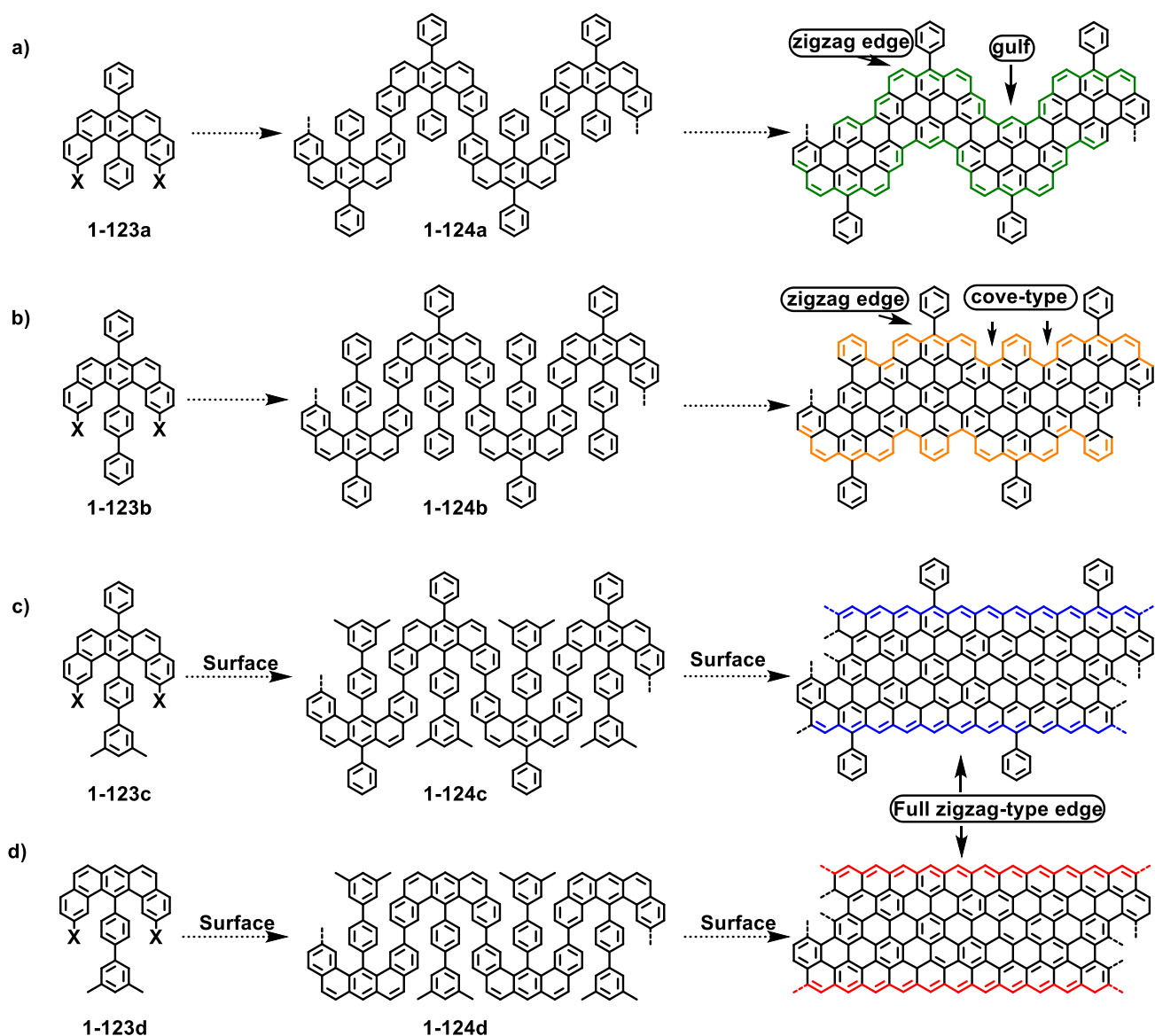


Figure 1-35. Assumed design for the GNRs with zigzag edge structures based on the four monomers **1-123a-d** and their corresponding intermediated polymers. a) GNR with a hybrid of zigzag-type and gulf-type edges; b) GNR with a hybrid of zigzag-type and cove-type edges; c) and d) GNR with full zigzag-type edge.

1.5.2 Attempts of synthesizing novel NGs with zigzag edge structures

Similar to the fabrication of GNRs, a series of armchair-type NGs including classical HBC, C60, C96, and biggest NG molecule C222 have been synthesized before (section 1.3). However, there was lack of zigzag type NGs and only few cases of NGs with partial zigzag edges have been reported^{205,206}. This part of our work was dedicated to the synthesis of novel NGs with zigzag edge structure derived from HBC, particularly the NG with full zigzag edges as shown in Fig 1-36. Our

strategy is extending the π -conjugated system on the armchair periphery of HBC by fusing additional carbon-carbon double bonds. Finally, a novel NG with zigzag edge, namely “full zigzag HBC” could be possibly obtained as the target molecule. Considering possible difficulties during the whole synthetic procedure, a novel NG molecule with partial zigzag edges, namely “tetra zigzag HBC” is chosen as another target.

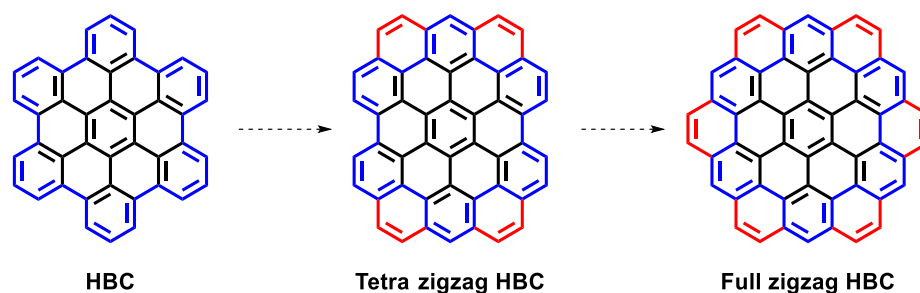


Figure 1-36. Synthetic strategy towards “tetra zigzag HBC” and “full zigzag HBC” from HBC.

1.5.3 Chemical functionalization of NGs

As mentioned above, chemical functionalization is an alternative way to yield novel NGs with tunable electronic properties. As the last part of this dissertation, reduction and edge chlorination of NGs have been chosen as our synthetic strategies. For the reduction, inspired by Mark Watson’s successful work in hydrogenation of HBC to defined peralkylated coronene, our objective is to apply the same method to other larger conjugate systems such as C₆₀, C₉₆ molecules, expecting that novel NGs with similarly hydrogenated periphery can be obtained. On the other hand, precise edge chlorination provides possibilities to achieve atomically precise novel NG structures and to manipulate their physical properties. Together with [REDACTED], we anticipate that the atomically precise chlorination of parent HBC molecule can be achieved by using quite straightforward synthetic strategy as displayed in Fig. 1-37b. Afterwards, the same strategy can be applied to other large NGs from C₆₀H₂₄ to C₂₂₂H₄₂. In comparison with the insoluble parent NGs, the edge-chlorinated NGs are expected to have high solubility as well as relatively lower bandgap.

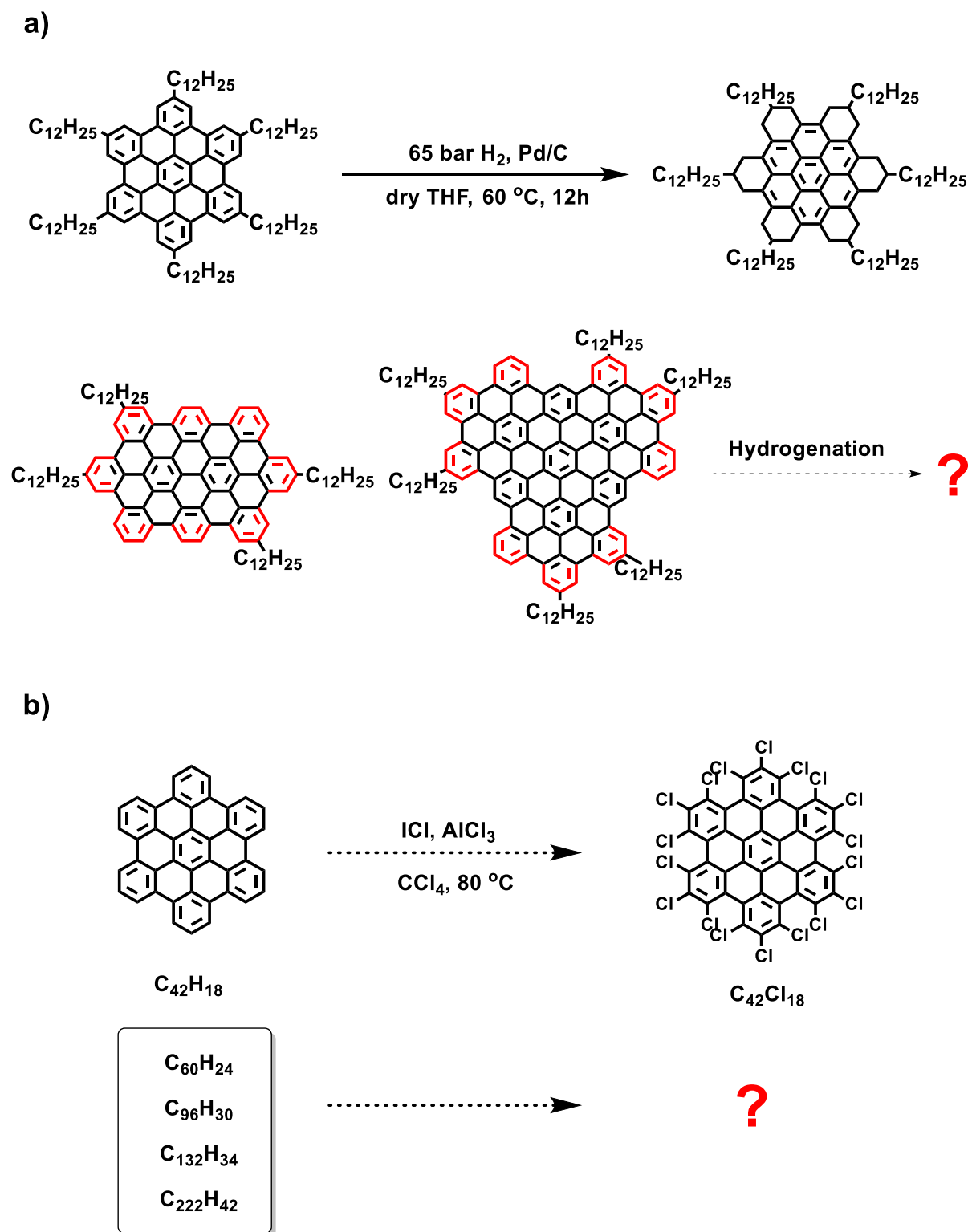


Figure 1-37. a) top) Mark Watson's work; down) possible same strategy can be applied in larger aromatic system like C_{60} and C_{96} . b) Assumed Edge chlorination protocol towards corresponding chlorinated NGs.

1.6 References

- (1) Watson, M. D.; Fechtenkotter, A.; Mullen, K. *Chemical Reviews* **2001**, *101*, 1267.
- (2) Wu, J. S.; Pisula, W.; Mullen, K. *Chemical Reviews* **2007**, *107*, 718.
- (3) Grimsdale, A. C.; Mullen, K. *Angew Chem Int Edit* **2005**, *44*, 5592.
- (4) Clar, E. *Polycyclic Hydrocarbons. Academic Press: New York, 1964, Vol. I/II.*
- (5) Dias, J. R. *Handbook of Polycyclic Hydrocarbons. Elsevier: Amsterdam 1988.*
- (6) G. Harvey, R. *Polycyclic Aromatic Compounds Wiley-VCH: New York 1997.*
- (7) Heeger, A. J. *Rev Mod Phys* **2001**, *73*, 681.
- (8) Shirakawa, H. *Angew Chem Int Edit* **2001**, *40*, 2575.
- (9) MacDiarmid, A. G. *Angew Chem Int Edit* **2001**, *40*, 2581.
- (10) Laschat, S.; Baro, A.; Steinke, N.; Giesselmann, F.; Hagele, C.; Scalia, G.; Judele, R.; Kapatsina, E.; Sauer, S.; Schreivogel, A.; Tosoni, M. *Angew Chem Int Edit* **2007**, *46*, 4832.
- (11) Debad, J. D.; Morris, J. C.; Magnus, P.; Bard, A. J. *J Org Chem* **1997**, *62*, 530.
- (12) Holtrup, F. O.; Muller, G. R. J.; Quante, H.; Defeyter, S.; DeSchryver, F. C.; Mullen, K. *Chem-Eur J* **1997**, *3*, 219.
- (13) van de Craats, A. M.; Stutzmann, N.; Bunk, O.; Nielsen, M. M.; Watson, M.; Mullen, K.; Chanzy, H. D.; Sirringhaus, H.; Friend, R. H. *Adv Mater* **2003**, *15*, 495.
- (14) Pisula, W.; Menon, A.; Stepputat, M.; Lieberwirth, I.; Kolb, U.; Tracz, A.; Sirringhaus, H.; Pakula, T.; Mullen, K. *Adv Mater* **2005**, *17*, 684.
- (15) Allard, S.; Forster, M.; Souharce, B.; Thiem, H.; Scherf, U. *Angew Chem Int Edit* **2008**, *47*, 4070.
- (16) Wong, W. W. H.; Singh, T. B.; Vak, D.; Pisula, W.; Yan, C.; Feng, X. L.; Williams, E. L.; Chan, K. L.; Mao, Q. H.; Jones, D. J.; Ma, C. Q.; Mullen, K.; Bauerle, P.; Holmes, A. B. *Adv Funct Mater* **2010**, *20*, 927.
- (17) Hiramoto, M.; Kishigami, Y.; Yokoyama, M. *Chem Lett* **1990**, 119.
- (18) Schmidt-Mende, L.; Fechtenkotter, A.; Mullen, K.; Moons, E.; Friend, R. H.; MacKenzie, J. D. *Science* **2001**, *293*, 1119.
- (19) Schmidtke, J. P.; Friend, R. H.; Kastler, M.; Mullen, K. *J Chem Phys* **2006**, *124*.
- (20) Wong, W. W. H.; Jones, D. J.; Yan, C.; Watkins, S. E.; King, S.; Haque, S. A.; Wen, X. M.; Ghiggino, K. P.; Holmes, A. B. *Org Lett* **2009**, *11*, 975.
- (21) Boehm, H. P.; Clauss, A.; Fischer, G. O.; Hofmann, U. *Z Anorg Allg Chem* **1962**, *316*, 119.
- (22) Boehm, H. P.; Setton, R.; Stumpp, E. *Pure Appl Chem* **1994**, *66*, 1893.

- (23) Forbeaux, I.; Themlin, J. M.; Debever, J. M. *Phys Rev B* **1998**, *58*, 16396.
- (24) Saito, R.; Fujita, M.; Dresselhaus, G.; Dresselhaus, M. S. *Phys Rev B* **1992**, *46*, 1804.
- (25) Fradkin, E. *Phys Rev B* **1986**, *33*, 3257.
- (26) Novoselov, K. S.; Geim, A. K.; Morozov, S. V.; Jiang, D.; Zhang, Y.; Dubonos, S. V.; Grigorieva, I. V.; Firsov, A. A. *Science* **2004**, *306*, 666.
- (27) Geim, A. K.; Novoselov, K. S. *Nat Mater* **2007**, *6*, 183.
- (28) Service, R. F. *Science* **2009**, *325*, 267.
- (29) Novoselov, K. S.; Fal'ko, V. I.; Colombo, L.; Gellert, P. R.; Schwab, M. G.; Kim, K. *Nature* **2012**, *490*, 192.
- (30) Novoselov, K. S.; Jiang, Z.; Zhang, Y.; Morozov, S. V.; Stormer, H. L.; Zeitler, U.; Maan, J. C.; Boebinger, G. S.; Kim, P.; Geim, A. K. *Science* **2007**, *315*, 1379.
- (31) Zhang, Y. B.; Tan, Y. W.; Stormer, H. L.; Kim, P. *Nature* **2005**, *438*, 201.
- (32) Bolotin, K. I.; Sikes, K. J.; Jiang, Z.; Klima, M.; Fudenberg, G.; Hone, J.; Kim, P.; Stormer, H. L. *Solid State Commun* **2008**, *146*, 351.
- (33) Faccio, R.; Denis, P. A.; Pardo, H.; Goyenola, C.; Mombro, A. W. *J Phys-Condens Mat* **2009**, *21*.
- (34) Frank, I. W.; Tanenbaum, D. M.; Van der Zande, A. M.; McEuen, P. L. *J Vac Sci Technol B* **2007**, *25*, 2558.
- (35) Scarpa, F.; Adhikari, S.; Phani, A. S. *Nanotechnology* **2009**, *20*.
- (36) Chae, H. K.; Siberio-Perez, D. Y.; Kim, J.; Go, Y.; Eddaoudi, M.; Matzger, A. J.; O'Keeffe, M.; Yaghi, O. M. *Nature* **2004**, *427*, 523.
- (37) Brunauer, S.; Emmett, P. H.; Teller, E. *J Am Chem Soc* **1938**, *60*, 309.
- (38) Rao, C. N. R.; Sood, A. K.; Subrahmanyam, K. S.; Govindaraj, A. *Angew Chem Int Edit* **2009**, *48*, 7752.
- (39) Stoller, M. D.; Park, S. J.; Zhu, Y. W.; An, J. H.; Ruoff, R. S. *Nano Lett* **2008**, *8*, 3498.
- (40) Novoselov, K. S.; Geim, A. K.; Morozov, S. V.; Jiang, D.; Katsnelson, M. I.; Grigorieva, I. V.; Dubonos, S. V.; Firsov, A. A. *Nature* **2005**, *438*, 197.
- (41) Westervelt, R. M. *Science* **2008**, *320*, 324.
- (42) Morozov, S. V.; Novoselov, K. S.; Katsnelson, M. I.; Schedin, F.; Elias, D. C.; Jaszczak, J. A.; Geim, A. K. *Phys Rev Lett* **2008**, *100*.
- (43) Schedin, F.; Geim, A. K.; Morozov, S. V.; Hill, E. W.; Blake, P.; Katsnelson, M. I.; Novoselov, K. S. *Nat Mater* **2007**, *6*, 652.
- (44) Dua, V.; Surwade, S. P.; Ammu, S.; Agnihotra, S. R.; Jain, S.; Roberts, K. E.; Park, S.; Ruoff, R. S.; Manohar, S. K. *Angew Chem Int Edit* **2010**, *49*, 2154.

- (45) Dreyer, D. R.; Bielawski, C. W. *Chem Sci* **2011**, *2*, 1233.
- (46) Scheuermann, G. M.; Rumi, L.; Steurer, P.; Bannwarth, W.; Mulhaupt, R. *J Am Chem Soc* **2009**, *131*, 8262.
- (47) Pumera, M. *Energ Environ Sci* **2011**, *4*, 668.
- (48) Sun, Y. Q.; Wu, Q. O.; Shi, G. Q. *Energ Environ Sci* **2011**, *4*, 1113.
- (49) Avouris, P.; Chen, Z. H.; Perebeinos, V. *Nat Nanotechnol* **2007**, *2*, 605.
- (50) Eda, G.; Chhowalla, M. *Nano Lett* **2009**, *9*, 814.
- (51) Mullen, K.; Rabe, J. P. *Accounts Chem Res* **2008**, *41*, 511.
- (52) Berger, C.; Song, Z. M.; Li, T. B.; Li, X. B.; Ogbazghi, A. Y.; Feng, R.; Dai, Z. T.; Marchenkov, A. N.; Conrad, E. H.; First, P. N.; de Heer, W. A. *J Phys Chem B* **2004**, *108*, 19912.
- (53) Bae, S.; Kim, H.; Lee, Y.; Xu, X. F.; Park, J. S.; Zheng, Y.; Balakrishnan, J.; Lei, T.; Kim, H. R.; Song, Y. I.; Kim, Y. J.; Kim, K. S.; Ozyilmaz, B.; Ahn, J. H.; Hong, B. H.; Iijima, S. *Nat Nanotechnol* **2010**, *5*, 574.
- (54) Hernandez, Y.; Nicolosi, V.; Lotya, M.; Blighe, F. M.; Sun, Z. Y.; De, S.; McGovern, I. T.; Holland, B.; Byrne, M.; Gun'ko, Y. K.; Boland, J. J.; Niraj, P.; Duesberg, G.; Krishnamurthy, S.; Goodhue, R.; Hutchison, J.; Scardaci, V.; Ferrari, A. C.; Coleman, J. N. *Nat Nanotechnol* **2008**, *3*, 563.
- (55) Blake, P.; Brimicombe, P. D.; Nair, R. R.; Booth, T. J.; Jiang, D.; Schedin, F.; Ponomarenko, L. A.; Morozov, S. V.; Gleeson, H. F.; Hill, E. W.; Geim, A. K.; Novoselov, K. S. *Nano Lett* **2008**, *8*, 1704.
- (56) Englert, J. M.; Rohrl, J.; Schmidt, C. D.; Graupner, R.; Hundhausen, M.; Hauke, F.; Hirsch, A. *Adv Mater* **2009**, *21*, 4265.
- (57) Torrisi, F.; Hasan, T.; Wu, W. P.; Sun, Z. P.; Lombardo, A.; Kulmala, T. S.; Hsieh, G. W.; Jung, S. J.; Bonaccorso, F.; Paul, P. J.; Chu, D. P.; Ferrari, A. C. *Acs Nano* **2012**, *6*, 2992.
- (58) Li, J. T.; Ye, F.; Vaziri, S.; Muhammed, M.; Lemme, M. C.; Ostling, M. *Adv Mater* **2013**, *25*, 3985.
- (59) Secor, E. B.; Prabhumirashi, P. L.; Puntambekar, K.; Geier, M. L.; Hersam, M. C. *J Phys Chem Lett* **2013**, *4*, 1347.
- (60) Wang, J. Z.; Manga, K. K.; Bao, Q. L.; Loh, K. P. *J Am Chem Soc* **2011**, *133*, 8888.
- (61) Brodie, B. C. *Phil. Trans.* **1859**, *149*, 249.
- (62) Hummers, W. S.; Offeman, R. E. *J Am Chem Soc* **1958**, *80*, 1339.
- (63) Eda, G.; Chhowalla, M. *Adv Mater* **2010**, *22*, 2392.
- (64) Su, Q.; Pang, S. P.; Alijani, V.; Li, C.; Feng, X. L.; Mullen, K. *Adv Mater* **2009**, *21*, 3191.

- (65) Liang, Y. Y.; Frisch, J.; Zhi, L. J.; Norouzi-Arasi, H.; Feng, X. L.; Rabe, J. P.; Koch, N.; Mullen, K. *Nanotechnology* **2009**, *20*.
- (66) Vitchev, R.; Malesevic, A.; Petrov, R. H.; Kemps, R.; Mertens, M.; Vanhulsel, A.; Van Haesendonck, C. *Nanotechnology* **2010**, *21*.
- (67) Reina, A.; Jia, X. T.; Ho, J.; Nezich, D.; Son, H. B.; Bulovic, V.; Dresselhaus, M. S.; Kong, J. *Nano Lett* **2009**, *9*, 3087.
- (68) Wei, D. C.; Liu, Y. Q.; Wang, Y.; Zhang, H. L.; Huang, L. P.; Yu, G. *Nano Lett* **2009**, *9*, 1752.
- (69) Schwierz, F. *Nat Nanotechnol* **2010**, *5*, 487.
- (70) Liang, Y. T.; Hersam, M. C. *Macromol Chem Physic* **2012**, *213*, 1091.
- (71) Rodriguez-Manzo, J. A.; Cretu, O.; Banhart, F. *Acs Nano* **2010**, *4*, 3422.
- (72) Berger, C.; Song, Z. M.; Li, X. B.; Wu, X. S.; Brown, N.; Naud, C.; Mayou, D.; Li, T. B.; Hass, J.; Marchenkov, A. N.; Conrad, E. H.; First, P. N.; de Heer, W. A. *Science* **2006**, *312*, 1191.
- (73) Emtsev, K. V.; Bostwick, A.; Horn, K.; Jobst, J.; Kellogg, G. L.; Ley, L.; McChesney, J. L.; Ohta, T.; Reshanov, S. A.; Rohrl, J.; Rotenberg, E.; Schmid, A. K.; Waldmann, D.; Weber, H. B.; Seyller, T. *Nat Mater* **2009**, *8*, 203.
- (74) Ohta, T.; Bostwick, A.; Seyller, T.; Horn, K.; Rotenberg, E. *Science* **2006**, *313*, 951.
- (75) de Heer, W. A.; Berger, C.; Wu, X. S.; First, P. N.; Conrad, E. H.; Li, X. B.; Li, T. B.; Sprinkle, M.; Hass, J.; Sadowski, M. L.; Potemski, M.; Martinez, G. *Solid State Commun* **2007**, *143*, 92.
- (76) Virojanadara, C.; Syvajarvi, M.; Yakimova, R.; Johansson, L. I.; Zakharov, A. A.; Balasubramanian, T. *Phys Rev B* **2008**, *78*.
- (77) Kedzierski, J.; Hsu, P. L.; Healey, P.; Wyatt, P. W.; Keast, C. L.; Sprinkle, M.; Berger, C.; de Heer, W. A. *Ieee T Electron Dev* **2008**, *55*, 2078.
- (78) Huang, H.; Chen, W.; Chen, S.; Wee, A. T. S. *Acs Nano* **2008**, *2*, 2513.
- (79) Zhou, S. Y.; Gweon, G. H.; Fedorov, A. V.; First, P. N.; De Heer, W. A.; Lee, D. H.; Guinea, F.; Castro Neto, A. H.; Lanzara, A. *Nat Mater* **2007**, *6*, 916.
- (80) Lang, K. F.; Kalow, J.; Buffleb, H. *Chem Ber-Recl* **1962**, *95*, 1052.
- (81) Lang, K. F.; Kalow, J.; Buffleb, H. *Chem Ber-Recl* **1964**, *97*, 494.
- (82) Lang, K. F.; Buffleb, H. *Chem Ber-Recl* **1962**, *95*, 1049.
- (83) Lang, K. F.; Buffleb, H.; Zander, M. *Angew Chem Int Edit* **1963**, *75*, 170.
- (84) Sullivan, R. F.; Boduszynski, M. M.; Fetzer, J. C. *Energ Fuel* **1989**, *3*, 603.
- (85) Affoune, A. M.; Prasad, B. L. V.; Sato, H.; Enoki, T.; Kaburagi, Y.; Hishiyama, Y. *Chem Phys Lett* **2001**, *348*, 17.

- (86) Lu, J.; Yeo, P. S. E.; Gan, C. K.; Wu, P.; Loh, K. P. *Nat Nanotechnol* **2011**, *6*, 247.
- (87) Loh, K. P.; Bao, Q. L.; Eda, G.; Chhowalla, M. *Nat Chem* **2010**, *2*, 1015.
- (88) Clar, E.; Schmidt, W. *Tetrahedron* **1979**, *35*, 1027.
- (89) Clar, E.; Schmidt, W. *Tetrahedron* **1979**, *35*, 2673.
- (90) Clar, E.; Stewart, D. G. *J Am Chem Soc* **1953**, *75*, 2667.
- (91) Scholl, R.; Seer, C. *Justus Liebigs Annalen Der Chemie* **1912**, *394*, 111.
- (92) Scholl, R.; Seer, C. *Ber Dtsch Chem Ges* **1922**, *55*, 109.
- (93) Scholl, R.; Seer, C.; Weitzenbock, R. *Ber Dtsch Chem Ges* **1910**, *43*, 2202.
- (94) Morita, Y.; Suzuki, S.; Sato, K.; Takui, T. *Nat Chem* **2011**, *3*, 197.
- (95) Reid, D. H. *Tetrahedron* **1958**, *3*, 339.
- (96) Goto, K.; Kubo, T.; Yamamoto, K.; Nakasuji, K.; Sato, K.; Shiomi, D.; Takui, T.; Kubota, M.; Kobayashi, T.; Yakusi, K.; Ouyang, J. Y. *J Am Chem Soc* **1999**, *121*, 1619.
- (97) Haddon, R. C.; Hirani, A. M.; Kroloff, N. J.; Marshall, J. H. *J Org Chem* **1983**, *48*, 2115.
- (98) Pagni, R. M.; Peebles, W.; Haddon, R. C.; Chichester, S. V. *J Org Chem* **1990**, *55*, 5595.
- (99) Peebles, W.; Pagni, R. M.; Haddon, R. C. *Tetrahedron Lett* **1989**, *30*, 2727.
- (100) Kaplan, M. L.; Haddon, R. C.; Hirani, A. M.; Schilling, F. C.; Marshall, J. H. *J Org Chem* **1981**, *46*, 675.
- (101) Haddon, R. C.; Chichester, S. V.; Stein, S. M.; Marshall, J. H.; Majsce, A. M. *J Org Chem* **1987**, *52*, 711.
- (102) Koutentis, P. A.; Chen, Y.; Cao, Y.; Best, T. P.; Itkis, M. E.; Beer, L.; Oakley, R. T.; Cordes, A. W.; Brock, C. P.; Haddon, R. C. *J Am Chem Soc* **2001**, *123*, 3864.
- (103) Haddon, R. C.; Wudl, F.; Kaplan, M. L.; Marshall, J. H.; Cais, R. E.; Bramwell, F. B. *J Am Chem Soc* **1978**, *100*, 7629.
- (104) Morita, Y.; Aoki, T.; Fukui, K.; Nakazawa, S.; Tamaki, K.; Suzuki, S.; Fuyuhiko, A.; Yamamoto, K.; Sato, K.; Shiomi, D.; Naito, A.; Takui, T.; Nakasuji, K. *Angew Chem Int Edit* **2002**, *41*, 1793.
- (105) Morita, Y.; Kawai, J.; Fukui, K.; Nakazawa, S.; Sato, K.; Shiomi, D.; Takui, T.; Nakasuji, K. *Org Lett* **2003**, *5*, 3289.
- (106) Morita, Y.; Ohba, T.; Haneda, N.; Maki, S.; Kawai, J.; Hatanaka, K.; Sato, K.; Shiomi, D.; Takui, T.; Nakasuji, K. *J Am Chem Soc* **2000**, *122*, 4825.
- (107) Kubo, T.; Katada, Y.; Shimizu, A.; Hirao, Y.; Sato, K.; Takui, T.; Uruichi, M.; Yakushi, K.; Haddon, R. C. *J Am Chem Soc* **2011**, *133*, 14240.

- (108) Umeda, R.; Hibi, D.; Miki, K.; Tobe, Y. *Org Lett* **2009**, *11*, 4104.
- (109) Wu, T. C.; Chen, C. H.; Hibi, D.; Shimizu, A.; Tobe, Y.; Wu, Y. T. *Angew Chem Int Edit* **2010**, *49*, 7059.
- (110) Clar, E.; Ironside, C. T. *P Chem Soc London* **1958**, 150.
- (111) Clar, E.; Ironside, C. T.; Zander, M. *J Chem Soc* **1959**, 142.
- (112) Halleux, A.; Martin, R. H.; King, G. S. D. *Helv Chim Acta* **1958**, *41*, 1177.
- (113) Hendel, W.; Khan, Z. H.; Schmidt, W. *Tetrahedron* **1986**, *42*, 1127.
- (114) Stabel, A.; Herwig, P.; Mullen, K.; Rabe, J. P. *Angewandte Chemie-International Edition In English* **1995**, *34*, 1609.
- (115) Iyer, V. S.; Yoshimura, K.; Enkelmann, V.; Epsch, R.; Rabe, J. P.; Mullen, K. *Angew Chem Int Edit* **1998**, *37*, 2696.
- (116) Feng, X. L.; Wu, J. S.; Ai, M.; Pisula, W.; Zhi, L. J.; Rabe, J. P.; Mullen, K. *Angew Chem Int Edit* **2007**, *46*, 3033.
- (117) Muller, M.; Iyer, V. S.; Kubel, C.; Enkelmann, V.; Mullen, K. *Angewandte Chemie-International Edition In English* **1997**, *36*, 1607.
- (118) Dotz, F.; Brand, J. D.; Ito, S.; Gherghel, L.; Mullen, K. *J Am Chem Soc* **2000**, *122*, 7707.
- (119) Iyer, V. S.; Wehmeier, M.; Brand, J. D.; Keegstra, M. A.; Mullen, K. *Angewandte Chemie-International Edition In English* **1997**, *36*, 1604.
- (120) Tomovic, Z.; Watson, M. D.; Mullen, K. *Angew Chem Int Edit* **2004**, *43*, 755.
- (121) Morgenroth, F.; Reuther, E.; Mullen, K. *Angewandte Chemie-International Edition In English* **1997**, *36*, 631.
- (122) Palermo, V.; Morelli, S.; Simpson, C.; Mullen, K.; Samori, P. *J Mater Chem* **2006**, *16*, 266.
- (123) Simpson, C. D.; Brand, J. D.; Berresheim, A. J.; Przybilla, L.; Rader, H. J.; Mullen, K. *Chem-Eur J* **2002**, *8*, 1424.
- (124) Bohnen, A.; Koch, K. H.; Luttke, W.; Mullen, K. *Angewandte Chemie-International Edition In English* **1990**, *29*, 525.
- (125) Koch, K. H.; Mullen, K. *Chem Ber* **1991**, *124*, 2091.
- (126) Pschirer, N. G.; Kohl, C.; Nolde, T.; Qu, J. Q.; Mullen, K. *Angew Chem Int Edit* **2006**, *45*, 1401.
- (127) Petit, M.; Hayakawa, R.; Shirai, Y.; Wakayama, Y.; Hill, J. P.; Ariga, K.; Chikyow, T. *Appl Phys Lett* **2008**, *92*.

- (128) Oh, J. H.; Lee, W. Y.; Noe, T.; Chen, W. C.; Konemann, M.; Bao, Z. A. *J Am Chem Soc* **2011**, *133*, 4204.
- (129) Fort, E. H.; Donovan, P. M.; Scott, L. T. *J Am Chem Soc* **2009**, *131*, 16006.
- (130) Li, J. L.; Jiao, C. J.; Huang, K. W.; Wu, J. S. *Chem-Eur J* **2011**, *17*, 14672.
- (131) Yao, J. H.; Chi, C. Y.; Wu, J. S.; Loh, K. P. *Chem-Eur J* **2009**, *15*, 9299.
- (132) Zhang, K.; Huang, K. W.; Li, J. L.; Luo, J.; Chi, C. Y.; Wu, J. S. *Org Lett* **2009**, *11*, 4854.
- (133) Konishi, A.; Hirao, Y.; Nakano, M.; Shimizu, A.; Botek, E.; Champagne, B.; Shiomi, D.; Sato, K.; Takui, T.; Matsumoto, K.; Kurata, H.; Kubo, T. *J Am Chem Soc* **2010**, *132*, 11021.
- (134) Haworth, R. D.; Mavin, C. R. *J Chem Soc* **1932**, 1485.
- (135) Haworth, R. D.; Mavin, C. R. *J Chem Soc* **1932**, 2720.
- (136) Haworth, R. D. *J Chem Soc* **1932**, 1125.
- (137) Haworth, R. D.; Bolam, F. M. *J Chem Soc* **1932**, 2248.
- (138) Clar, E.; Zander, M. *J Chem Soc* **1957**, 4616.
- (139) Fechtenkotter, A.; Tchegotareva, N.; Watson, M.; Mullen, K. *Tetrahedron* **2001**, *57*, 3769.
- (140) Ito, S.; Wehmeier, M.; Brand, J. D.; Kubel, C.; Epsch, R.; Rabe, J. P.; Mullen, K. *Chem-Eur J* **2000**, *6*, 4327.
- (141) Kubel, C.; Eckhardt, K.; Enkelmann, V.; Wegner, G.; Mullen, K. *J Mater Chem* **2000**, *10*, 1469.
- (142) Muller, M.; Kubel, C.; Mullen, K. *Chem-Eur J* **1998**, *4*, 2099.
- (143) Mallory, F. B.; Gordon, J. T.; Wood, C. S.; Lindquist, L. C.; Savitz, M. L. *J Am Chem Soc* **1962**, *84*, 4361.
- (144) Xiao, S.; Myers, M.; Miao, Q.; Sanaur, S.; Pang, K.; Steigerwald, M. L.; Nuckolls, C. *Angewandte Chemie* **2005**, *44*, 7390.
- (145) Treier, M.; Pignedoli, C. A.; Laino, T.; Rieger, R.; Mullen, K.; Passerone, D.; Fasel, R. *Nat Chem* **2011**, *3*, 61.
- (146) Boorum, M. M.; Vasil'ev, Y. V.; Drewello, T.; Scott, L. T. *Science* **2001**, *294*, 828.
- (147) Scott, L. T.; Boorum, M. M.; McMahon, B. J.; Hagen, S.; Mack, J.; Blank, J.; Wegner, H.; de Meijere, A. *Science* **2002**, *295*, 1500.
- (148) Diederich, F.; Staab, H. A. *Angewandte Chemie-International Edition In English* **1978**, *17*, 372.
- (149) Krieger, C.; Diederich, F.; Schweitzer, D.; Staab, H. A. *Angewandte Chemie-International Edition In English* **1979**, *18*, 699.

- (150) Staab, H. A.; Diederich, F. *Chem Ber-Recl* **1983**, *116*, 3487.
- (151) Cho, B. P.; Harvey, R. G. *J Org Chem* **1987**, *52*, 5668.
- (152) Cho, B. P.; Harvey, R. G. *Tetrahedron Lett* **1987**, *28*, 861.
- (153) Goldfinger, M. B.; Crawford, K. B.; Swager, T. M. *J Am Chem Soc* **1997**, *119*, 4578.
- (154) Zhang, Q.; Peng, H. Q.; Zhang, G. S.; Lu, Q. Q.; Chang, J.; Dong, Y. Y.; Shi, X. Y.; Wei, J. F. *J Am Chem Soc* **2014**, *136*, 5057.
- (155) Fujita, M.; Wakabayashi, K.; Nakada, K.; Kusakabe, K. *J Phys Soc Jpn* **1996**, *65*, 1920.
- (156) Nakada, K.; Fujita, M.; Dresselhaus, G.; Dresselhaus, M. S. *Phys Rev B* **1996**, *54*, 17954.
- (157) Wakabayashi, K.; Fujita, M.; Ajiki, H.; Sigrist, M. *Phys Rev B* **1999**, *59*, 8271.
- (158) Barone, V.; Hod, O.; Scuseria, G. E. *Nano Lett* **2006**, *6*, 2748.
- (159) Son, Y. W.; Cohen, M. L.; Louie, S. G. *Phys Rev Lett* **2006**, *97*.
- (160) Chen, Z. H.; Lin, Y. M.; Rooks, M. J.; Avouris, P. *Physica E* **2007**, *40*, 228.
- (161) Han, M. Y.; Ozyilmaz, B.; Zhang, Y. B.; Kim, P. *Phys Rev Lett* **2007**, *98*.
- (162) Bai, J. W.; Duan, X. F.; Huang, Y. *Nano Lett* **2009**, *9*, 2083.
- (163) Li, X. L.; Wang, X. R.; Zhang, L.; Lee, S. W.; Dai, H. J. *Science* **2008**, *319*, 1229.
- (164) Higginbotham, A. L.; Kosynkin, D. V.; Sinitskii, A.; Sun, Z. Z.; Tour, J. M. *Acs Nano* **2010**, *4*, 2059.
- (165) Kosynkin, D. V.; Higginbotham, A. L.; Sinitskii, A.; Lomeda, J. R.; Dimiev, A.; Price, B. K.; Tour, J. M. *Nature* **2009**, *458*, 872.
- (166) Jiao, L. Y.; Zhang, L.; Wang, X. R.; Diankov, G.; Dai, H. J. *Nature* **2009**, *458*, 877.
- (167) Wang, Z. F.; Li, Q. X.; Zheng, H. X.; Ren, H.; Su, H. B.; Shi, Q. W.; Chen, J. *Phys Rev B* **2007**, *75*.
- (168) Horn, T.; Wegener, S.; Mullen, K. *Macromol Chem Physic* **1995**, *196*, 2463.
- (169) Sastri, V. R.; Schulman, R.; Roberts, D. C. *Macromolecules* **1982**, *15*, 939.
- (170) Kaur, I.; Jazdyk, M.; Stein, N. N.; Prusevich, P.; Miller, G. P. *J Am Chem Soc* **2010**, *132*, 1261.
- (171) Kaur, I.; Stein, N. N.; Kopreski, R. P.; Miller, G. P. *J Am Chem Soc* **2009**, *131*, 3424.
- (172) Zade, S. S.; Bendikov, M. *Angew Chem Int Edit* **2010**, *49*, 4012.
- (173) Landis, C. A.; Parkin, S. R.; Anthony, J. E. *Japanese Journal Of Applied Physics Part 1-Regular Papers Brief Communications & Review Papers* **2005**, *44*, 3921.
- (174) Mondal, R.; Shah, B. K.; Neckers, D. C. *J Am Chem Soc* **2006**, *128*, 9612.

- (175) Watanabe, M.; Chang, Y. J.; Liu, S. W.; Chao, T. H.; Goto, K.; Islam, M. M.; Yuan, C. H.; Tao, Y. T.; Shinmyozu, T.; Chow, T. J. *Nat Chem* **2012**, *4*, 574.
- (176) Stille, J. K.; Freeburg, M. E. *J Polym Sci Pol Lett* **1967**, *5*, 989.
- (177) Kellman, R.; Marvel, C. S. *J Polym Sci Pol Chem* **1975**, *13*, 2125.
- (178) Schluter, A. D.; Loffler, M.; Enkelmann, V. *Nature* **1994**, *368*, 831.
- (179) Scherf, U.; Mullen, K. *Makromol Chem-Rapid* **1991**, *12*, 489.
- (180) Scherf, U.; Mullen, K. *Macromolecules* **1992**, *25*, 3546.
- (181) Chmil, K.; Scherf, U. *Makromol Chem-Rapid* **1993**, *14*, 217.
- (182) Chmil, K.; Scherf, U. *Acta Polym* **1997**, *48*, 208.
- (183) Goldfinger, M. B.; Swager, T. M. *J Am Chem Soc* **1994**, *116*, 7895.
- (184) Shifrina, Z. B.; Averina, M. S.; Rusanov, A. L.; Wagner, M.; Mullen, K. *Macromolecules* **2000**, *33*, 3525.
- (185) Wu, J. S.; Gherghel, L.; Watson, M. D.; Li, J. X.; Wang, Z. H.; Simpson, C. D.; Kolb, U.; Mullen, K. *Macromolecules* **2003**, *36*, 7082.
- (186) Fogel, Y.; Zhi, L. J.; Rouhanipour, A.; Andrienko, D.; Rader, H. J.; Mullen, K. *Macromolecules* **2009**, *42*, 6878.
- (187) Narita, A.; Feng, X. L.; Hernandez, Y.; Jensen, S. A.; Bonn, M.; Yang, H. F.; Verzhbitskiy, I. A.; Casiraghi, C.; Hansen, M. R.; Koch, A. H. R.; Fytas, G.; Ivasenko, O.; Li, B.; Mali, K. S.; Balandina, T.; Mahesh, S.; De Feyter, S.; Mullen, K. *Nat Chem* **2014**, *6*, 126.
- (188) Narita, A.; Verzhbitskiy, I. A.; Frederickx, W.; Mali, K. S.; Jensen, S. A.; Hansen, M. R.; Bonn, M.; De Feyter, S.; Casiraghi, C.; Feng, X.; Mullen, K. *Acs Nano* **2014**, *8*, 11622.
- (189) Yang, X. Y.; Dou, X.; Rouhanipour, A.; Zhi, L. J.; Rader, H. J.; Mullen, K. *J Am Chem Soc* **2008**, *130*, 4216.
- (190) Dossel, L.; Gherghel, L.; Feng, X. L.; Mullen, K. *Angew Chem Int Edit* **2011**, *50*, 2540.
- (191) Schwab, M. G.; Narita, A.; Hernandez, Y.; Balandina, T.; Mali, K. S.; De Feyter, S.; Feng, X. L.; Mullen, K. *J Am Chem Soc* **2012**, *134*, 18169.
- (192) Vo, T. H.; Shekhirev, M.; Kunkel, D. A.; Morton, M. D.; Berglund, E.; Kong, L. M.; Wilson, P. M.; Dowben, P. A.; Enders, A.; Sinitskii, A. *Nat Commun* **2014**, *5*.
- (193) Cai, J. M.; Ruffieux, P.; Jaafar, R.; Bieri, M.; Braun, T.; Blankenburg, S.; Muoth, M.; Seitsonen, A. P.; Saleh, M.; Feng, X. L.; Mullen, K.; Fasel, R. *Nature* **2010**, *466*, 470.
- (194) Talirz, L.; Sode, H.; Cai, J. M.; Ruffieux, P.; Blankenburg, S.; Jafaar, R.; Berger, R.; Feng, X. L.; Mullen, K.; Passerone, D.; Fasel, R.; Pignedoli, C. A. *J Am Chem Soc* **2013**, *135*, 2060.

- (195) Chen, Y. C.; de Oteyza, D. G.; Pedramrazi, Z.; Chen, C.; Fischer, F. R.; Crommie, M. F. *Acs Nano* **2013**, *7*, 6123.
- (196) Bronner, C.; Stremlau, S.; Gille, M.; Brausse, F.; Haase, A.; Hecht, S.; Tegeder, P. *Angew Chem Int Edit* **2013**, *52*, 4422.
- (197) Koch, M.; Ample, F.; Joachim, C.; Grill, L. *Nat Nano* **2012**, *7*, 713.
- (198) Linden, S.; Zhong, D.; Timmer, A.; Aghdassi, N.; Franke, J. H.; Zhang, H.; Feng, X.; Mullen, K.; Fuchs, H.; Chi, L.; Zacharias, H. *Phys Rev Lett* **2012**, *108*.
- (199) Ruffieux, P.; Cai, J. M.; Plumb, N. C.; Patthey, L.; Prezzi, D.; Ferretti, A.; Molinari, E.; Feng, X. L.; Mullen, K.; Pignedoli, C. A.; Fasel, R. *Acs Nano* **2012**, *6*, 6930.
- (200) Cai, J. M.; Pignedoli, C. A.; Talirz, L.; Ruffieux, P.; Sode, H.; Liang, L. B.; Meunier, V.; Berger, R.; Li, R. J.; Feng, X. L.; Mullen, K.; Fasel, R. *Nat Nanotechnol* **2014**, *9*, 896.
- (201) Chen, Y. C.; Cao, T.; Chen, C.; Pedramrazi, Z.; Haberer, D.; de Oteyza, D. G.; Fischer, F. R.; Louie, S. G.; Crommie, M. F. *Nat Nanotechnol* **2015**, *10*, 156.
- (202) Riss, A.; Wickenburg, S.; Gorman, P.; Tan, L. Z.; Tsai, H. Z.; de Oteyza, D. G.; Chen, Y. C.; Bradley, A. J.; Ugeda, M. M.; Etkin, G.; Louie, S. G.; Fischer, F. R.; Crommie, M. F. *Nano Lett* **2014**, *14*, 2251.
- (203) Sun, Q.; Zhang, C.; Li, Z. W.; Kong, H. H.; Tan, Q. G.; Hu, A. G.; Xu, W. *J Am Chem Soc* **2013**, *135*, 8448.
- (204) Bennett, P. B.; Pedramrazi, Z.; Madani, A.; Chen, Y. C.; de Oteyza, D. G.; Chen, C.; Fischer, F. R.; Crommie, M. F.; Bokor, J. *Appl Phys Lett* **2013**, *103*.
- (205) Kastler, M.; Schmidt, J.; Pisula, W.; Sebastiani, D.; Mullen, K. *J Am Chem Soc* **2006**, *128*, 9526.
- (206) Wang, Z. H.; Tomovic, E.; Kastler, M.; Pretsch, R.; Negri, F.; Enkelmann, V.; Mullen, K. *J Am Chem Soc* **2004**, *126*, 779

Chapter 2. Bottom-Up Synthesis of GNRs with Zigzag Edge Structures: Surface-Assisted Synthesis

2.1 Introduction

The earlier theoretical studies of GNRs have been done in particular by Nakada et al. in 1996¹ and later by Son et al. in 2006² using DFT and tight bonding theory. According to their calculations, the determining factors of the GNR's electronic properties are the quantum confinement effect (QCE) as well as the edge effects. In contrast to armchair-type GNRs (AGNR) showing semiconducting behavior with a direct energy gap, the GNRs with zigzag edge structures (ZGNR) show unique electronic properties including profound lowering of the bandgap and the presence of localized edge states that can be spin-polarized. For the AGNR, the DFT calculation indicated that there was no density of states (DOS) at the Fermi level (E_F) as displayed in figure 2-1a and c. Regarding the ZGNR, the DFT calculation showed a set of edge-state bands at the E_F without considering the spin states (Fig. 2-1d), which leads to magnetic states. However, by inclusion of the spin degrees of freedom within DFT methods, the zigzag GNRs were predicted to have a non-magnetic ground state with ferromagnetic ordering at each zigzag edge, and antiparallel spin orientation between the two edges. The spin-density plot clearly shows that spin moments are mainly distributed at the edge carbon atoms (Fig. 2-1e).

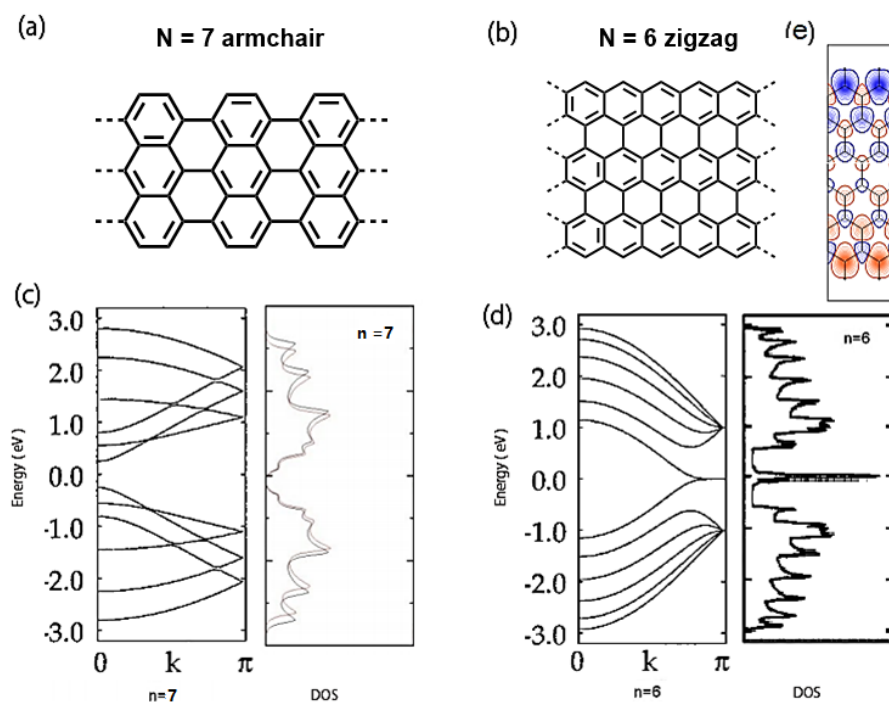


Figure 2-1. Schematic structures of GNR with a) an armchair edge and b) a zigzag edge; Energy dispersion for c) $N_a = 7$ AGNR with an armchair edge and d) $N_z = 6$ ZGNR with a zigzag edge together with the corresponding DOSs. e) Spin density for $N_z = 6$ ZGNR, red and blue represent different spin direction. Ref.[1] *Physical review B*, 1996.

Besides the aforementioned computational calculations of ZGNR, its properties such as edge states and magnetism have been experimentally observed and investigated in a number of GNR systems with less well-defined zigzag edge structures. In 2013, Roman Fasel et al.³ reported that the states localized at the zigzag ends of the surface-synthesized finite 7-AGNRs can be observed. Later, Ijäs, M. et al.⁴ studied the electronic states localized at zigzag termini of finite 7-AGNRs by the Hubbard model and DFT method. The results exhibited a qualitatively matching of DFT calculation and the Hubbard model. In 2014, Magda, G. Z. et al.⁵ used a nanofabrication technique based on STM to define GNRs with nanometer precision and well-defined crystallographic edge orientations. In contrast to “armchair-type” GNRs that displayed quantum confinement gaps, the ZGNRs with width less than 7 nm exhibited spin-polarized edge states along their edges, which further led to an electronic bandgap of about 0.2-0.3 eV. Moreover, by increasing the width of ZGNRs, a semiconductor-to-metal transition was revealed, indicating the switch of magnetic coupling between opposite GNR edges from antiferromagnetic to ferromagnetic configuration (See Fig. 2-2).

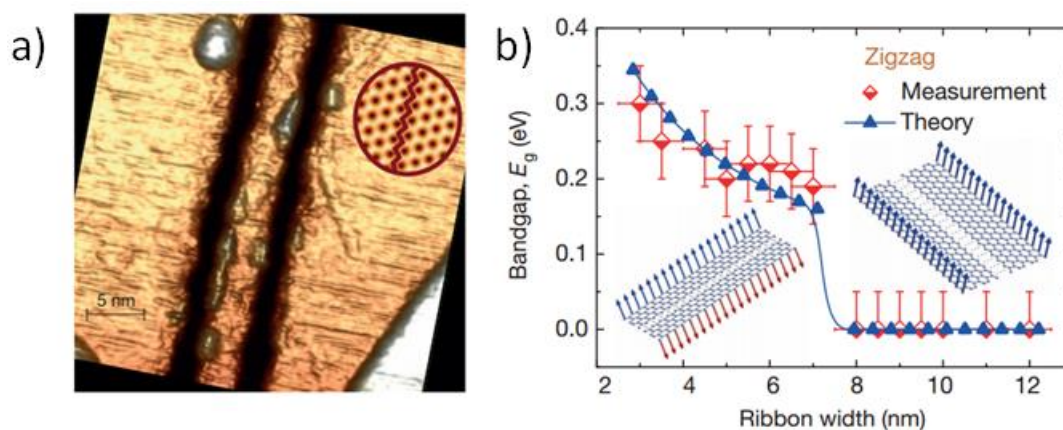


Figure 2-2. a) STM image of a 6.5 nm-wide GNR with edges of precisely zigzag orientation. b) The bandgap measured by tunneling spectroscopy as a function of ribbon width in zigzag GNRs. The band structure was governed by emerging edge magnetism and a sharp semiconductor (antiferromagnetic) to metal (ferromagnetic) transition for zigzag GNRs.

As demonstrated above, the ZGNRs exhibit semiconductor behavior with two localized electronic edge states. These two states are ferromagnetically ordered at each edge and antiferromagnetically coupled with each other, which means that the total spin of ZGNRs is zero. Therefore, how to utilize this amazing property (spin polarized edge-state) becomes an interesting question. Son et al.⁶ have also investigated the question and found that the effects of an external transverse field are significant.⁶ The half-metallic property can be revealed by applying external electric fields. Once the external electric field is applied, the energy gaps of one spin channel will be closed, leaving the other one insulating. Thus, the half-metallicity comes from the relative movement in energy of edge states under electrostatic potential, rendering the ZGNRs as potential spintronic materials.

Although the ZGNRs were predicted to exhibit amazing properties based on the above theoretical studies, these properties had been barely observed in experiment. In order to explore the fundamental electronic and magnetic properties related to zigzag edges and to realize specific carbon nanostructures with properties such as spin confinement or spin filtering, fabrication of ZGNRs with atomically precise edge structures are needed. In this chapter, we demonstrate that our method of GNR synthesis on conducting surfaces can be further developed to provide the first GNRs with geometrically perfect zigzag edge structures as well as GNRs with partial zigzag structures. Moreover, the electronic and magnetic properties of the fabricated $N = 6$ ZGNRs (**f** and **f'**) have been investigated and compared with aforementioned predictions.

2.2 Surface-assisted synthesis of GNRs with zigzag edge

2.2.1 Synthetic strategy

According to previously reported procedures of fabricating GNRs, the simplest and most efficient way to achieve novel GNRs with zigzag edges is to use specifically designed monomers with zigzag edges as key building blocks. Dibenzo[*a,j*]anthracene-based monomer **1-123** with two reactive halogen substituents (X) was thus designed to fabricate the desired GNRs with zigzag edges. Thermally induced aryl-aryl coupling will allow the polymerization that leads to a snake like polymer **1-124** (Fig. 1-34). It is the beauty of this design that additional phenyl or biphenyl substituents (Ar) in the interior of the “U-shape” would allow to fill the “trough” positions like in polymers **1-124a** and **b** (Fig. 1-34). In these two cases, apart from the polymerization and planarization, an oxidative ring closure will lead to the formation of GNR **d** with a hybrid of zigzag and gulf edges with the phenyl substituent as Ar, as well as GNR **e** with partial zigzag and cove edge

structures with biphenyl group as Ar (Fig. 2-3). Furthermore, the starting monomers (**1-123c, d**), which bear 1,3-dimethyl-biphenyl substituent as Ar, are expected to establish the $N_z = 6$ GNR (**f** and **f'**) with the perfect zigzag structures via forming two new six-membered rings between two methyl substituents and neighboring benzene rings (Fig. 2-3).

As introduced in section 1.4.3.2, the successful strategy for the atomically precise bottom-up fabrication of low-dimensional GNRs has been developed by [REDACTED] in 2010.⁷ Subsequently, series of novel GNRs such as nitrogen doped GNRs as well as armchair GNRs (AGNR) with different widths were also fabricated *via* the same surface-assisted protocol.^{8,9} In this part, we cooperated with [REDACTED] (EMPA, Switzerland) for the surface-assisted fabrications of novel GNR structures with zigzag edges.

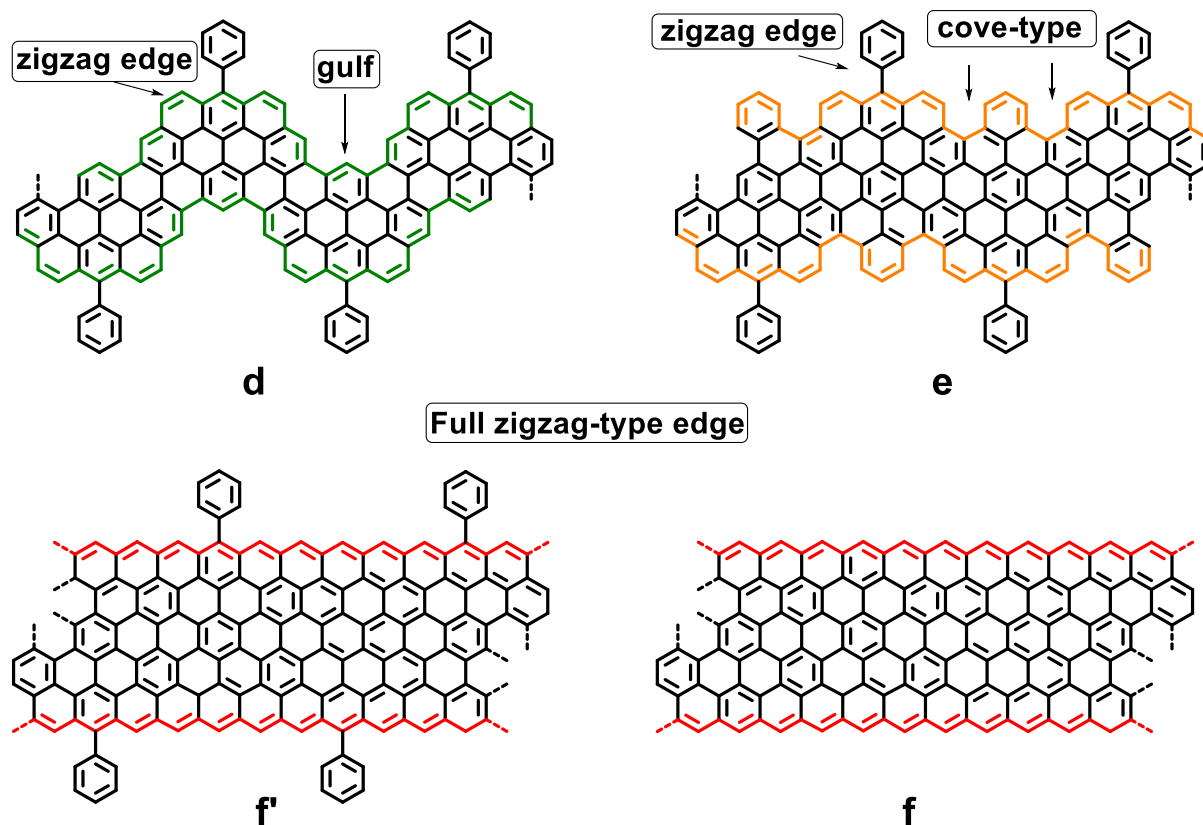


Figure 2-3. Assumed novel GNR structures with various edge structures.

There are several synthetic approaches in the literature toward the backbone of “U-shaped” building block. As shown in Fig. 2-4, the three most promising synthetic methods based on: 1)

photochemistry¹⁰⁻¹⁵; 2) pyrylium chemistry¹⁶⁻²⁴; 3) transition-metal catalyzed cyclization²⁵⁻³¹ were considered. Theoretically, series of monomers with substituents Ar_1 and R/Ar_2 could be thus synthesized by employing these methods. Methods such as 4) metathesis or ring expansion etc. were excluded because of the complicated procedure and low yields.³²⁻³⁴

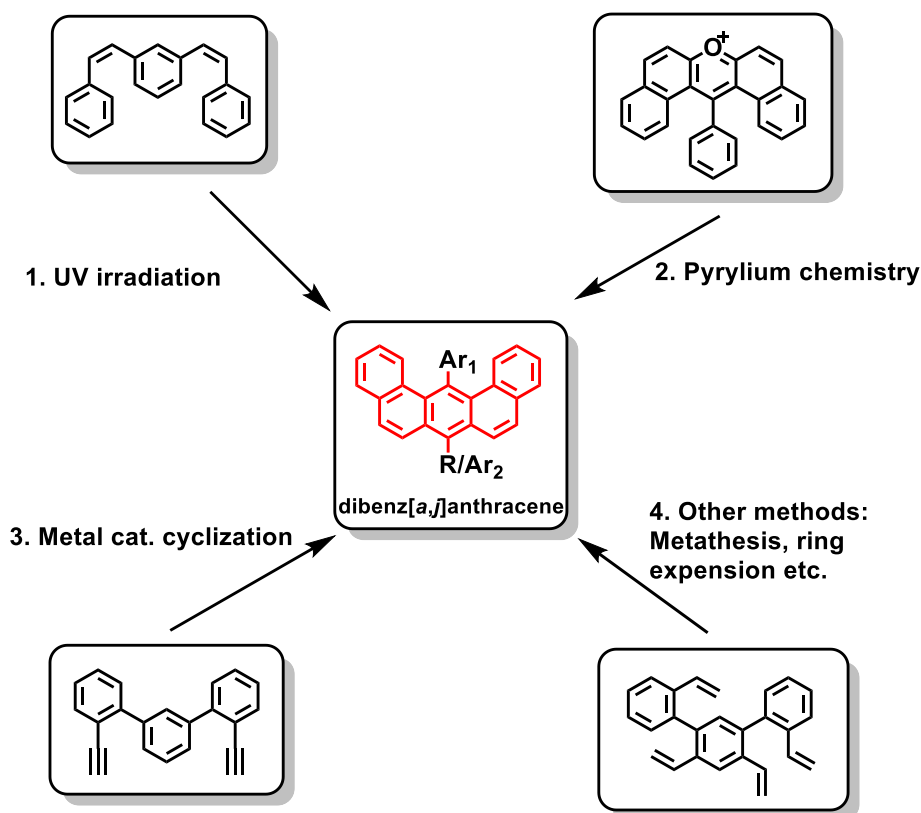


Figure 2-4. Possible synthetic methods including 1) photocyclization, 2) pyrylium chemistry, 3) transition-metal catalyzed cyclization, and 4) metathesis etc. toward backbone structure of “U-shaped“ monomer.

2.2.2 Attempts of Synthesizing monomers based on photochemistry

As described in the previous section 1.3.2.3, the photocyclization had a long history as a powerful tool in building up classes of conjugated systems. Nevertheless, there was also a disadvantage for this method in applications, which was the possible rearrangement during the reaction that led to final products with different configurations. Figure 2-5a shows one typical example in the synthesis of helicene from (*Z*)-1,2-di(naphthalen-2-yl)ethane precursor. Actually, three products were finally obtained due to the rearrangement during the photocyclization. Therefore, one critical issue for the application of photocyclization in our system will be the possible side product owing to the

rearrangement (Fig. 2-5b). Regarding our target, the one with dibenzo[*a,j*]anthracene backbone is our desired product.

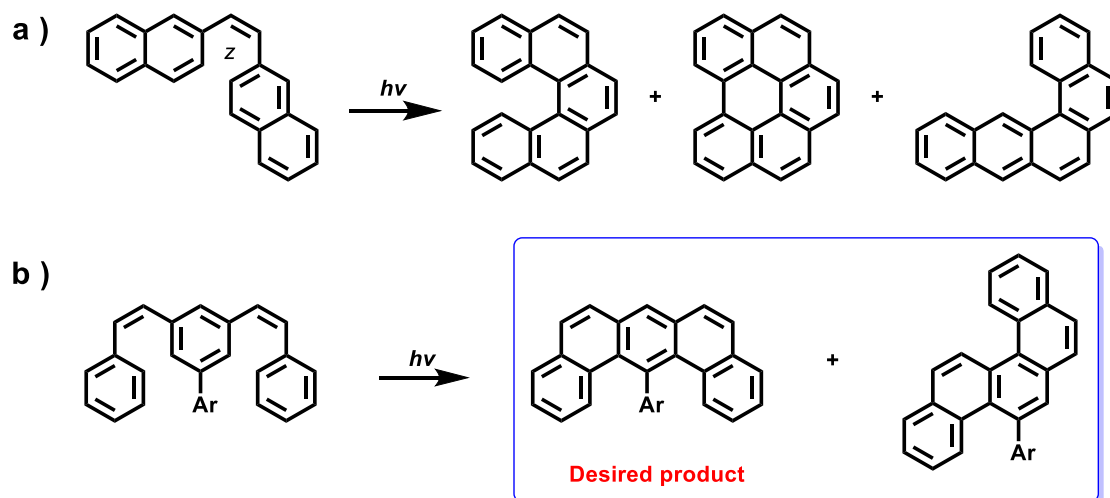


Figure 2-5. Pathways for photocyclization reactions: a) Rearrangement during the reaction. b) Two possible products after photocyclization.

At the beginning, the synthetic route based on photocyclization shown in Fig. 2-6 was carried out. Firstly, *Suzuki* coupling of 5-bromoisophthalaldehyde and 4-biphenylboronic acid was performed to give aldehyde **2-1** in 86% yield. Afterward a *Wittig* reaction was performed between compound **2-1** and 4-bromobenzyl bromide to afford compound **2-2** in 96% yields. Once **2-2** was obtained in hand, it was subjected to photocyclization reaction by 350 nm UV irradiation for 12 h. The resulting mixture was subjected to FD-MS measurement. The spectra showed the peak with m/z of 587 indicating the formation of photocyclized products. However, there were two possible configurations of the final resulting products with same molecular weight: compounds **2-3** and **2-4** (Fig. 2-6). The crude mixture was allowed to pass through a short pad of silica gel column to remove iodine and evaporated. Afterward the solid residue was re-precipitated from chloroform/methanol. Then, the precipitation was dissolved in chloroform and left to stand with a low evaporation rate for growing single crystals.

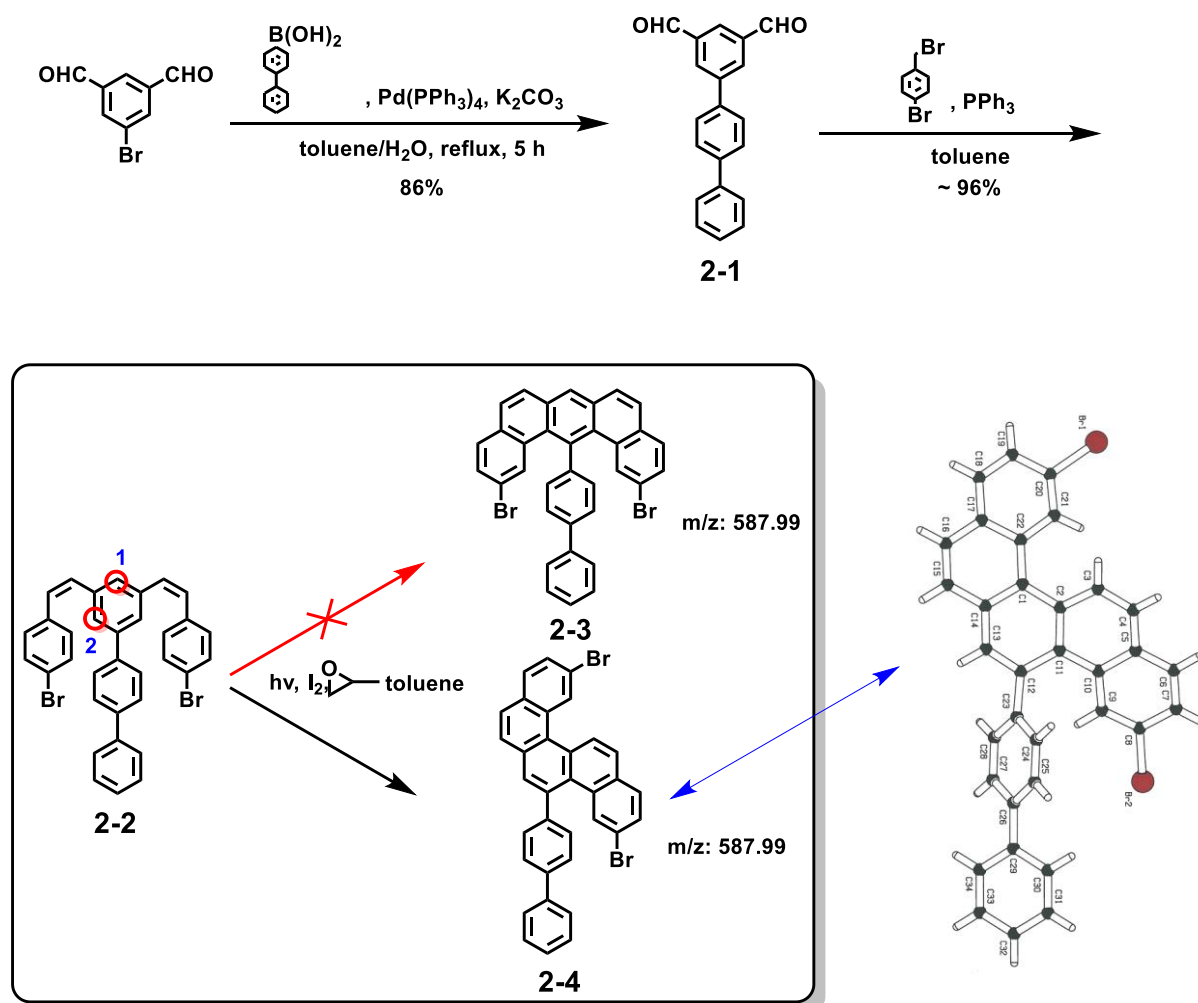


Figure 2-6. Synthetic route towards target molecule

After 1 week, single crystals suitable for X-ray analysis were obtained and the crystallographic results indicated that the final product was actually compound **2-4** instead of our desired compound **2-3**. The unexpected result can be explained by the isomerization during reaction, favoring the constitution of **2-4** than **2-3**. The cyclization actually occurred on site 1 instead of 2 (marked with red circle in Fig. 2-6). Being aware of the undesired situation, a possible solution was conceived: Could we employ a alkyl group on site 1 to prevent the photocyclization occurring at this position? So we revised the synthetic route, which employed a dodecyl alkyl chain on the site 1 to avoid the formation of the undesired isomer and obtain the desired backbone structure (Fig. 2-7).

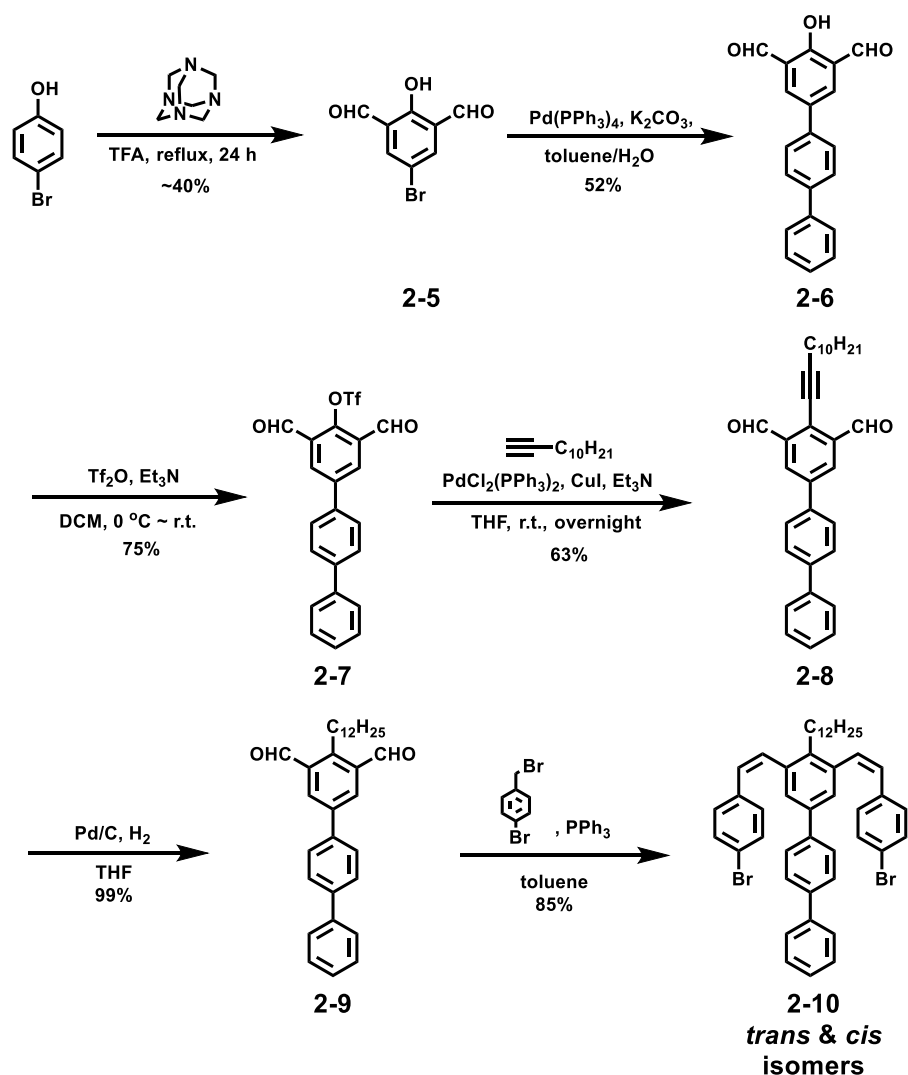


Figure 2-7. Scheme of new synthetic route toward compound 2-10

The synthetic route started from a diformylation³⁵ between 4-bromophenol and two equivalent of hexamethylenetetramine in refluxing trifluoroacetic acid to give pure 4-bromo-2,6-diformylphenol **2-5** in about 40% yield after purification by filtration through a short silica gel column. Afterward a *Suzuki* coupling of **2-5** and 4-biphenylboronic acid was performed to give compound **2-6** in 52% yield. Triflate **2-7** was obtained by treating **2-6** with trifluoromethanesulfonic anhydride (Tf_2O) in 75% yield.³⁶ Then, a *Sonogashira* coupling reaction of **2-7** with 1-dodecyne yielded compound **2-8** in 63% yield.³⁷ Subsequently, **2-8** was subjected to hydrogenation catalyzed by palladium on active carbon (Pd/C , 10%) to give aldehyde **2-9** in 99% yield. Once **2-9** with a long alkyl chain was obtained in hand, a *Wittig* reaction of **2-9** with 4-bromobenzyl bromide was performed to afford compound **2-10** in 85% yield.³⁸

Figure 2-8. a) Photocyclization condition and possible product; b) FD-MS spectra (inset: chemical structure of product); c) ^1H NMR spectra of photocyclized products obtained from **2-2** (blue) and **2-10** (red).

After the successful synthesis of compound **2-10**, the most critical issue was the photocyclization in the next step. The photocyclization of **2-10** was thus carried out under typical conditions (Fig. 2-8a),¹³ and then the resulting mixture was subjected to FD-MS measurement. However, the obtained result was not what we expected. The mass spectra showed existence of a mass peak with m/z value of 587, which was exactly coinciding with the molecular weight observed in the previous case (**2-3** or **2-4**) (Fig. 2-8b). This result also indicated that the dodecyl chain was chopped off during the cyclization and that **2-4** was still the more preferred constitution. This conclusion was proven by following single-crystal analysis result: the same crystallographic structure as **2-4** was obtained, as well as by comparing the ^1H -NMR spectra of photocyclized products obtained from **2-2** and **2-10** (Fig. 2-8c).

Based on the above-mentioned results, we concluded that the photocyclization method could not achieve our target molecule with desired “U-shaped” backbone. Another synthetic method was thus needed to synthesize the target molecule.

2.2.3 Synthesis of monomers based on Perylium chemistry

After the failure of obtaining “U-shaped” molecule via the photocyclization method, another promising method based on perylium chemistry was tested.

During the last decades, small oxygen containing aromatic hydrocarbons with a positive charge, namely perylium salts, have attracted increasing attentions from physicists and chemists both for theoretical studies and for their potential application with their electron deficient nature. Typical examples of the perylium salts, **2-11**, **2-12**, **2-13**, and **2-14**, are shown in Fig. 2-9. The perylium salt **2-11** is very reactive against nucleophilic agents and thus serves as a significant intermediate for the formation of a range of carbocyclic or heterocyclic PAH molecules^{18,23,24,39,40}. The xanthylium salt **2-12** and 2,4,6-triarylperylium salt **2-13** as well as the dibenzoxanthylium cation **2-14** were also reported recently in organic and physical chemistry for investigation of their electronic properties, synthesis of novel functional molecules including macrocycles or dye material, as well as use as polymeric membrane electrode.^{16,20,41-44} The analogues of compound **2-14** were also synthesized and reported by the Muellen group.^{21,22}

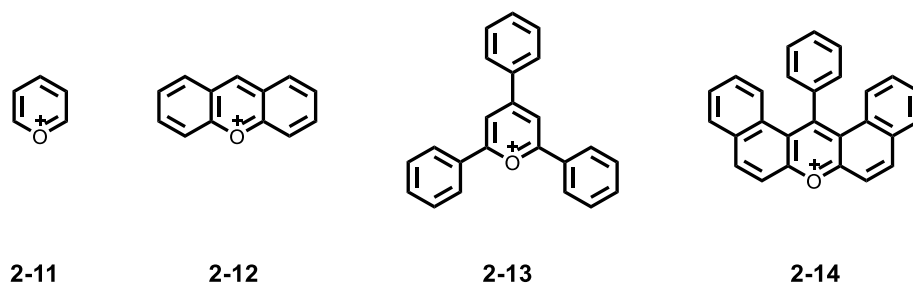


Figure 2-9. Typical oxygen doped PAHs with positive charge

In 1987, Zimmermann et al. developed a significant method to transform pyrylium salts into corresponding full-carbon PAH molecules by the condensation with sodium phenylacetate²⁴. The same reaction procedure^{17,45} could be applied to both pyrylium salt analogues such as **2-13** or **2-14** to afford condensed full-carbon molecules **2-15** and **2-16**, respectively (Fig. 2-10).

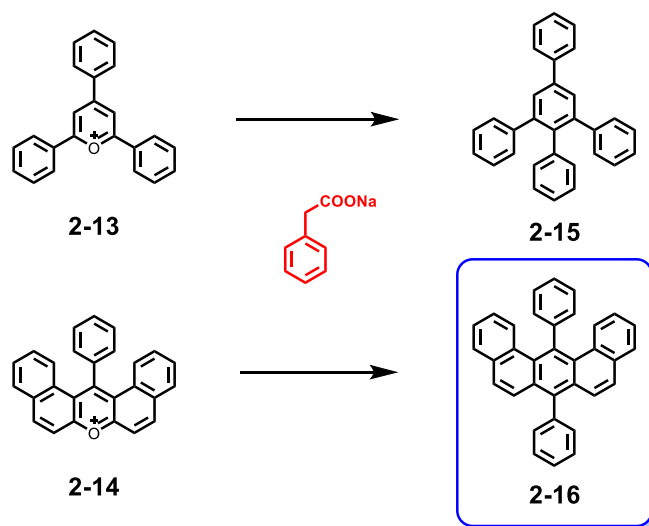


Figure 2-10. Scheme of condensation between pyrylium salts and sodium phenylacetate.

The condensation reaction of pyrylium salt **2-14** and sodium phenylacetate is relevant to our case due to its capability of fabricating “U-shaped” backbone structures. Based on the pyrylium chemistry, we designed a new synthetic route, which eventually led to the successful synthesis of our target molecules (Fig. 2-10).

As shown in Fig. 2-11, “U-shaped” monomers **2-20a**, **2-20b**, and **2-20c** were synthesized based on the aforementioned pyrylium chemistry. First, dibenzo[*a,j*]xanthenes **2-17a–c** were prepared by condensation of 2-bromo-7-hydroxynaphthalene and corresponding aryl aldehyde (R = H, phenyl and 3, 5-dimethylphenyl) under neat condition⁴⁶, followed by oxidation with lead (IV) oxide to afford dibenzo[*a,j*]xanthen-14-ol **2-18a–c**. Then, crude products of **2-18a–c** were directly treated

with tetrafluoroboric acid solution (48 wt. % in water) to afford pyrylium salts **2-19a-c**^{21,22}. Finally, after a condensation reaction of **2-19a-c** with sodium 2-phenylacetate^{15, 16}, the target “U-shaped” monomers **2-20a-c** were obtained in 34–38% yield.

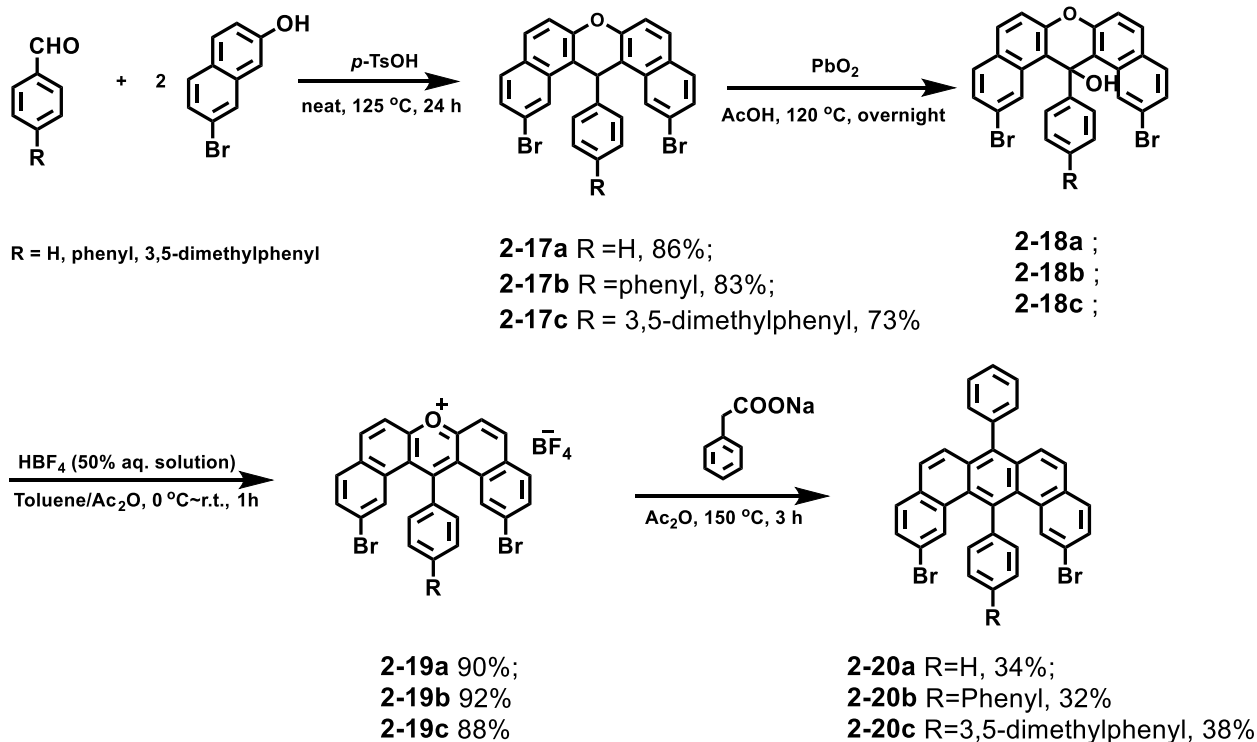
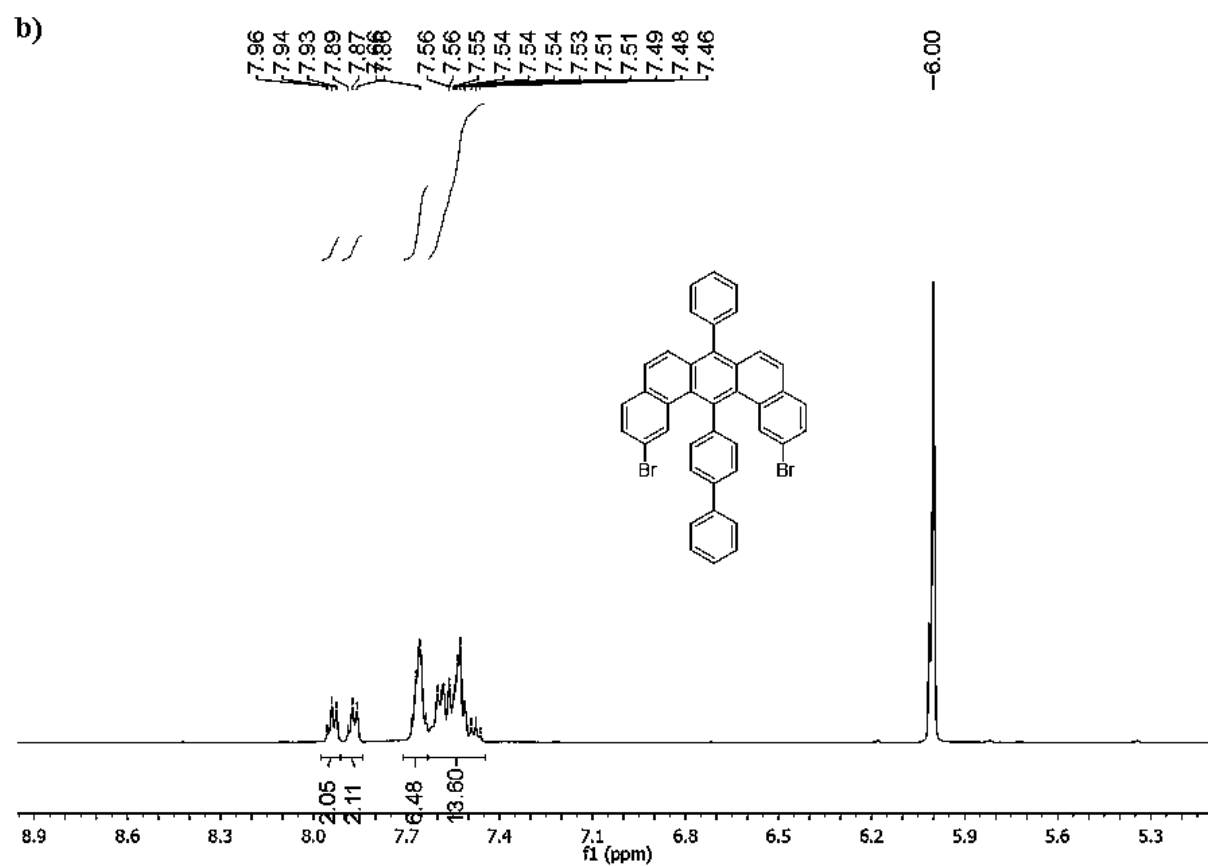
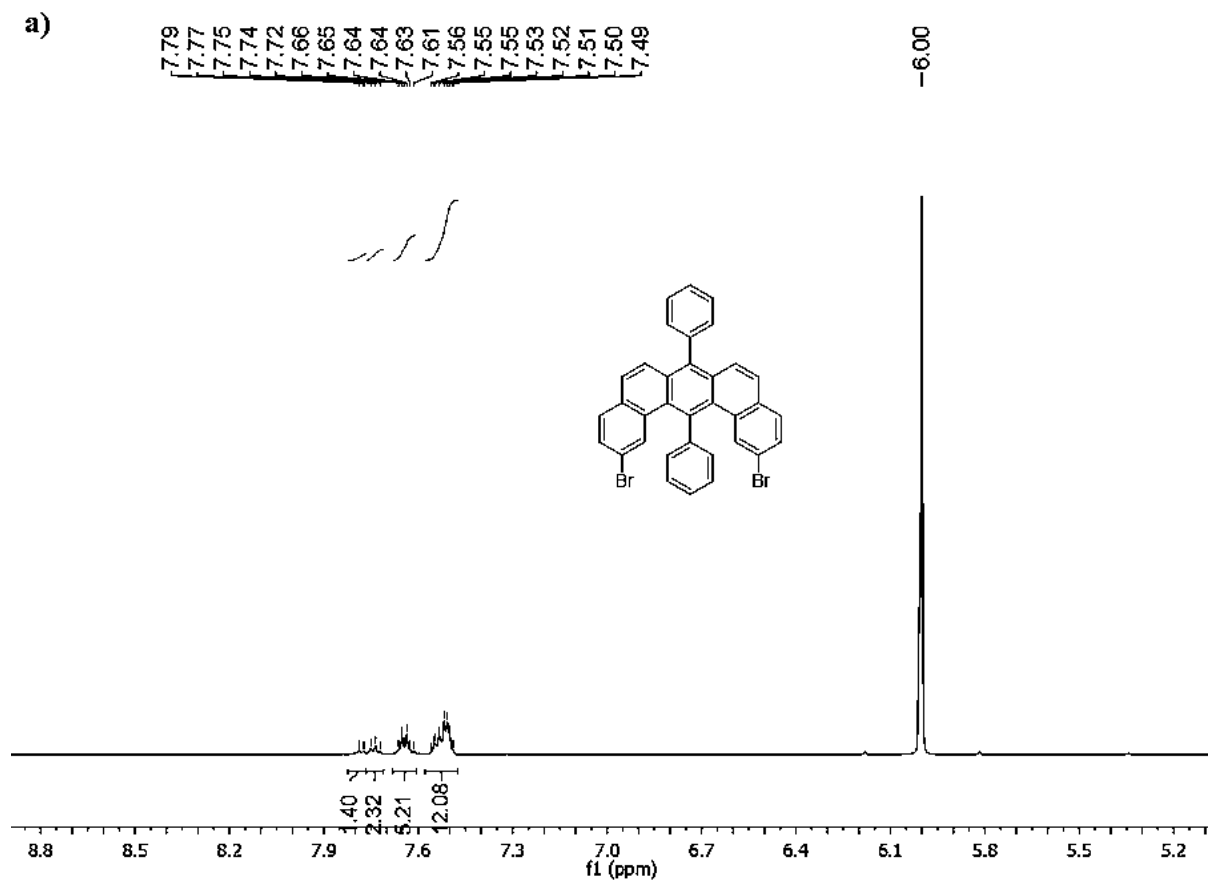


Figure 2-11. Synthetic route toward “U-shaped” monomers **2-20** based on pyrylium chemistry.

In previous investigations of surface-assisted synthesis of GNRs, high purity of monomeric building blocks was significant in decreasing structural defects during the process. In order to achieve monomers **2-20a-c** with high purity, we tried to recrystallize these monomers. However, the three monomers barely dissolved in common organic solvents including chloroform, tetrahydrofuran, and toluene at room temperature. Thus we tried to purify the monomers *via* re-precipitation. The monomers were firstly stirred in hot toluene until being totally dissolved; afterward the solution was cooled down to room temperature. Finally, the resulted precipitate was filtered off and collected. This procedure was repeated for three times to remove impurities as much as possible. Afterwards, the purified monomers **2-20a-c** were subjected to various characterizations including ¹H NMR, ¹³C NMR, high-resolution mass spectroscopy (HR-MS), melting points, and the thermal gravity analysis (TGA) to verify their chemical structures and purities .

As displayed in Fig. 2-12, the $^1\text{H-NMR}$ spectra of monomers **2-20a~c** clearly indicated their high purities, and the integration of the aromatic proton signals were in agreement with expected values as well. The MALDI-TOF and HR-APPI mass spectra of three monomers exhibited in Fig. 2-13 displayed the exact molecular weight of $m/z = 587.9911$, 664.0251 , and 692.0544 , which was consistent with the simulated values of monomers **2-20a**, **b**, and **c**. Moreover, the isotopic distribution of HR-MS spectra was in perfect agreement with the simulated pattern, which further provided the high purities of three monomers.

Besides, the melting points of three monomers were determined by a Büchi hot stage apparatus. However, no obvious melting phenomenon can be observed for all three monomers during the measuring range of the apparatus (r.t. - $400\text{ }^\circ\text{C}$). Instead, we subjected **2-20a~c** (5 mg for each) to thermal gravimetric analysis (TGA) analysis. The TGA results exhibited in Fig. 2-14 were measured from r.t. to $600\text{ }^\circ\text{C}$ under a nitrogen purge with a heating-rate of $\sim 10\text{ }^\circ\text{C}/\text{min}$, which clearly indicated the variation of the thermal degradations of the three monomers **2-20a**, **b**, and **c**. All three monomers started to lose weight at $\sim 420\text{ }^\circ\text{C}$.



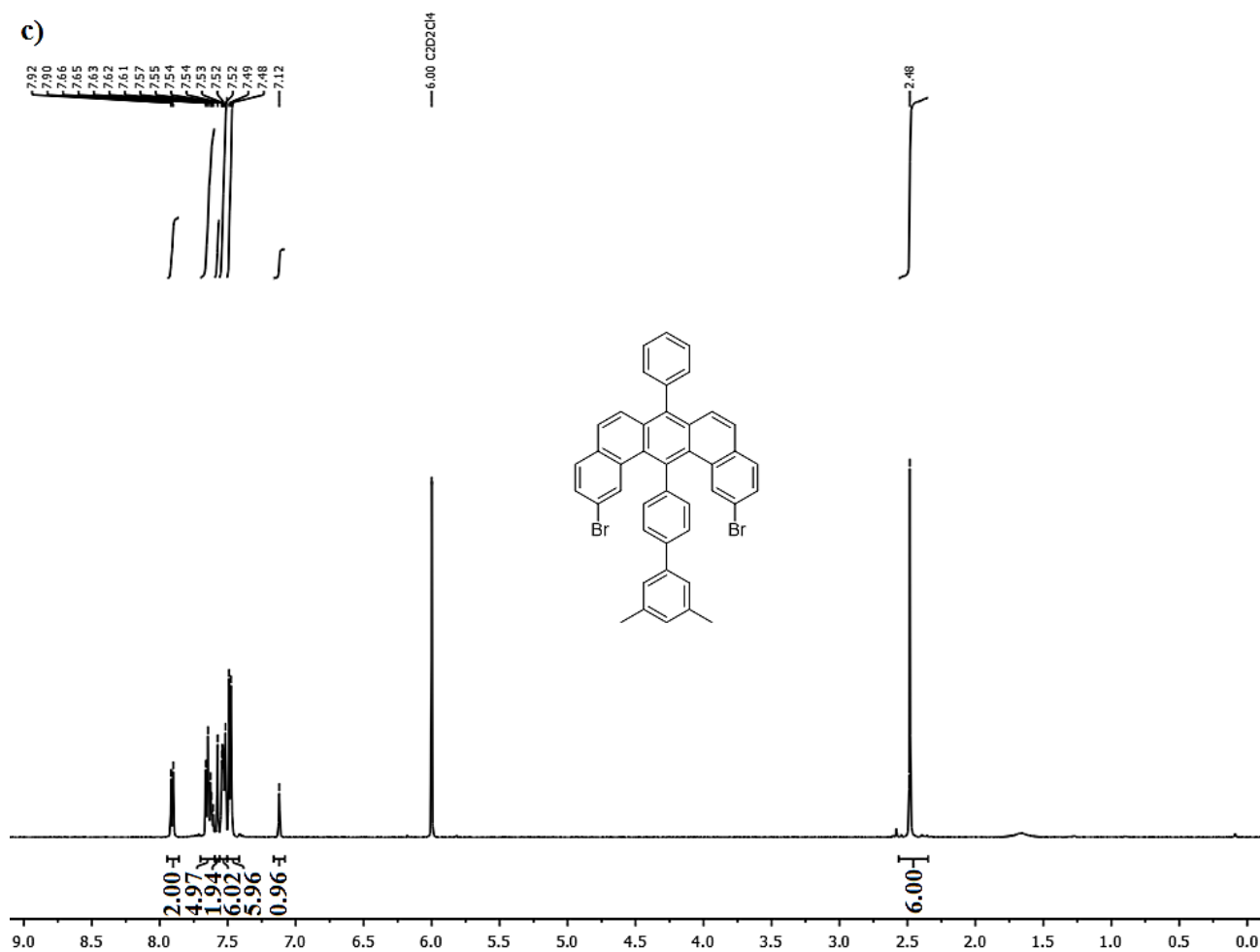
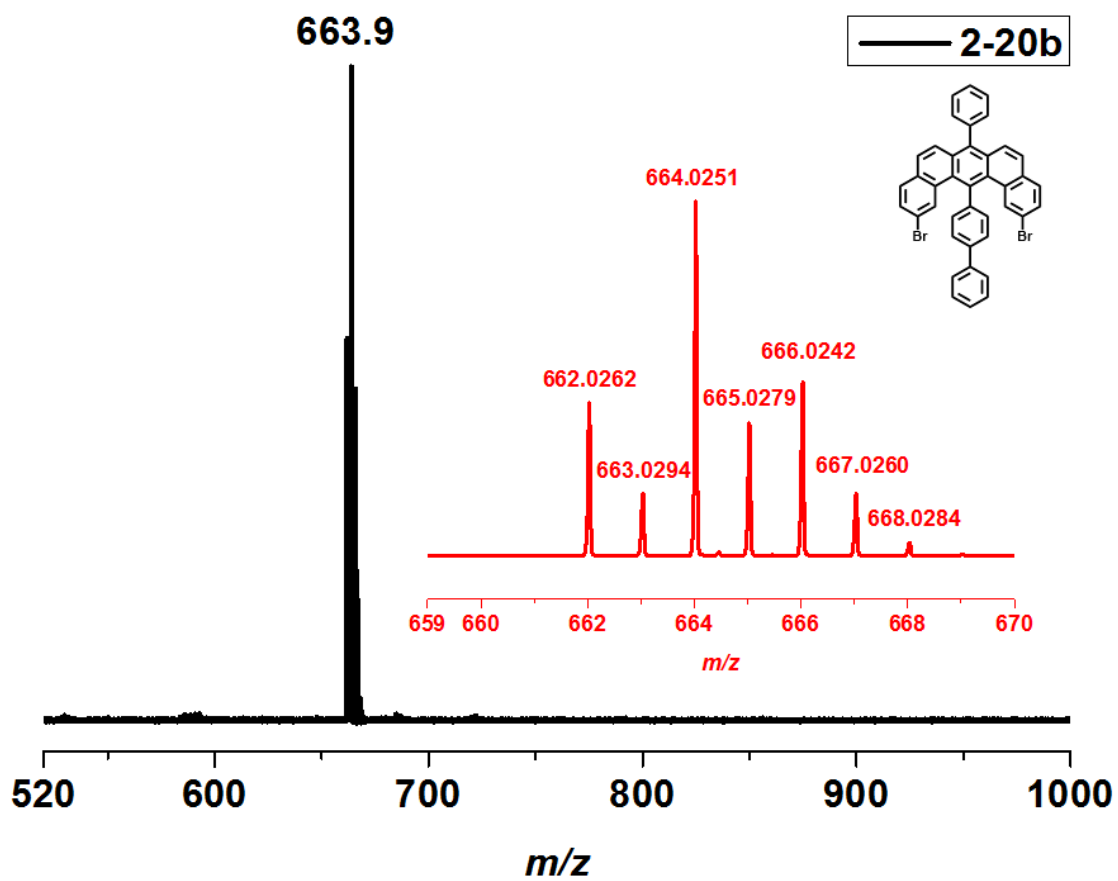
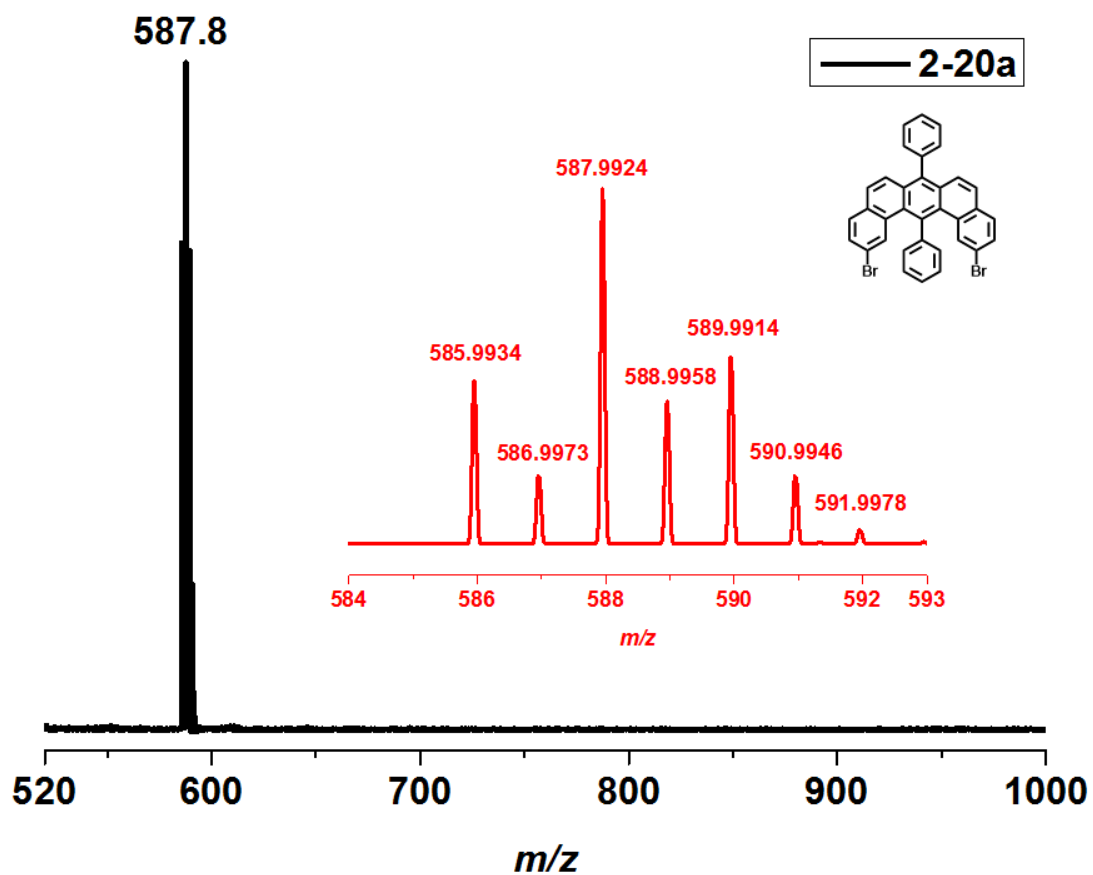


Figure 2-12. ¹H-NMR spectra of a) monomer **2-20a** in C₂D₂Cl₄ at 353K; b) monomer **2-20b** in in C₂D₂Cl₄ at 353K; c) monomer **2-20c** in C₂D₂Cl₄ at 353K.



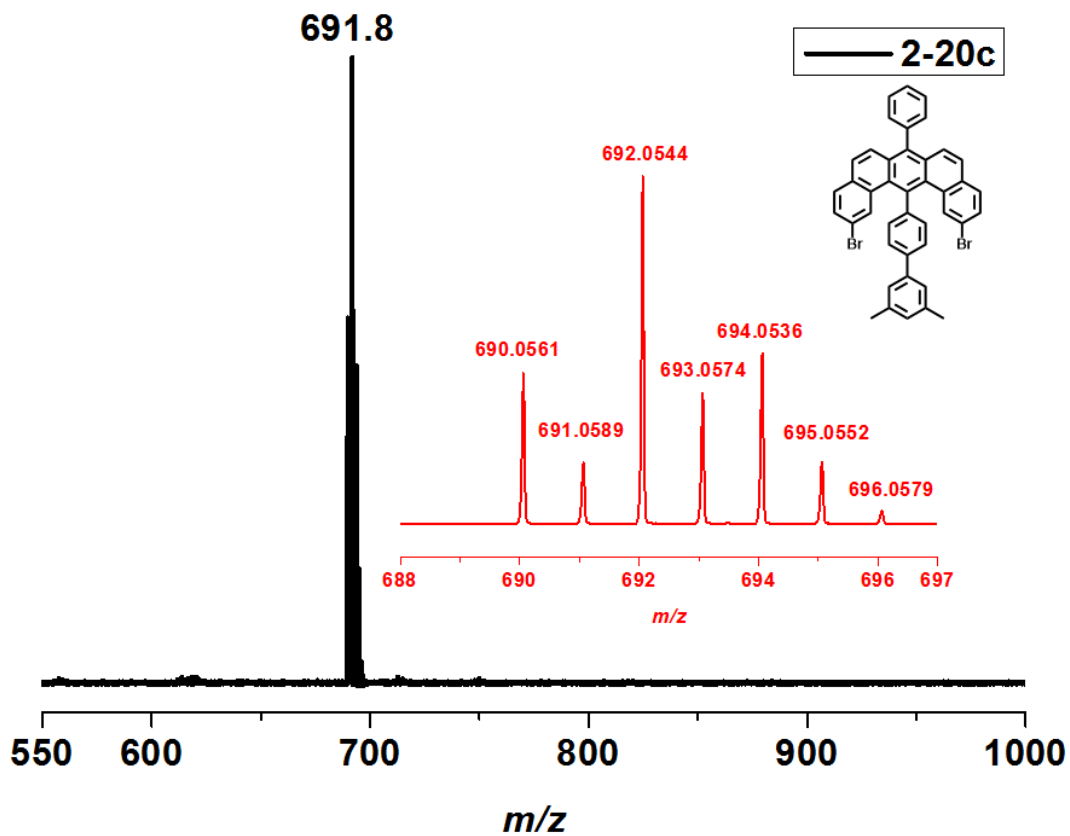


Figure 2-13. MALDI-TOF MS spectra of monomer **2-20a**, **b**, and **c**, respectively. Insets: Chemical structures of monomers and HR-APPI-TOF (positive) MS spectra and their isotropic distributions.

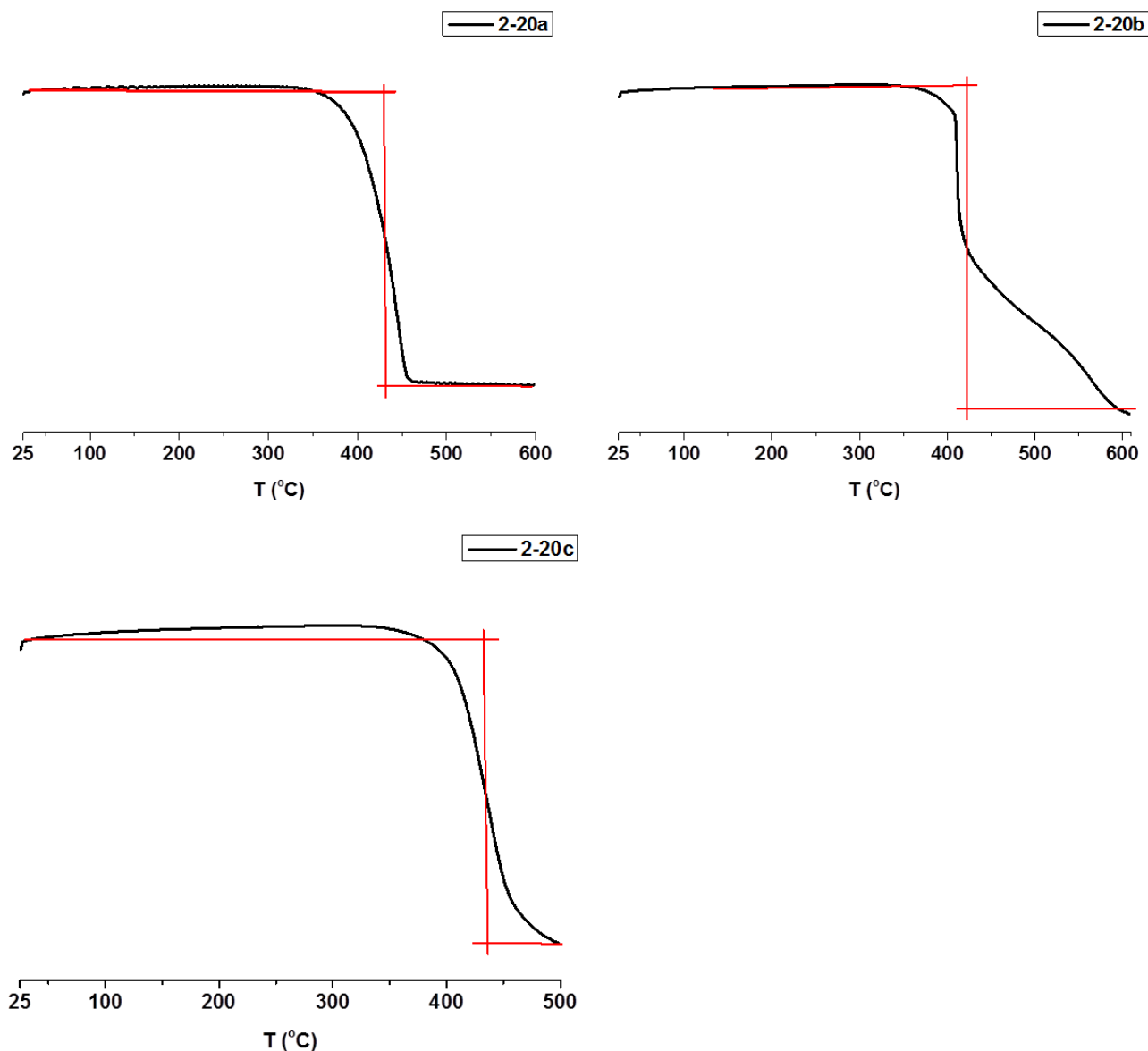


Figure 2-14. TGA results of monomers **2-20a**, **b** and **c**, showing their thermal degradation.

With the help of all the above characterizations, we concluded that three “U-shaped” monomers **2-20a~c** have been successfully synthesized with high chemical-purities. Next, we could finally apply these monomers to the surface-assisted synthesis of the novel GNRs with different edges as displayed in Fig 2-3. In particular, monomer **2-20c** was expected to afford long-awaited $N = 6$ ZGNRs (**f'**) with zigzag structure (Fig. 2-3).

2.2.4 Surface synthesis of GNR with partial zigzag edge

With help from our collaborators [REDACTED], [REDACTED], [REDACTED] and [REDACTED] from the [REDACTED], the above synthesized monomers **2-20a~c** could be utilized for the surface-assisted fabrication of ZGNRs. The typical procedure of surface-assisted synthesis of GNR is: precursor monomer was deposited onto the clean substrate surfaces (usually Au (111), due to its technical advantages and relative ease in achieving a clean atomically flat surface.) by sublimation from a six-fold evaporator. The substrate was maintained at around 200 °C (depending on different monomers) during monomer deposition to induce dehalogenation and radical addition. After deposition, the sample was post-annealed to higher temperature (usually > 400 °C) to cyclodehydrogenate the polymers into GNRs. This procedure could also be employed to our cases (GNR **d**, **e**, and **f**), except that the slightly different substrate temperatures were used during monomer deposition and post-annealing steps.

Moreover, the whole synthesis process has not only been observed *via* in-situ high resolution scanning tunneling microscopy (STM), but also by non-contact atomic force microscopy (nc-AFM). The nc-AFM has achieved superior resolution in real-space recently, which enabled the identification of the chemical structure, adsorption configurations, and chemical transformation of individual molecules^{47,48}. In particular, by using a specific technique, a CO-functionalized tip can be prepared after transferring a CO molecule to the AFM tip apex. The subsequent AFM studies with this tip could give enhanced-resolution images with atomic precision. There have already been a series of achievements accomplished using AFM with CO-functionalized tip, i.e., chemical identification of single surface atoms⁴⁹, measurements of the exchange force with atomic resolution^{50,51}, and the single molecules as well as single-walled carbon nanotubes^{52,53}. For our case, in order to get high-resolution microscopic images of desired GNRs (**d**, **e**, and **f**), imaging by the nc-AFM with CO-functionalized tip was also performed.

In analogy to surface-assisted synthesis of AGNRs, the two-steps on-surface synthesis of chevron-type GNR **d** (hybrid of partial zigzag and gulf edges) from monomer precursor **2-20a** are shown above: Generally the sample was annealed from 200 °C to 300 °C, and then to around 350 ~ 400 °C with 10 min per step. Each step is described below in more details.

Step 1: Sublimation of monomer **2-20a** to the metal substrate (Au (111)) at 280 °C. The substrate was heated from 200 to 300 °C to induce dehalogenation and radical addition. According to previous

work by Roman Fasel et al.⁷, the mechanism of the surface reaction was displayed in Fig. 2-15a. The Au(111) surface plays an immensely important role as the catalyst for the dehalogenation process. Though pristine Au surface is unable to dissociate hydrogen and oxygen molecules^{54,55}, it significantly lowers the temperature for dehydrogenation that is an important step in assembly of covalently bonded nanostructures and GNRs^{7,56}. During this step, the generated biradical intermediates have enough thermal energy to diffuse along the Au surface and form covalent C-C bonds between each monomer to give polymer chains (Fig. 2-15a). And the C-C covalent interlinking of biradical intermediates proceeded until totally converted to polymers on the surface. As displayed in Fig. 2-15b, the *in-situ* STM images clearly showed snake-like polymer chains formed on the Au surface.

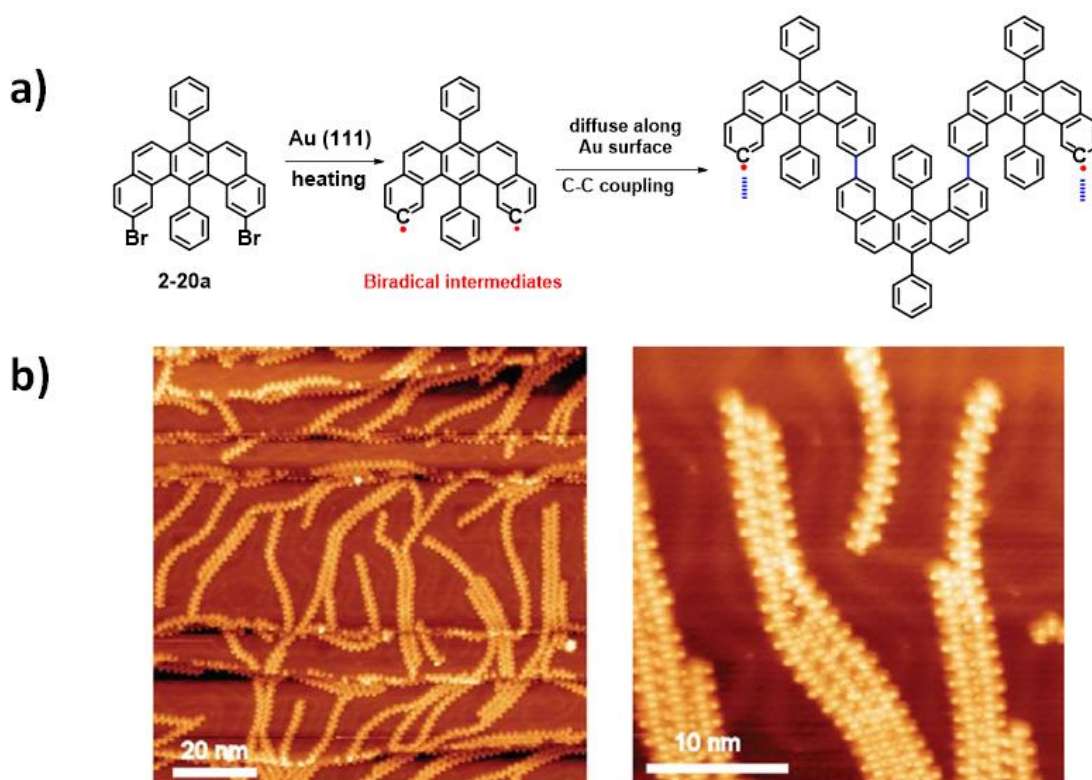


Figure 2-15. a) Possible reaction mechanism of the biradical coupling reaction on a Au surface. b) STM images of sample annealed at 300 °C.

Step 2: The temperature was increased to 350 °C. The dehydrogenation occurred and planar GNRs structures were formed. However, an unexpected five-membered ring (fluoranthrene units) generated between the additional phenyl group and the zigzag edge. This finding can be explained by the high reactivity of the zigzag edge at high temperatures. As displayed in Fig. 2-16a, the additional phenyl

ring can randomly fused with either carbon atoms of the neighboring zigzag edge, thus no fully periodic arrangement of the fluoranthrene subunits can be expected (Fig. 2-16b). Besides STM, a non-contact atomic force microscopy (nc-AFM) was used as well, which clearly revealed the resulted GNR **d** with additional fluoranthrene subunits.

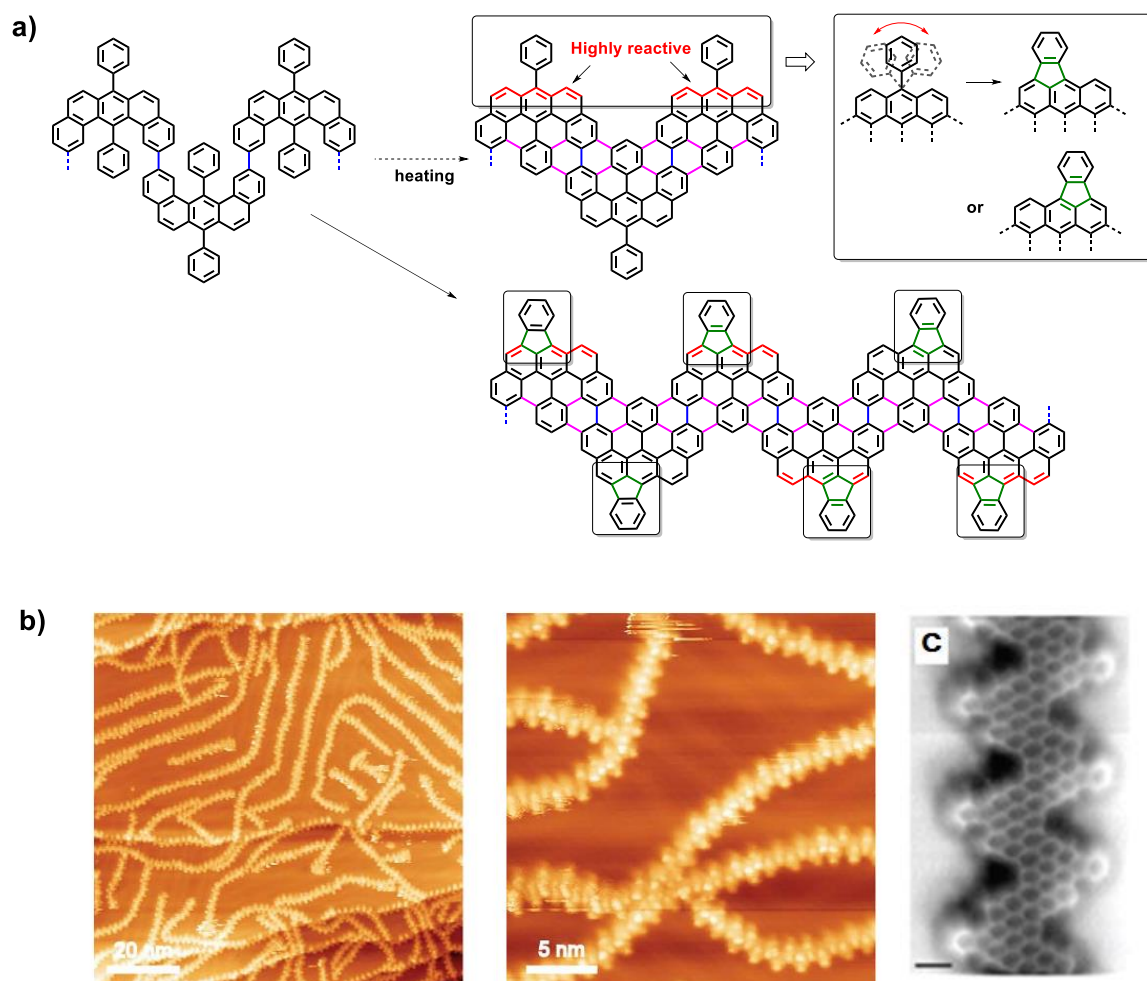


Figure 2-16. a) Possible mechanism of the dehydrogenation process. b) STM and c) nc-AFM images of GNR **d** formed at 350 °C (inset: unexpected five-membered ring formed)

Based on the successful surface synthesis of chevron-type GNR **d** from monomer precursor **2-20a**, the monomeric precursors **2-20b** and **2-20c** were next subjected to the same synthetic procedure. The preparation process toward GNRs **e** and **f'** from the two monomers **2-20b** and **2-20c** is identical, except for slight differences in the annealing temperatures for each step. It is noted that monomer **2-20c** began to be dehydrogenated at 300 °C, but the dehydrogenation of monomers **2-20a** and **2-20b** did not occur until 350 °C. Moreover, compared with the surface-assisted fabrication of GNR **d**, the

side phenyl groups on the peripheries of GNR **e** and **f** were more easily chopped off during the annealing process. As shown in Fig. 2-17b, some part of GNR **f** fabricated from monomer **2-20c** has short segments with perfect zigzag edge structure as a result of side phenyl groups detachment. In particular, in contrast to monomer **2-20b**, the two additional methyl substituents on the monomer **2-20c** allowed to fill the holes in the interior of the undulating polymer. As shown in Fig. 2-17c, apart from the polymerization and planarization, an oxidative ring closure including the methyl groups could finally led to the establishment of two new six-membered rings together with the zigzag edge structures.

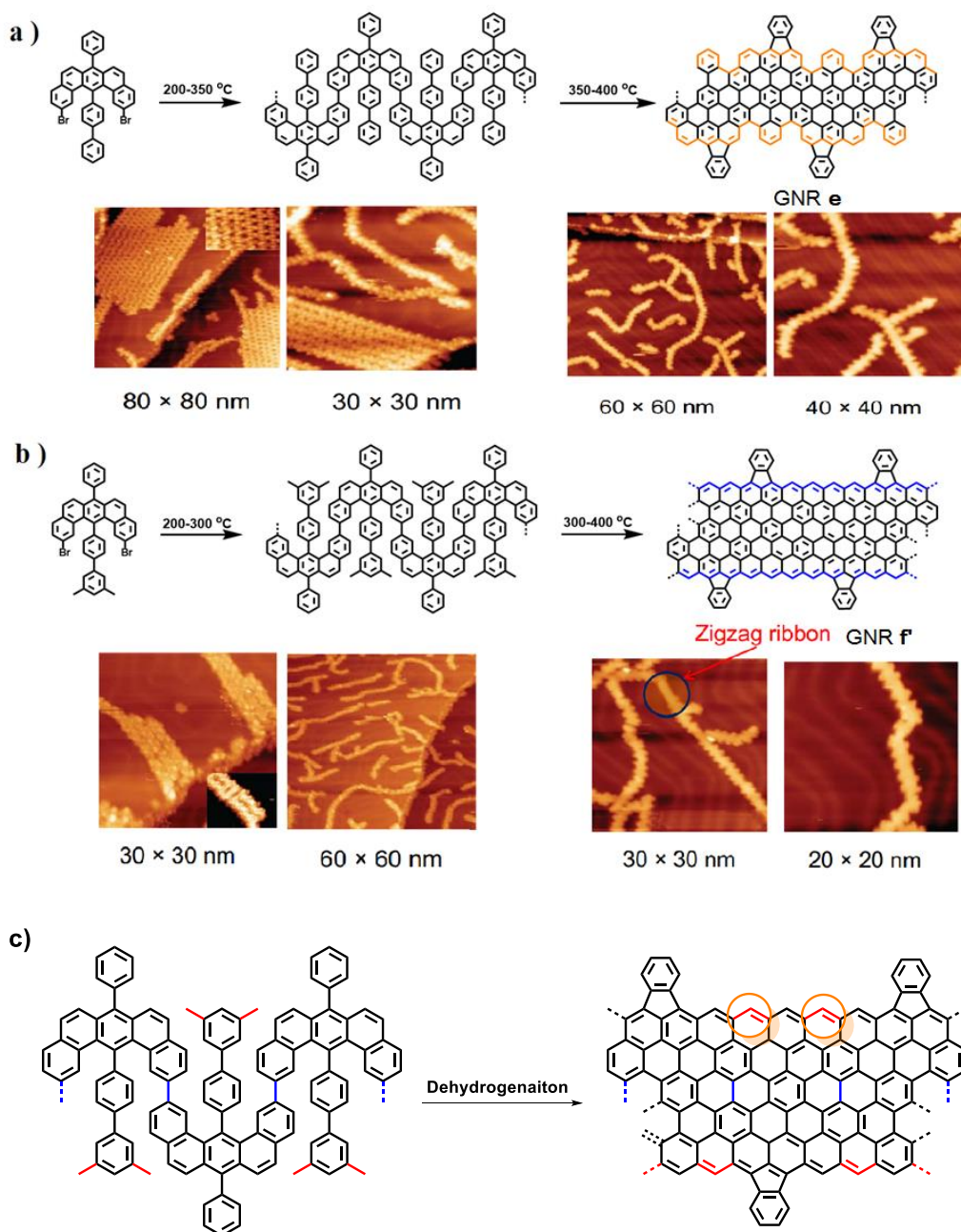


Figure 2-17. Synthetic schemes toward GNRs derived from a) monomer **2-20b** and its STM images during annealing; b) monomer **2-20c** and its STM images during annealing procedure. c) Oxidative ring closure between two methyl groups and their neighboring carbon atoms to form zigzag edge structures.

Regarding the resulting novel GNR structures by surface-assisted synthesis, we can conclude that all the experimental procedures were performed successfully. Three kinds of novel GNRs **d**, **e**, and **f'** have been successfully synthesized with atomic precision. Notably, these GNRs with novel partial zigzag edge structures significantly expanded the scope of the obtainable GNRs with varying edge patterns. Among these novel GNRs, the ZGNR that attached fluoranthrene type subunit with five membered ring based on monomer **2-20c** was named as N = 6 ZGNR plus (**f'**) (Fig. 2-18a). Figure 2-18b and c clearly reveal the structure of the ZGNRs plus (**f'**) in an analogous thermally induced polymerization – cyclization procedure. The nc-AFM images clearly show that the phenyl group undergoes a ring closure under the formation of a fluoranthrene type subunit with a five-membered ring at the cyclodehydrogenation temperature of 573 K. Similar to the synthesis of GNR **d** and **e**, the subunits were distributed along the zigzag edges of ZGNR plus (**f'**) without periodicity. This was confirmed by the nc-AFM image shown in Fig. 2-18c, which reveals the possible three, four, and five zigzag cusps separated by neighboring fluoranthrene subunits.

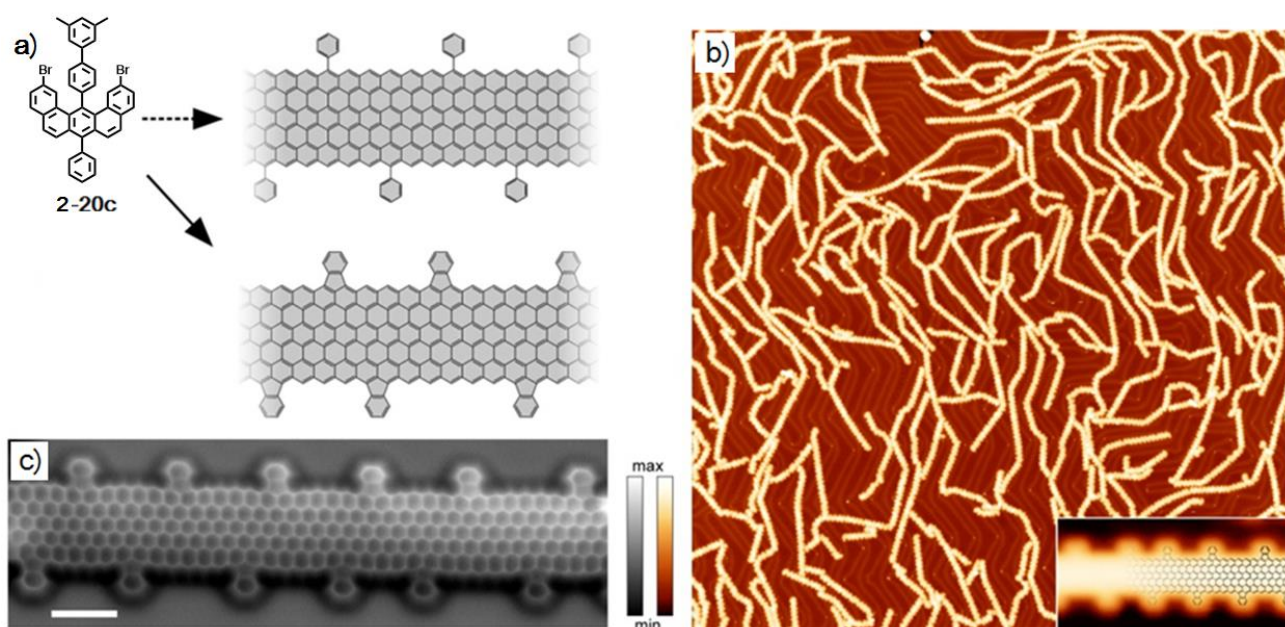


Figure 2-18. a) Monomer **2-20c**, with an additional phenyl group comparing to the monomer **2-20d**, which is synthesized to afford an edge-modified 6-ZGNR plus (**f'**) upon polymerization and subsequent cyclization. b) Overview STM image of edge-modified 6-ZGNR plus (**f'**) fabricated on a Au(111) surface (200 nm x 200 nm,

$U = -1.5\text{V}$, $I = 150\text{ pA}$). The inset shows a high-resolution STM image ($7.5\text{ nm} \times 3.5\text{ nm}$, $U = 0.15\text{V}$, $I = 2\text{ pA}$). c) Constant-height AFM frequency-shift image of edge-modified ZGNR ($A_{\text{osc}} = 0.7\text{ \AA}$, $U = 25\text{ mV}$).

2.2.5 Synthesis of novel monomer 2-20d based on Pt catalyzed cyclization

As described above, the unexpected formation of the five-membered rings between the peripheral phenyl groups and the zigzag edges did not allow the perfection of full zigzag edge of $N=6$ ZGNR (**f**). As we discussed in section 2.1, the electronic properties of ZGNRs were strongly governed and sensitive to their edge structures. Therefore, one important question would be that if we could synthesize monomers without the phenyl ring to avoid the five-membered-ring formation along the zigzag edges of the resulting ZGNRs. As shown in Fig. 2-19, if the additional phenyl substituent can be removed, it will be possible to synthesis the first $N = 6$ ZGNR (**f**) with perfect zigzag edge structure, which will be an important breakthrough in both chemical and physic fields.

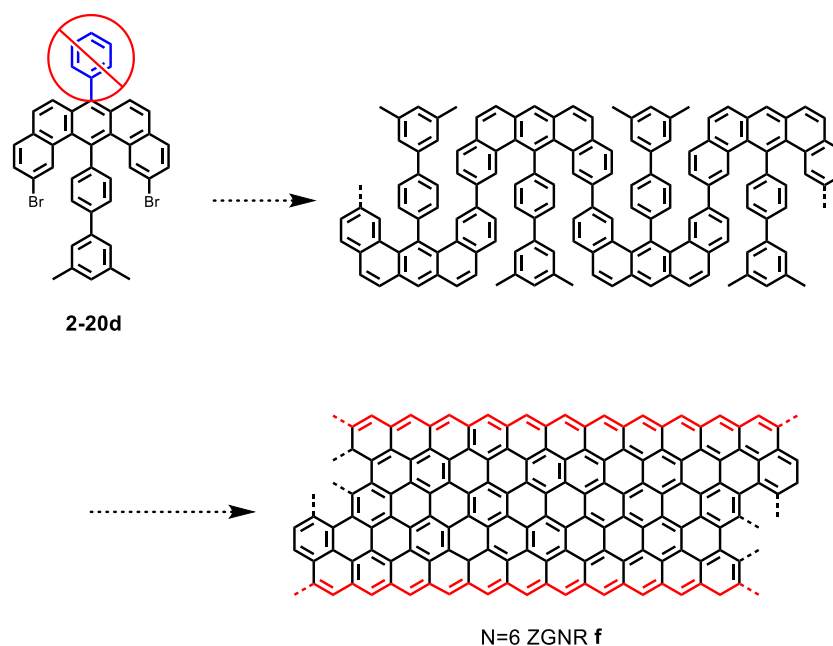


Figure 2-19. Proposed synthetic scheme towards $N=6$ ZGNR (**f**) from monomer **2-20d** without additional phenyl group

For the preparation of monomers without the additional phenyl ring, we first tried to modify the synthetic route via the pyrylium chemistry, since there were reported methods using other kinds of nucleophiles replacing sodium phenylacetate such as malonate ester, malonate salts, nitromethane

and phosphine ylide.^{57,58} By using pyrylium salt **2-19a** as a starting reactant, we tried the condensation of **2-19a** and nucleophiles listed below with or without base (*t*-BuOK, *n*-BuLi) at high temperatures (Fig. 2-20). However, all of these attempts did not give desired product.

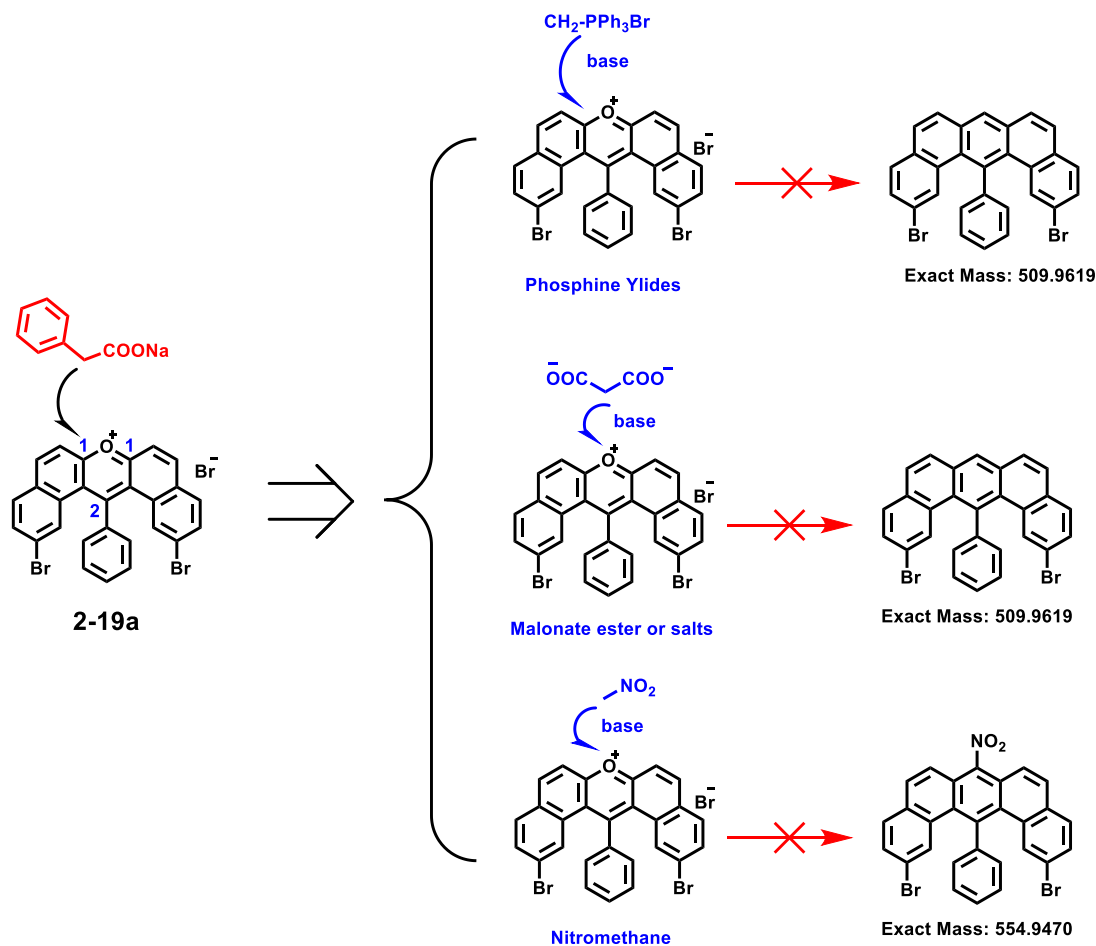
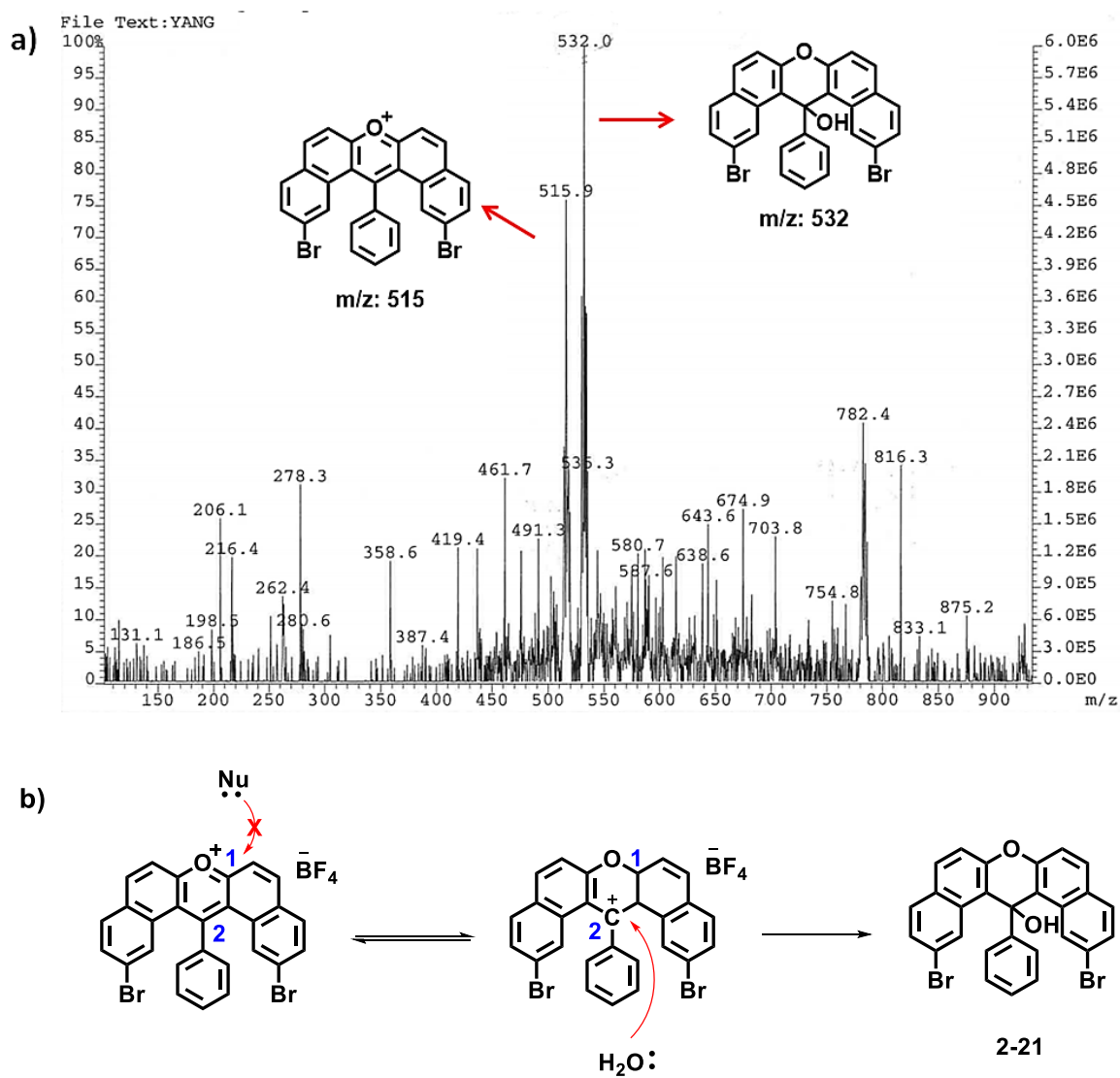


Figure 2-20. Unsuccessful attempts to synthesize monomer precursor without additional phenyl group based on pyrylium chemistry.

As displayed in Fig. 2-21, three nucleophiles have been used to react with pyrylium salt **2-19a**, and the mass values (*m/z*) of expected products are 509 for phosphine ylide and malonate ester cases, and 554 for nitromethane case. Nevertheless, the FD-MS spectra of the crude samples of the three reactions showed similar results as that in Fig. 2-21a. The peak with *m/z* value of 515 corresponded to reactant pyrylium salt **2-19a**, and the peak with *m/z* value of 532 most probably corresponds to side product **2-21**. There was no peak with the desired *m/z* values of 509 and 554 observed from the FD-MS spectra. The reason can be explained by the proposed mechanism of the reaction (Fig. 2-21b). The electrophiles did not attack the carbon atom next to the neighboring oxygen atom (position 1), which would lead to the desired ring opening. On the contrary, a side reaction occurred as exhibited in Fig. 2-21b. The reactions between pyrylium salt **2-19a** and other nucleophilic reagents such as

small amounts of water, mainly led to the addition reactions on the carbon atom at the para position of oxygen atom (position 2). Therefore, extremely dried solvents including THF and toluene were used. A high boiling point solvent like dichlorobenzene was also used to avoid this side reaction and to overcome the possible energy barrier of desired condensation reaction. However, these reactions still could not give desired products showed in Fig. 2-21.



Because the photochemistry and pyrylium chemistry failed to fabricate monomers like **2-20d**, another method in our chemistry toolkit, i.e., transition-metal catalyzed cycloisomerization reaction, was next employed to synthesize “U-shaped” monomer **2-20d** without additional phenyl group.

During the last decades, transition-metal catalyzed cycloisomerizations have been used widely in the fabrication of conjugated systems. Typical cases include the synthesis of phenanthrene, pyrene, coronene, and other PAH analogues^{25-27,29-31}, as well as coranulene or higher Fullerenes^{59,60} and other carbon rich organic materials (Fig. 2-22).

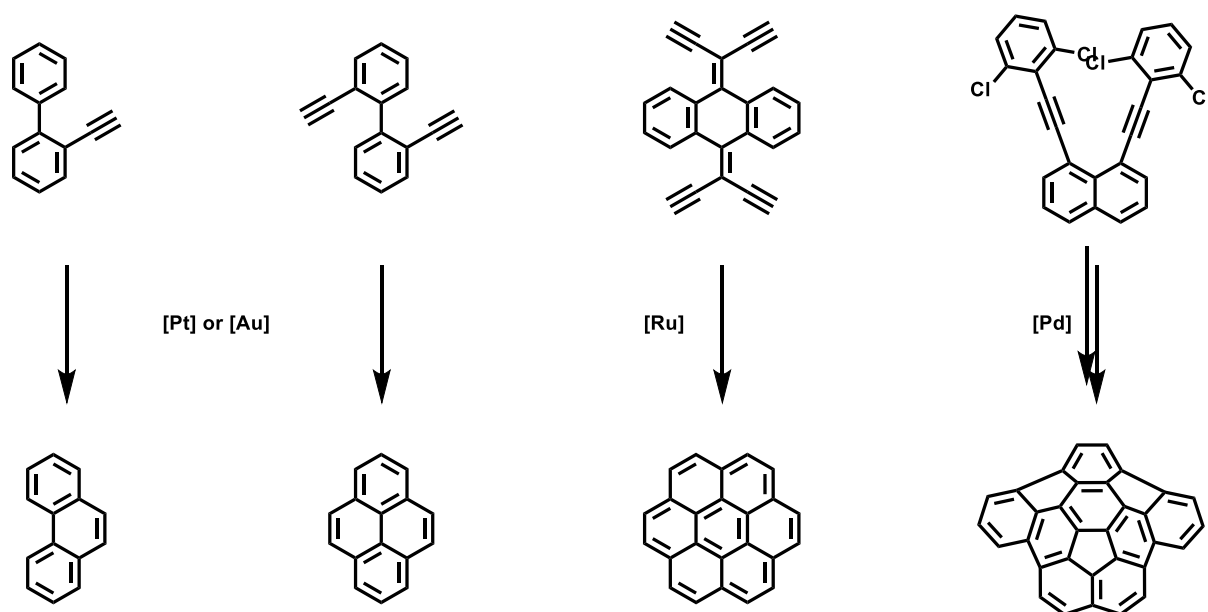


Figure 2-22. Typical cases of transition-metal catalyzed cycloisomerization or C-C bond formation reactions

According to the chemistry shown above, a new synthetic route towards our target “U-shaped” molecule **2-20d** was conceived and performed following the schemes as described in Fig. 2-23.

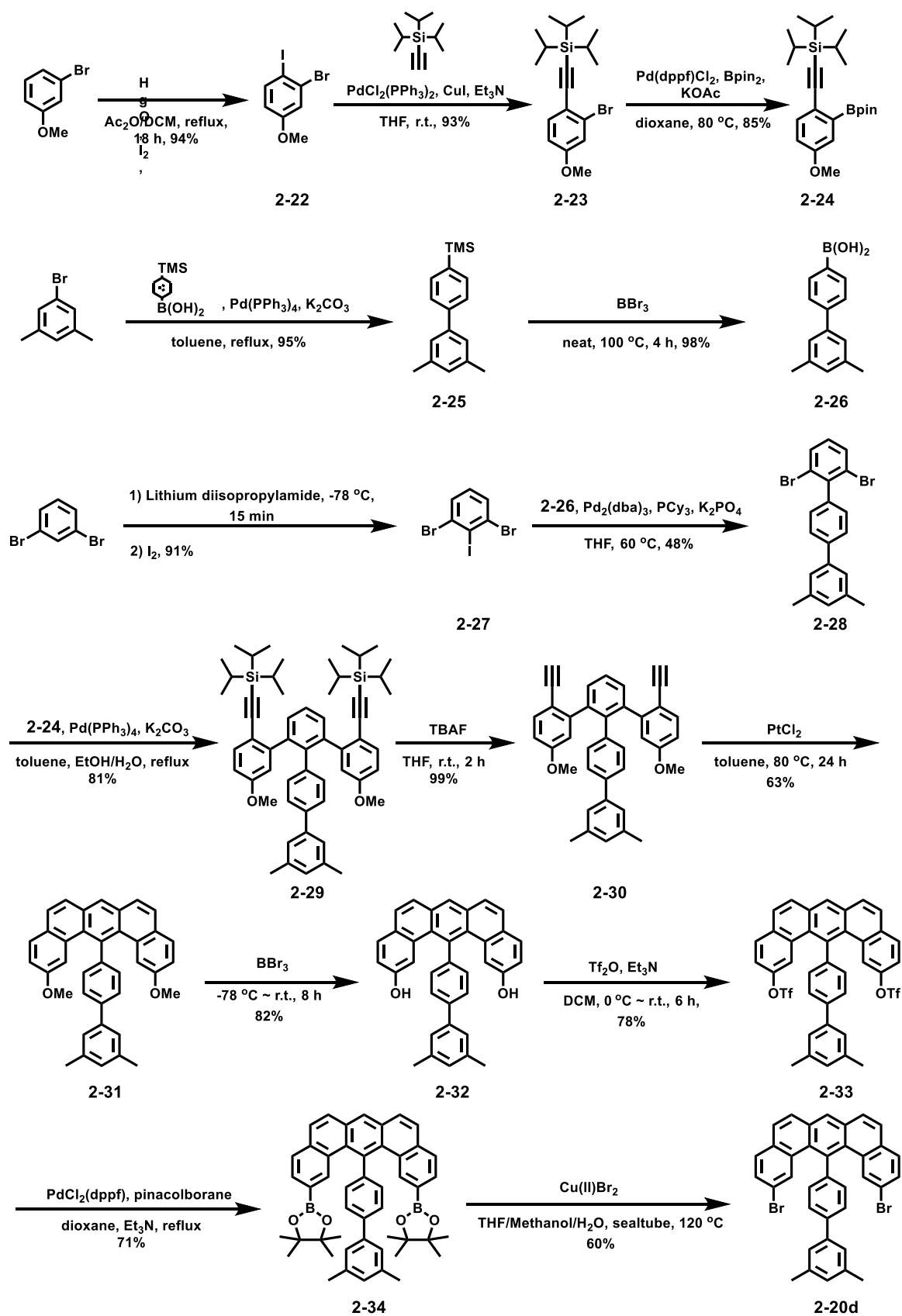


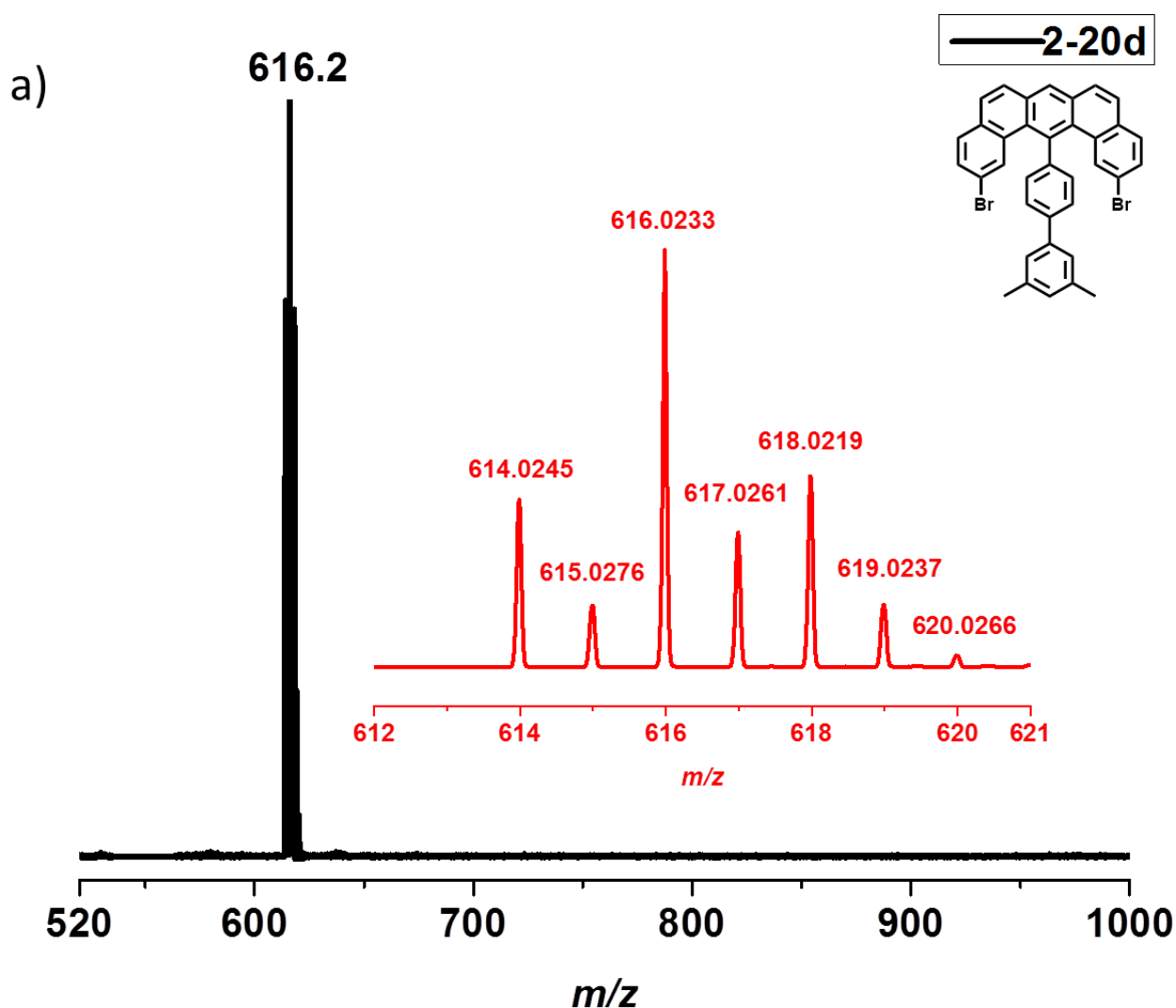
Figure 2-23 Synthetic scheme towards “U-shaped” monomer **2-20d** based on transition-metal catalyzed cyclisomerization.

2-Bromo-1-iodo-4-methoxybenzene (**2-22**) has been obtained after iodination of 1-bromo-3-methoxybenzene, which had been reported previously⁶¹. Then, *Sonogashira* coupling reaction of **2-22** with (triisopropylsilyl)acetylene yielded ((2-bromo-4-methoxyphenyl)ethynyl)triisopropylsilane (**2-23**) in 93% yield. Boronic ester **2-24** has been synthesized by borylation reaction of **2-23** with bis(pinacolato)diboron in 85% yield⁶². In parallel, (3',5'-dimethyl-[1,1'-biphenyl]-4-yl)trimethylsilane (**2-25**) has been prepared by *Suzuki* coupling of 1,3-dimethyl-5-bromobenzene with 4-(trimethylsilyl)phenylboronic acid in 95% yield. Then, compound **2-25** has been treated with boron tribromide (BBr₃) under neat condition to afford boronic acid **2-26** in 98% yield⁶³. Meanwhile, 1,3-dibromo-2-iodobenzene (**2-27**) has been synthesized *via* an iodination reaction⁶⁴ of 1,3-dibromobenzene with iodine in 91% yield. Then, 2,6-dibromo-3",5"-dimethyl-1,1':4',1"-terphenyl (**2-28**) has been obtained through a selective *Suzuki* coupling of **2-27** with **2-26** in 48% yield⁶⁵. This step had to be performed for long time (3 days) due to the steric hindrance, otherwise would led to a low yield.

In the following steps, 2,6-di[5-methoxy-2-((triisopropylsilyl)ethynyl)phenyl]-3",5"-dimethyl-1,1':4',1"-terphenyl (**2-29**) has been prepared via a two-fold *Suzuki* coupling of **2-24** with **2-28** in 81% yield and subsequently treated with tetrabutylammonium fluoride (TBAF) solution to remove triisopropyl (TIPS) group⁶⁶ to afford the 2,6-di[5-methoxy-2-ethynyl-phenyl]-3",5"-dimethyl-1,1':4',1"-terphenyl (**2-30**) in 99% yield. Notably, the crude product **2-30** was used directly for next step without further purification. The 14-(3',5'-dimethyl-[1,1'-biphenyl]-4-yl)-2,12-dimethoxy-dibenzo[a,j]anthracene (**2-31**) was then prepared after a catalytic cyclization reaction by treating **2-30** with platinum (II) chloride catalyst in 63% yield²⁷. After demethylation reaction⁶⁷ by treating **2-31** with boron BBr₃, crude product 14-(3',5'-dimethyl-[1,1'-biphenyl]-4-yl)-dibenzo[a,j]anthracene-2,12-diol (**2-32**) has been obtained and used directly for the next step. Triflate **2-33** has been yielded by treating **2-32** with trifluoromethanesulfonic anhydride (Tf₂O) in 78% yield⁶⁸. Then, 14-(3',5'-dimethyl-[1,1'-biphenyl]-4-yl)-dibenzo[a,j]anthracene-2,12-diyl-bis(4,4,5,5-tetramethyl-1,3,2-dioxaborolane) (**2-34**) has been synthesized through borylation of **2-33** with pinacolborane in 71% yield³⁶. At last, target "U-shaped" monomer **2-20d** has been obtained in 60% yield after treatment of **2-34** with copper (II) bromide in a sealed tube at 120 °C^{36,69}. It should be noted that the reaction in this step had to be performed in a sealed pressure-tube; otherwise no desired product will be obtained.

Similar to previous monomers **2-20a~c**, the high chemical purity was required for the surface-assisted synthesis. In contrast to **2-20a~c**, monomer **2-20d** exhibited good solubility in common organic solvents, such as chloroform, tetrahydrofuran and toluene. Therefore, it can be purified by recrystallization from chloroform and methanol. The structure of monomer **2-20d** was further

characterized and confirmed by MALDI-TOF MS, HR-APPI MS, ^1H and ^{13}C NMR, as well as single-crystal X-ray structural analysis. As shown in Fig. 2-24a, the MALDI-TOF and HR-APPI MS spectra indicated the high purity of **2-20d** and its isotopic distribution was in perfect agreement with the simulated pattern. The ^1H -NMR spectra exhibited in Fig. 2-24b also proved the high purity of **2-20d**. With the help of the relative intensities of proton peaks as well as its single crystal structure (Fig. 2-24c), the chemical structure of **2-20d** was further validated.



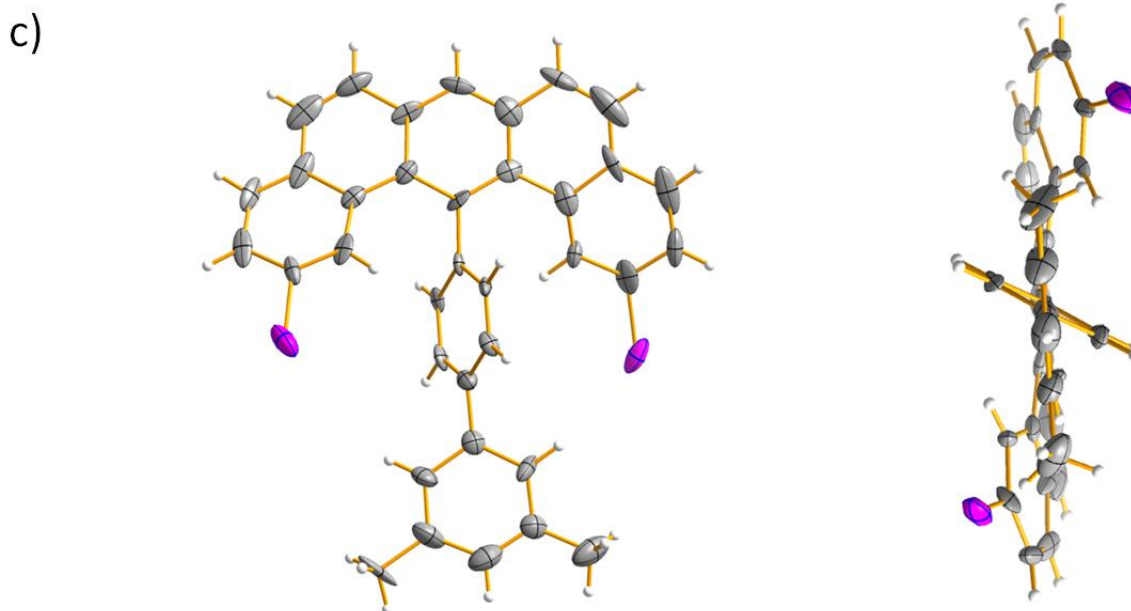
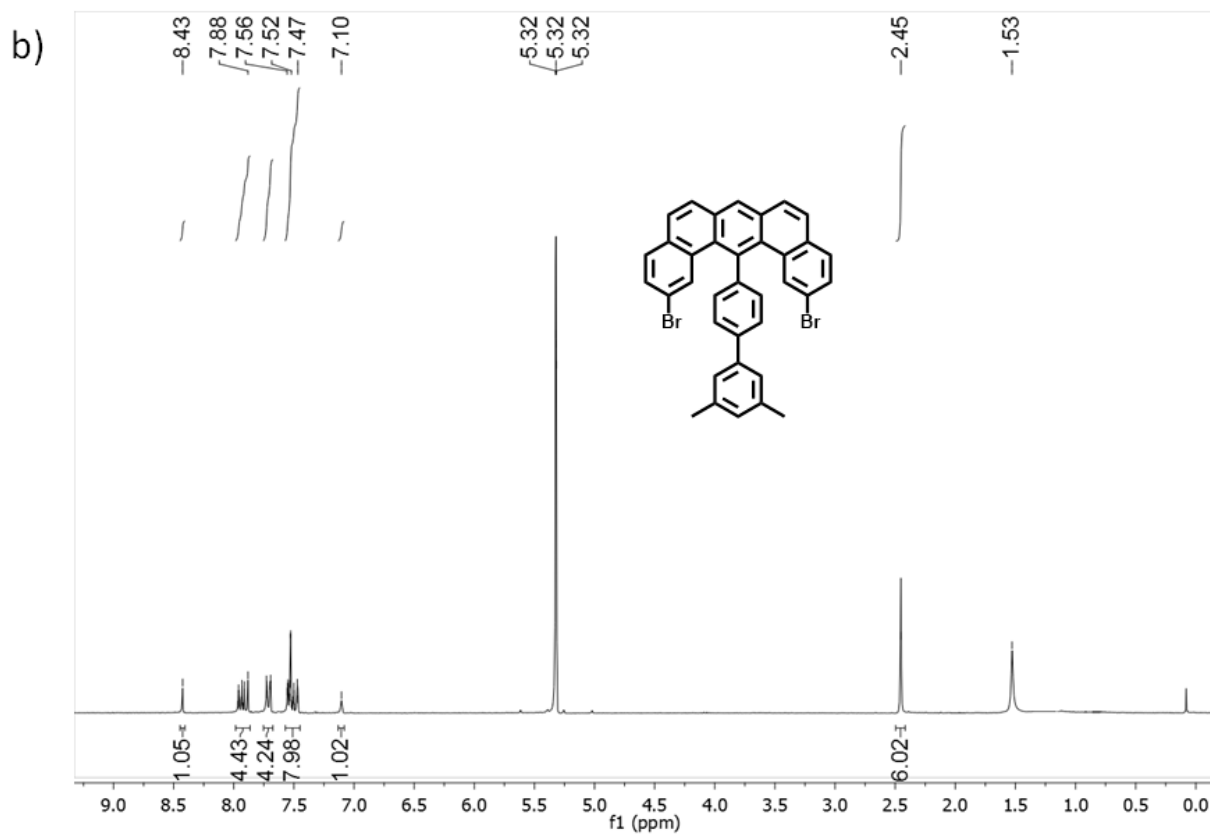


Figure 2-24. Characterization of **2-20d**: **a)** MALDI-TOF MS spectra; inset: HR-APPI MS spectra; **b)** ^1H NMR of **2-20d** in $\text{CD}_2\text{Cl}_2\text{-}d_2$ at r.t.; **c)** Single crystal structure (Front view and side view).

2.2.6 Surface synthesis of GNR with perfect zigzag edge

Using the tailor-made monomer **2-20d**, we could eventually test our idea of fabricating ZGNR (**f**) with perfect zigzag edge structures on surfaces (Fig. 2-25). We could also compare the electronic band structures between $N = 6$ ZGNR (**f**) and obtained $N = 6$ ZGNR plus (**f'**). The two ZGNRs have similar chemical structures, except the fluoranthrene subunits on ZGNR (**f'**) disrupting the perfection of the zigzag edge compared with ZGNR (**f**). In contrast to ZGNR (**f**) with a perfect zigzag edge, the ZGNR (**f'**) had been proven to possess an edge structure with possible three, four, and five zigzag cusps that separated by neighboring fluoranthrene subunits (Fig.2-18c and Fig. 2-25). Additionally, according to calculations by Nakada et al.¹, only three or four zigzag sites per sequence along the edge of ZGNR were enough to show an edge state. Thus, it is highly interesting to fabricate both $N = 6$ ZGNR (**f**) and (**f'**) and compare their electronic properties.

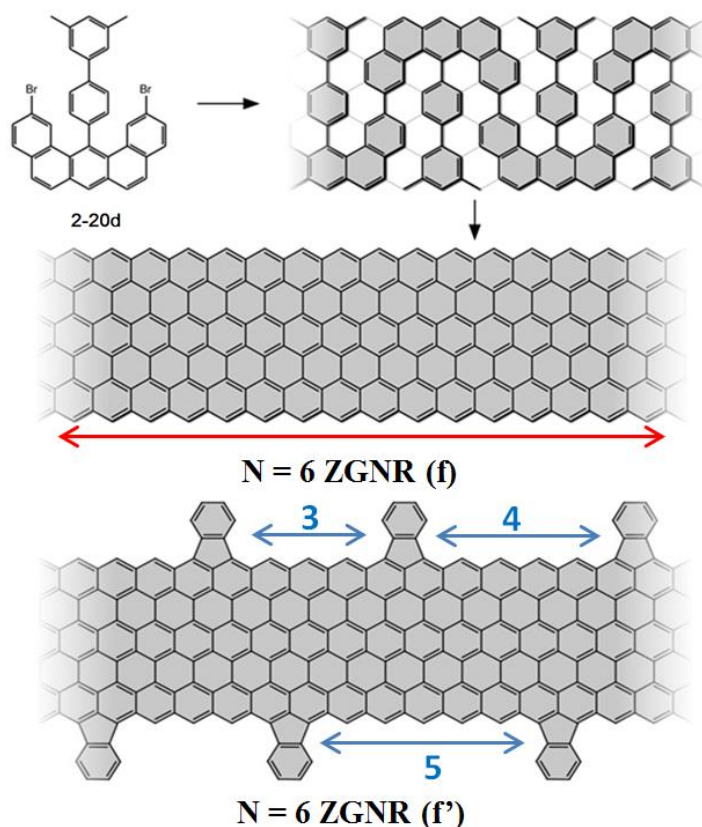


Figure 2-25. Fabrication of $N=6$ ZGNR (**f**) from “U-shaped” monomer **2-20d** and compare with $N = 6$ ZGNR (**f'**).

The surface-assisted fabrication of the $N=6$ ZGNR (**f**) using monomer **2-20d** was performed under similar conditions as previous monomers **2-20a~c** fabricated *via* pyrylium chemistry. Indeed

the remarkable N=6 ZGNR (**f**) structures formed. Here we show the two steps of the surface-synthesis and the details during the ZGNR fabrication below:

Step 1 : The monomer **2-20d** was deposited at 150 °C and post-annealed at 200 °C for 20 min. The STM images (Fig. 2-26a) showed the formation of individual polymers and no cross-coupling between polymer strips at this temperature. The polymer crossed the step edges of Au (111) substrates and extended the length over 100 nm. The growth direction of the polymer chains can be attributed to be slightly influenced by Au (111) surface reconstruction. The unique surface reconstruction of Au has been investigated and characterized by STM⁷⁰⁻⁷² and other surface science techniques. In general, the structure of the Au surface can be reconstructed from cubic structure into a different symmetry, and the reconstruction depends on the temperature. Furthermore, the periodicity along the edge was 1.55 nm, which was consistent with the expected value (1.48nm) of the covalent polymer, evidencing covalent bond formation. The maximum apparent height of 0.3 nm is attributed to the sterically induced out-of-plane conformation of the phenyl ring carrying the methyl groups.

Step 2 : Further annealing the substrate to 350 °C resulted in a complete planarization of the linear structures and an apparent height of 0.2 nm, consistent with the formation of the fully conjugated N = 6 ZGNR (**f**) structure (Fig. 2-26b). The small-scale STM images (inset of Fig. 2-26b) indicated the completely smooth and flat edge areas. Further structural details can be revealed by aforementioned nc-AFM imaging with a CO-functionalized tip (Fig. 2-26c), which allows for a direct imaging of the local bond configurations at small distances. This high resolution allowed to directly confirm that the width and edge morphology correspond to the expected N = 6 ZGNR (**f**) as defined as described in Fig. 2-25. Furthermore, the zigzag edge atoms with expected mono-hydrogen termination also can be confirmed according above images. In addition, the absence of defect (distinct maxima marked in Fig. 2-26c) can be observed, and assigned to H₂ edge termination. Other possible termination such as radical edges derived from complete dehydrogenation can be discarded due to the absence of bending across the ribbon.

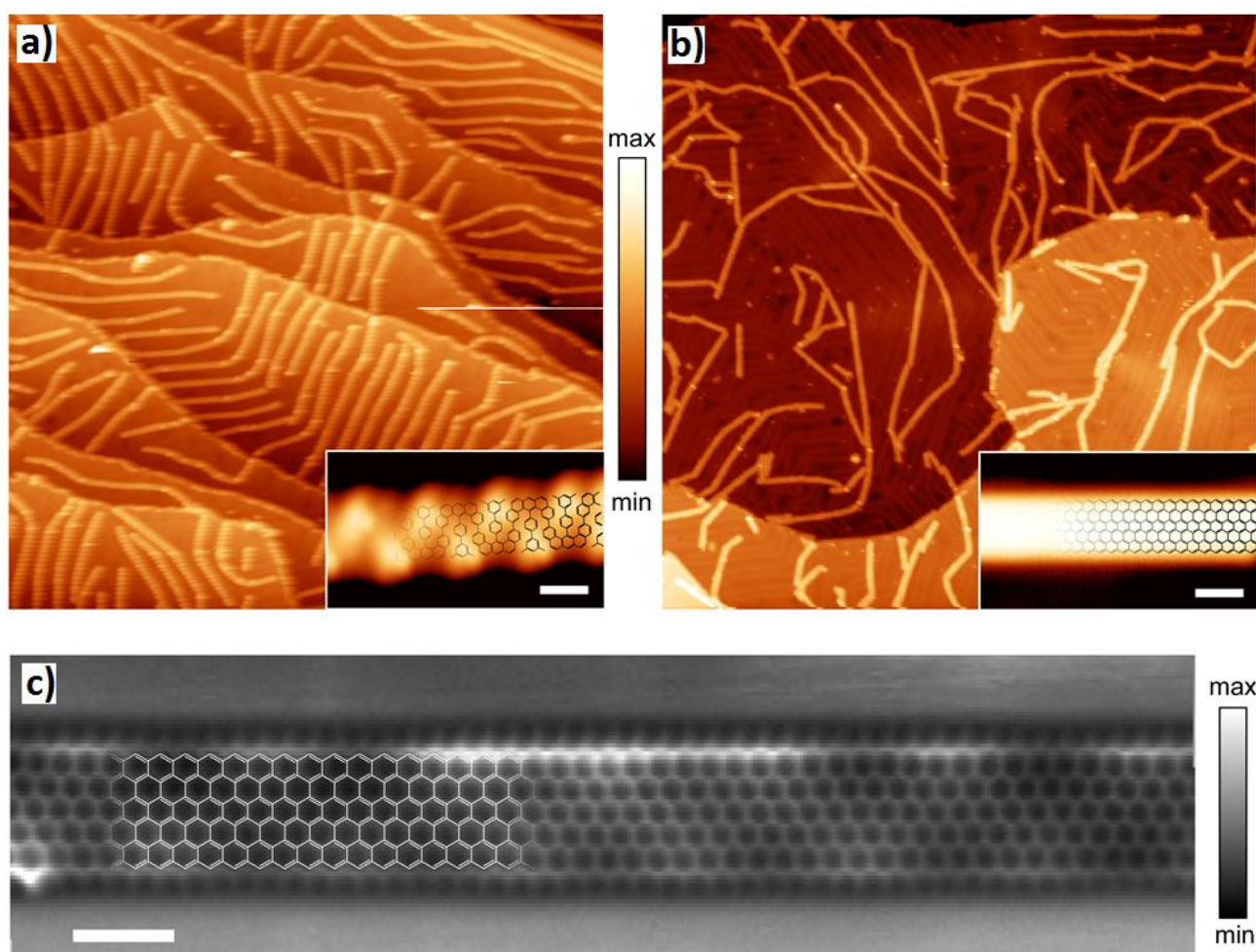


Figure 2-26. Synthesis and characterization of atomically precise 6-ZGNRs (**f**). a) Large-scale STM image (200 nm x 200 nm) of the Au(111) surface after deposition of monomer 1a on the surface held at 475 K. Formation of snake-like polymers is observed ($V = -1.5$ V, $I = 40$ pA). Inset: High-resolution STM image of the polymers. Zigzag alternation of bright maxima indicates the lifting and/or tilting of the phenyl rings carrying the methyl groups. A structural model is superimposed for comparison. (10.8 nm x 4.2 nm, $I = 10$ pA, $V = -1.3$ V). b) Large-scale STM image (200 nm x 200 nm) of the Au (111) surface after annealing at 625 K. Flatter appearance, reduced apparent height and no internal structure indicate the complete cyclodehydrogenation of the polymers and the formation of 6-ZGNRs (**f**) ($I = 20$ pA, $V = -1.0$ V). Inset: High-resolution STM of the 6-ZGNRs, which is in excellent agreement with the superimposed structural model (3.7 nm x 12.4 nm, $I = 5$ pA, $V = -0.3$ V). c) nc-AFM image taken with a CO-functionalized tip. Intra-ribbon resolution shows the formation of 6-ZGNRs with atomically precise CH edges. A CH_2 defect is seen in the lower left corner. (4.2 nm x 12.0 nm, $A_{\text{osc}} = 0.7$ Å, sample voltage $V = 5$ mV).

All GNRs (**d**, **e**, **f**, and **f'**) with zigzag edge structures were now clearly confirmed by both STM and nc-AFM images. As mentioned in section 5.1, ZGNRs are predicted to exhibit spin-

polarized edge states, a relatively lower bandgap, and unique magnetic properties. With $N = 6$ ZGNR (**f**) and (**f'**) in hand (Fig. 2-27), the further investigation and comparison of their electronic band structures and edge states are immensely interesting and significant.

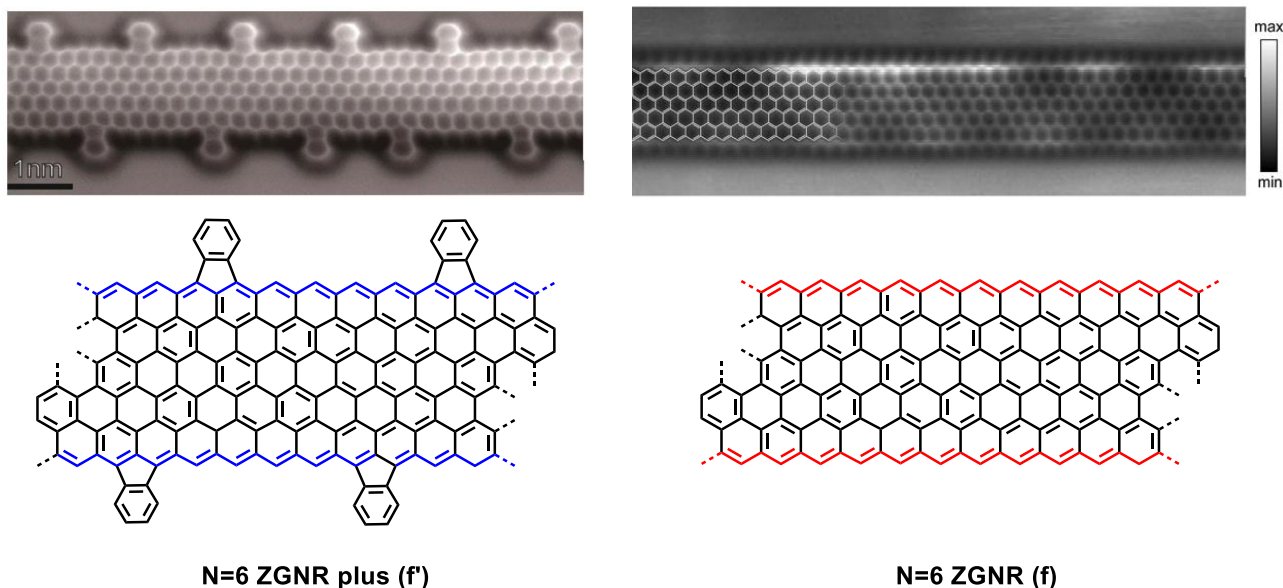


Figure 2-27. The nc-AFM images of two different $N = 6$ ZGNRs (**f'**) and (**f**) and their corresponding chemical structures.

2.2.7 Edge state characterization of 6-ZGNR (**f**) and 6-ZGNR plus (**f'**)

As mentioned in section 2.1, several edge state characterizations of less well-defined zigzag edges have been observed and investigated. These measurements were performed using the spin-polarized scanning tunneling microscopy (SP-STM), which is a general-purpose technique for imaging spin structure of surfaces with the ultimate in spatial resolution.⁷³ The SP-STM combines inherited spatial resolution of STM and sensitivity to surface magnetization vector. These two features make it an unprecedented technique that enables the characterization of spin-edge states and electronic band structure of ZGNRs (Fig. 2-28).

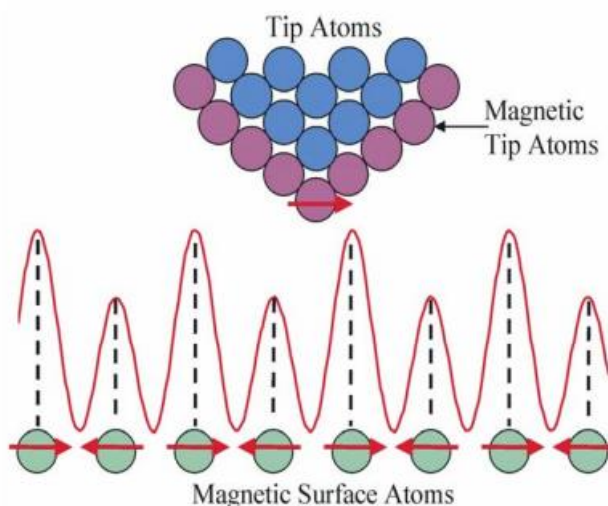


Figure 2-28. Schematic illustration of the SP-STM method. The tunneling current and thus the height depends on the relative orientations between tip and sample spins.

Although the above studies in section 2.1 on edge states of ZGNRs have been performed experimentally, the GNRs samples were less-well defined or only possessed zigzag termini. Thus, the investigation of the edge states of defect-free ZGNRs by employing the above technique has a significant meaning. For the first time, we can investigate the predicted spin-polarized edge states of the perfect 6-ZGNRs and compare with their computational simulation results. The chemistry of the 6-ZGNR (**f**) fabrication process faces various complications such as frequent thermally induced chemical cross-linking of ribbons during the cyclization step. Moreover, a strong electronic coupling between the ribbons and the metal surface obscures the detection of the electronic edge states. In fact, no evidence for increased intensity at the zigzag edges could be obtained in differential conductance (dI/dV) maps taken with a tunneling resistance down to $0.6 \text{ M}\Omega$, and spectra taken above the 6-ZGNRs are dominated by the (somewhat up-shifted) surface state of the underlying Au(111) substrate. First fingerprints of the 6-ZGNR edge states could be obtained in dI/dV maps taken with a special tip (of unknown termination) that featured a high density of states at the Fermi energy. Clear and unambiguous evidence for the sought-after edge states can, however, be obtained for 6-ZGNRs manipulated with the STM tip onto post-deposited insulating NaCl islands, where they are electronically decoupled from the underlying metal substrate.⁷⁴ Fig. 2-29A shows the example of a STM image of a 6-ZGNR bridging between two NaCl islands. Fig. 2-29D displays a dI/dV spectrum taken at the edge of the decoupled ZGNR segment. In sharp contrast to the result on Au(111), the spectrum clearly shows three resonance peaks near the Fermi level, with an energy splitting of $\Delta^0 = 1.5 \text{ eV}$ and $\Delta^1 = 1.9 \text{ eV}$ between the two unoccupied states and the occupied one, respectively (Fig.

2-29B). dI/dV maps acquired at these peaks show that the corresponding states are highly localized at the zigzag edges (Fig. 2-29D). Their characteristic features, such as a protrusion at each outermost zigzag carbon atom and an enhanced intensity at the ribbon terminus, are in excellent agreement with the local density of states of the corresponding Kohn-Sham DFT orbitals shown in Fig. 2-29E. While effective mean-field theories, such as Kohn-Sham DFT or the mean-field Hubbard model, in many cases provide reliable information about energy level ordering and the shape of orbitals, the same is not true for the size of the electronic gap. We have therefore calculated quasiparticle corrections to the band structure within the G_0W_0 approximation of many-body perturbation theory.⁷⁵ The resulting band structure and the corresponding DOS are shown in Fig. 2-29C. The obtained energy splittings of $\Delta^0 = 1.4$ eV and $\Delta^1 = 1.7$ eV fit the experimental values very well. While edge states have previously been observed in a number of systems with less well-defined zigzag edges,^{4,5,76-78} their reported energy splitting varied greatly and was significantly smaller than in the present case, indicating that the electronic structure of zigzag edges is extremely sensitive to the edge roughness and interactions with the supporting substrate.

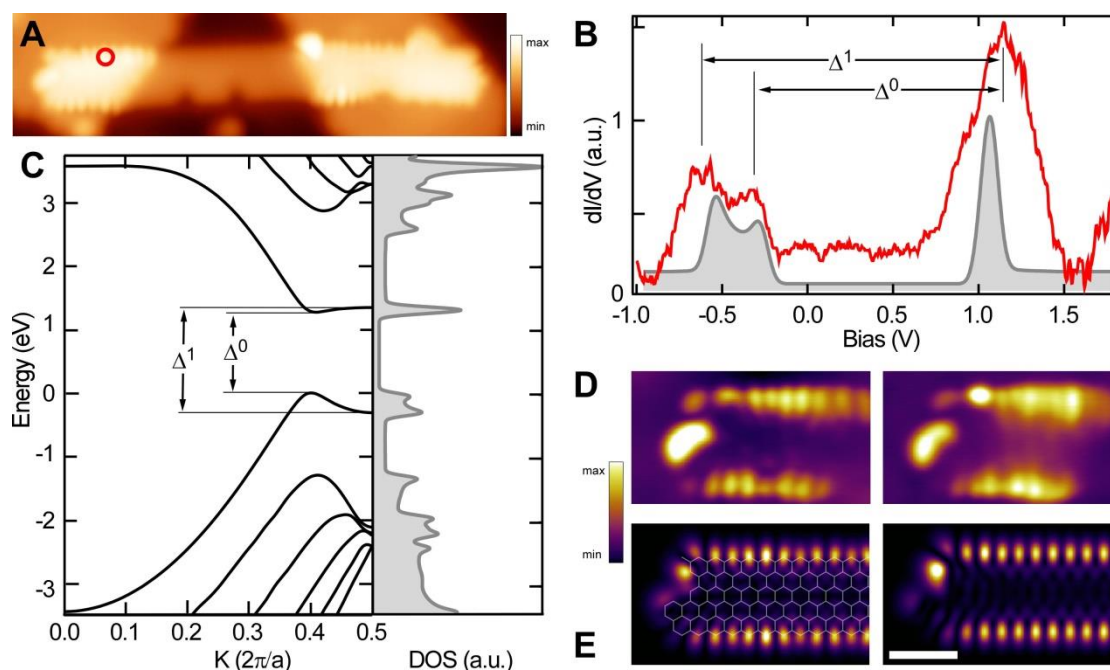


Figure 2-29. Edge state characterization of 6-ZGNR (f). (A) STM topography image (12.0 nm x 3.0 nm, $U = -0.25$ V, $I = 100$ pA) of a 6-ZGNR bridging between two NaCl monolayer islands, achieved through STM manipulation. (B) Differential conductance (dI/dV) spectrum taken at the zigzag edge marked by the red dot in (A). (C) GW band structure (left) and density of states (gray, right panel). (D) Differential conductance maps of filled (left) and empty (right) edge states taken at a sample bias of -0.3 V and 1.0 V, respectively. (E)

DFT-based local density of states at 4 Å tip-sample distance, showing the spatial distribution of filled (left, with overlaid structural model) and empty (right) edge states (scale bar for **D** and **E**: 1 nm).

Now that ZGNRs (**f**) with perfect zigzag edge periphery are available and edge states are proven, there are tremendous opportunities and challenges not only for analysis of the electronic, optical, and magnetic properties but also for their engineering via modified ZGNR types. Moreover, similar ZGNR plus (**f'**) that bears additional fluoranthrene subunits was also investigated with the same method (Fig. 2-30). We expected that due to the steric hindrance brought about by the twisted phenyl group, the growing ribbons were more efficiently decoupled from the surface and potentially also better shielded from neighboring GNRs. Controlled edge modification is an immensely attractive aspect for controlling the band structure. Our emphasis, however, is that in the present case the edge modification reduces the ZGNR-substrate interaction sufficiently to allow STM to map the typical features of the edge state. Moreover, as introduced in the above sections, band structures of ZGNRs are highly sensitive to their widths and edge structures (defects, doping, etc.), thus investigation and comparison of the edge states of 6-ZGNR (**f'**) and (**f**) are important.

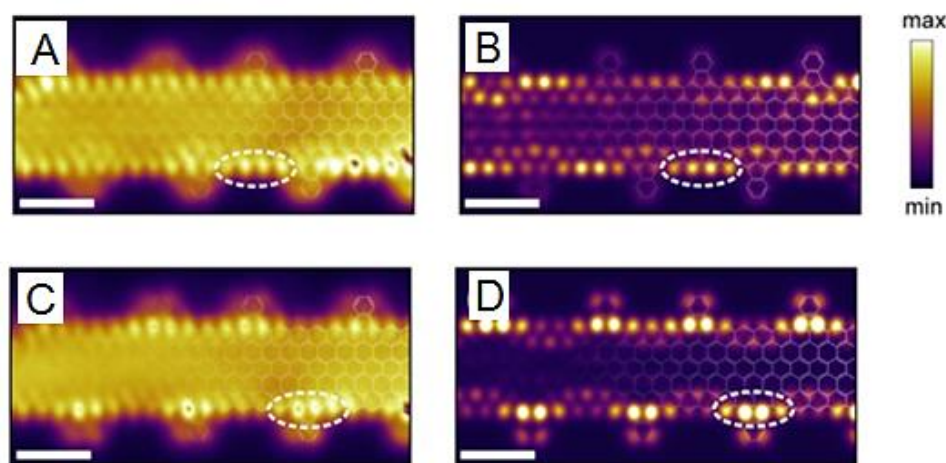


Figure 2-30. Edge state characterization of 6-ZGNR plus (**f'**). A) Constant height dI/dV map of the occupied states ($U = -0.15$ V). B) DFT-based density of states of the highest occupied state C) Constant height dI/dV map of the unoccupied states ($U = 0.15$ V). D) DFT-based density of states of lowest unoccupied level. All scale bars: 1 nm.

Figure 2-30A and F show constant-height differential conductance maps acquired at -0.15 and 0.15 eV, respectively, which clearly reveal increased intensity along the ZGNR edges. While the edge states at pristine zigzag edges occupy exclusively one carbon sublattice (e.g. sublattice A),¹ in

the case of the edge-modified 6-ZGNR the five-membered ring of the fluoranthrene subunit locally disturbs the bipartite character of the graphene lattice by directly connecting carbon atoms belonging to the same sublattice. This topological defect breaks translational symmetry along the zigzag edge and gives rise to a linear combination of Bloch states with nodes at the defects (Fig. 2-30 A,B) and nodes in between defects (Fig. 2-30 C,D), as can be seen both in STS experiments and DFT-based simulations. The energetic ordering of these “edge bands” localized on unmodified edge sections and “defect bands” localized on the pentagon-decorated section of the edge⁷⁹ is determined by a delicate interplay between kinetic and Coulomb energy contributions and will be the subject of future work.

2.3 Summary

In summary, we designed and synthesized series of “U-shaped” monomer precursors from **2-20a** to **2-20d**, which were subsequently subjected to surface-assisted fabrication of novel GNRs with partial zigzag edge structures as well as full zigzag edge (Fig. 2-31). The successful bottom-up synthesis of atomically precise ZGNRs opens tremendous opportunities and challenges not only for analysis of the electronic band structure but also for magnetic measurements including the use of spin-polarized STM and the creation of spin valves. The strong interaction of the pristine 6-ZGNR with the metal substrate, which totally obstructs the spectral features of the edge states, however, raises important questions regarding the chemical reactivity of the zigzag edges, which need to be controlled in order to study and apply these materials under ambient conditions. The present work is believed to be a milestone case of surface chemistry which only becomes possible by a combination of creative chemical design and *in-situ* STM monitoring of surface bound reactions.

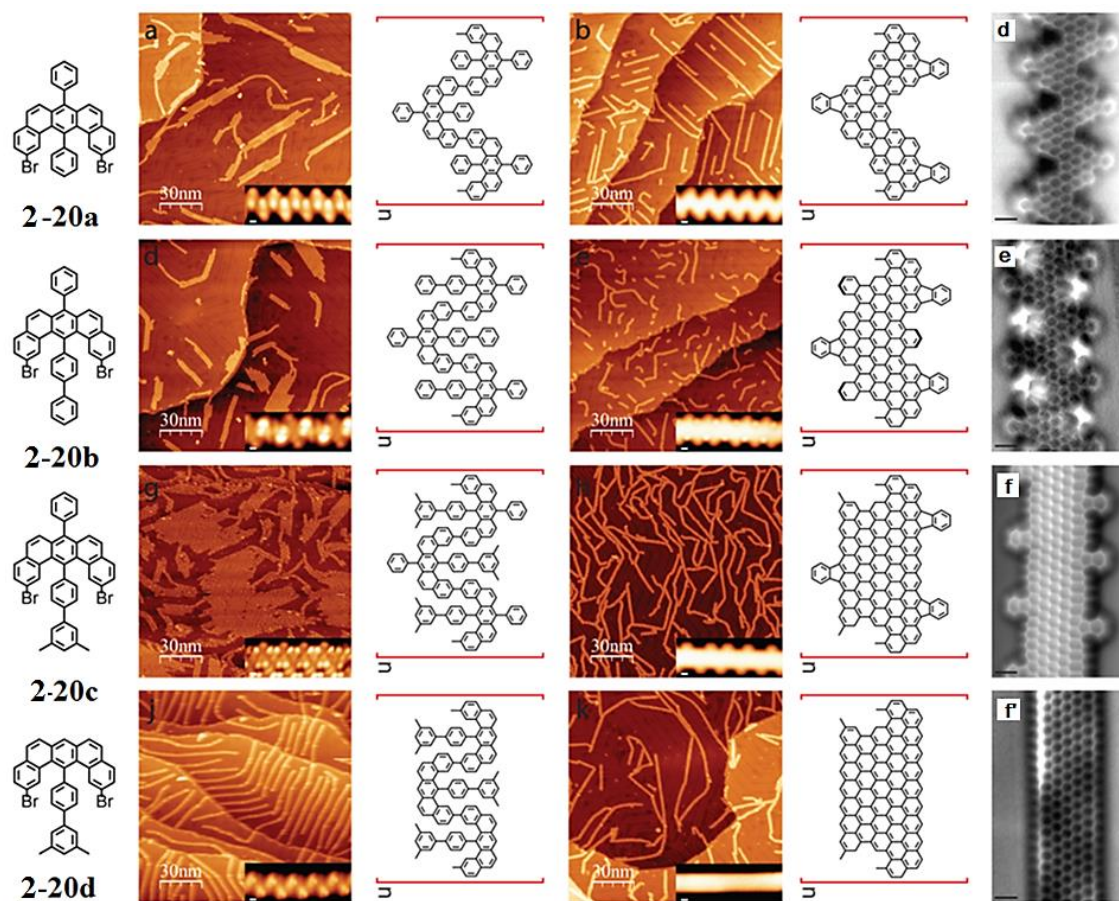


Figure 2-31. Surface-assisted approaches towards novel GNRs (d), (e), (f) and (f') from "U-shaped" monomers 2-20a, 2-20b, 2-20c and 2-20d, respectively.

2.4 References

- (1) Nakada, K.; Fujita, M.; Dresselhaus, G.; Dresselhaus, M. S. *Phys Rev B* **1996**, *54*, 17954.
- (2) Son, Y. W.; Cohen, M. L.; Louie, S. G. *Phys Rev Lett* **2006**, *97*.
- (3) Talirz, L.; Sode, H.; Cai, J. M.; Ruffieux, P.; Blankenburg, S.; Jafaar, R.; Berger, R.; Feng, X. L.; Mullen, K.; Passerone, D.; Fasel, R.; Pignedoli, C. A. *J Am Chem Soc* **2013**, *135*, 2060.
- (4) Ijas, M.; Ervasti, M.; Uppstu, A.; Liljeroth, P.; van der Lit, J.; Swart, I.; Harju, A. *Phys Rev B* **2013**, *88*.
- (5) Magda, G. Z.; Jin, X. Z.; Hagymasi, I.; Vancso, P.; Osvath, Z.; Nemes-Incze, P.; Hwang, C. Y.; Biro, L. P.; Tapasztó, L. *Nature* **2014**, *514*, 608.
- (6) Son, Y. W.; Cohen, M. L.; Louie, S. G. *Nature* **2006**, *444*, 347.
- (7) Cai, J. M.; Ruffieux, P.; Jaafar, R.; Bieri, M.; Braun, T.; Blankenburg, S.; Muoth, M.; Seitsonen, A. P.; Saleh, M.; Feng, X. L.; Mullen, K.; Fasel, R. *Nature* **2010**, *466*, 470.
- (8) Bronner, C.; Stremlau, S.; Gille, M.; Brausse, F.; Haase, A.; Hecht, S.; Tegeder, P. *Angew Chem Int Edit* **2013**, *52*, 4422.
- (9) Cai, J. M.; Pignedoli, C. A.; Talirz, L.; Ruffieux, P.; Sode, H.; Liang, L. B.; Meunier, V.; Berger, R.; Li, R. J.; Feng, X. L.; Mullen, K.; Fasel, R. *Nat Nanotechnol* **2014**, *9*, 896.
- (10) Floyd, A. J.; Dyke, S. F.; Ward, S. E. *Chemical Reviews* **1976**, *76*, 509.
- (11) Laarhoven, W. H. *Recl Trav Chim Pay B* **1983**, *102*, 185.
- (12) Laarhoven, W. H. *Recl Trav Chim Pay B* **1983**, *102*, 241.
- (13) Liu, L. B.; Yang, B. W.; Katz, T. J.; Poindexter, M. K. *J Org Chem* **1991**, *56*, 3769.
- (14) Mallory, F. B.; Wood, C. S.; Gordon, J. T. *J Am Chem Soc* **1964**, *86*, 3094.
- (15) Wood, C. S.; Mallory, F. B. *J Org Chem* **1964**, *29*, 3373.
- (16) Klyatskaya, S.; Dingenouts, N.; Rosenauer, C.; Müller, B.; Hoger, S. *J Am Chem Soc* **2006**, *128*, 3150.
- (17) Mahler, C.; Müller, U.; Müller, W. M.; Enkelmann, V.; Moon, C.; Brunklaus, G.; Zimmermann, H.; Hoger, S. *Chem Commun* **2008**, 4816.
- (18) Moghimi, A.; Rastegar, M. F.; Ghandi, M.; Taghizadeh, M.; Yari, A.; Shamsipur, M.; Yap, G. P. A.; Rahbarnoohi, H. *J Org Chem* **2002**, *67*, 2065.
- (19) Ohlendorf, G.; Mahler, C. W.; Jester, S. S.; Schnakenburg, G.; Grimme, S.; Hoger, S. *Angew Chem Int Edit* **2013**, *52*, 12086.
- (20) Shamsipur, M.; Rouhani, S.; Mohajeri, A.; Ganjali, M. R.; Rashidi-Ranjbar, P. *Anal Chim Acta* **2000**, *418*, 197.

- (21) Wu, D. Q.; Feng, X. L.; Takase, M.; Haberecht, M. C.; Mullen, K. *Tetrahedron* **2008**, *64*, 11379.
- (22) Wu, D. Q.; Pisula, W.; Haberecht, M. C.; Feng, X. L.; Mullen, K. *Org Lett* **2009**, *11*, 5686.
- (23) Zimmermann, T. *J Prak Chem-Chem Ztg* **1994**, *336*, 303.
- (24) Zimmermann, T.; Fischer, G. W. *J Prakt Chem* **1987**, *329*, 975.
- (25) Chen, T. A.; Liu, R. S. *Org Lett* **2011**, *13*, 4644.
- (26) Eversloh, C. L.; Li, C.; Mullen, K. *Org Lett* **2011**, *13*, 4148.
- (27) Furstner, A.; Mamane, V. *J Org Chem* **2002**, *67*, 6264.
- (28) Mamane, V.; Gress, T.; Krause, H.; Furstner, A. *J Am Chem Soc* **2004**, *126*, 8654.
- (29) Mamane, V.; Hannen, P.; Furstner, A. *Chem-Eur J* **2004**, *10*, 4556.
- (30) Shen, H. C.; Tang, J. M.; Chang, H. K.; Yang, C. W.; Liu, R. S. *J Org Chem* **2005**, *70*, 10113.
- (31) Storch, J.; Sykora, J.; Cermak, J.; Karban, J.; Cisarova, I.; Ruzicka, A. *J Org Chem* **2009**, *74*, 3090.
- (32) Sehnal, P.; Stara, I. G.; Saman, D.; Tichy, M.; Misek, J.; Cvacka, J.; Rulisek, L.; Chocholousova, J.; Vacek, J.; Goryl, G.; Szymonski, M.; Cisarova, I.; Stary, I. *P Natl Acad Sci USA* **2009**, *106*, 13169.
- (33) Snatzke, G.; Kunde, K. *Chem Ber-Recl* **1973**, *106*, 1341.
- (34) Yang, Y. H.; Dai, W. X.; Zhang, Y. Z.; Petersen, J. L.; Wang, K. K. *Tetrahedron* **2006**, *62*, 4364.
- (35) Lindoy, L. F.; Meehan, G. V.; Svenstrup, N. *Synthesis-Stuttgart* **1998**, 1029.
- (36) Thompson, A. L. S.; Kabalka, G. W.; Akula, M. R.; Huffman, J. W. *Synthesis-Stuttgart* **2005**, 547.
- (37) Chen, Q. Y.; Yang, Z. Y. *Tetrahedron Lett* **1986**, *27*, 1171.
- (38) Amsharov, K. Y.; Kabdulov, M. A.; Jansen, M. *Eur J Org Chem* **2009**, 6328.
- (39) Comes, M.; Marcos, M. D.; Martinez-Manez, R.; Sancenon, F.; Soto, J.; Villaescusa, L. A.; Amoros, P.; Beltran, D. *Adv Mater* **2004**, *16*, 1783.
- (40) G. Harvey, R. *Wiley-VCH: New York* **1997**.
- (41) Cozens, F. L.; Cano, M. L.; Garcia, H.; Schepp, N. P. *J Am Chem Soc* **1998**, *120*, 5667.
- (42) Dauben, H. J.; Wilson, J. D. *Chem Commun* **1968**, 1629.
- (43) Heyes, D.; Menon, R. S.; Watt, C. I. F.; Wiseman, J.; Kubinski, P. *J Phys Org Chem* **2002**, *15*, 689.

- (44) Khenkin, A. M.; Weiner, L.; Wang, Y.; Neumann, R. *J Am Chem Soc* **2001**, *123*, 8531.
- (45) Cheng, X. H.; Hoger, S.; Fenske, D. *Org Lett* **2003**, *5*, 2587.
- (46) Khosropour, A. R.; Khodaei, M. M.; Moghannian, H. *Synlett* **2005**, *2005*, 0955.
- (47) Zhang, J.; Chen, P.; Yuan, B.; Ji, W.; Cheng, Z.; Qiu, X. *Science* **2013**, *342*, 611.
- (48) Gross, L.; Mohn, F.; Moll, N.; Liljeroth, P.; Meyer, G. *Science* **2009**, *325*, 1110.
- (49) Sugimoto, Y.; Pou, P.; Abe, M.; Jelinek, P.; Perez, R.; Morita, S.; Custance, O. *Nature* **2007**, *446*, 64.
- (50) Kaiser, U.; Schwarz, A.; Wiesendanger, R. *Nature* **2007**, *446*, 522.
- (51) Schmidt, R.; Lazo, C.; Holscher, H.; Pi, U. H.; Caciuc, V.; Schwarz, A.; Wiesendanger, R.; Heinze, S. *Nano Lett* **2009**, *9*, 200.
- (52) Ashino, M.; Obergfell, D.; Haluska, M.; Yang, S. H.; Khlobystov, A. N.; Roth, S.; Wiesendanger, R. *Nat Nanotechnol* **2008**, *3*, 337.
- (53) Ashino, M.; Schwarz, A.; Behnke, T.; Wiesendanger, R. *Phys Rev Lett* **2004**, *93*, 136101.
- (54) Haruta, M. *Cattech* **2002**, *6*, 102.
- (55) Hammer, B.; Norskov, J. K. *Nature* **1995**, *376*, 238.
- (56) Björk, J.; Stafström, S.; Hanke, F. *J Am Chem Soc* **2011**, *133*, 14884.
- (57) Dimroth, K. *Angewandte Chemie* **1960**, *72*, 331.
- (58) Dimroth, K.; Wolf, K. H.; Wache, H. *Angewandte Chemie International Edition in English* **1963**, *2*, 621.
- (59) Wu, T. C.; Chen, M. K.; Lee, Y. W.; Kuo, M. Y.; Wu, Y. T. *Angew Chem Int Edit* **2013**, *52*, 1289.
- (60) Wu, T. C.; Hsin, H. J.; Kuo, M. Y.; Li, C. H.; Wu, Y. T. *J Am Chem Soc* **2011**, *133*, 16319.
- (61) Rasolofonjatovo, E.; Provot, O.; Hamze, A.; Bignon, J.; Thoret, S.; Brion, J.-D.; Alami, M. *European Journal of Medicinal Chemistry* **2010**, *45*, 3617.
- (62) Ishiyama, T.; Murata, M.; Miyaura, N. *J Org Chem* **1995**, *60*, 7508.
- (63) Tilford, R. W.; Gemmill, W. R.; zur Loye, H.-C.; Lavigne, J. J. *Chemistry of Materials* **2006**, *18*, 5296.
- (64) Leroux, F. R.; Bonnafoux, L.; Heiss, C.; Colobert, F.; Lanfranchi, D. A. *Advanced Synthesis & Catalysis* **2007**, *349*, 2705.
- (65) Zou, L.; Wang, X.-Y.; Shi, K.; Wang, J.-Y.; Pei, J. *Organic Letters* **2013**, *15*, 4378.
- (66) Keller, J. M.; Schanze, K. S. *Organometallics* **2009**, *28*, 4210.
- (67) Shragina, L.; Buchholtz, F.; Yitzchaik, S.; Krongauz, V. *Liquid Crystals* **1990**, *7*, 643.

- (68) Yang, S.; Denny, W. A. *The Journal of Organic Chemistry* **2002**, *67*, 8958.
- (69) Battagliarin, G.; Zhao, Y.; Li, C.; Müllen, K. *Organic Letters* **2011**, *13*, 3399.
- (70) Hanke, F.; Bjork, J. *Phys Rev B* **2013**, *87*.
- (71) Jaklevic, R. C.; Elie, L. *Phys Rev Lett* **1988**, *60*, 120.
- (72) Barth, J. V.; Brune, H.; Ertl, G.; Behm, R. J. *Phys Rev B* **1990**, *42*, 9307.
- (73) Kubetzka, A.; Bode, M.; Pietzsch, O.; Wiesendanger, R. *Phys Rev Lett* **2002**, *88*, 057201.
- (74) Repp, J.; Meyer, G.; Paavilainen, S.; Olsson, F. E.; Persson, M. *Phys Rev Lett* **2005**, *95*.
- (75) Hybertsen, M. S.; Louie, S. G. *Phys Rev B* **1986**, *34*, 5390.
- (76) Ritter, K. A.; Lyding, J. W. *Nat Mater* **2009**, *8*, 235.
- (77) Tao, C. G.; Jiao, L. Y.; Yazyev, O. V.; Chen, Y. C.; Feng, J. J.; Zhang, X. W.; Capaz, R. B.; Tour, J. M.; Zettl, A.; Louie, S. G.; Dai, H. J.; Crommie, M. F. *Nat Phys* **2011**, *7*, 616.
- (78) van der Lit, J.; Boneschanscher, M. P.; Vanmaekelbergh, D.; Ijas, M.; Uppstu, A.; Ervasti, M.; Harju, A.; Liljeroth, P.; Swart, I. *Nat Commun* **2013**, *4*.
- (79) Bhattacharjee, J. *J Chem Phys* **2012**, *137*.

Chapter 3. Bottom-up synthesis of GNR with zigzag edges in solution

3.1 Introduction

As mentioned in section 2.1, GNRs with zigzag edge structures preserve unique properties including profound lowering of the bandgaps and localized edge states that can be spin-polarized.^{1,2} These properties render them highly interesting and potentially applicable in spintronics.³ There are two general protocols for synthesizing GNRs, namely surface-assisted and solution-mediated methods. In the last chapter, we successfully applied surface-assisted protocol in the fabrication of novel GNRs with zigzag edge structures. Comparing the two protocols, the latter has advantages including capabilities of producing GNRs in large scale, rendering GNRs processable from liquid phase by employing bulky substituents, which enables direct integration into electronic devices. In this chapter, we demonstrate the synthesis and characterization of novel GNRs with partial zigzag edges through solution-mediated synthesis.

3.2 Synthetic strategy

In the chapter 1, we described the idea of fabricating GNRs from a “U-shaped” building blocks with dibenzo[*a,j*]anthracene as the core structure, which was substituted with reactive halogen groups (X) (Fig.1-34). Polymerization of such “U-shaped” monomers leads to wavy, “snake-like” polymers, with aryl substituents Ar₁ and Ar₂ at the “trough” and the “peak”, respectively. Here, *Yamamoto* coupling reaction of “U-shaped” monomers **3-1** was carried out during the solution-mediated fabrication to obtain snake-like polyphenylene **3-2**, and the subsequent oxidative cyclodehydrogenation led to desired GNRs **3-3** with a hybrid of zigzag and gulf-type edge structures (Fig.3-1). As mentioned in the last chapter, various GNRs can be obtained from “U-shaped” monomers **3-1** through the surface-assisted synthesis by modulating Ar₁ and Ar₂. For the solution synthesis, the phenyl group was used as Ar₁ and phenyl group with *para*-substituted groups R as Ar₂. As the substituted groups R, H, *tert*-butyl, and 4-decylhexadecyl groups were used and termed as a, b, and c, respectively. It is worth noting that the substituent Ar₂ protects the active *meso*-position of the zigzag edges in the resulting GNR **3-3** and simultaneously enhances its dispersibility with the bulky alkyl chains (GNR **3-3c**).

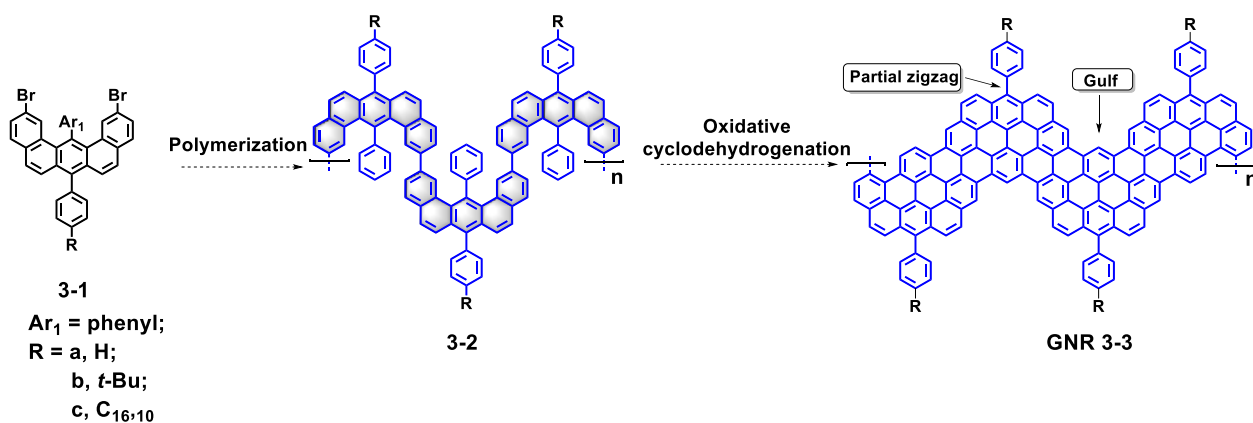


Figure 3-1. a) “U-shaped” monomers and wavy polymers; b) tailored monomers for solution-mediated synthesis of GNR **3-3**.

3.2.1 Synthesis of monomers (building blocks)

The synthetic route towards monomer **3-1** was planned based on the pyrylium chemistry^{4,5} in the same manner as the syntheses shown in chapter 2 (Fig. 3-2c). To obtain monomer **3-1**, sodium 2-phenylacetate **3-5a-c** with different substituent group R (**a**, R = H; **b**, *t*-Bu; and **c**, I) as well as 11-(prop-2-yn-1-yl)tricosane **3-7** were initially synthesized according to the reported procedures in one step.^{4,6} Sodium phenylacetate **3-5** was prepared from 4-substituted phenylacetic acid **3-4** with one equivalent of sodium methylate (0.5 M methanol solution) in 99% yield (Fig. 3-2a). Compound **3-7** was prepared from 2-decyltetradecyl bromide **3-6** with lithium acetylide-ethylenediamine complex in DMSO in 95% yield (Fig. 3-2b).⁶

Monomer **3-1a** was synthesized as described in chapter 2. Here, dibenzo[*a,j*]xanthenes **2-17a**, dibenzo[*a,j*]xanthen-14-ol **2-18a**, pyrylium salts **2-19a**, and “U-shaped” monomer **2-20a** prepared in the last chapter are termed as **3-9**, **3-10**, **3-11**, and **3-1a**, respectively, in this chapter.

14-Phenyl-14*H*-dibenzo[*a,j*]xanthene **3-9** was prepared by condensation of 7-bromonaphthol (**3-8**) with 0.5 equivalents of benzaldehyde under a neat condition at 125 °C. Oxidation of **3-9** with an excess amount of lead oxide in acetic acid at 120 °C afforded 14-phenyl-14*H*-dibenzo[*a,j*]xanthen-14-ol (**3-10**), which was collected by reprecipitation and used for the next step without further purification. Subsequent treatment of **3-10** with tetrafluoroboric acid solution (50 wt. % aq.) provided pyrylium salt **3-11** in 68% yield for two steps. Next, pyrylium salt **3-11** was subjected to condensation reactions at 150 °C with sodium phenylacetates **3-5** bearing different substituents (R), leading to the formation of monomers **3-1a**, **3-1b**, and **3-12** with hydrogen, *tert*-butyl, and iodine

as R, respectively, in relatively low yield (29–34%). *Sonogashira* coupling of **3-12** with 11-(prop-2-yn-1-yl)tricosane (**3-7**) and subsequent hydrogenation⁷ afforded monomer **3-1c** with a 4-decylhexadecyl chain in 85% yield for two steps. All the monomers (**3-1a**, **b**, and **c**) were identified by ¹H and ¹³C NMR as well as MALDI-TOF MS measurements.

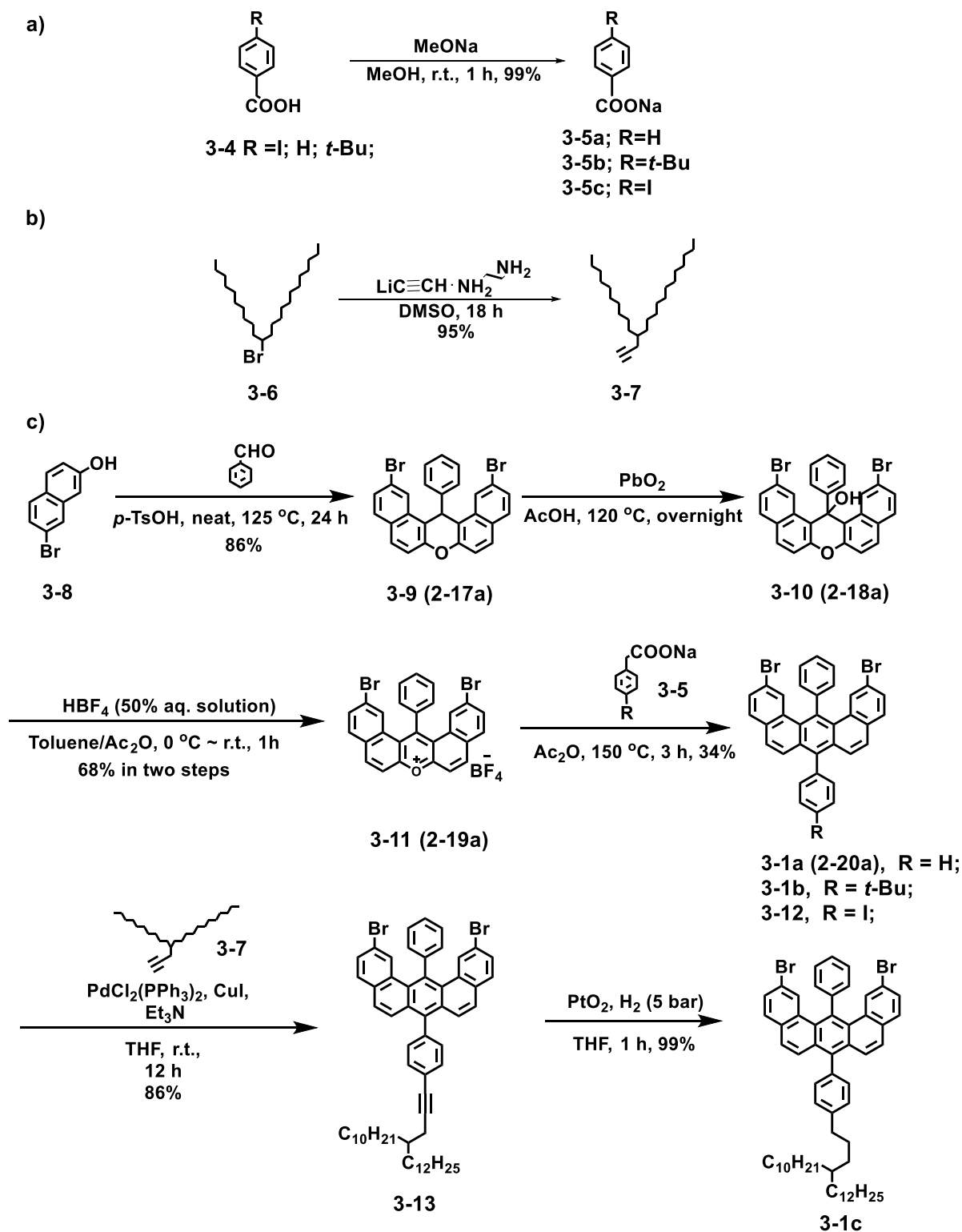


Figure 3-2. Synthetic schemes towards a) sodium phenylacetates **3-5a~c**; b) compound **3-7**; c) monomers **3-1a~c**.

3.2.2 Synthesis of model compounds **3-15**, **3-17**, and **3-19**

In order to examine the suitability of polymer precursor **3-2** for the fabrication of GNR **3-3** via intramolecular oxidative cyclodehydrogenation, oligomers **3-14**, **3-16**, and **3-18** were designed and synthesized as model compounds, which corresponded to short segments of polymer **3-2** (Fig. 3-3).

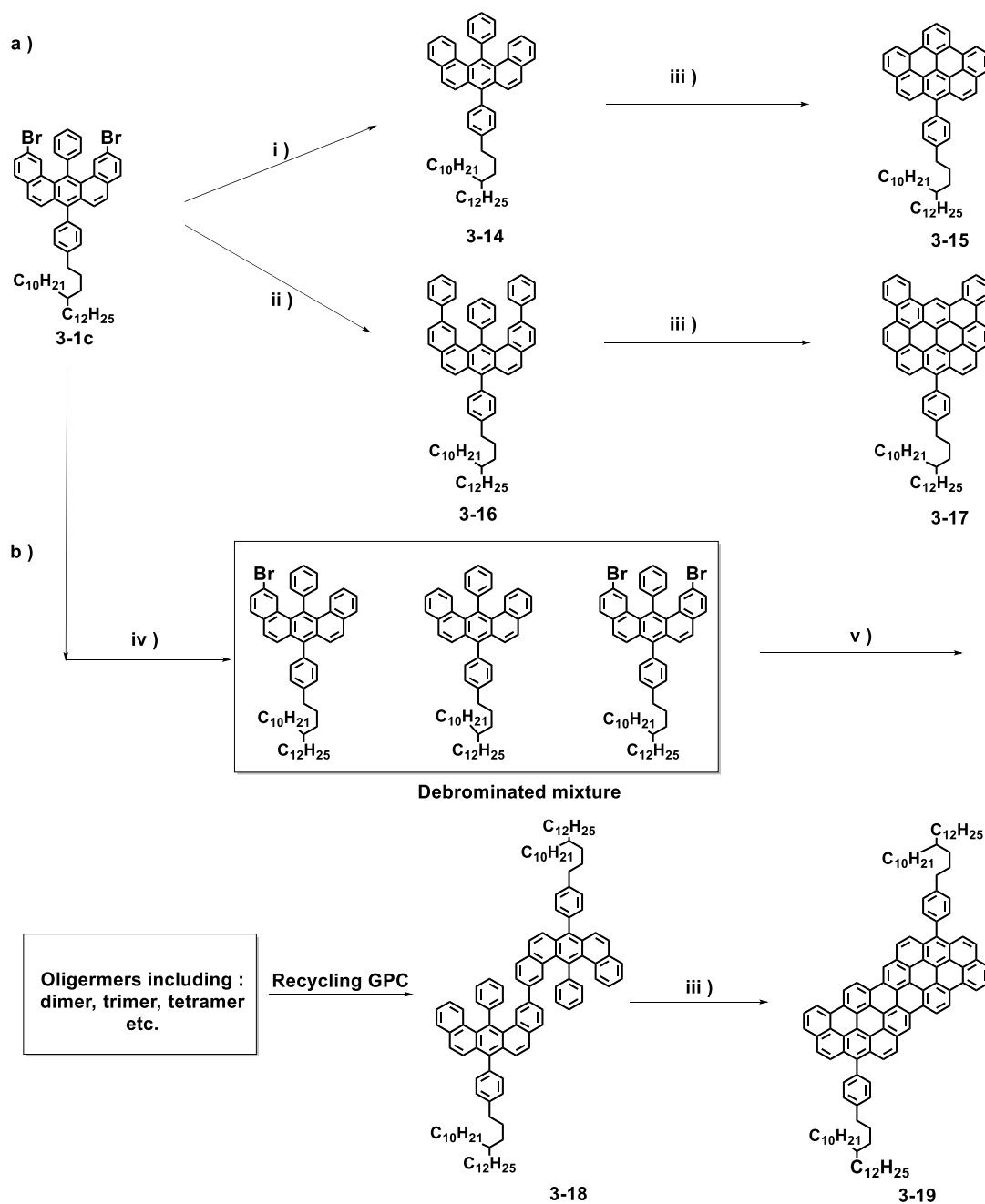


Figure 3-3. General synthetic routes to model compounds: a) model compounds **3-15** and **3-17**; b) model compound **3-19**; conditions: i) 2.0 eq. of *n*-BuLi, THF, $-78\text{ }^{\circ}\text{C}$, then MeOH; ii) phenylboronic acid, Pd(PPh₃)₄, K₂CO₃, toluene/H₂O, reflux; iii) **1**. DDQ/TFA, DCM, $0\text{ }^{\circ}\text{C}$ – r.t.; **2**. FeCl₃/DCM, argon bubbling; **3**. Cu(OTf)₂/AlCl₃, CS₂, $30\text{ }^{\circ}\text{C}$; iv) 1.0 eq. of *n*-BuLi, THF, $-78\text{ }^{\circ}\text{C}$, then MeOH; v) Ni(COD)₂, 2,2'-bipyridine, COD, $60\text{--}80\text{ }^{\circ}\text{C}$.

Synthesis of model compounds **3-15**, **3-17**, and **3-19** were carried out from monomer **3-1c** as shown in Fig. 3-3. A debromination reaction was performed by adding two equivalent of *n*-butyllithium solution to afford precursor 7-(4-(4-decylhexadecyl)phenyl)-14-phenylbenzo[*m*]tetraphene **3-14**. Then, 14-(4-(4-decylhexadecyl)phenyl)phenanthro[2,3,4,5-pqra]perylene **3-15** can be obtained by using different cyclodehydrogenation procedures, namely with DDQ/TFA^{8,9}, FeCl₃^{10,11}, Cu(OTf)₂/AlCl₃^{12,13} as Lewis acid and oxidative reagents (Fig. 3-3, condition iii). Notably, all three procedures are capable to give desired product **3-15**. Nevertheless, the latter two procedures required precise control of reaction time, otherwise further chlorinated side products would be generated. On the contrary, the former DDQ/TFA method could avoid further chlorination after cyclodehydrogenation of precursor **3-14**. However, this procedure also has disadvantages in that it will generate oxidative side products due to the strongly oxidative and acidic environment in the liquid-phase and the unstable nature of zigzag structures in our model compounds. Fortunately, these oxidative side products can be removed after purification by column chromatography. Based on the above situation, the DDQ/TFA procedure was eventually applied for the cyclodehydrogenation of precursors **3-14**, **3-16**, and **3-18**. Precursor 7-(4-(4-decylhexadecyl)phenyl)-2,12,14-triphenylbenzo[*m*]tetraphen **3-16** was prepared by *Suzuki* coupling of monomer **3-1c** with phenylboronic acid in 71% yield. Afterward cyclodehydrogenation of **3-16** yielded target model compound 9-(4-(4-decylhexadecyl)phenyl)dibenzo[*a,r*]ovalene **3-17** in 81% yield (Fig. 3-3a).

The synthesis of model compound **3-19** could be achieved in four steps (Fig. 3-3b). First, monomer **3-1c** was treated with one equivalent of *n*-butyllithium solution to give a partially debrominated mixture, including mono-brominated, di-brominated, and none-brominated products. This is in contrast to the synthesis of precursor **3-14**, where used two equivalent of *n*-butyllithium to one equivalent of **3-1c**. Then, a *Yamamoto* coupling reaction was performed by using this mixture to give an oligomers mixture, including dimer (**3-18**), trimer, tetramer, etc. Afterwards, the oligomers were subjected to the recycling size exclusion chromatography (SEC) to isolate 7,7'-bis(4-(4-decylhexadecyl)phenyl)-14,14'-diphenyl-2,2'-bibenzo[*m*] tetraphene **3-18** as one of the main products. Once the precursor **3-18** was obtained, the oxidative cyclodehydrogenation was

subsequently carried out to afford crude target model compound **3-19** with a yield of ~67%. The further purification by recycling SEC afforded pure **3-19** for the spectroscopic and microscopic analyses.

The MALDI-TOF MS analysis of model compound **3-15** displayed the exact molecular weight of $m/z = 790.25$, which was consistent with the simulated value of $m/z = 790.54$, attesting the formation of model compound **3-15** (Fig. 3-4, inset). Moreover, the isotopic distribution of **3-15** was in perfect agreement with the simulated pattern, which provided a strong evidence for the highly efficient “graphitization” of precursor **3-14** into model compound **3-15**. Similar to **3-15**, other two model compounds **3-17** and **3-19** exhibited exact molecular weight of $m/z = 938.66$ and 1575.03 , respectively. Their isotopic distributions were also in perfect agreement with the simulated pattern, which indicated the excellent cyclodehydrogenation efficiency (Fig. 3-4, inset). Furthermore, all the model compounds showed no other peak in the MS spectrum, which supported their high purities.

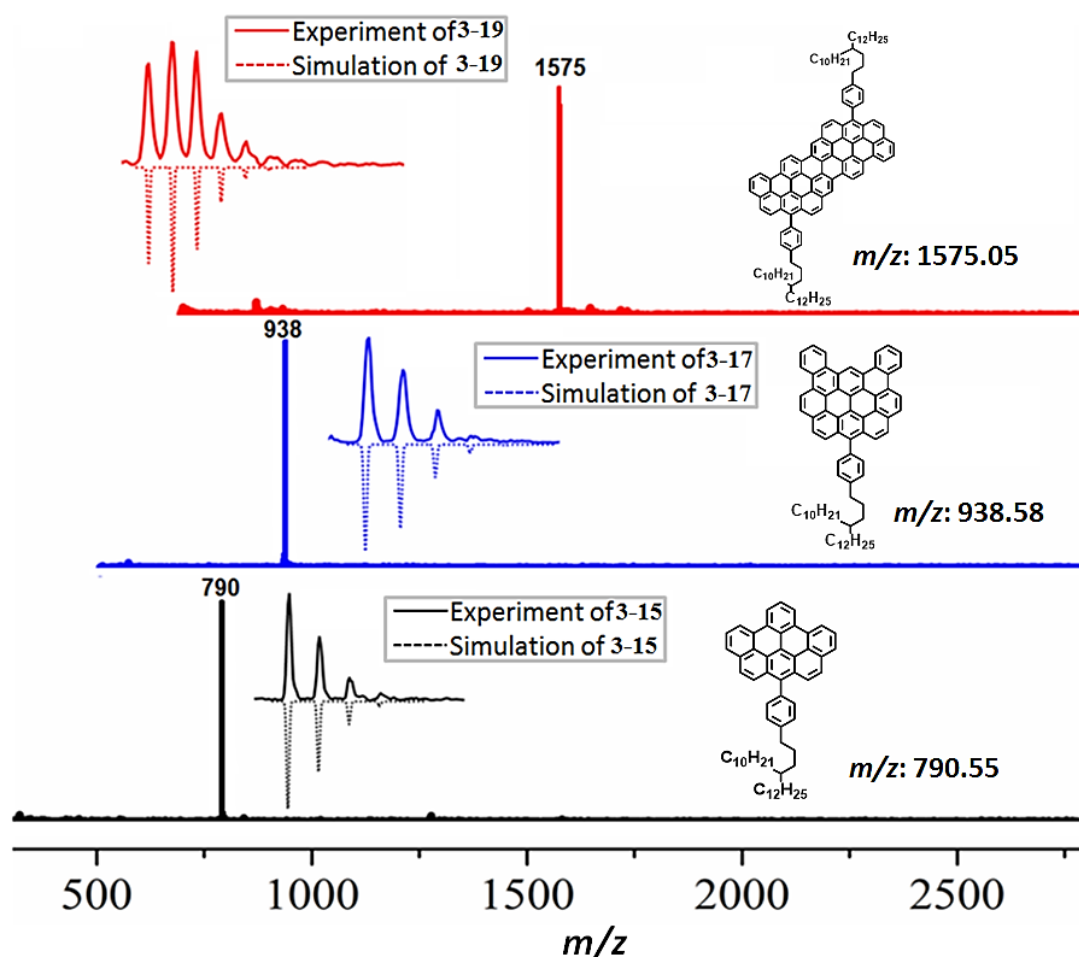


Figure 3-4. Reflectron-mode MALDI-TOF MS analysis of model compounds **3-15**, **3-17**, and **3-19** (solid-state sample preparation, matrix: TCNQ); inset: isotopic distribution obtained by MALDI-TOF MS measurements in perfect agreement with the simulation.

^1H NMR investigations of **3-15** and its precursor **3-14** were carried out as displayed in Fig. 3-5a. Generally, extended PAHs suffer from strong aggregation in solution, which results in broadening of peaks in ^1H NMR spectra.^{12,14} Nevertheless, the well-resolved ^1H NMR spectra of **3-15** and **3-17** could be recorded at room temperature and 393K, respectively. Comparing the ^1H NMR spectra of **3-15** and **3-14**, the signals corresponding to aromatic protons (marked with blue ring) shifted to the lower field (down to $\delta = 9.0$) and the integrations of these aromatic proton signals were in agreement with expected values as well, attesting to the formation of dehydrocyclized compound **3-15**. The reason for the downfield -shift of the aromatic protons signals can be explained by the ring current effect, which resulted from the extended π -conjugation after “planerization”. Similarly, **3-17** and its precursor **3-16** were subjected to ^1H NMR measurement, showing similar shifts of the aromatic proton signals. **3-17** was measured at elevated temperatures using high-boiling-point solvents, namely at 393 K in 1,1,2,2-tetrachloroethane- d_2 , which enabled the observation of weak peaks in the aromatic region despite the stronger aggregation of the extended aromatic system. Notably, the signals of the aromatic protons on **3-16** and **3-17** marked with red ring displayed a strong down-shift (down to $\delta = 10.4$) after cyclodehydrogenation.

Afterwards, the 2D ^1H - ^1H COSY NMR spectra of **3-15** and **3-17** were investigated, in order to further prove their high purities as well as to give clear assignments of aliphatic and aromatic protons on these two compounds. As displayed in Fig. 3-6a and b, the 2D ^1H - ^1H COSY NMR spectra of **3-15** and **3-17** were recorded in dichloromethane- d_2 at 25 °C and 1,1,2,2-tetrachloroethane- d_2 at 393K, respectively. With the help of the 2D COSY NMR spectra and intensities of the above 1D ^1H NMR spectra, the protons of **3-15** and **3-17** can be finally assigned as shown in Fig. 3-6c and d, which further verified the successful synthesis of these two PAH molecules.

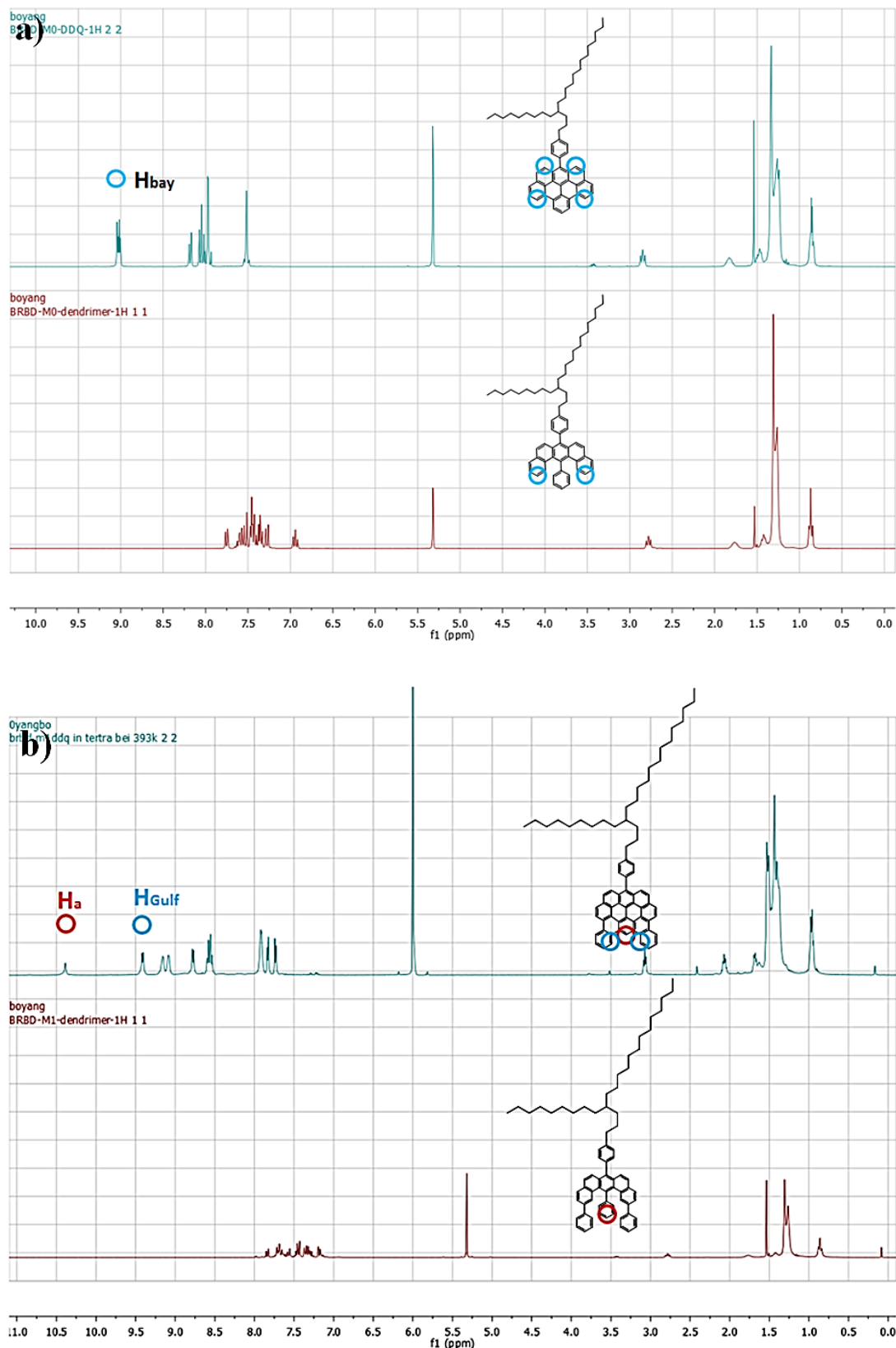
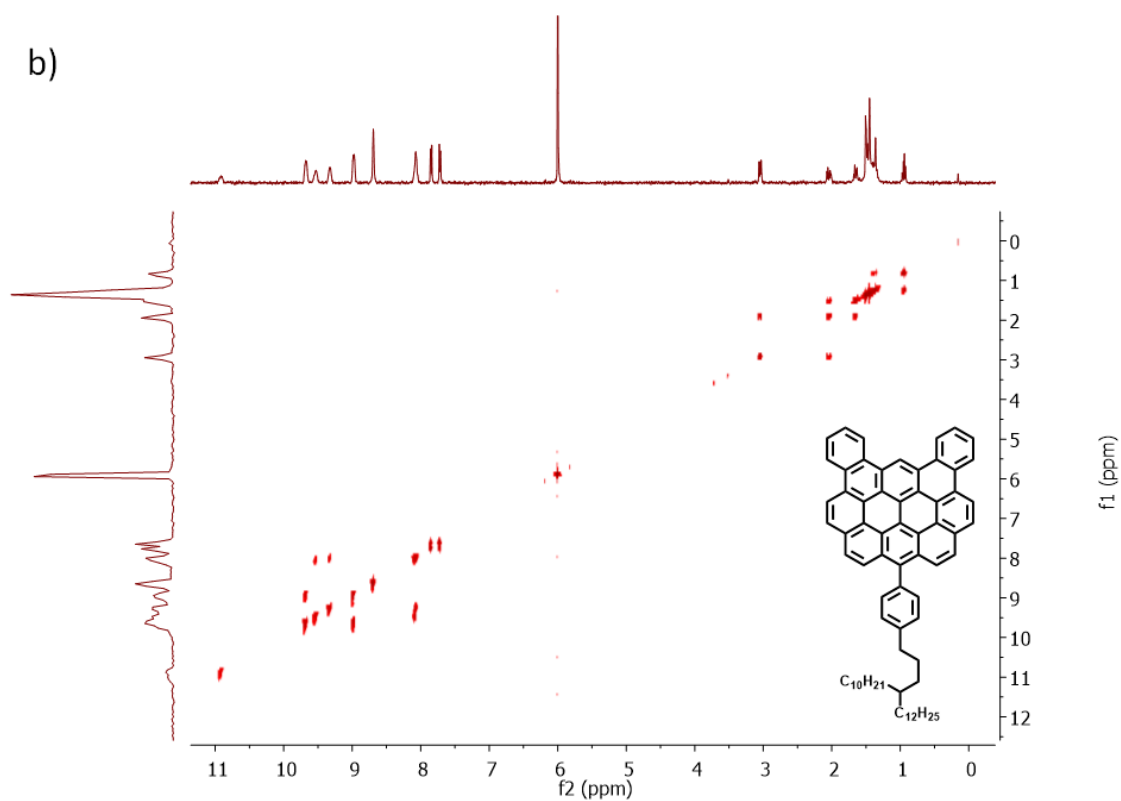
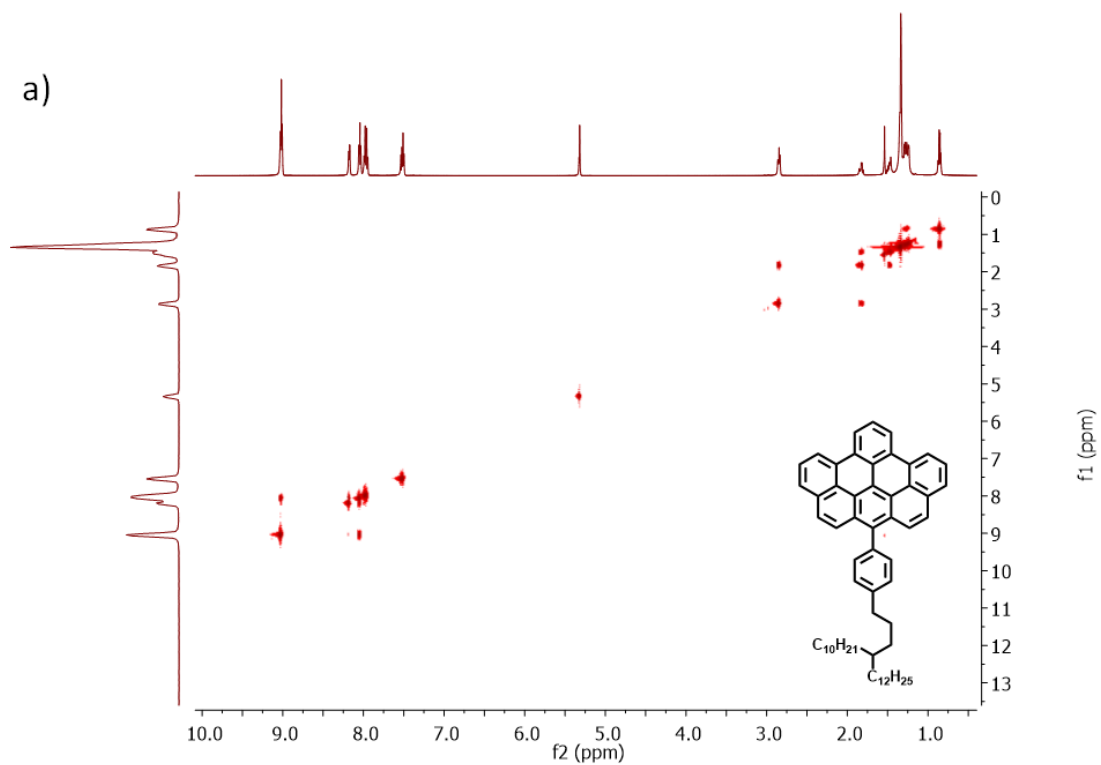


Figure 3-5. ^1H NMR spectrum of a) **3-15** (up) and its precursor **3-14** (down) in dichloromethane- d_2 at room temperature (250 MHz); inset: the aromatic protons and their corresponding signals in the spectrum, which were marked with blue rings; b) **3-17** (up) in 1,1,2,2-tetrachloroethane- d_2 at 393 K (500 MHz) and its

precursor **3-16** (down) in dichloromethane- d_2 at room temperature (250 MHz); inset: the aromatic protons and their corresponding signals in the spectrum, which were marked with blue and red rings.



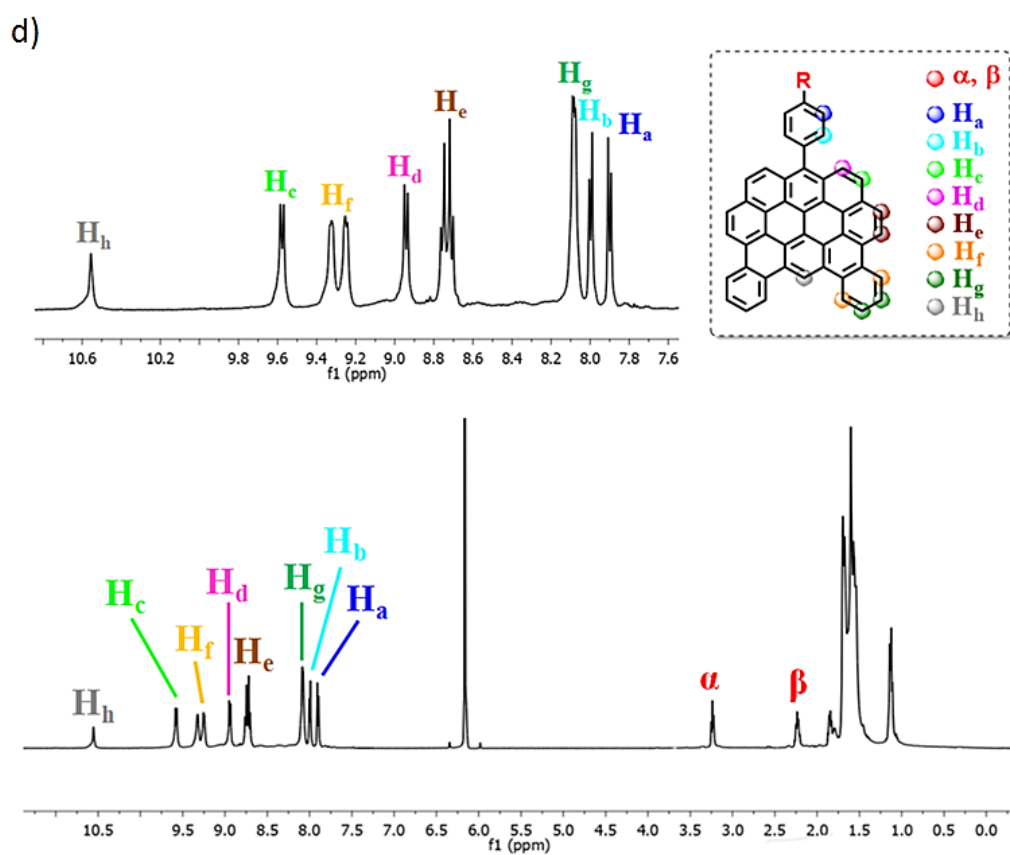
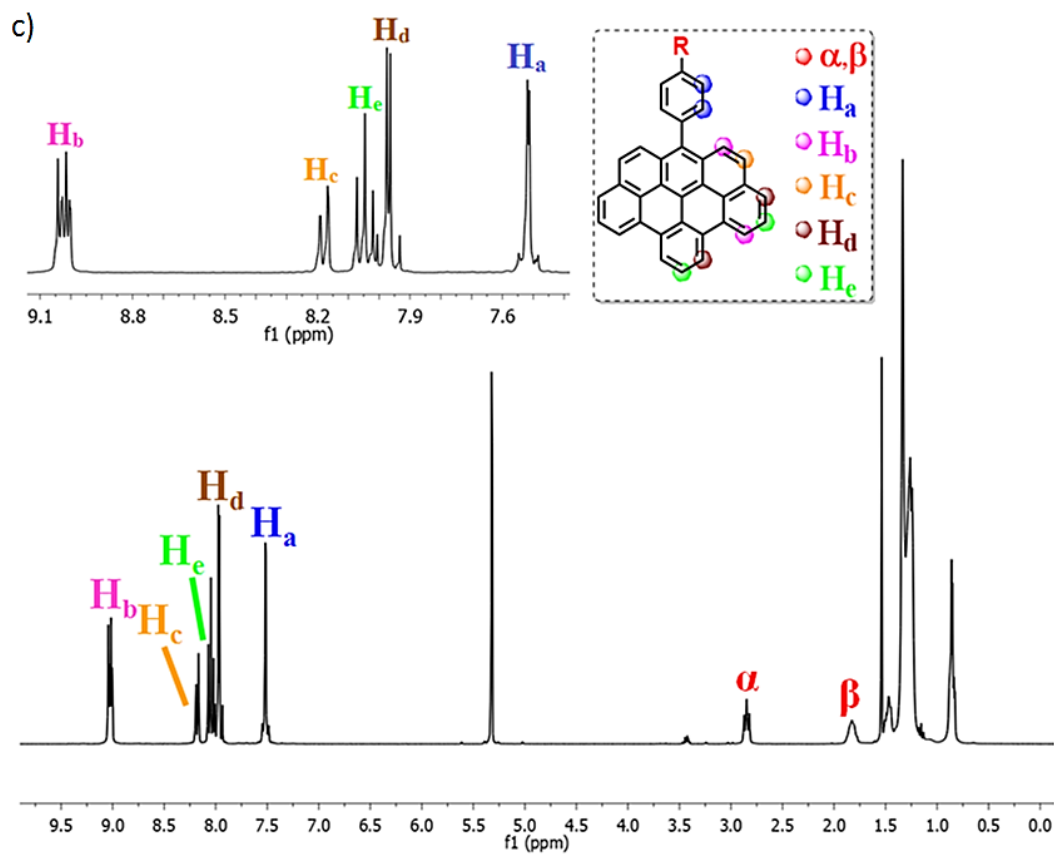


Figure 3-6. The 2D ^1H - ^1H NMR spectra of **a)** **3-15** in dichloromethane- d_2 at 25 °C and **b)** **3-17** in 1,1,2,2-tetrachloroethane- d_2 at 393K. **c)** and **d)** the 1D ^1H NMR spectra of **3-15** and **3-17** with the assignment of aliphatic and aromatic protons (inset).

The 1D ^1H NMR spectra of **3-19** and its precursor **3-18** were also studied. Comparing to **3-17**, the resolution of signals in the aromatic region was decreased, which can be ascribed to the further extension of π -conjugated system. The signals of the aromatic protons marked with green ring were also shifted down-field (down to $\delta = 9.5$), which was similar to the other two smaller PAHs (Fig. 3-7). The aliphatic and aromatic protons of **3-19** could be integrated as well and consisted with expected values. The 2D ^1H - ^1H COSY NMR spectra of **3-19** could not be obtained with enough resolution at elevated temperature due to the extended π -conjugation compared with **3-15** and **3-17**.

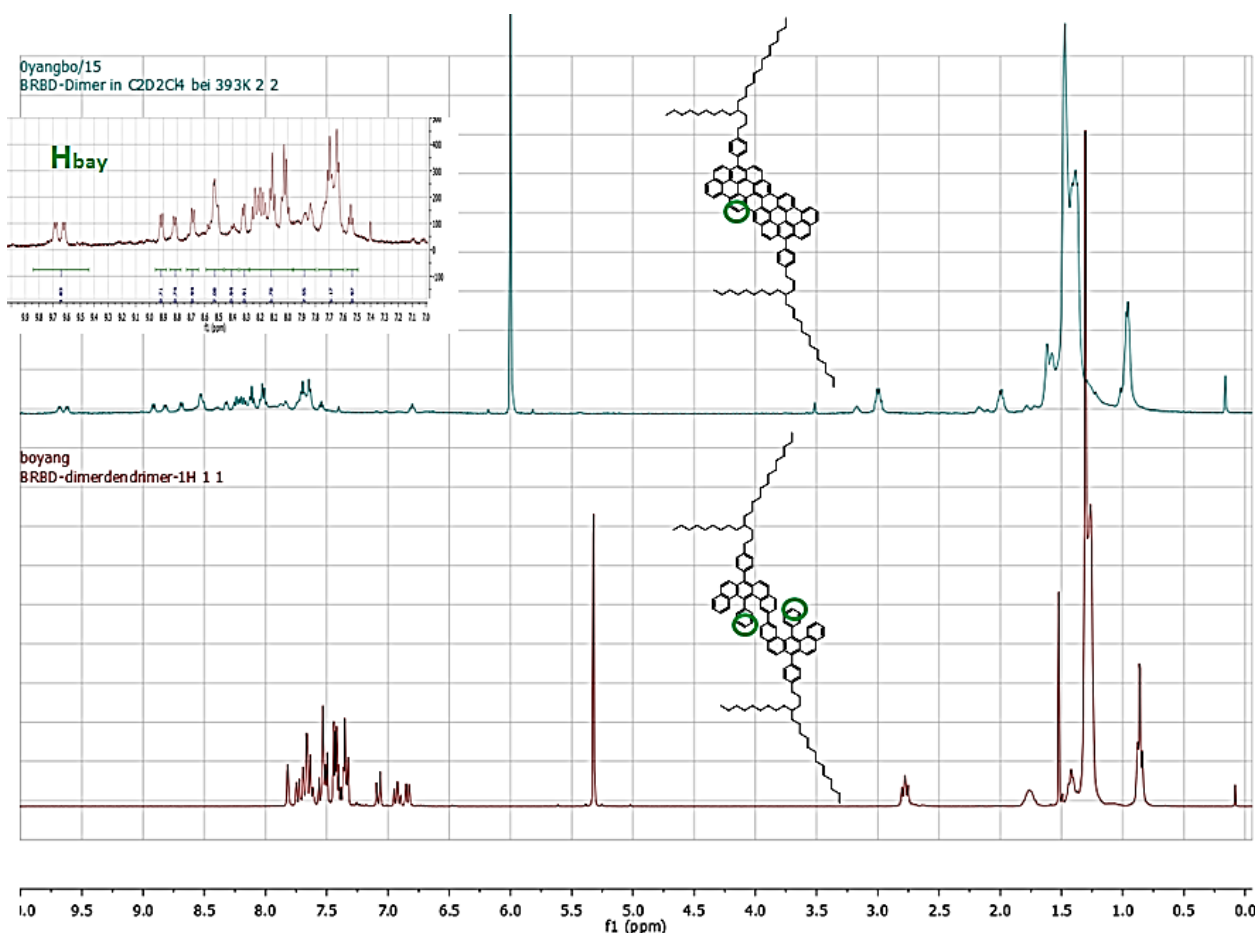


Figure 3-7. ^1H NMR spectrum of **3-19** (up) in 1,1,2,2-tetrachloroethane- d_2 at 393 K (500 MHz) and its precursor **3-18** (down) in dichloromethane- d_2 at room temperature (250 MHz); inset: the aromatic protons and their corresponding signals in the spectrum which were marked with green rings, as well as magnified spectrum of the aromatic region of **3-19**.

In order to further prove the purities of the three PAH molecules (**3-15**, **3-17**, and **3-19**), their UV-Vis absorption and emission spectra were first measured. Afterwards, the excitation spectra were measured at the maxima of their emission spectra. In general, the UV-Vis absorption spectra of PAH molecules are in good agreement with their excitation spectra. And their excitation spectra are more sensitive to their chemical structures. Thus, by comparing the UV-Vis and their corresponding excitation spectra, we can examine the purities of **3-15**, **3-17**, and **3-19**. As displayed in Fig. 3-8, the UV-Vis spectra and corresponding excitation spectra of above PAHs were compared. It appeared that all UV-Vis spectrums were highly consistent with corresponding excitation spectra, which further validated the high purities of three PAHs.

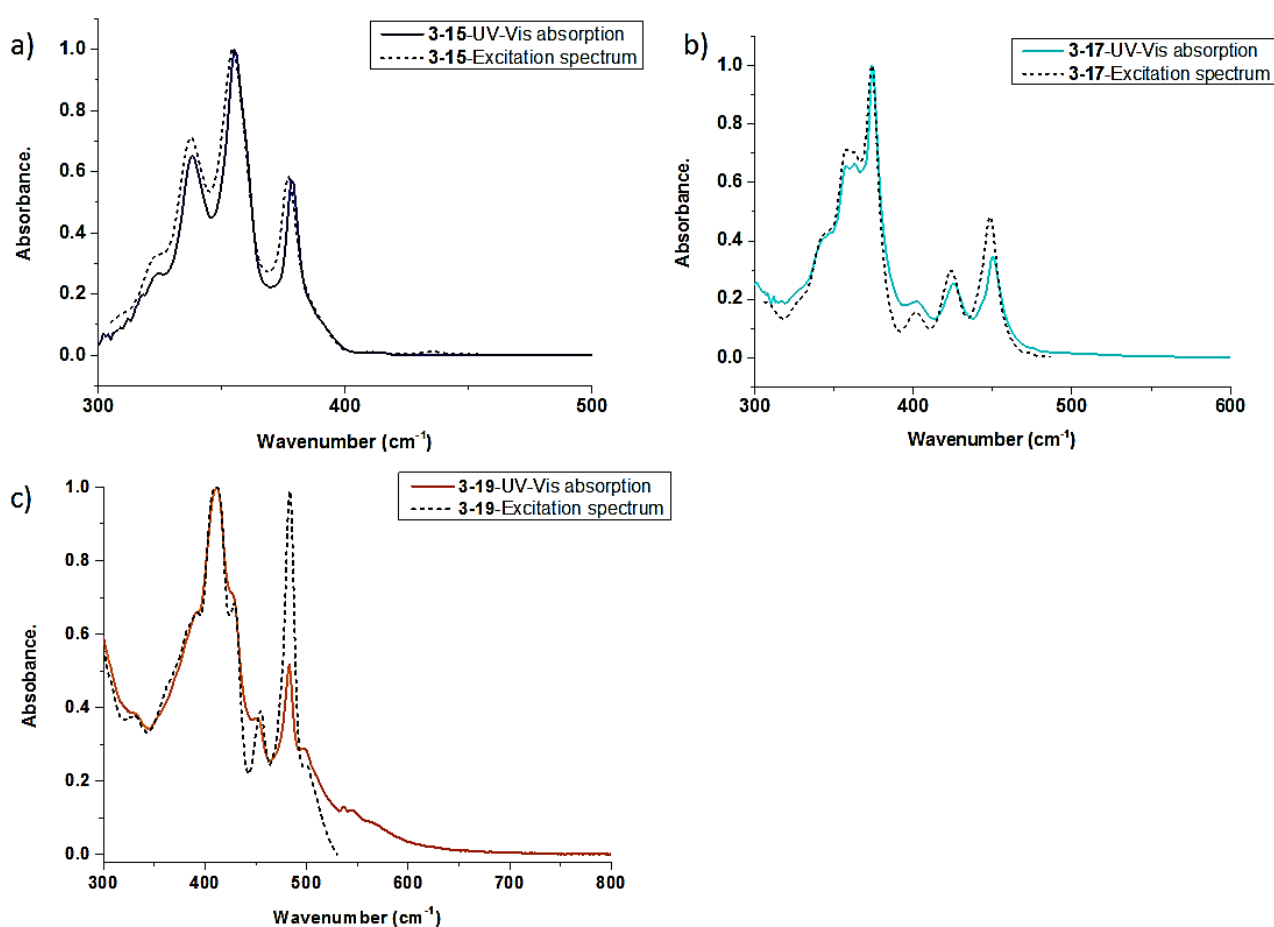


Figure 3-8. Comparison of UV-Vis absorption spectra and corresponded excitation spectra of PAH molecules **3-15**, **3-17**, and **3-19**.

Moreover, three model PAHs have been characterized by HR-APPI MS as well (see chapter 7). Considering all above characterizations, we can claim that **3-15**, **3-17**, and **3-19** were synthesized successfully with high purities.

employed for the *Yamamoto* polymerization to obtain polymer precursor **3-2c** with good solubility in common organic solvents. Precursor **3-2c** could thus be characterized not only by MALDI-TOF MS (Fig. 3-8d) but also by solution-state NMR, UV–Vis absorption spectroscopy, and SEC analysis. Moreover, precursor **3-2c** could be fractionated with recycling preparative SEC to obtain high-molecular-weight fractions free of smaller oligomers (see the section 3.2.5).

The *Yamamoto* polymerization of monomer **3-1c** was performed with two different procedures, namely, by heating at 80 °C in an oil bath for 3 days and by stirring under microwave irradiation at 120 °C for 24 h to yield polymer precursors **3-2c-I** and **3-2c-II**, respectively.

3.2.4 MALDI-TOF MS analysis of polymer precursors 3-2a~c

MALDI-TOF MS analysis in linear mode of the obtained polymer precursor **3-2a** showed regular peaks from $m/z = \sim 1200$ up to $\sim 15,000$ with an interval of $m/z = \sim 427$, corresponding to the mass of one repeating unit, i.e. 428 (Fig. 3-10a). Polymers with molecular weight higher than 15,000 g/mol were not detected owing to the limitation of MALDI-TOF MS for the analysis of high-molecular-weight polymers with broad molecular weight distribution. The reflectron-mode MALDI-TOF MS analysis of precursor **3-2a** was performed as well, which showed peaks of oligomers with higher resolution, i.e. trimer, tetramer, pentamer, hexamer, heptamer, and octamer at $m/z = 1,286, 1,715, 2,143, 2,572, 3,001, \text{ and } 3,429$, respectively (Fig. 3-10b). These values are in perfect agreement with the calculated molecular weights of oligomers from the trimer to the octamer. The polymer precursors **3-2b** and **3-2c** were subjected to MALDI-TOF MS analysis, and the resulting mass spectra displayed regular peaks as well. The mass spectra of **3-2b** and **3-2c** displayed an interval of $m/z = \sim 484$ and ~ 792 , respectively (Fig. 3-10c and 3-10d). Besides, no other peak was observed except for those expected for the oligomers in all spectra, indicating the successful formation of polymer precursors **3-2a~c** with high purity.

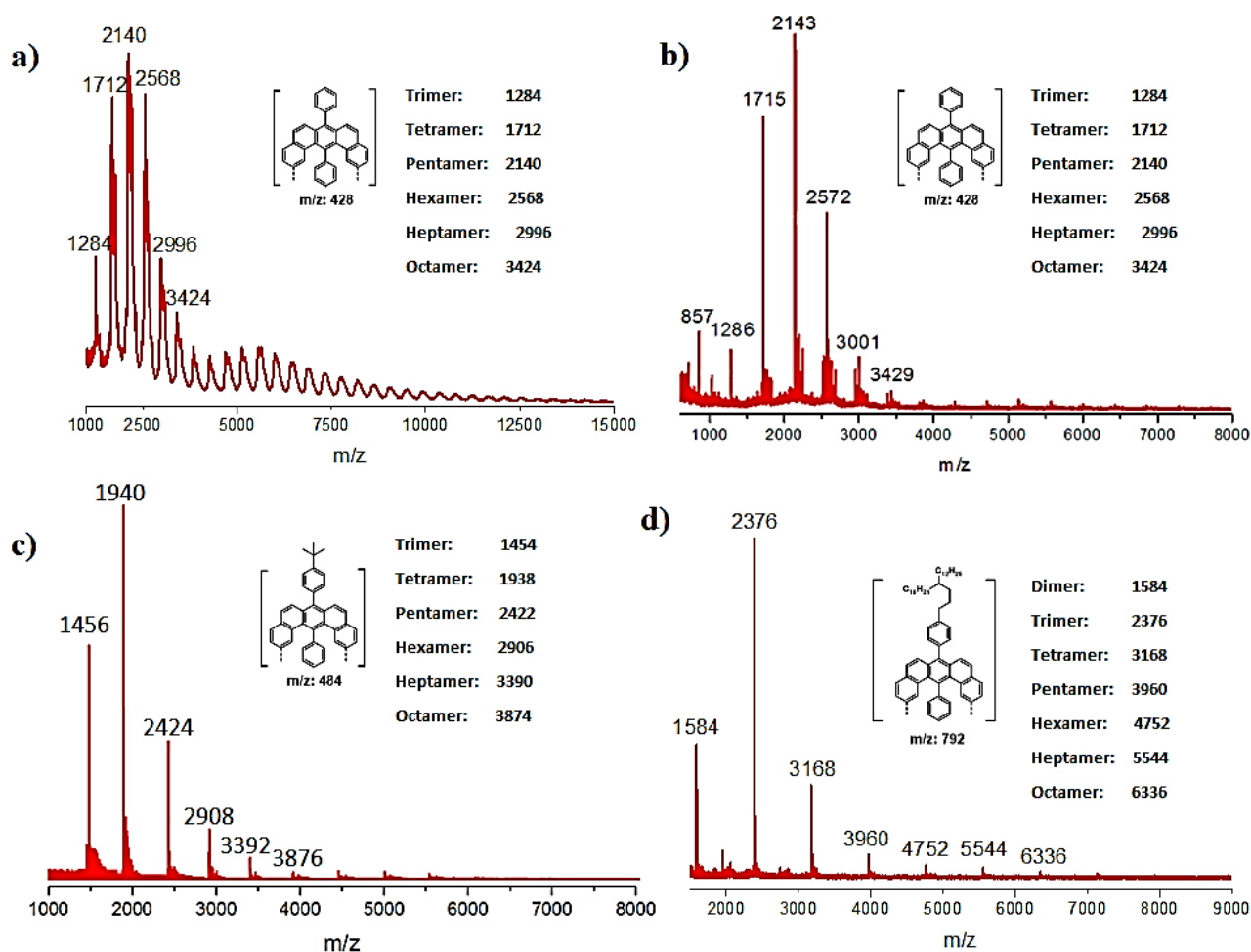


Figure 3-10. a) Linear-mode and b) reflectron-mode MALDI-TOF MS analysis of polymer precursor **3-2a**; c) Reflectron-mode MALDI-TOF MS analysis of polymer precursor **3-2b**; d) Reflectron-mode MALDI-TOF MS analysis of polymer precursor **3-2c-I** (solid-state sample preparation, matrix: TCNQ), inset: calculated m/z of oligomers.

3.2.5 Fractionation and SEC analysis of precursor 3-2c

As demonstrated above, both polymerization methods, including normal heating at 80 °C in an oil-bath and microwave-assisted heating at 120 °C, could generate the polymerized product successfully. In order to compare the efficiency of the two polymerization procedures, we performed the polymerization with both methods and analyzed the resulting polymers **3-2c-I** and **3-2c-II** using SEC.

SEC profiles of polymer precursor **3-2c-I** displayed two main peaks at retention time of ~22.5 and ~27 min (Fig. 3-11a). On the other hand, the SEC profile of polymer precursor **3-2c-II** showed a similar curve (Fig. 3-11c), which exhibited two main peaks at retention time of ~23 and ~26 min. Here, the former peak with retention time spanning from ~20 to ~25 min corresponded to the polymers with higher molecular weight, and the latter peak with retention time spanning from ~25 to ~30 min to the oligomers with molecular weight lower than 6,000 g mol⁻¹.

The curd polymer precursor **3-2c-I** was separated into two fractions by utilizing recycling preparative SEC, and the fraction of larger molecular weight was named as **3-2c-I'**. The SEC analysis of precursor **3-2c-I'** indicated the weigh-average molecular weight (M_w) of 42,000–92,000 g mol⁻¹ and polydispersity index (PDI) of 2.3–4.0, against poly(*para*-phenylene) (PPP) and polystyrene (PS) standards, after removal of the small oligomers (Table 3-1, entry 1'; Fig. 3-11b). According to the previously reported solution-mediated synthesis of GNRs^{10,11}, the absolute M_w measured by laser light scattering analysis (a technique for particle size analysis from 1 nm to 10 μm in highly diluted suspensions based on dynamic and static light scattering) was between the estimated values from the SEC analysis against PS and PPP standards. This could be explained by the fact that the polymer precursors in our case have a more rigid backbone structure than polystyrene, but less rigid backbone structure than poly(*para*-phenylene). Thus, the absolute M_w value of polymer precursor **3-2c** should be between the estimated values according to SEC analysis against PS and PPP standards. Regarding the above explanation, molecular weight values based on SEC analysis are only estimations based on PPP and PS standards; they are useful for comparing the size of similar polymers and have proven to provide good approximation of the absolute values for previously reported GNR precursor.^{7,10,14-16} On the other hand, precursor **3-2c-II'** showed M_w of 66,000–184,000 g mol⁻¹ and PDI of 1.5-1.9, based on the SEC analysis, after removal of the smaller oligomers (Table 3-1, entry 2'; Fig. 3-11d). These results indicated that the use of microwave can enhance the efficiency of the *Yamamoto* polymerization to afford precursor **3-2c** with higher M_w values.

Table 3-1. Polymerization conditions for monomer **3-1c** and resulting molecular weights and PDI values of polyphenylene precursors **3-2c**.

Entry	Name	Conditions	Time (h)	M_w (kg/mol)	M_n (kg/mol)	PDI
1	3-2c-I	80 °C, oil bath	72	29-32	10-14	3.2-4.6
1'	3-2c-I'	—	—	42-92	18-23	2.3-4.0
2	3-2c-II	120 °C, Microwave	24	55-110	16-26	3.4-4.2
2'	3-2c-II'	—	—	66-184	44-97	1.5-1.9

M_w and M_n were estimated by the SEC analysis based on PPP and PS standards and given with ranges, corresponding to $M_{w, PPP}$ - $M_{w, PS}$ and $M_{n, PPP}$ - $M_{n, PS}$, respectively (eluent: THF, UV detector). PDI values were calculated by M_w/M_n . Entries 1' and 2' represent M_w , M_n , and PDI obtained after the fractionation of precursor **3-2c-I** and **3-2c-II** in entries 1 and 2, respectively. All the SEC results have a margin of error of $\pm 10\%$. M_w : weight-average molecular weight; M_n : number-average molecular weight.

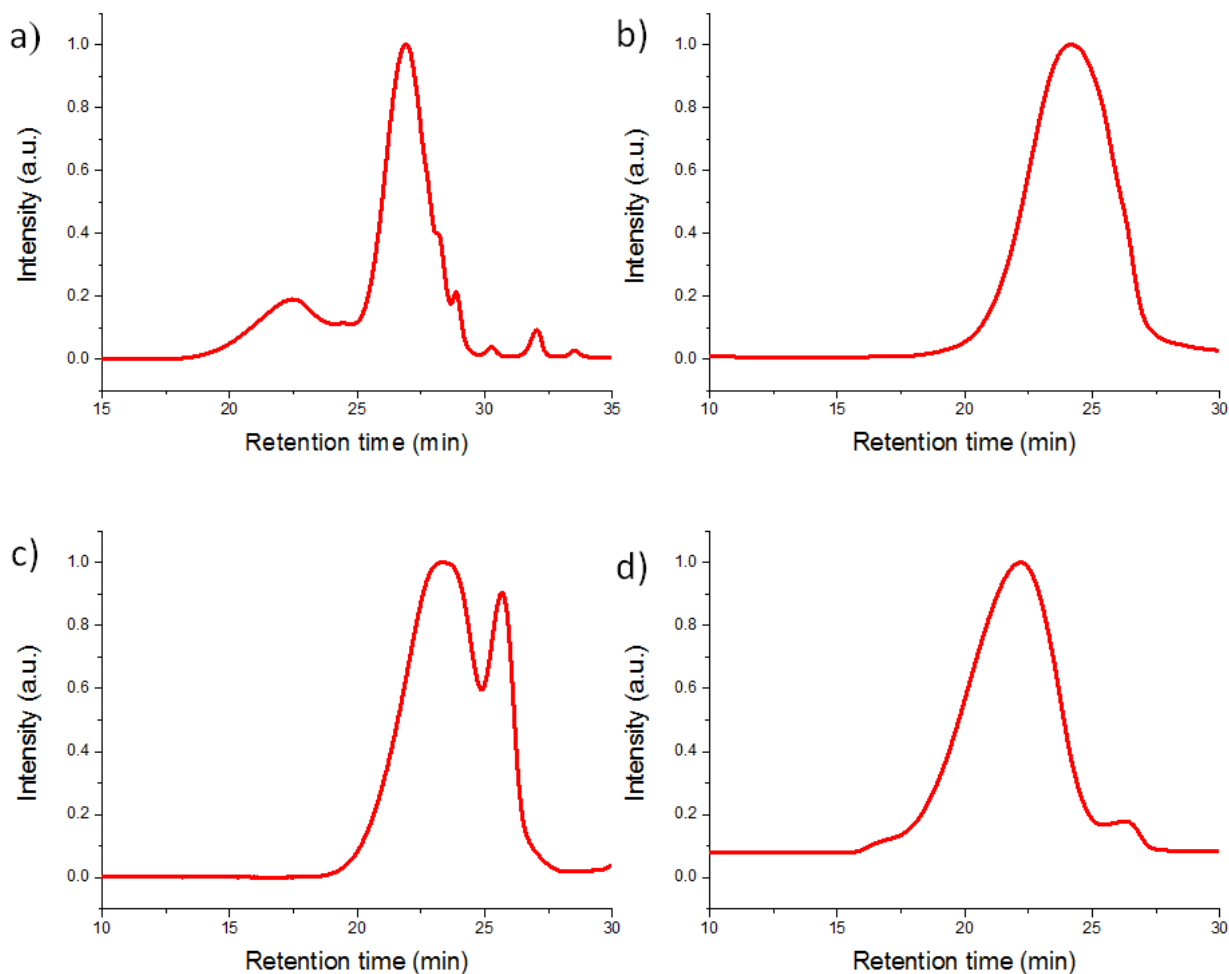


Figure 3-11. Normalized SEC profiles of polymer precursors (eluent: THF, 1 mL/min, UV-detector). a) **3-2c-I**, b) **3-2c-I'**, c) **3-2c-II**, and d) **3-2c-II'**.

Moreover, the UV-Vis absorption spectra of monomers **3-1a** and **3-1c**, polymer precursors **3-2a**, **3-2c-I** and **3-2c-II** were measured and compared as displayed in Fig. 3-12. For monomers **3-1a** and **3-1c**, they showed the same spectra due to the same skeleton structure. The UV-Vis spectra of polymer **3-2a** showed a broad absorption peak, which can be explained by its stronger aggregation effect of polymers due to the lack of bulky substituents. Compared with the spectra of **3-2c-I** and **3-2c-II**, the absorption maximum of the latter slightly red-shifted due to the relatively longer conjugated repeating units compared to that of the former.

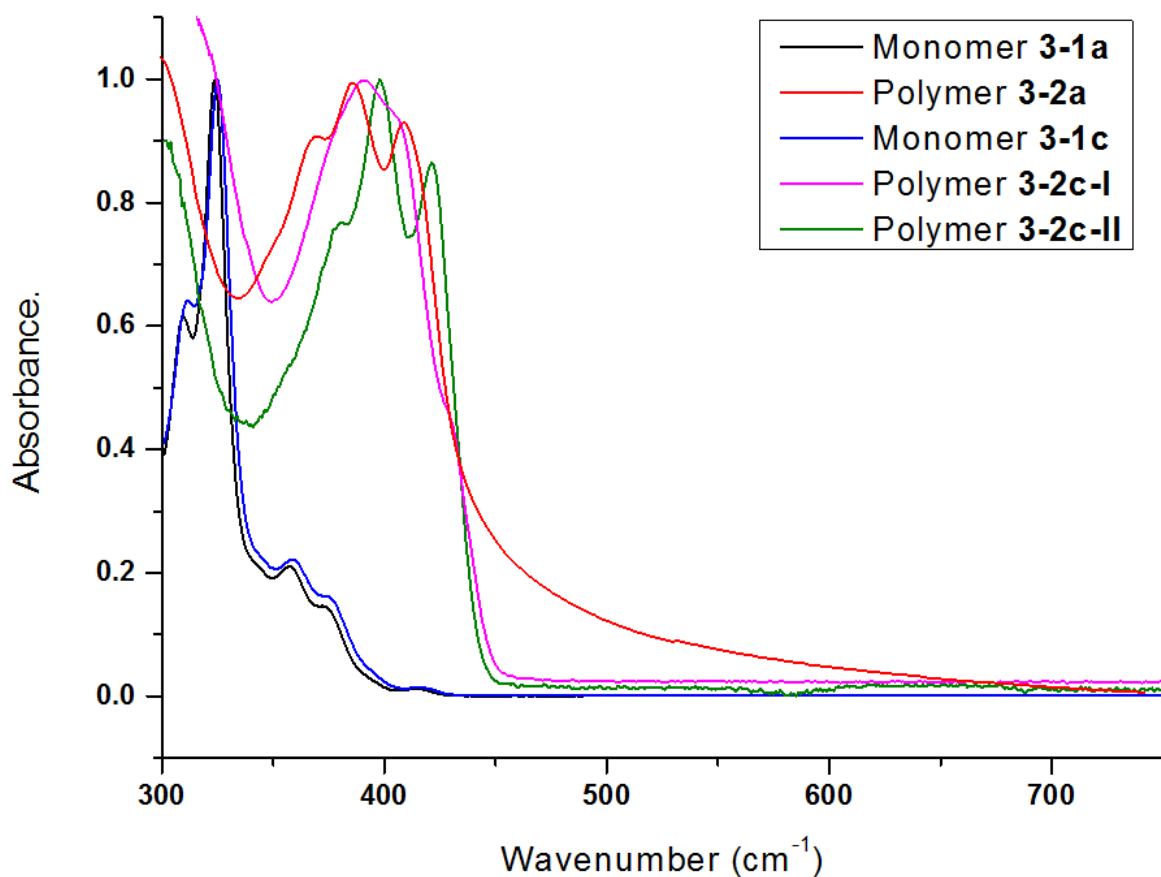


Figure 3-12. Comparison of UV-Vis spectra of monomer **3-1a** and **3-1c**, polymers **3-2a**, **3-2c-I'** and **3-2c-II'**.

3.2.6 Graphitization towards GNR

Subsequently, polymer precursors **3-2c-I'** and **3-2c-II'** were “graphitized” into GNRs **3-3c-I'** and **3-3c-II'**, respectively, by intramolecular oxidative cyclodehydrogenation. As mentioned in section 3.2.2, there were three synthetic procedures, namely FeCl_3 , $\text{Cu}(\text{OTf})_2/\text{AlCl}_3$, and DDQ/TFA procedures applied for the cyclodehydrogenation of model PAH molecules. All the three procedures successfully gave the desired products. The latter procedure (DDQ/TFA) yielded extra oxidative side products, which could be easily removed by column chromatography. For the cyclodehydrogenation of GNRs system, the latter method was not applicable because the further oxidative side reaction could disrupt the GNR structures and couldn't be removed via normal purification procedure. Thus, the former two methods were employed for the cyclodehydrogenation of precursor **3-2c-I'**, namely by using FeCl_3 (condition 1) and combination of $\text{Cu}(\text{OTf})_2/\text{AlCl}_3$ (condition 2). Both conditions were carried out by stirring at room temperature for 3 days, which afforded GNR **3-3c-I' (Fe)** and GNR **3-3c-I' (Cu)** through conditions 1 and 2, respectively. As already known, the cyclodehydrogenation of

large NGs usually takes long time (> 1 day). Thus, a longer time was needed for GNR preserving larger conjugated system. In our work, precursor **3-2c-I'** was subjected to the cyclodehydrogenation for 3 days with 7 equivalents of iron(III) chloride (condition 1) as well as for 3 days with 5 equivalents of copper (II) triflate and aluminium (III) chloride (condition 2), for one hydrogen to be removed.

In order to compare the efficiency of the “graphitization” under these two conditions, the UV-Vis absorption spectra of the resulting GNR **3-3c-I'** (Fe) and **3-3c-I'** (Cu) were measured and compared as shown in Fig.3-15. The UV-Vis absorption analyses of GNRs **3-3c-I'** (Fe) and **3-3c-I'** (Cu) exhibit a red-shift, i.e. absorption maxima of GNR **3-3c-I'** (Fe) and **3-3c-I'** (Cu) changed from 508 to 556 nm, and the optical band gap value decreased from 1.59 to 1.54 eV (Fig. 3-15), which suggested that the latter was “graphitized” with a higher efficiency than the former, leaving less open C-C bonds. It must be noted that it is highly challenging to unambiguously quantify the degree of the “graphitization” by the available spectroscopic and microscopic methods, and the UV-Vis absorption spectra are useful to qualitatively compare the efficiency of different cyclodehydrogenation conditions.

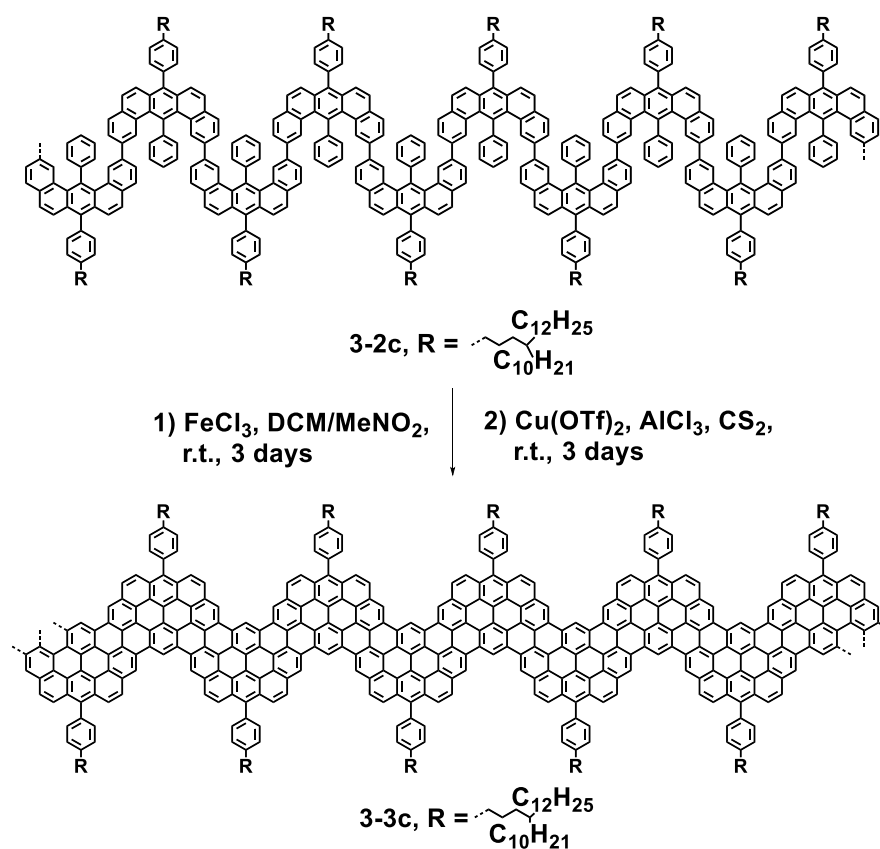


Figure 3-13. Cyclodehydrogenation of polymer precursor **3-2c** into GNR **3-3c**.

Thus, the condition 2 was finally used for the “graphitization” of precursors **3-2c-I'** and **3-2c-II'** into GNR **3-3c-I'** and GNR **3-3c-II'**, respectively. Based on the M_w of polymer precursors **3-2c-I'** (42,000–92,000 g mol⁻¹) and **3-2c-II'** (66,000–184,000 g mol⁻¹), the numbers of repeating units of **3-2c-I'** and **3-2c-II'** were estimated to be 54–117 and 84–233, respectively. Further, we calculated the length of a short segment of GNR **3-2c** with 10 repeating units by Spartan08, which was ~ 7.6 nm. Thus, the average lengths of GNRs **3-3c-I'** and **3-3c-II'** could be estimated by the numbers of repeating units divided by 10, and then multiplied by 7.6 nm to be *ca.* 41–89 and 64–179 nm, respectively. GNR **3-3c-I'** and **3-3c-II'** were identical within the spectra of FTIR, Raman, UV-Vis absorption, indicating they were sufficiently extended to reach the plateau in their properties such as electronic band structure.

3.3 Characterization and analysis

Once the “graphitization” of polymer precursors **3-2c-I'** and **3-2c-II'** was performed and finally yielded GNRs **3-3c-I'** and **3-3c-II'**, respectively, these GNRs as well as model compounds **3-15**, **3-17** and **3-19** were subjected to various of characterizations including UV-vis and PL absorption spectroscopy, cyclic voltammetry (CV) and DFT calculation, fourier transform infrared (FTIR) and Raman spectroscopy, solid-state ¹H and ¹³C NMR spectroscopy, as well as AFM and STM visualization.

3.3.1 UV-vis and PL analysis (model compounds and GNR)

Thanks to the long and branched alkyl chain with a freely rotating phenyl ring attached on the partial zigzag periphery, PAHs **3-15**, **3-17**, and **3-19** could be dissolved in common organic solvents such as THF, toluene, chlorobenzene, and 1,2,4-trichlorobenzene (TCB). GNR **3-3c** also displayed a good dispersibility in THF, TCB, and *N*-methylpyrrolidone (NMP). Mild sonication of GNR **3-3c** in the aforementioned solvents generated purple dispersions. Some of GNR powders remained undispersed, presumably due to declining dispersibility of longer GNRs with stronger aggregation between the extended aromatic cores and/or stronger packing of a part of the GNRs. Nevertheless, such large aggregates could be removed *via* centrifugation or filtration through a syringe filter (pore size: 5 μm), giving dispersions with typical concentrations of approximately 0.03 mg/mL without visible particles. These dispersions were stable, showing no precipitation over 3 weeks, and allowed further spectroscopic characterizations in dispersion as well as their processing from a liquid phase.

UV-Vis absorption and photoluminescence spectroscopic analyses of the model compounds were performed with their solutions in THF (Fig. 3-14a). Model compounds **3-15**, **3-17**, and **3-19** showed distinct bathochromic shift with the increasing size of the π -conjugated aromatic cores, exhibiting the absorption maxima at 355, 374, and 412 nm and optical bandgaps of 3.19, 2.69, and 2.29 eV, respectively, based on the UV-Vis absorption onsets. Additionally, all model compounds **3-15**, **3-17**, and **3-19** displayed photoluminescence (PL), and their PL spectra revealed the emission maxima at 459, 488, and 514 nm with excitation at their absorption peaks. The features of their PL spectra were in agreement with their UV-Vis absorption spectra with an obvious red-shift of the emission maximum (Fig. 3-14a and Table 3-2). On the other hand, the UV-Vis spectrum of GNR **3c-II'(Cu)** in a NMP dispersion revealed an absorption maximum at 556 nm and an optical bandgap of 1.54 eV (Fig. 3-14b). These results indicated that the bandgap decreased with longitudinal extension to reach a plateau at 1.54 eV.

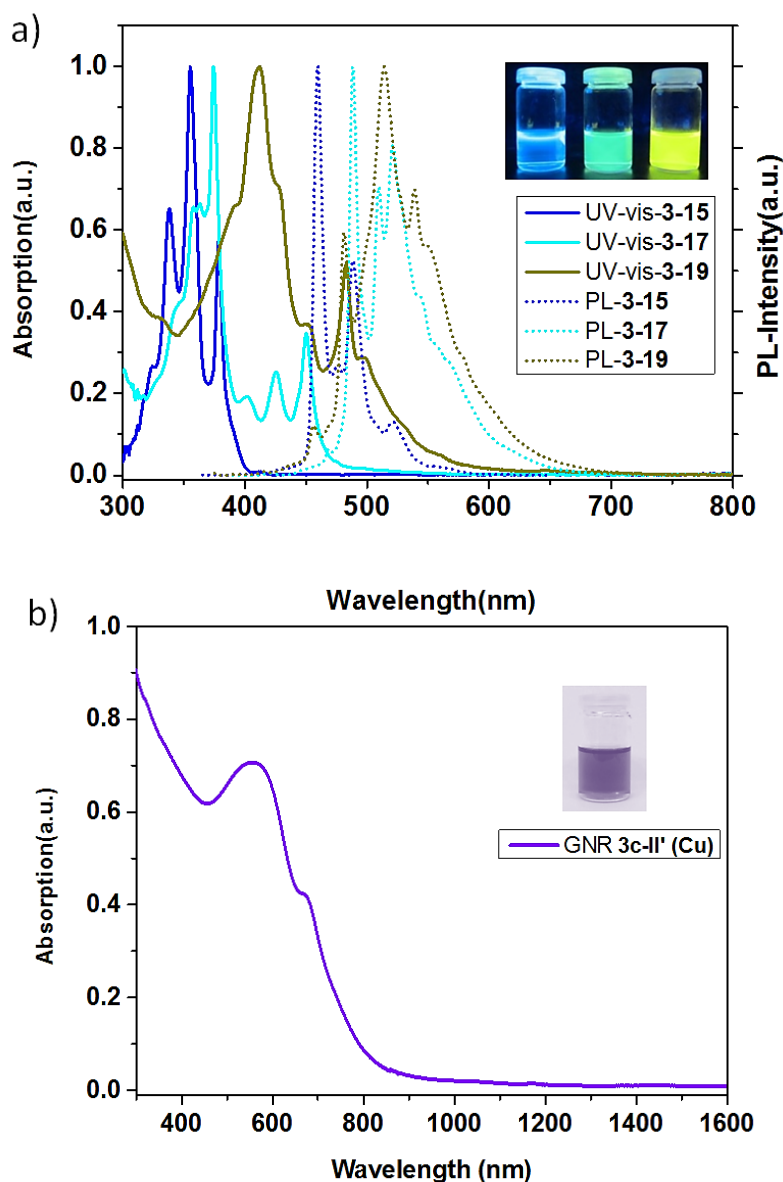


Figure 3-14. UV-vis absorption and photoluminescence (PL) spectra of a) model PAHs **3-15**, **3-17**, and **3-19** (normalized), inset: photographs of PL emitted by **3-15**, **3-17**, and **3-19** in THF solution under 254 nm UV light; b) UV-vis-NIR absorption spectra of partial zigzag GNR **3-3c-II'** (Cu), inset: photograph of dispersion of GNR **3-3c-II'** (Cu) in NMP.

It is worthwhile noting that dispersions of GNR **3-3c** in different solvents (e.g. THF and NMP) displayed basically identical absorption spectra, except for slight shifts of the absorption maximum presumably due to different degree of aggregations. Moreover, the maximum UV-Vis absorptions of GNR **3-3c-I'** (Cu) and GNR **3-3c-II'** (Cu) appeared at 531 and 556 nm, respectively. The optical bandgap calculated according to their absorption edges were 1.53 and 1.54 eV, respectively.

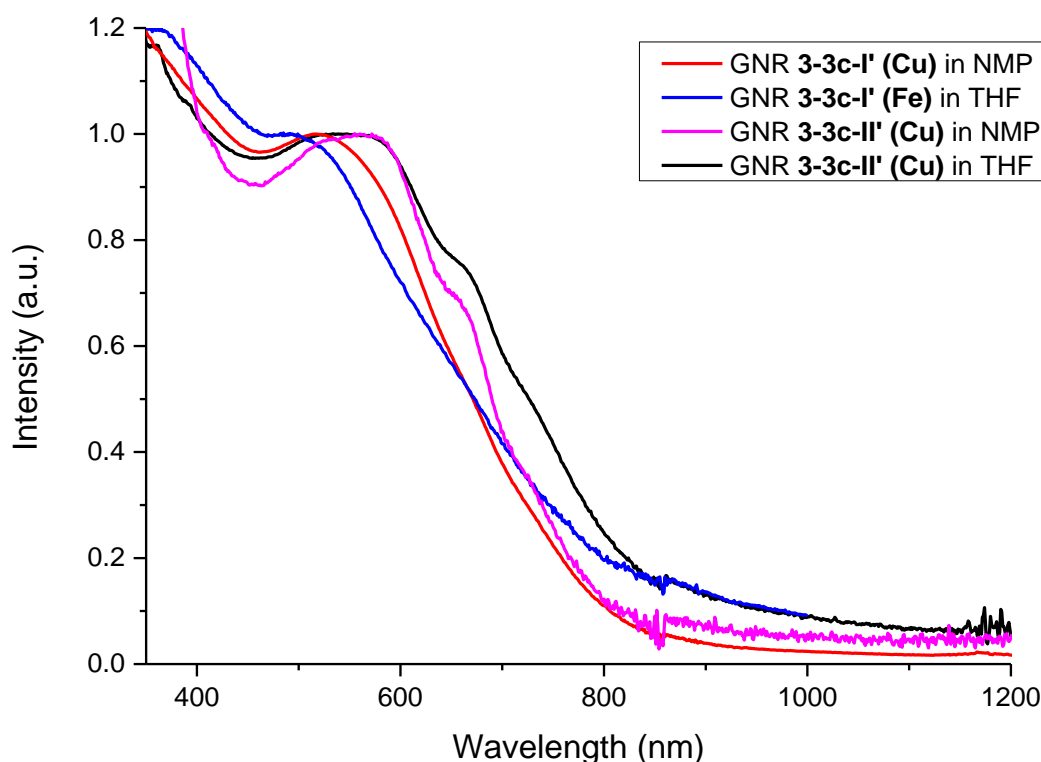


Figure 3-15. UV-vis absorption spectra of GNR **3-3c-I'** and **3-3c-II'** generated via different “graphitization” methods (termed as (Fe) and (Cu)) as well as measured in different solvents (NMP and THF).

3.3.2 Electronic properties analysis and DFT calculation

The HOMO and the LUMO energy levels and HOMO-LUMO gaps of the model compounds (**3-15**~**3-19**) as well as top of the valence band, bottom of the conducting band, and the bandgap of GNR **3-3c** were calculated by our colleague [REDACTED] based on density functional theory (DFT) using B3LYP method (Table 3-2; Fig. 3-16a). The calculated results were compared with experimental results, which were obtained by cyclic voltammetry (CV) (Fig. 3-16b) and optical bandgaps as shown in Table 3-2. The electrochemical potentials of the three model PAHs **3-15**, **3-17**, and **3-19** were investigated by CV in THF solutions (Fig. 3-16b). **3-15** and **3-17** showed one reversible oxidation, while **3-19** exhibited one reversible oxidation as well as one reversible reduction. The HOMO energy levels of **3-15**, **3-17**, and **3-19** were estimated from the onsets of the reversible oxidation peaks to be -5.49 , -5.23 , and -4.98 eV, respectively (Table 3-2). The LUMO energy levels were then calculated from these HOMO levels and the optical bandgaps to be -2.30 , -2.54 , and -2.68 eV for **3-15**, **3-17**, and **3-19**, respectively. The variation trend of electrochemical potentials and optical gaps from **3-15** to GNR **3-3c** was consistent with the estimated values based on DFT calculation. The deviation of the calculated bandgap of GNR **3-3c** from the experimental optical bandgap was relatively larger compared to that of previously prepared GNRs,^{10,11,14} which might be caused by the partial zigzag edge structures. For example, the GNR with hybrid of armchair and gulf type edge structures as well as similar lateral width (~ 1 nm), which was synthesized by our colleague Akimitsu Narita, exhibited a calculated bandgap of 2.04 eV and an optical bandgap of 1.88 eV. Moreover, the bandgap of GNR **3-3c** was also calculated by [REDACTED] based on DFT calculation using different method (local density approximation (LDA)). Comparing with the bandgap value calculated by [REDACTED], the latter value (1.56 eV) showed much better consistency with optical bandgap (1.54 eV) as showed in table 3-2.

Table 3-2. Properties of model compounds and GNR 3-3c

Compounds	λ^{opt}			CV		Cal. ^{h)}		
	$\lambda_{\text{max}}^{\text{abs}}$	$\lambda_{\text{max}}^{\text{emi}}$	$E_{\text{g}}^{\text{opt}}$	E_{HOMO}	E_{LUMO}	$E_{\text{HOMO}}^{\text{cal}}$	$E_{\text{LUMO}}^{\text{cal}}$	$E_{\text{g}}^{\text{cal}}$
	[nm] ^{c)}	[nm] ^{d)}	[eV] ^{e)}	[eV] ^{f)}	[eV] ^{g)}	[eV]	[eV]	[eV]
3-15 ^{a)}	355	459	3.19	-5.4894	-2.2994	-5.2343	-1.5872	3.64 ⁱ⁾
3-17 ^{a)}	374	488	2.69	-5.2254	-2.5354	-4.9670	-1.9006	3.06 ⁱ⁾
3-19 ^{a)}	421	514	2.29	-4.9718	-2.6818	-4.8762	-2.0554	2.82 ⁱ⁾
GNR 3-3c-II ^{b)}	556	-	1.54	-	-	-4.7629 ^{k)}	-2.3179 ^{k)}	2.44 ^{i)/1.56^{j)}}

^{a)}Measured in THF solutions (1×10^{-6} M); ^{b)}Measured in NMP solution; ^{c)}Maximum absorption of UV-vis-NIR spectra; ^{d)}Maximum emission of photoluminescence spectra; ^{e)}Optical bandgaps estimated from the solution absorption edge onset; ^{f)}Energy levels determined by cyclic voltammetry (CV) measurements (see details in Fig.3-16b) and E_{HOMO} was estimated from the CV curve onset; ^{g)} $E_{\text{LUMO}} = E_{\text{HOMO}} + E_{\text{g}}^{\text{opt}}$; ^{h)}Energy levels and calculated electronic bandgaps ($E_{\text{g}}^{\text{cal}}$) estimated according to density functional theory (DFT) (see details in Fig.3-16a); Energy bandgaps i), calculated by [REDACTED]; j) calculated by [REDACTED]. k) Energy levels by computational calculation.

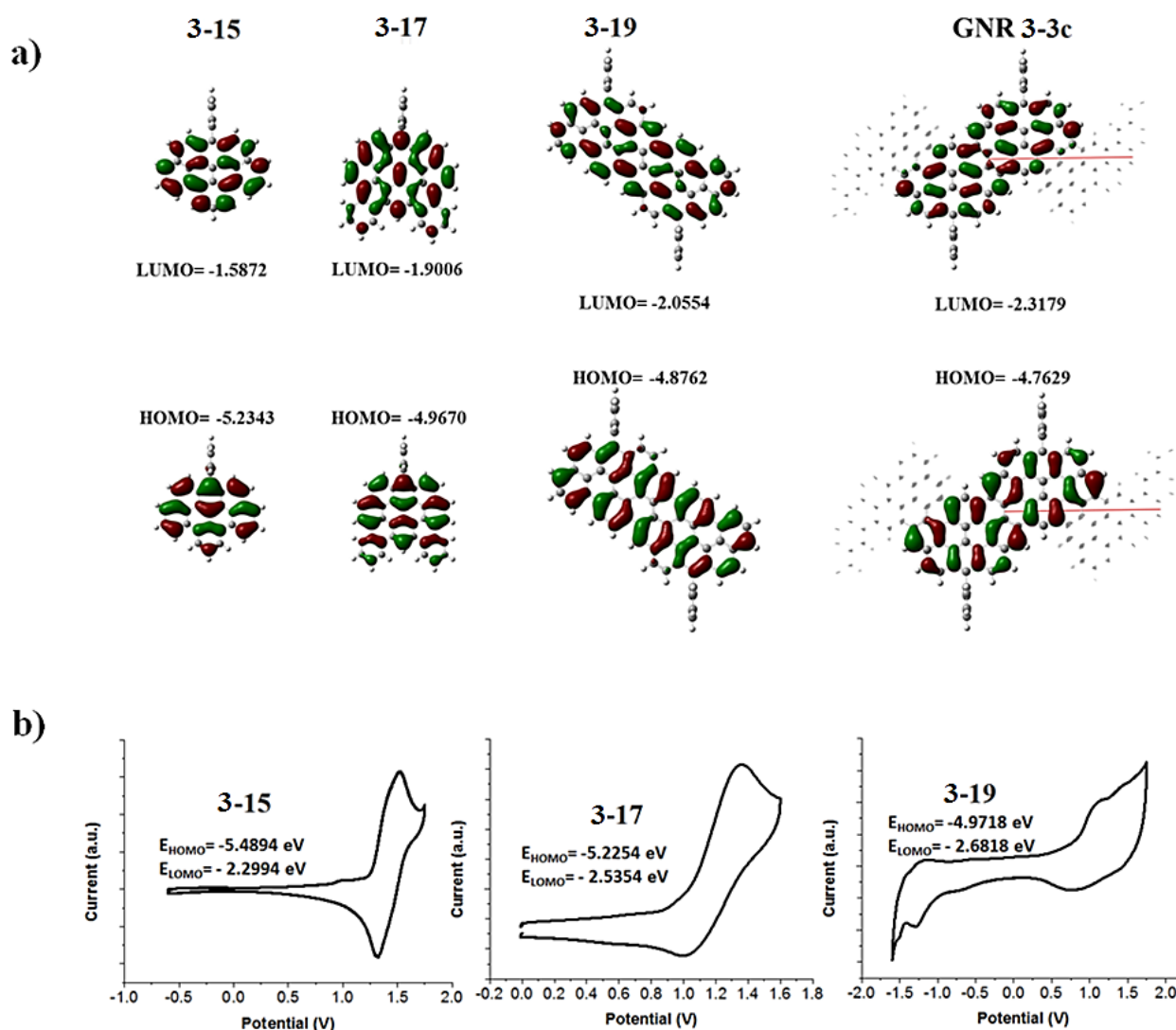


Figure 3-16. a) Density functional theory (DFT) (B3LYP method) calculated HOMOs and LUMOs of model compounds **3-15**, **3-17**, and **3-19** as well as GNR **3-3c** (without alkyl chain); b) Cyclic voltammograms of the model compounds measured in a DCM solution of Bu_4NPF_6 (0.1 M) at a scan rate of 50 mV/s at room temperature. The HOMO and LUMO energy levels were estimated based on the onset potentials and the empirical formulas $E_{\text{HOMO}} = -(E_{\text{ox}}^{\text{onset}} + 4.8 - E_{\text{Fc}/\text{Fc}^+}^{\text{onset}})$ eV and $E_{\text{LUMO}} = E_{\text{HOMO}} + E_{\text{g}}^{\text{opt}}$ (optical bandgap).

3.3.3 Raman and FTIR spectroscopy

The Raman spectroscopy has been intensely employed for the characterization of graphite,^{17,18} graphene,^{17,19-23} CNTs^{19,23} and GNRs^{17,22-24} to check their quality, structural definition, and uniformity. In this work, the Raman spectroscopic characterization of **3-15** and **3-17** as well as GNR **3-3c-I'** was performed by our collaborators [REDACTED] and [REDACTED] at Politecnico

di Milano (Fig. 3-17b). The Raman spectra of above samples were measured directly on a powder sample on silica wafer substrate with excitation wavelength of 1064 nm (model compounds) and 514 nm (GNR).

The Raman spectra of graphene and GNRs are dominated by the characteristic features associated to collective C-C stretching vibrations of the honeycomb structure, which are named G and D band.^{20,25,26} The Raman spectra of **3-15**, **3-17** and GNR **3-3c-I'** synthesized in this work are characterized by these specific peaks (Fig. 3-17 and 3-18).

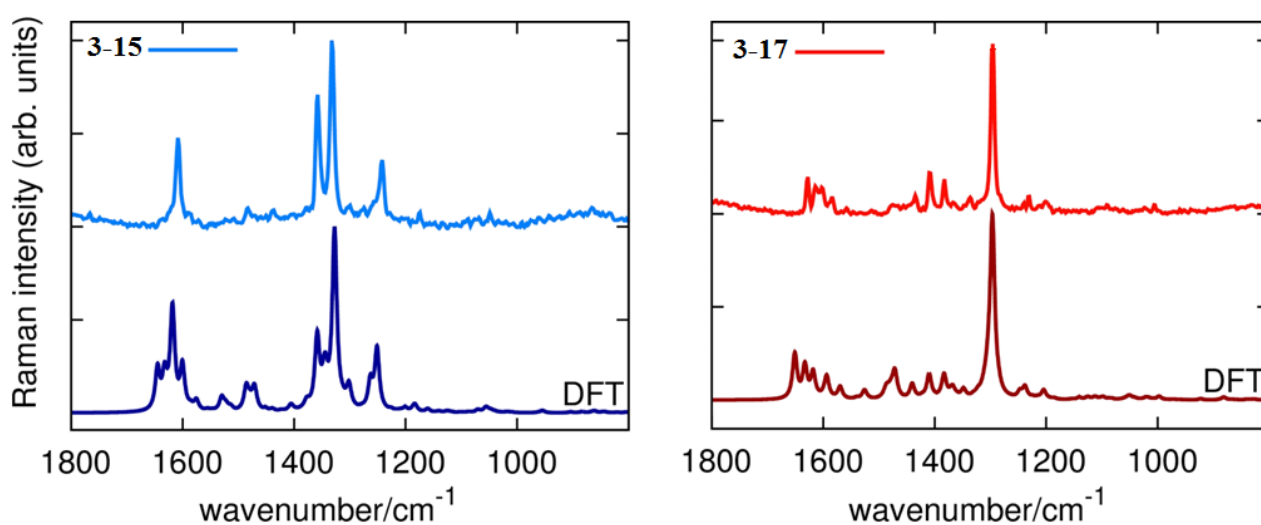


Figure 3-17. Experimental (top traces with light blue and red color) and Simulated (bottom traces with deep blue and brown color, frequency scaled by 0.98) FT-Raman spectra of **3-15** and **3-17** (1064 nm excitation).

DFT calculations on **3-15** and **3-17** allowed the identification of all minor features, which involve different normal modes related with collective breathing modes (D features) and ring stretching modes (G features). The multiplicity of D and G signals is a typical feature of PAHs and it is due to the coupling of characteristic collective C-C stretching coordinates with the in-plane C-H bending vibrations at the edge of the molecule.²⁷ Even though it is difficult to identify specific edge markers, i.e., peaks originating from specific edge structures, it is clear from the comparison of the Raman spectra of **3-15** and **3-17** that the manifold of peaks in the G and D region, as a whole, can be regarded as the fingerprint of the molecular structures. DFT calculations provide simulated Raman spectra of **3-15** and **3-17**, which well correlate with the experimental results (Fig. 3-17: D features at 1323 cm⁻¹ and G features at 1685, 1651 cm⁻¹ for **3-15**; D features at 1277 cm⁻¹ and G features at 1651 cm⁻¹ for **3-17**).

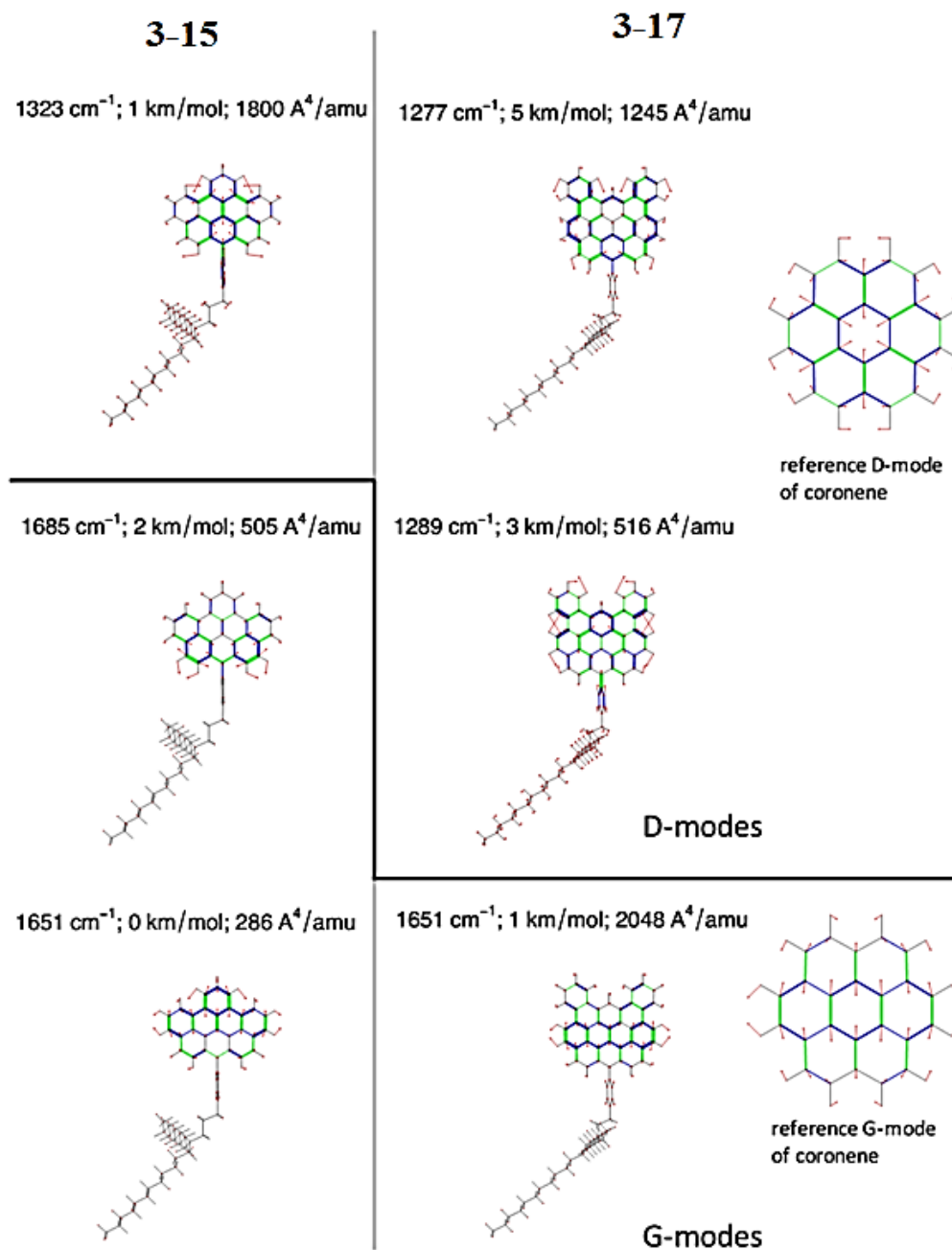


Figure 3-18. Nuclear displacements associated to the most intense G and the D features in **3-15** and **3-17** (from DFT calculations). Red arrows represent displacement vectors; CC bonds are represented as green (blue) lines of different thickness according to their relative stretching (shrinking). The nuclear displacements of the G and D modes of coronene are displayed for comparison.

Inspection of the normal modes associated with the intense Raman peaks reveals the expected nuclear displacements for G and D modes (see Fig. 3-18). The simulated Raman spectra of **3-15** and

3-17 indeed show good agreement with our experimental results, suggesting identical chemical structure of **3-15** and **3-17**.

The experimental Raman spectrum of the GNR **3-3c-I'** displayed the G and D features in addition to their overtones and combinations (2D, G+D, 2G), which were similar to those of GNRs previously synthesized by the solution-mediated protocol (Figure 3-19b).^{14,28} The G peak was slightly up-shifted ($1,604\text{ cm}^{-1}$) compared to that of graphene. The intense D peak observed at $\sim 1305\text{ cm}^{-1}$ was activated by the confinement of π -electrons into the narrow ribbon structures.^{25,27,29} Raman spectrums of GNR **3-3c-I'** also exhibited second-order 2D, G + D, and 2G peaks in agreement with the previous bottom-up synthesized GNRs.¹⁴ Moreover, there was no peak around 994 cm^{-1} observed, which supported the absence of monosubstituted benzene rings.¹⁵

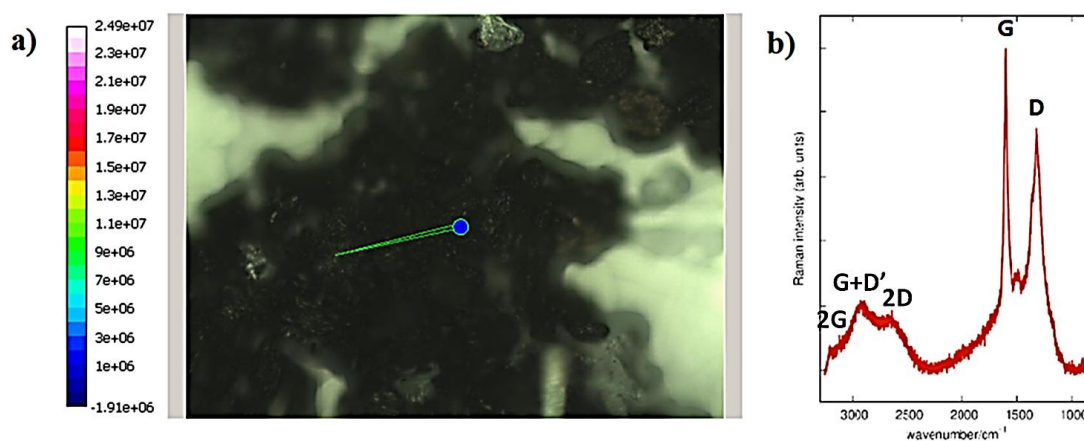


Figure 3-19. a) Picture of powder sample of GNR **3-3c-I'** for measurement and b) Raman spectrum of GNR **3-3c-I'** measured with a Jobin-Yvon Labram HR800UV spectrometer equipped with the 514.5 nm excitation of an Ar⁺ laser.

The FTIR spectroscopy is a powerful characterization that frequently used for the identifying the structures of carbonaceous materials.^{14-16,30} Similar to aforementioned Raman characterizations, the FTIR measurement of model compounds **3-15**, **3-17**, and **3-19** and GNR **3-3c-I'** as well as their precursors **3-14**, **3-16**, and **3-18** and polymer **3-2c-I'** were firstly carried out by myself and compared as displayed in Fig. 3-20. Afterward, the FTIR spectroscopy analyses of **3-15**, **3-17**, and GNR **3-3c-I'** were also performed by our collaborators Prof. [REDACTED] and Prof. [REDACTED], who carried out DFT-based simulation of the FTIR spectra (Fig. 3-21 and Fig. 3-22).

The FTIR signals of PAHs in the CH out-of-plane (*opla*) bending region (980-650 cm^{-1} range) are informative of the molecular structure and edge topology.³¹ Thus, it is interesting to examine and compare the IR spectra of the model compounds and GNR as well as their precursors in this region. Besides, the signals in the region from 2800 to 3100 cm^{-1} also play an important role in providing better understanding of the measured compounds.

As described in section 3.2.2., the chemical structures of model PAHs **3-15**, **3-17** and **3-19** were identified by strong evidences from 1D and 2D ^1H NMR, MALDI-TOF MS, UV-Vis absorption and corresponding excitation spectra.

Comparing with the chemical structures of model PAHs **3-15** and **3-17** and their precursors **3-14** and **3-16**, respectively, the obvious variations of their chemical structures induce changes of the FTIR features from precursors to cyclodehydrogenated products. As displayed in Fig. 3-20, from precursors **3-14** and **3-16** to model PAHs **3-15** and **3-17**, the free-rotating mono-substituted phenyl rings are fused into the dibenzo[*a, j*]anthracene backbone after cyclodehydrogenation. Thus, the IR features originating from the mono-substituted phenyl ring should vanish after the “planarization”. This change can be observed from the spectra displayed in fig. 3-21. Comparing the spectra of three model PAHs and their precursors, the out-of-plane (*opla*) C-H deformation bands at ~ 700 , ~ 830 , and $\sim 796 \text{ cm}^{-1}$ which are typical for mono- and di-substituted benzene rings, disappeared or diminished in line with the successful cyclodehydrogenation. Moreover, the bands of ~ 3027 and $\sim 3048 \text{ cm}^{-1}$ from aromatic C-H stretching vibrations are faded after cyclodehydrogenation, due to the removal of protons after cyclodehydrogenation. The aforementioned changes can also be observed in the IR spectra of **3-19** and its precursor **3-18**. Notably, the di-substituted phenyl group always exists in our system before and after “planarization”. Thus, the IR features originating from free-rotated phenyl rings and di-substituting phenyl rings will be preserved.

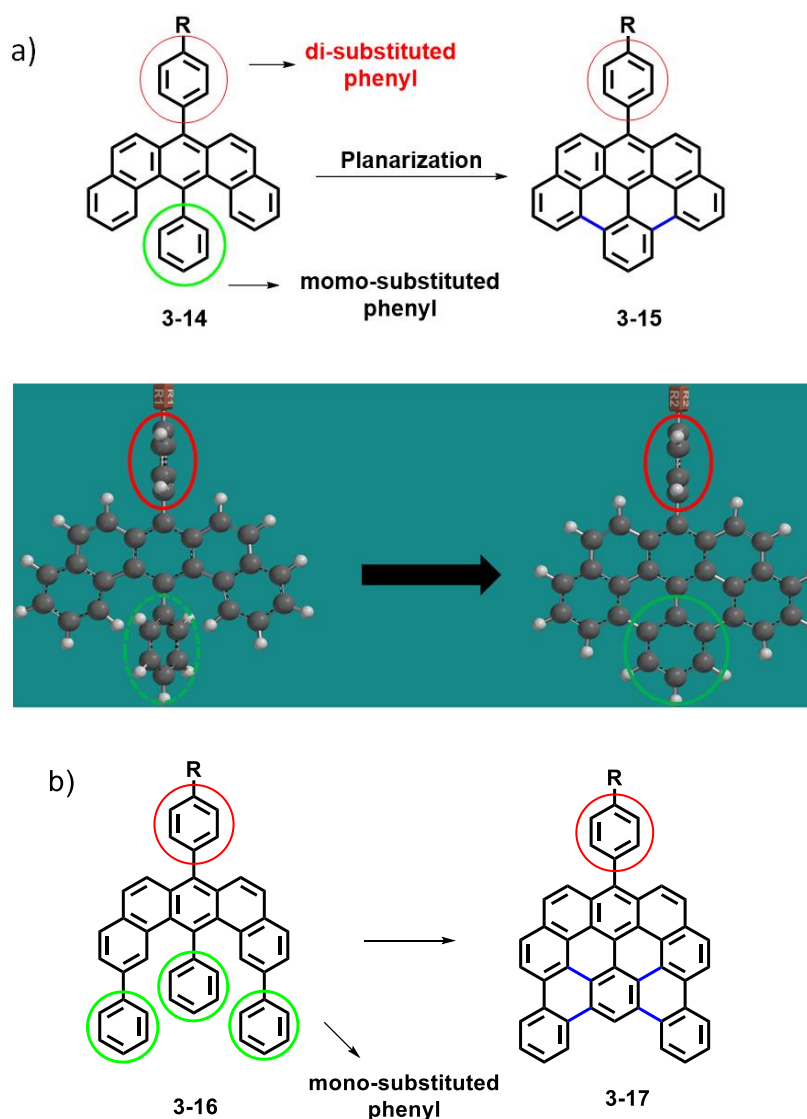


Figure 3-20. a) Reaction scheme of “planarization” from **3-14** to **3-15**. b) “Planarization” from **3-16** to **3-17**.

For polymer precursor **3-2c-I'**, its FTIR spectra (Fig. 3-21) also show *opla* C-H deformation bands at 699, 750, and 834 cm^{-1} similar to PAHs **3-14**, **3-16**, and **3-18**, which are typical for the mono- and di-substituted benzene rings. In contrast, the spectrum of GNR **3-3c-I'** is obviously different from its polymer precursor, where the peaks around ~ 700 and ~ 796 cm^{-1} vanish or diminish, indicating the occurrence of cyclodehydrogenation. Furthermore, the signals from aromatic C-H stretching vibrations of polymer precursor **3-2c-I'** at 3027 and 3048 cm^{-1} are clearly attenuated upon the conversion to GNR **3-3c-I'** (Fig. 3-21, inset). All above observations were in line with the changes displayed upon the cyclodehydrogenation of precursors **3-14**, **3-16**, and **3-18** into model compounds **3-15**, **3-17**, and **3-19**, respectively. Additionally, the band at 720 cm^{-1} could be assigned to $-\text{CH}_2-$ rocking mode from the decylhexadecyl chains.

It should be noted that the FTIR could not be a sufficient proof for the structural perfection, but the results exhibited above supported the successful “graphitization” of precursors **3-14**, **3-16**, **3-18**, and **3-2c-I'** into corresponding model compounds and GNR.

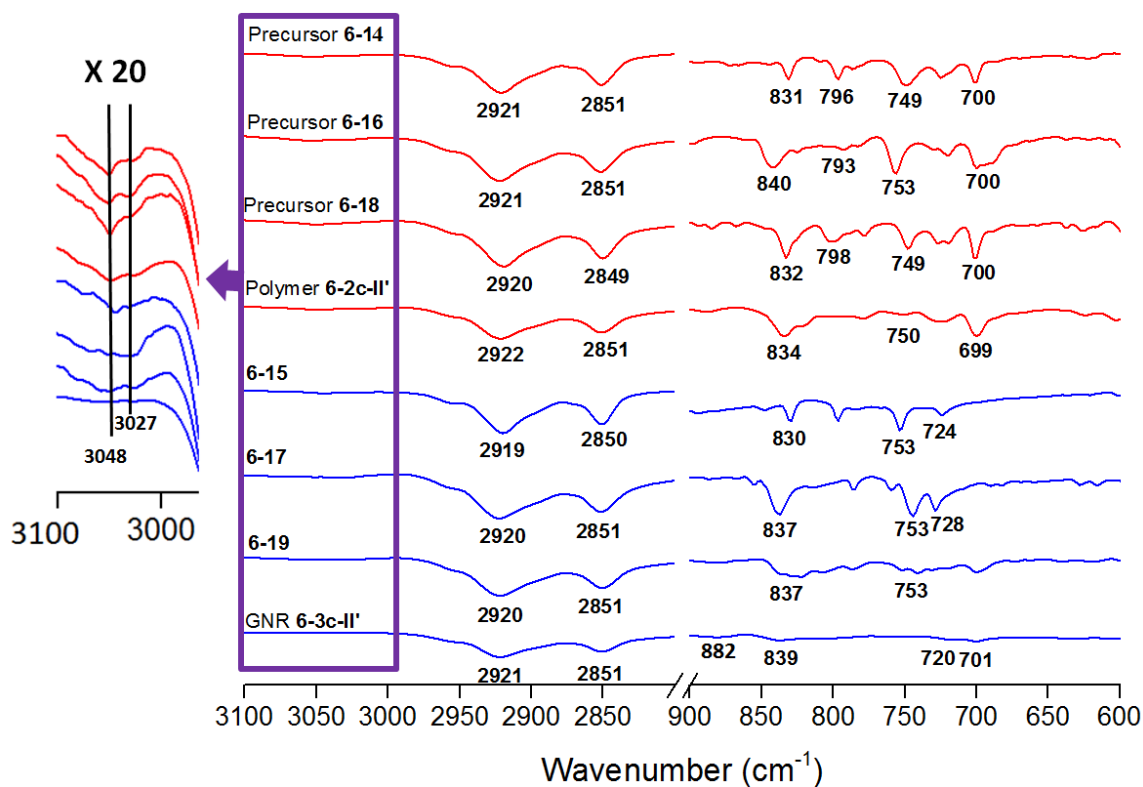


Figure 3-21. FTIR spectra of precursors **3-14**, **3-16**, **3-18** and **3-2c-I'** (red lines), as well as model compounds **3-15**, **3-17**, **3-19** and GNR **3-3c-I'** (blue lines). Inset: Magnified FTIR spectral regions from 3,000 to 3,100 cm^{-1} in 20 times.

To obtain deeper insight into the FTIR spectroscopy of model compounds **3-15** and **3-17**, DFT-based simulation of the FTIR spectra were performed by our collaborators and compared with experimental IR spectra recorded on powder samples (Fig. 3-22a). The comparison between theory and experiment was fair, with better agreement for model compounds **3-15** and **3-17**. Deviations between theory and experiment are presumably due to the role of intermolecular interactions at solid state, since the calculations were performed for isolated molecules. Moreover, the presence of alkyl substituents could play a role through contributions arising from the vast manifold of possible conformers that have not been considered in the simulation. In fact, to focus on the *CH-*o*pla* markers

and limit the computational cost, the models were only with fully *trans*-planar conformations of the substituents (see Fig. 3-22b for their graphical representation).

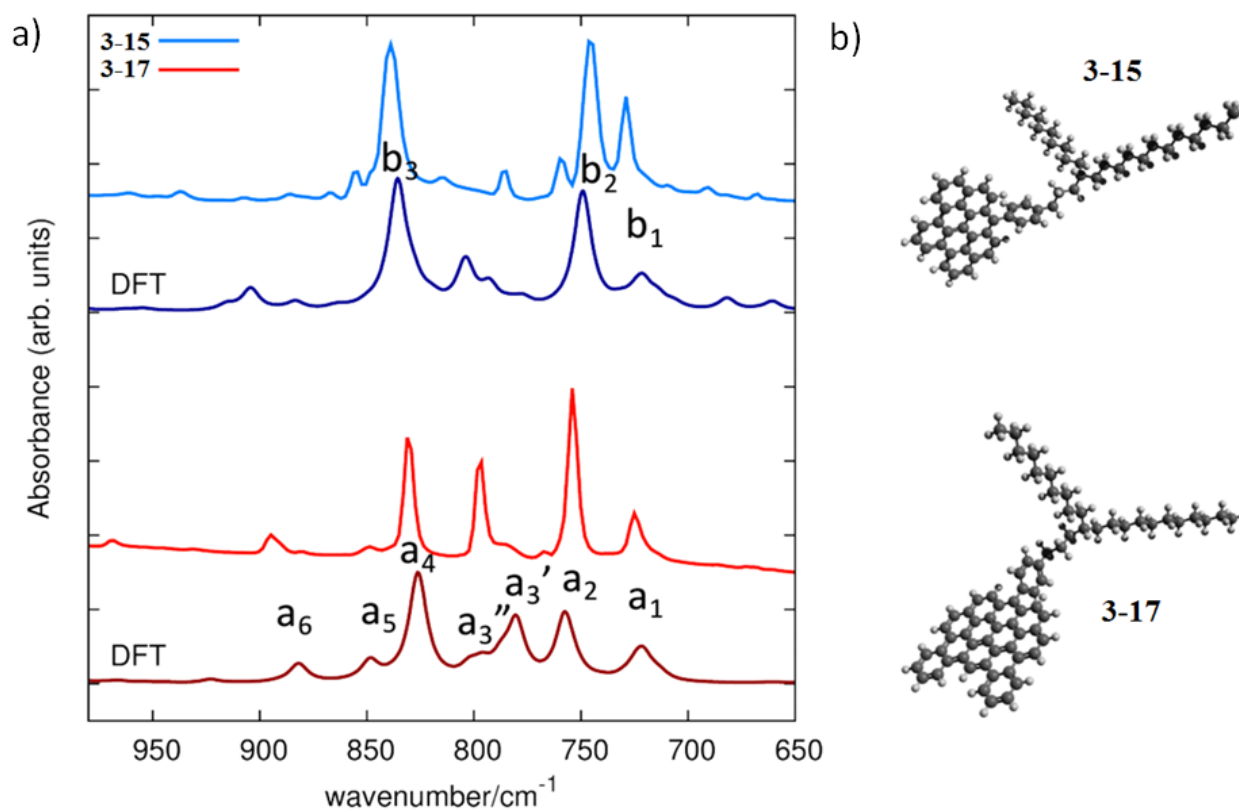


Figure 3-22. a) Simulated and experimental IR spectra of **3-15**, **3-17** in the fingerprint out-of-plane CH bending region. In comparing simulated IR spectra with experimental data, computed wavenumbers have been uniformly scaled by 0.98 and are reported below each corresponding experimental spectrum (see text for details). b) Ball and stick representation of the molecular models considered for the quantum chemical calculations.

In Fig. 3-23, the a_1 IR feature of **3-15** was assigned to the rocking modes of the alkyl chains; b_1 was the rocking mode in **3-17**. The remaining features labeled in the IR spectra of Fig. 3-21 were all due to *opla* vibrations of CH bonds. With the exception of the weak a_5 feature, assigned to the lateral phenyl substitution, these IR signals (i.e., a_2 , a_3' , a_3'' , a_4 , a_6 in **3-15** and b_2 , b_3 in **3-17**) were characteristic of the topology of the molecular edges. Adopting the mode naming also described in reported literature,³¹ based on the pattern of the normal modes, the b_2 signal in **3-17** can be described as QUATRO and b_3 as DUO (Fig. 3-23, inset). The a_2 and a_3' features of **3-15** can be described as TRIO and a_4 as DUO. The remaining two modes (a_3'' , a_6) have a more complex pattern of in-phase/out-of-phase CH-*opla* contributions.

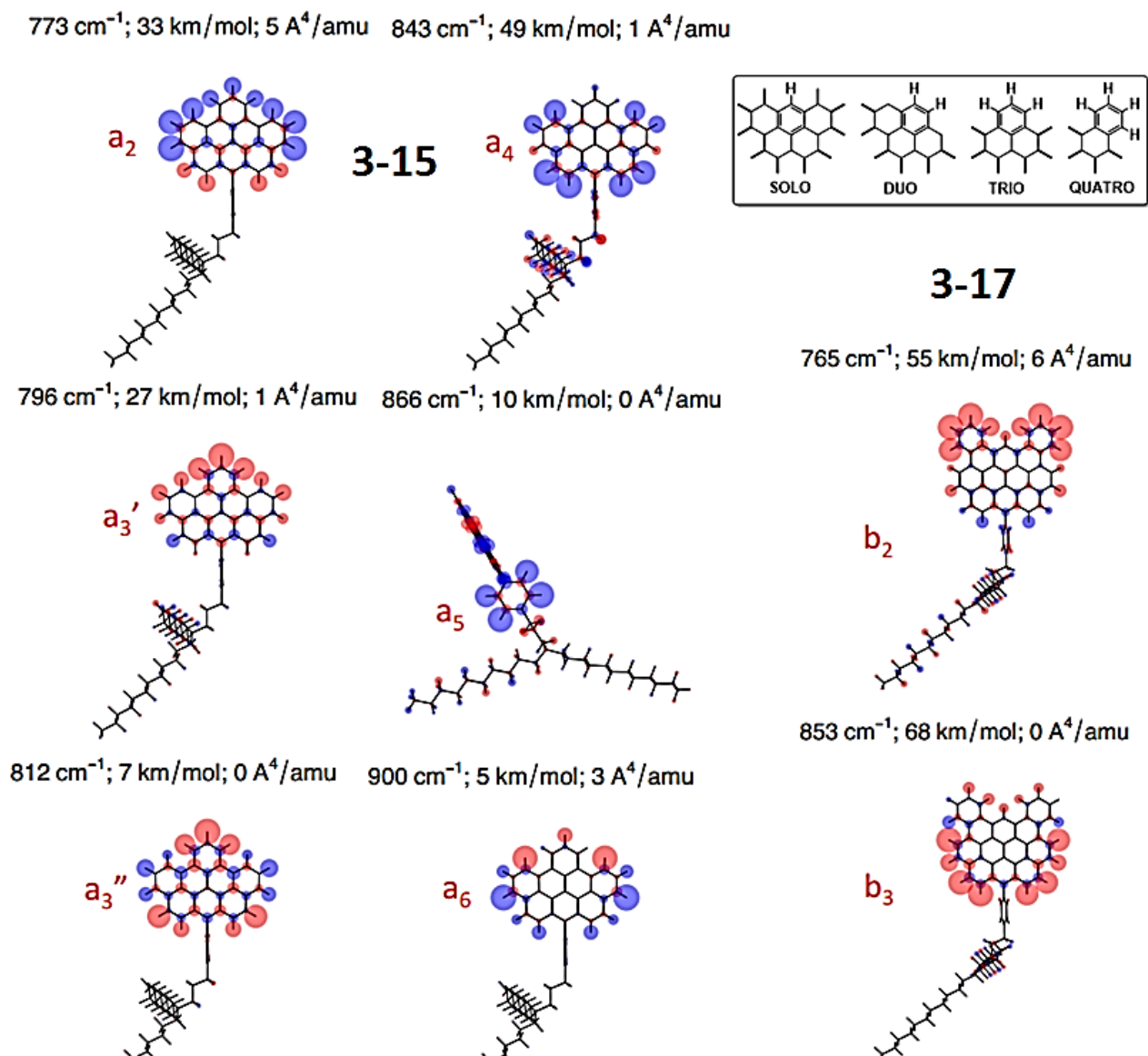


Figure 3-23. Representation of the normal modes associated to the IR spectra features labeled in Fig. 3-21. The size of blue/red circles on the molecular sketches is proportional to positive/negative nuclear displacements along the out-of-plane direction

In order to obtain a deeper insight into the variations of FTIR spectra before and after “planarization”, we further compared the FTIR spectra of our experimental results of GNR **3-3c-I** and its polymer precursor **3-2c-I**, as well as the simulated IR spectra of GNR **3-3c**. As shown in Figure 3-24, the FTIR spectra of polymer precursor **3-2c-I** showed *ortho* C-H deformation bands at 699 and 750 cm^{-1} , which are typical for mono-substituted benzene rings as in the case of PAH. These bands vanished or diminished in the FTIR spectrum of GNR **3-3c-I**, indicating successful cyclodehydrogenation of precursor **3-2c-I**. The remaining signal at 701 cm^{-1} most probably corresponds to the c1 feature, which is associated to a collective in-plane CCC deformation mode with a rather complex pattern (see Fig. 3-24b). The peak at 882 cm^{-1} can be presumably assigned to c3 band, which is the most characteristic fingerprint signal of the “gulf” topology of GNR **3-3c-I**. Furthermore, the signals from aromatic C-H stretching vibrations of polymer precursor **3-2c-I** at 3027 and 3048 cm^{-1} are clearly attenuated upon the conversion to GNR **3-3c-I**, which is in line with the decreased number of aromatic C-H bonds after the “graphitization” (Fig. 3-21, and Fig. 3-24a). Additionally, the band at 720 cm^{-1} corresponds to the c2 feature that originates from the overlap of rocking modes of the 4-decylhexadecyl chains and in-plane CCC deformation modes. The weak simulated intensities of the rocking modes is due to the short alkyl chains adopted in the DFT model of GNR **3-3c** (Fig. 3-24b).

In summary, all these Raman and FTIR characterizations of model compounds (**3-15** and **3-17**) indicated good agreement with corresponding DFT calculations. For GNR **3-3c-I**, the Raman and FTIR also displayed reasonable features in proving the successful “graphitization”. The broad feature of the spectra and the deviation between calculation and experiment results of GNR **3-3c-I** could be ascribed to the decomposition during the Raman measurement as well as the relatively lower stability of GNR **3-3c** with the partial zigzag edge structures that could be relatively reactive and might be gradually oxidized in air.

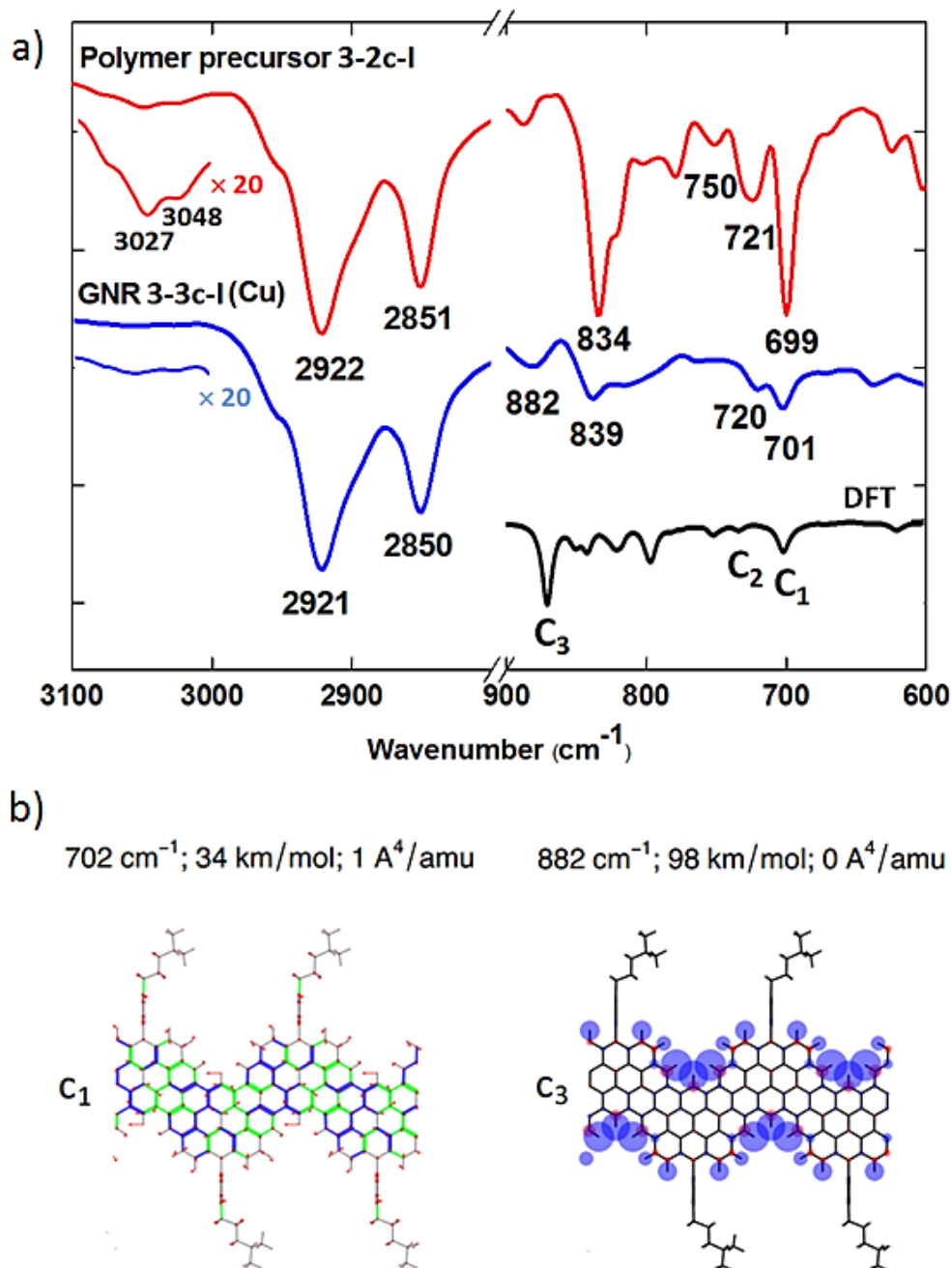


Figure 3-24. a) Representative experimental FTIR spectral regions of polymer precursor **3-2c-I** (red lines) and GNR **7c-I (Cu)** (blue lines). Simulated IR spectra (frequency scaled by 0.98) of GNR **3-3c-I (Cu)** in the fingerprint out-of-plane CH bending region is shown below below the experimental spectrum. b) Representation of normal modes associated to the IR spectra features labeled in b). The size of blue/red circles on the molecular sketches is proportional to positive/negative nuclear displacements along the out-of-plane direction. In the sketch of nuclear displacement patterns red segment represent displacement vectors; CC bonds are represented as green (blue) lines of different thickness according to their relative stretching (shrinking).

3.3.4 Solid-state NMR analysis

The solid-state NMR characterization of GNR **3-3c-I'** was performed by our collaborators [REDACTED] and [REDACTED] at Aarhus University, Denmark.

Solid-state ^1H and ^{13}C magic-angle-spinning (MAS) NMR spectroscopy mentioned above were employed to characterize polymer precursor **3-2c-I'** and GNR **3-3c-I' (Cu)** (Fig. 3-25). Fig. 3-25a and 3-25d show the 1D ^1H DQ filtered spectra of precursor **3-2c-I'** and GNR **3-3c-I' (Cu)**, respectively, with schematic representations of the samples in Fig. 3-25c and 3-25f. A 1D ^1H DQ filtered experiment was chosen to probe the rigid regions. The 2D ^1H - ^1H DQ-SQ spectra recorded with two rotor periods of dipolar recoupling are shown in Fig 3-25b and 3-25e. Addressing initially the precursor **3-2c-I'**, the ^1H signals of the aliphatic and aromatic protons are easily distinguished in the 1D spectrum. In the 2D correlation spectrum, we see the aliphatic and aromatic protons in the SQ (direct) dimension in broad ranges centered at ca. 1.2 ppm and ca. 7.1 ppm, respectively. In the DQ (indirect) dimension, the broad correlations appearing at the sum of the chemical shifts demonstrated the spatial proximity between the aliphatic protons and aromatic ones. For short mixing times, the correlations are among aromatic protons being closest in the space to the aliphatic ones. Turning to GNR **3-3c-I' (Cu)**, we observed a significant broadening of the ^1H signals compared to the polymer precursor which indicated that the protons are a part of an extended π -conjugated system with heterogeneous packing.^{11,32-34} The ^1H signals of the aliphatic and aromatic protons are observed in the SQ dimension in broad ranges centered at ca. 1.3 and ca. 7.7 ppm, respectively. In the DQ dimension, the broad correlations appearing approximately at the sum of the chemical shifts demonstrate the spatial proximity between the aliphatic protons and the aromatic ones. Note that the auto correlation in the aromatic region appeared at slightly higher ppm value in the direct dimension than the cross correlation did. This shift in autocorrelation might be ascribed to the aromatic protons in the coves as these give rise to signals at higher ppm values. The spectra from 2D ^1H - ^1H DQ-SQ spectrum suggests that the quality of graphene nanoribbons is comparable to those that have been reported previously in the literature.^{10,11}

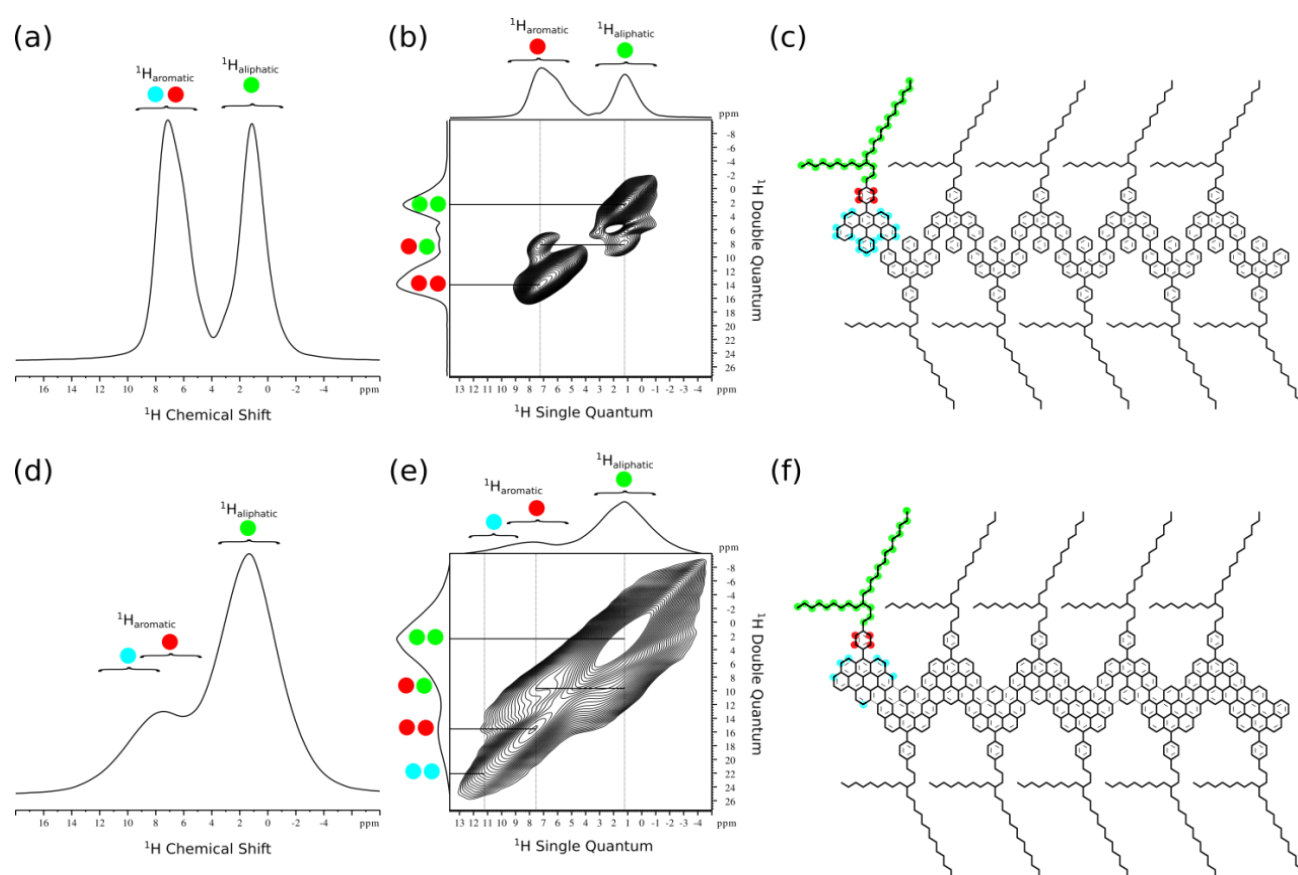


Figure 3-25. The DQ filtered ^1H spectra (a and d) and the 2D ^1H - ^1H DQ-SQ correlation spectra with two rotor periods recoupling (b and e) were recorded at 16.4 T using a MAS frequency of 59524 Hz. Subfigures (a, b and c) address the precursor **3-2c-I'** while (d, e and f) address GNR **3-3c-I'** (**Cu**). The regions marked by curly brackets in (a, b, d and e) illustrate the broad range of ^1H chemical shifts resulting from a heterogeneous packing. (c and f) Assignment scheme.

The ^{13}C spectra of precursor **3-2c-I'** and GNR **3-3c-I'** (**Cu**) based on the $^{13}\text{C}\{^1\text{H}\}$ REPT-HSQC experiment are displayed in Fig 3-26a and 3-26b. A short recoupling time of two rotor periods was employed to observe mainly ^{13}C nuclei at or near the edges and in the aliphatic chain. In the resulting $^{13}\text{C}\{^1\text{H}\}$ REPT-HSQC spectrum of the precursor **3-2c-I'**, two main regions can be assigned to the signals of the aromatic carbons at ca. 136–121 ppm ($^{13}\text{C}_{\text{aromatic}}$) and the aliphatic carbons at ca. 41–21 ppm ($^{13}\text{C}_{\text{aliphatic}}$). In case of GNR **3-3c-I'** (**Cu**), we likewise assign the signals of the aromatic carbons at ca. 149–112 ppm ($^{13}\text{C}_{\text{aromatic}}$) and the aliphatic carbons at ca. 60–0 ppm ($^{13}\text{C}_{\text{aliphatic}}$). It should be mentioned that these regions are estimated manually by visual inspection. The ^{13}C signals of GNR **3-3c-I'** (**Cu**), especially in the aliphatic region, are broadened significantly compared to those of the precursor **3-2c-I'**.

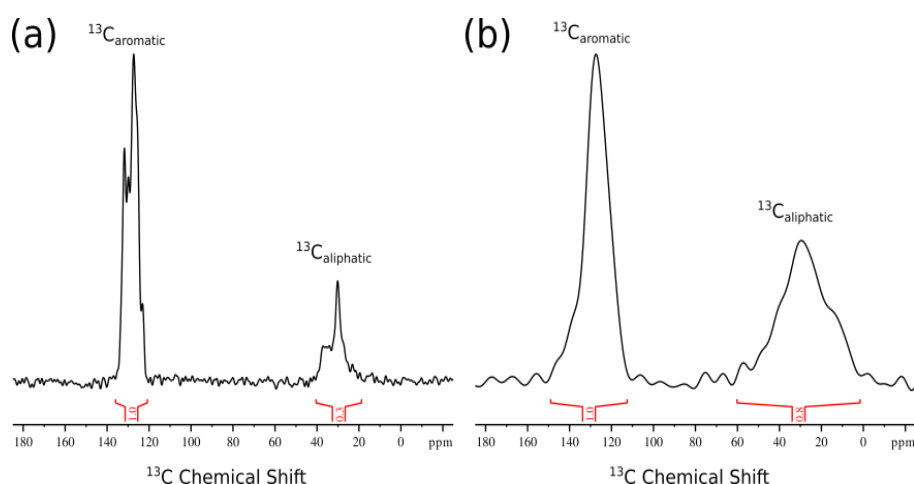


Figure 3-26. The $^{13}\text{C}\{^1\text{H}\}$ REPT-HSQC with two rotor periods of REDOR recoupling spectra (a and b). Subfigure (a) addresses the precursor **3-2c-I'** while (b) addresses GNR **3-3c-I'** (**Cu**).

Moreover, another batch of polymer precursor **3-2c-I'*** and its corresponding GNR **3-3c-I'*** (**Fe**), which was dehydrocyclized via FeCl_3 method were also investigated by the same solid-state ^1H and ^{13}C magic-angle-spinning (MAS) NMR spectroscopy characterization to compare the efficiency of the two dehydrocyclization methods (Fig. 3-27a-f). In overall, the spectra of the two batches of precursors **3-2c-I'** as well as GNR **3-3c-I'*** (**Fe**) and **3-3c-I'** (**Cu**) are similar, and structures of them are basically identical by solid-state NMR. By looking in detail, however, the solid-state NMR data suggested that the ratio between the signals in the aromatic regions and those in the aliphatic regions are slightly different between the two batches of polymer precursor **3-2c-I'**. The ratio is more in favor of signals in the aliphatic region of precursor **3-2c-I'*** than in the case of precursor **3-2c-I'**. These observations were apparent in the 1D ^1H DQ filtered spectra but can also be extracted in normal 1D ^1H spectra and from the ^{13}C spectra. The small variations might be ascribed to the fact that the molecular weight is different for the two batches of polymer precursors. In conclusion, we find the starting points of the dehydrogenation processes to be almost equal.

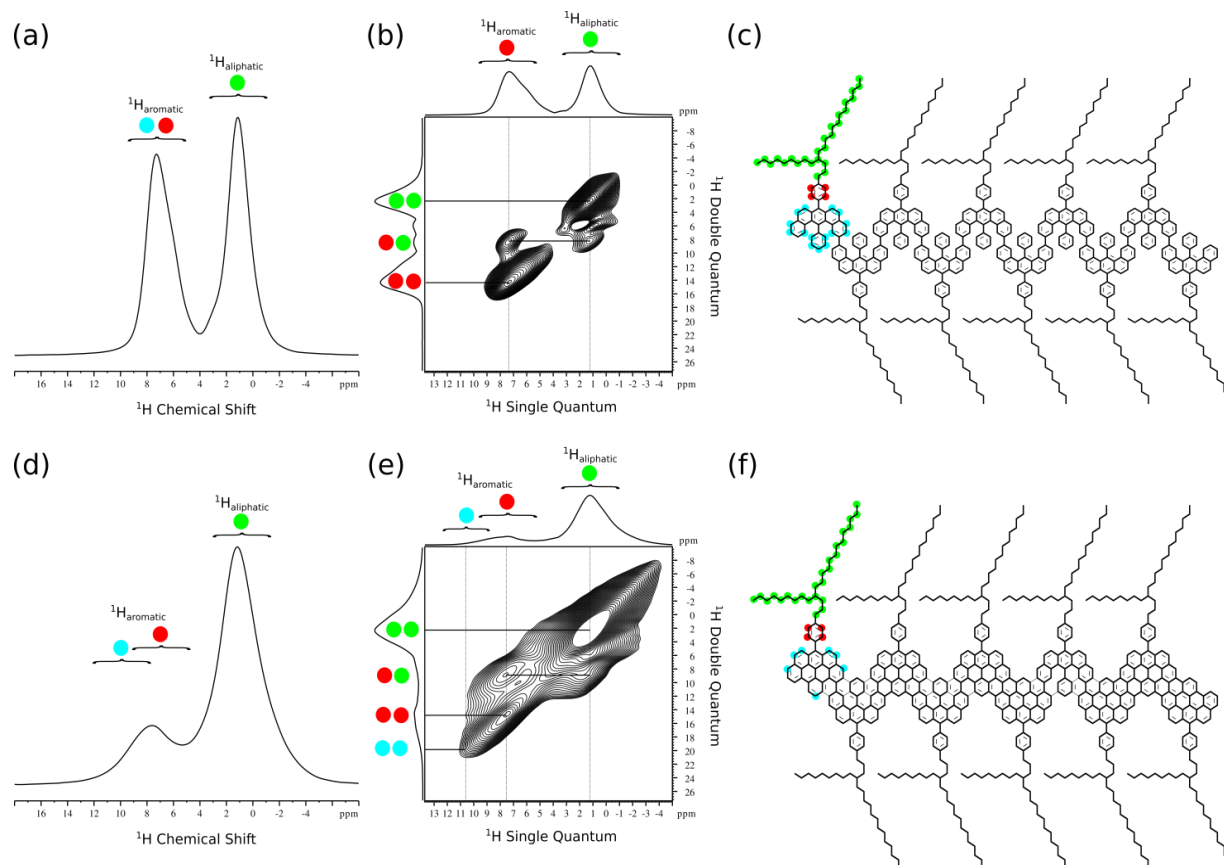


Figure 3-27. The DQ filtered ^1H spectra (a and d) and the 2D ^1H - ^1H DQ-SQ correlation spectra with two rotor periods recoupling (b and e) were recorded at 16.4 T using a MAS frequency of 59524 Hz. Subfigures (a, b and c) address the precursor **3-2c-I'** while (d, e and f) address GNR **3-3c-I'** (Fe). The regions marked by curly brackets in (a, b, d and e) illustrate the broad range of ^1H chemical shifts resulting from a heterogeneous packing. (c and f) Assignment scheme.

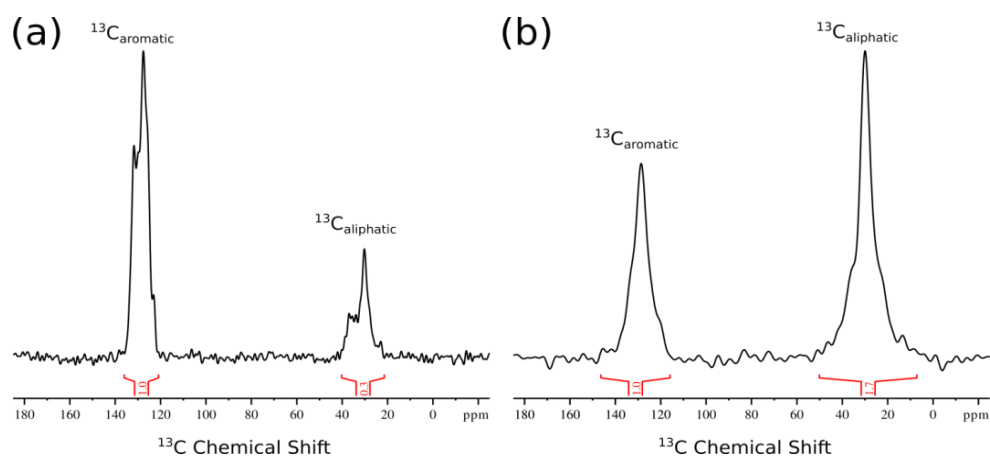


Figure 3-28. The $^{13}\text{C}\{^1\text{H}\}$ REPT-HSQC with two rotor periods of REDOR recoupling spectra (a and b). Subfigure (a) addresses the precursor **3-2c-I'** while (b) addresses GNR **3-3c-I'** (Fe).

Addressing the GNR **3-3c-I'** (**Fe**) and the GNR **3-3c-I'** (**Cu**) samples, we observed stronger broadening of the ^1H signals in the latter case (Fig. 3-25 and 3-27). The enhanced broadening is evident in both the 1D ^1H DQ filtered spectra and in the 2D ^1H - ^1H DQ-SQ spectra. For the GNR **3-3c-I'** (**Cu**) sample, we observe less prominent aromatic-aliphatic proton correlations compared to those in GNR **3-3c-I'** (**Fe**). This might be ascribed to more spread out ^1H signals which again can originate in better extended π -conjugated systems with correspondingly heterogeneously packing.

In the $^{13}\text{C}\{^1\text{H}\}$ REPT-HSQC spectrum of GNR **3-3c-I'** (**Cu**), we saw a significant broadening of the signals relative to those of GNR **3-3c-I'** (**Fe**). A broadening effect can originate in the packing of the GNR. For example such an effect can be ascribed to more spacious aliphatic chains in case of GNR **3-3c-I'** (**Fe**) than that of GNR **3-3c-I'** (**Cu**). In turn, this can point to better extended π -conjugated systems with correspondingly more heterogeneously packing in samples of GNR **3-3c-I'** (**Cu**). We furthermore observe less aliphatic ^{13}C signals relative to aromatic ^{13}C signals in case of GNR **3-3c-I'** (**Cu**), i.e. the ratio of the aliphatic region relative to the aromatic region is seen to be 0.8 in Fig. 3-26b. This is contrast to Fig. 3-28b where the ratio is 1.7 for the aliphatic region relative to the aromatic region. A reasonable explanation can be that the alkyl chains can be chopped off or rearranged under the $\text{Cu}(\text{OTf})_2/\text{AlCl}_3$ condition.³⁵ GNR **3-3c-I'** (**Cu**) simply has fewer alkyl chains which might be at different positions, resulting in stronger aggregations.

3.3.5 AFM and STM visualization

Whereas the spectroscopic characterizations such as IR, Raman, solid-state NMR, and UV-Vis absorption spectroscopy fail to provide a clear and unambiguous proof for the formation of structurally perfect GNRs, microscopic analyses by scanning probe microscopy (SPM) can in principle directly study the atomic structures of the GNRs. Nevertheless, it is highly challenging to visualize solution-synthesized GNRs with longitudinal length over 50 nm. The reason can be ascribed to the strong aggregation behavior and their low dispersibility as well as the bulky alkyl chains at the peripheral positions, which could hinder the analysis of the aromatic cores.^{14,16} In this work, the intensely installed alkyl chains along the periphery of GNR **3-3c-II'** enhanced its dispersibility, which further enabled the liquid-phase processing of GNRs to form highly organized self-assembled films. The alkyl chains were nicely interdigitated and did not hamper the visualization. Although a highly resolved structures of the GNRs could not be observed, well-

organized films of GNR **3-3c-II'** could be visualized by the atomic force microscopy (AFM), revealing their actual dimensions.

The AFM visualization of GNR **3-3c-II'** was carried out by the group of [REDACTED] at Katholieke Universiteit Leuven, Belgium. The highly ordered drop-cast film of GNR **3-3c-II'** was prepared through several steps, e.g., 1) a dispersion of GNR with concentration of 1 $\mu\text{g/ml}$ in 1, 2, 4-trichlorobenzene (TCB) was prepared; 2) the GNR dispersion was sonicated at least 1 hour and heated 20~30 min at 120 $^{\circ}\text{C}$ before the deposition; 3) the hot deposition of a droplet from above GNR dispersion on highly oriented pyrolytic graphite (HOPG) was performed (solution and substrate at 120 $^{\circ}\text{C}$); 4) Subsequent rapid evaporation of the solvent by annealing the substrate at 120 $^{\circ}\text{C}$ gave the dry monolayers of GNR **3-3c-II'**. 5) The sample on HOPG above was thoroughly rinsed with 1 mL of pure TCB (Pasteur pipette) to allow the formation of molecular films with submonolayer coverage.

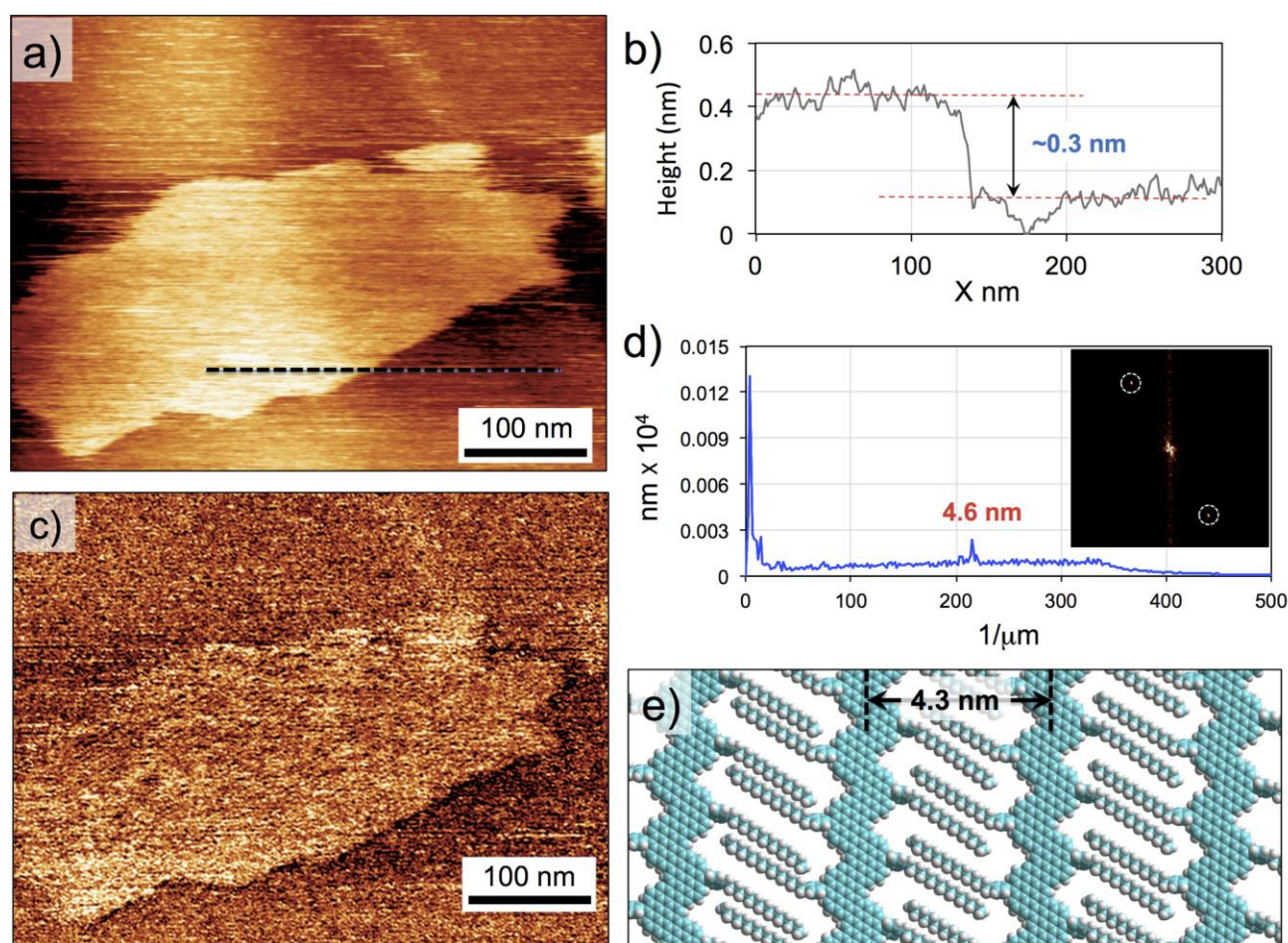


Figure 3-29. AFM analysis of self-assembled monolayer of GNR **3-3c-II'** (dry film) formed on HOPG. (a) AFM height image showing an isolated domain. (b) Representative line profile, which was measured along the dotted line in the height image shown in panel (a), shows formation of a monolayer film upon drying. (c) Corresponding AFM phase image. The inset shows Fourier analysis of the image showing two peaks that

correspond to the periodicity of 4.6 nm. (d) Power spectrum density (PSD) analysis of the AFM phase image provided in panel (c) showing a periodicity of 4.6 nm for the surface adsorbed GNR **3-3c-II'** assembly. (e) A molecular model depicting the plausible arrangement of GNR **3-3c-II'** in the organized domains.

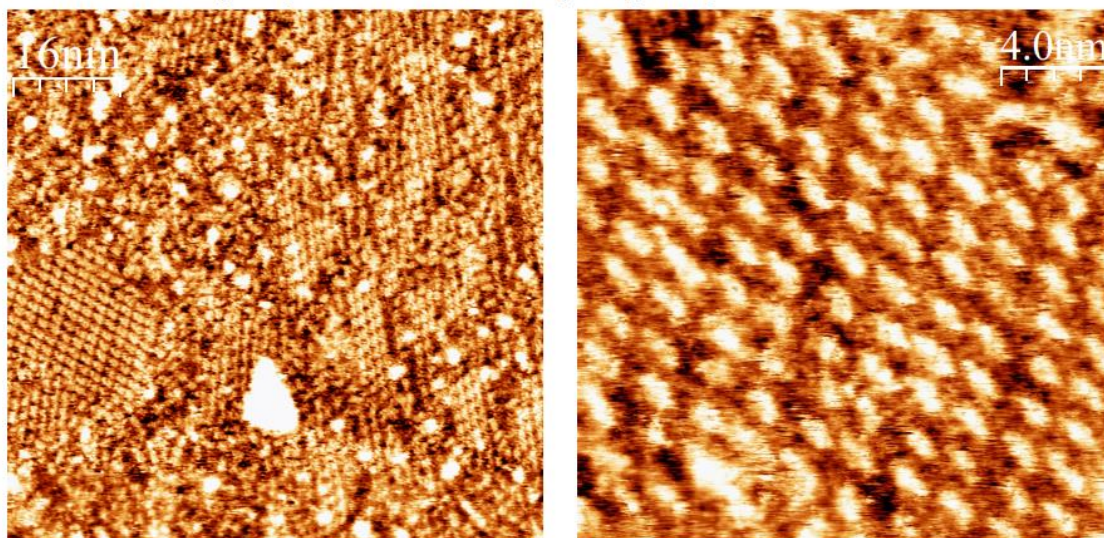
AFM revealed organized domains of GNR **3-3c-II'** adsorbed on the surface of HOPG. Fig. 3-29a shows the AFM height image of a typical self-assembled GNR domain. Such domains typically extend over a few hundred nanometers. Given the estimated length of the GNR **3-3c-II'** (90-110 nm), the size of the domains is indicative of good lateral as well as end-to-end stacking between individual GNRs in the domain. A representative line trace (black dashed line) on the AFM image shows a height difference of roughly 3 Å between the substrate and the GNR domain (Fig. 3-29b) consistent with the expected monolayer thickness.

AFM phase images were used for estimating the periodicities of the GNR assemblies. Panel (c) in Fig. 3-29 shows an AFM phase image corresponding to the height image provided in Fig. 3-29a. The phase image exhibits relatively clearer and distinguishable stripes within the domain of GNRs. Fourier transform (inset Fig. 3-29c) as well as power spectrum density (PSD, Fig. 3-29d) analysis of the AFM phase images provided a periodicity of 4.6 ± 0.2 nm. This periodicity appears to be defined by the adsorbed hexadecyl chains. Fig. 3-29e shows a tentative molecular model depicting the packing of GNR **3-3c-II'** molecules within a domain. Only the hexadecyl chains are shown in the molecular model and the branched dodecyl chains are omitted for the sake of clarity. In contrast to the previously reported cove type GNRs^{10,11} which did not show interdigitation of alkyl chains upon surface adsorption, alkyl chains on adjacent molecules of GNR **3-3c** are plausibly interdigitated on the HOPG surface. A careful inspection of the molecular model also reveals that there is not enough space for adsorption of all dodecyl chains. These chains may be adsorbed on top of surface adsorbed hexadecyl chains, as the GNR film is dry. The molecular model shows possible interdigitation between the alkyl chains and the periodicity obtained from the molecular model (4.3 nm) is in reasonable agreement with the AFM data. The regularity of the stripes and the homogeneity of the distance between them prove the uniformity (as well as the linearity) of the GNRs composing such domains. The scanning probe microscopy data further confirms the degree of structural control provided by the bottom-up synthetic approach to GNRs.

For comparison, the STM measurements of **3-19** were also performed on solution-solid interface³⁶ (Au(111)/TCB and HOPG/TCB). The STM images of **3-19** showed very ordered assemblies with uniform coverage, and no polymorphism was observed (Fig. 3-30). The self-

assembled monolayer of **3-19** formed at the TCB/ HOPG interface is relatively fragile and is often easily perturbed by the STM tip. The solutions of **3-19** with two different concentrations were tested and corresponding STM images are shown below. Comparison of STM images in Fig. 3-30a and 3-30b indicated that the higher quality images can be obtained by using solution with lower concentration (0.1 mg/mL) on HOPG surface compared to those using high concentrated solution (1 mg/mL) on Au surface. Besides, the presence of clusters still can be observed in all STM images, possibly owing to the large aggregates of compound **3-19**.

a) STM on Au (111) - Concentration (1 mg/mL)



b) STM on HOPG - Concentration (0.1 mg/mL)

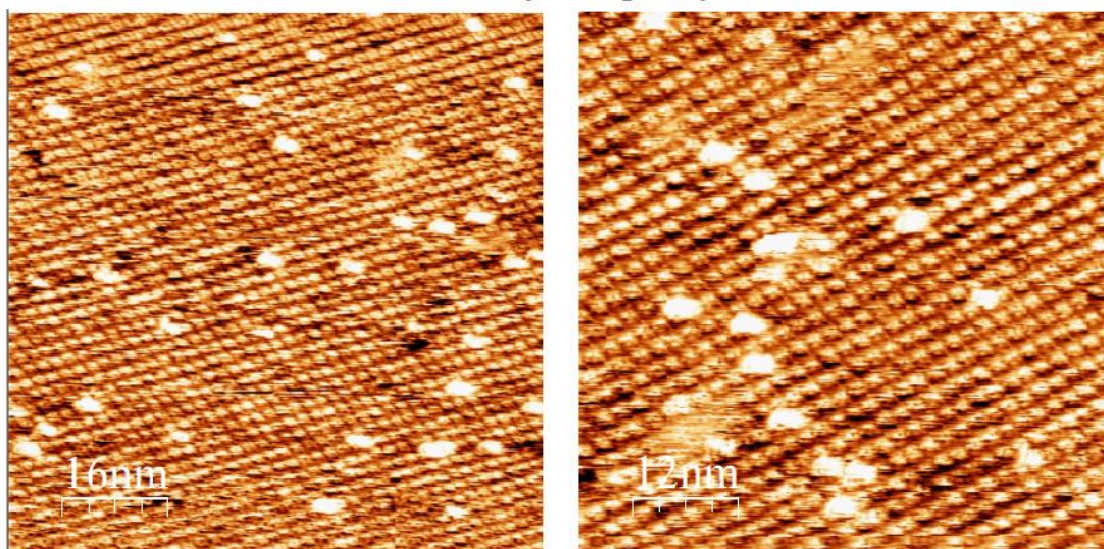


Figure 3-30. STM images of model compound **3-19** a) at Au (111) /TCB interface by using solution of **3-19** with concentration of 1 mg/mL; b) at HOPG/TCB interface by using solution of **3-19** with concentration of 0.1 mg/mL.

Further investigation of the STM images of **3-19** in smaller scale was performed afterward. Fig. 3-31a displays a representative STM image of the **3-19** monolayer in smaller scale corresponding to Fig. 3-30b, which shows rows of bright rectangular features stacked end-to-end. Each rectangular feature corresponds to the aromatic backbone of a single **3-19** molecule. The dimensions of the aromatic core extracted from calibrated STM images (length ~ 2.3 nm, width ~ 1.1 nm) are in good agreement with those obtained from a molecular mechanics based model (Fig. 3-31b). The bright rows are periodically separated by relatively darker troughs. The distance between the adjacent rows of bright features (unit cell vector *b*) indicates that the darker region hosts the dodecyl chains. The hexadecyl chain may be partially adsorbed or alternatively back-folded in the supernatant solution. The alkyl chains could not be resolved, possibly because of their mobility on the time scale of STM imaging. A simple molecular model displayed in Fig. 3-31b depicts the arrangement of **3-19** molecules within the self-assembled network. The empty regions in the molecular model could be occupied by the partially adsorbed hexadecyl chains or by mobile TCB molecules. Given that monomer **3-1c** is the repeating unit of the polymer precursor **3-2c**, the STM analysis of **3-19** indirectly reveals that the width of the aromatic backbone of the GNR **3-3c** is around 1 nm.

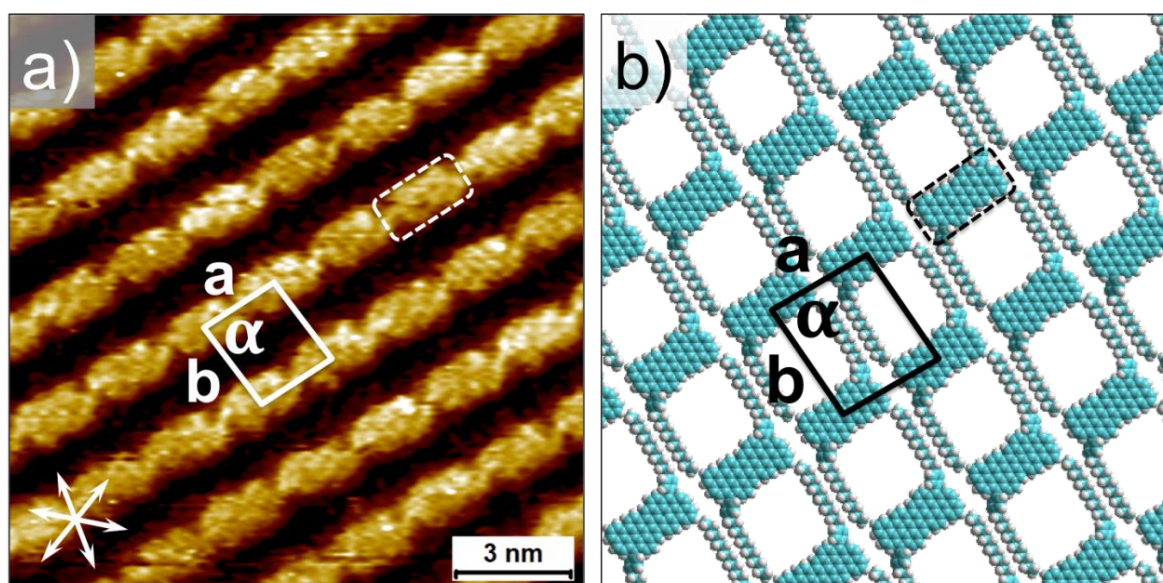


Figure 3-31. STM characterization of the model compound **3-19**. (a) STM image showing self-assembled network of **3-19** formed at the TCB/HOPG interface ($C_{6-19} = 6.3 \times 10^{-5}$ M). Dashed rectangle highlights the aromatic backbone of a single **3-19** molecule. The graphite symmetry axes are displayed in the lower left corner. The unit cell is overlaid on the STM image and the parameters are $a = 2.3 \pm 0.2$ nm, $b = 2.7 \pm 0.1$ nm, $\alpha = 84.5 \pm 3^\circ$. Imaging parameters: $I_{set} = 75$ pA, $V_{bias} = -1.125$ V. (b) Molecular model showing the arrangement of molecules within the self-assembled network. The unit cell parameter *b* indicates adsorption of the dodecyl chain on the surface and the hexadecyl chain is possibly back-folded in the supernatant solution. The hexadecyl chain is not shown for the sake of clarity.

3.4. Summary

In summary, we demonstrated the synthesis of a novel GNR **3-3c** with hybrid of zigzag and gulf-type edge structures via solution-mediated protocol, which can serve as the first step towards the fabrication of full zigzag-edged GNRs in solution. GNR **3-3c** had an estimated length of >100 nm and was comprehensively characterized by Raman, FTIR, UV-vis absorption, and solid-state NMR spectroscopies as well as AFM. In parallel, PAHs **3-15**, **3-17** and **3-19** were also synthesized and studied for comparison with GNRs as well as for the model studies of infinite GNRs. Regarding GNR **3-3c**, a relatively low optical bandgap of ~1.5 eV was exhibited for its narrow structure, which is induced by the partial zigzag edges.

3.5 References

- (1) Nakada, K.; Fujita, M.; Dresselhaus, G.; Dresselhaus, M. S. *Phys Rev B* **1996**, *54*, 17954.
- (2) Son, Y. W.; Cohen, M. L.; Louie, S. G. *Phys Rev Lett* **2006**, *97*.
- (3) Morita, Y.; Suzuki, S.; Sato, K.; Takui, T. *Nat Chem* **2011**, *3*, 197.
- (4) Wu, D. Q.; Feng, X. L.; Takase, M.; Haberecht, M. C.; Mullen, K. *Tetrahedron* **2008**, *64*, 11379.
- (5) Wu, D. Q.; Pisula, W.; Haberecht, M. C.; Feng, X. L.; Mullen, K. *Org Lett* **2009**, *11*, 5686.
- (6) Makabe, H.; Okajima, M.; Konno, H.; Kan, T.; Hirota, M. *Biosci Biotech Bioch* **2003**, *67*, 2658.
- (7) Dossel, L.; Gherghel, L.; Feng, X. L.; Mullen, K. *Angew Chem Int Edit* **2011**, *50*, 2540.
- (8) Chen, J. D.; Lu, H. Y.; Chen, C. F. *Chem-Eur J* **2010**, *16*, 11843.
- (9) Jones, D. J.; Purushothaman, B.; Ji, S. M.; Holmes, A. B.; Wong, W. W. H. *Chem Commun* **2012**, *48*, 8066.
- (10) Narita, A.; Feng, X. L.; Hernandez, Y.; Jensen, S. A.; Bonn, M.; Yang, H. F.; Verzhbitskiy, I. A.; Casiraghi, C.; Hansen, M. R.; Koch, A. H. R.; Fytas, G.; Ivasenko, O.; Li, B.; Mali, K. S.; Balandina, T.; Mahesh, S.; De Feyter, S.; Mullen, K. *Nat Chem* **2014**, *6*, 126.
- (11) Narita, A.; Verzhbitskiy, I. A.; Frederickx, W.; Mali, K. S.; Jensen, S. A.; Hansen, M. R.; Bonn, M.; De Feyter, S.; Casiraghi, C.; Feng, X.; Mullen, K. *Acs Nano* **2014**, *8*, 11622.
- (12) Muller, M.; Kubel, C.; Mullen, K. *Chem-Eur J* **1998**, *4*, 2099.
- (13) Simpson, C. D.; Brand, J. D.; Berresheim, A. J.; Przybilla, L.; Rader, H. J.; Mullen, K. *Chem-Eur J* **2002**, *8*, 1424.
- (14) Schwab, M. G.; Narita, A.; Hernandez, Y.; Balandina, T.; Mali, K. S.; De Feyter, S.; Feng, X. L.; Mullen, K. *J Am Chem Soc* **2012**, *134*, 18169.
- (15) Shifrina, Z. B.; Averina, M. S.; Rusanov, A. L.; Wagner, M.; Mullen, K. *Macromolecules* **2000**, *33*, 3525.
- (16) Wu, J. S.; Gherghel, L.; Watson, M. D.; Li, J. X.; Wang, Z. H.; Simpson, C. D.; Kolb, U.; Mullen, K. *Macromolecules* **2003**, *36*, 7082.
- (17) Ferrari, A. C. *Solid State Commun* **2007**, *143*, 47.
- (18) Reich, S.; Thomsen, C. *Philos T R Soc A* **2004**, *362*, 2271.
- (19) Dresselhaus, M. S.; Jorio, A.; Hofmann, M.; Dresselhaus, G.; Saito, R. *Nano Lett* **2010**, *10*, 751.
- (20) Ferrari, A. C.; Basko, D. M. *Nat Nanotechnol* **2013**, *8*, 235.

- (21) Ferrari, A. C.; Meyer, J. C.; Scardaci, V.; Casiraghi, C.; Lazzeri, M.; Mauri, F.; Piscanec, S.; Jiang, D.; Novoselov, K. S.; Roth, S.; Geim, A. K. *Phys Rev Lett* **2006**, *97*.
- (22) Malard, L. M.; Pimenta, M. A.; Dresselhaus, G.; Dresselhaus, M. S. *Phys Rep* **2009**, *473*, 51.
- (23) Saito, R.; Hofmann, M.; Dresselhaus, G.; Jorio, A.; Dresselhaus, M. S. *Adv Phys* **2011**, *60*, 413.
- (24) Jiao, L. Y.; Zhang, L.; Wang, X. R.; Diankov, G.; Dai, H. J. *Nature* **2009**, *458*, 877.
- (25) Castiglioni, C.; Tommasini, M.; Zerbi, G. *Philos T Roy Soc A* **2004**, *362*, 2425.
- (26) Maghsoumi, A.; Brambilla, L.; Castiglioni, C.; Müllen, K.; Tommasini, M. *J Raman Spectrosc* **2015**, n/a.
- (27) Negri, F.; Castiglioni, C.; Tommasini, M.; Zerbi, G. *J Phys Chem A* **2002**, *106*, 3306.
- (28) Cai, J. M.; Ruffieux, P.; Jaafar, R.; Bieri, M.; Braun, T.; Blankenburg, S.; Muoth, M.; Seitsonen, A. P.; Saleh, M.; Feng, X. L.; Mullen, K.; Fasel, R. *Nature* **2010**, *466*, 470.
- (29) Castiglioni, C.; Mapelli, C.; Negri, F.; Zerbi, G. *J Chem Phys* **2001**, *114*, 963.
- (30) Centrone, A.; Brambilla, L.; Renouard, T.; Gherghel, L.; Mathis, C.; Mullen, K.; Zerbi, G. *Carbon* **2005**, *43*, 1593.
- (31) Tommasini, M.; Lucotti, A.; Alfè, M.; Ciajolo, A.; Zerbi, G. *Spectrochimica Acta Part A: Molecular and Biomolecular Spectroscopy* **2016**, *152*, 134.
- (32) Brown, S. P.; Schnell, I.; Brand, J. D.; Mullen, K.; Spiess, H. W. *J Am Chem Soc* **1999**, *121*, 6712.
- (33) Ochsenfeld, C.; Brown, S. P.; Schnell, I.; Gauss, J.; Spiess, H. W. *J Am Chem Soc* **2001**, *123*, 2597.
- (34) Hansen, M. R.; Feng, X.; Macho, V.; Mullen, K.; Spiess, H. W.; Floudas, G. *Phys Rev Lett* **2011**, *107*.
- (35) Kivala, M.; Wu, D.; Feng, X.; Li, C.; Müllen, K. In *Mater Sci Tech-Lond*; Wiley-VCH Verlag GmbH & Co. KGaA: 2006.
- (36) Mali, K. S.; Adisoejoso, J.; Ghijssens, E.; De Cat, I.; De Feyter, S. *Accounts Chem Res* **2012**, *45*, 1309.

Chapter 4. Design and synthesis of nanographene molecules (NGs) with zigzag edges

In this chapter, several previously reported nanographene molecules (NGs) with partial zigzag edges have been introduced. Afterwards, a series of synthetic routes, including use of inter-molecular *McMurry* coupling, *Friedel-Craft* reaction, *Wittig* reaction, have been tested to obtain novel NGs with more zigzag edges. In particular, the synthesis of so-called full-zigzag hexa-*peri*-hexabenzocoronene (HBC) molecule has been tried.

4.1 Introduction

As mentioned in chapter 1, we demonstrated the classification of NGs including armchair-type, zigzag-type, as well as hybrid of both types. In contrast to a wide variety of armchair-type NGs, only a few NGs with zigzag edge structures had been reported in recent decades. The reason can be ascribed to the intrinsic instable nature of zigzag edge structures as well as lack of efficient synthetic methods. Nevertheless, the synthesis of novel NGs with zigzag edges, particularly with the full zigzag edge, is significant both in theoretical study and potential organic electronic applications.

In 2004, *Müllen et al.* reported the synthesis of novel NGs with partial zigzag periphery.¹ A key building block 9,11-diphenyl-10H-cyclopenta[*e*]pyren-10-one (**1**) was used as one reactant in Diels-Alder (D-A) reaction. Another reagent was phenylacetylene derivatives (**2**), which can be tailored according to molecular design. By using different phenylacetylene derivatives in D-A reaction and after subsequent cyclodehydrogenation, novel NGs with partial zigzag edges including **3** and **4** were successfully synthesized (Fig. 4-1a).

Later in 2006, *Müllen et al.* further reported the synthesis of other novel NGs with partial zigzag edges by fusing different number of carbon-carbon double bonds at the periphery of HBC, including **3**, **5** (fusing one additional double bond), **6**, **7** (fusing two double bonds) and **8** (fusing three double bonds) through similar synthetic method.² Notably, NGs **3** and **5** have same aromatic core except that the latter case has alkyl substitutes at the peripheral positions. Moreover, NGs from **5** to **8** have different symmetry as shown in Fig. 4-1b. The following investigations revealed that the change of

symmetry, which goes along with the partial change of the periphery type, had a pronounced influence upon their electronic properties.

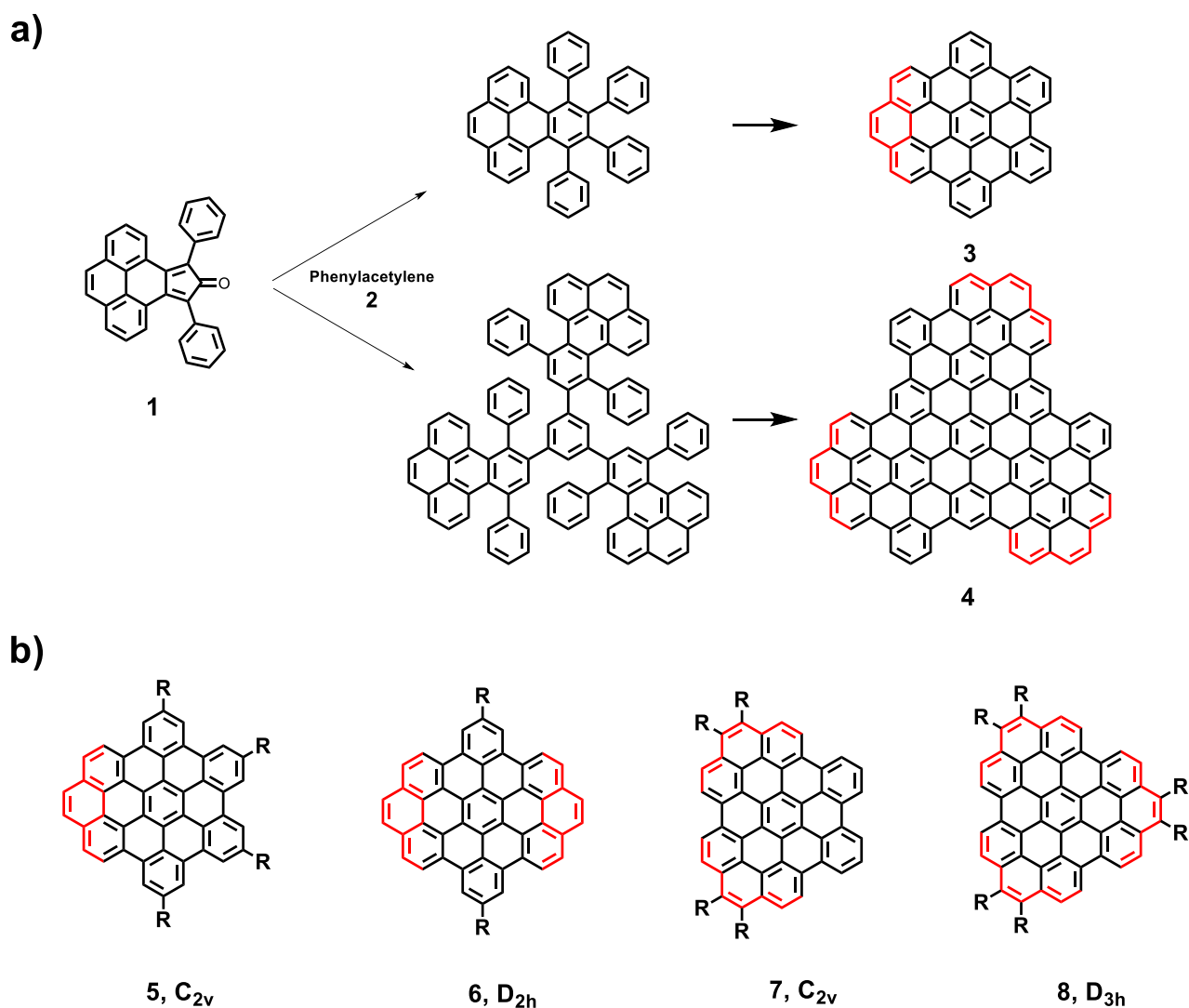


Figure 4-1. a) General synthetic route toward NGs 3 and 4 with partial zigzag edge structures. b) NGs 5, 6, 7, 8 with various partial zigzag edges as well as different symmetry.

Inspired by these excellent works, we can easily design molecules that fused more carbon-carbon double bonds on HBC based on same strategy as shown in Fig. 4-2 (Here, we name the NGs 5, 6, and 8 as 4-1, 4-2, and 4-3, respectively.). Importantly, NGs 4-4 with four zigzag sites and 4-5 with six zigzag sites have never been reported.

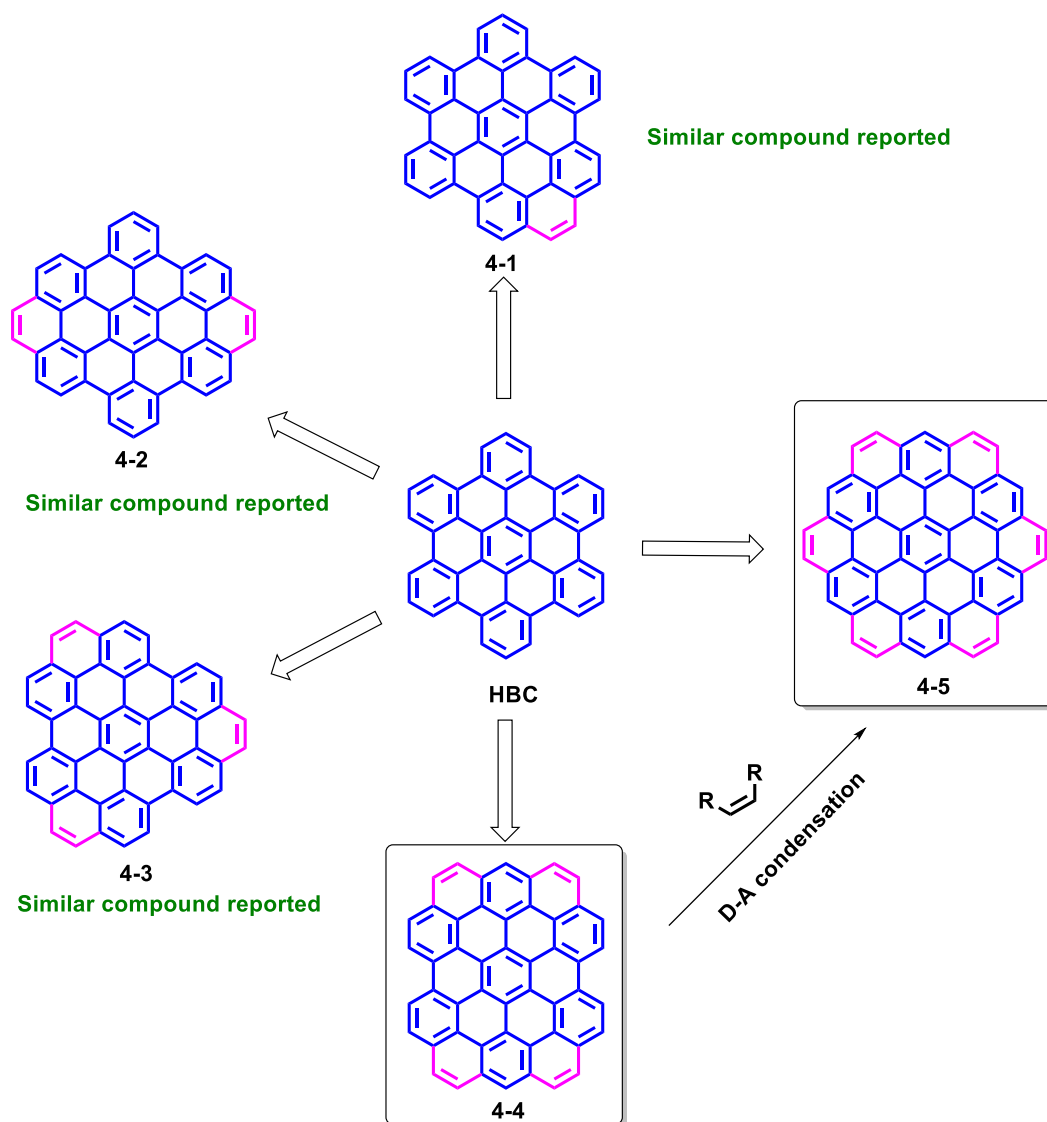


Figure 4-2. HBC and its derivatives fused with additional C-C double bonds

Herein, we targeted a synthesis of unreported NGs **4-4** and **4-5** with zigzag edge structures, which can be named as “tetra zigzag HBC” and “full zigzag HBC”, respectively (Fig. 4-3). By looking at their structures, it also appears to be possible to first synthesize compound **4-4**, and subsequently converted it to NG **4-5** by a two-fold Diels-Alder cycloaddition (Fig. 4-2).

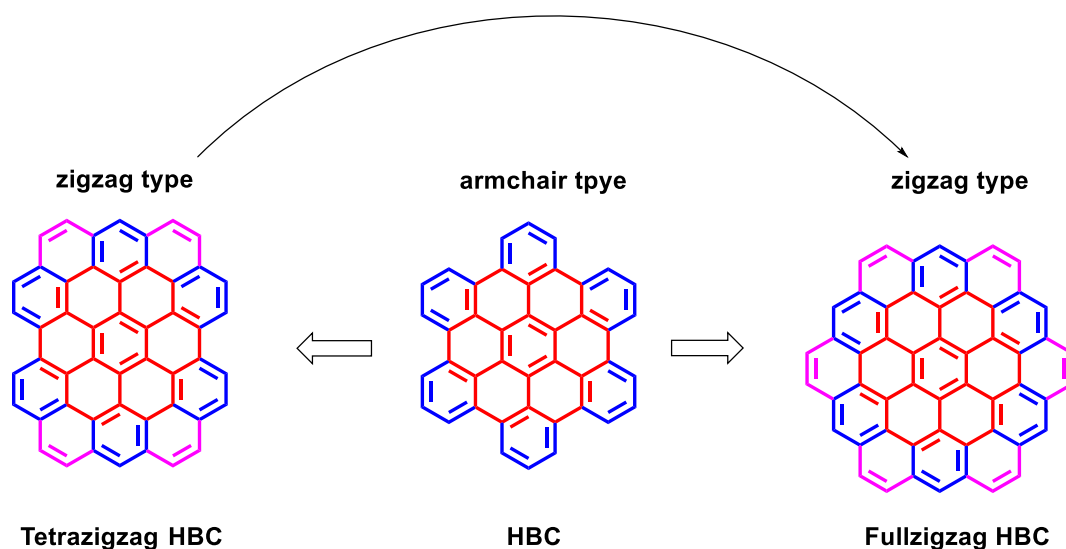


Figure 4-3. Structures of HBC and target molecules “tetra-zigzag HBC” and “full-zigzag HBC”

4.2 Target molecules and synthetic strategy

Considering the possible high reactivity of the zigzag edges and the synthetic feasibility, our strategy for the fabrication of full zigzag HBC **4-5** with D_{6h} symmetry was based on the initial preparation of substituted hexa-phenylbenzene (HPB) building blocks, and subsequent formation of six carbon-carbon double bonds, which can be carried out through chemical methods such as Metathesis³⁻⁵ and *McMurry* reactions (Fig. 4-4).⁶⁻¹⁰ Regarding the fabrication of tetra-zigzagHBC **4-4** with D_{2h} symmetry, the Friedel-Craft reaction¹¹⁻¹⁴ is selected. In this case, we can build up the HBC core firstly, and then fuse four carbon-carbon double bonds on the armchair edge.

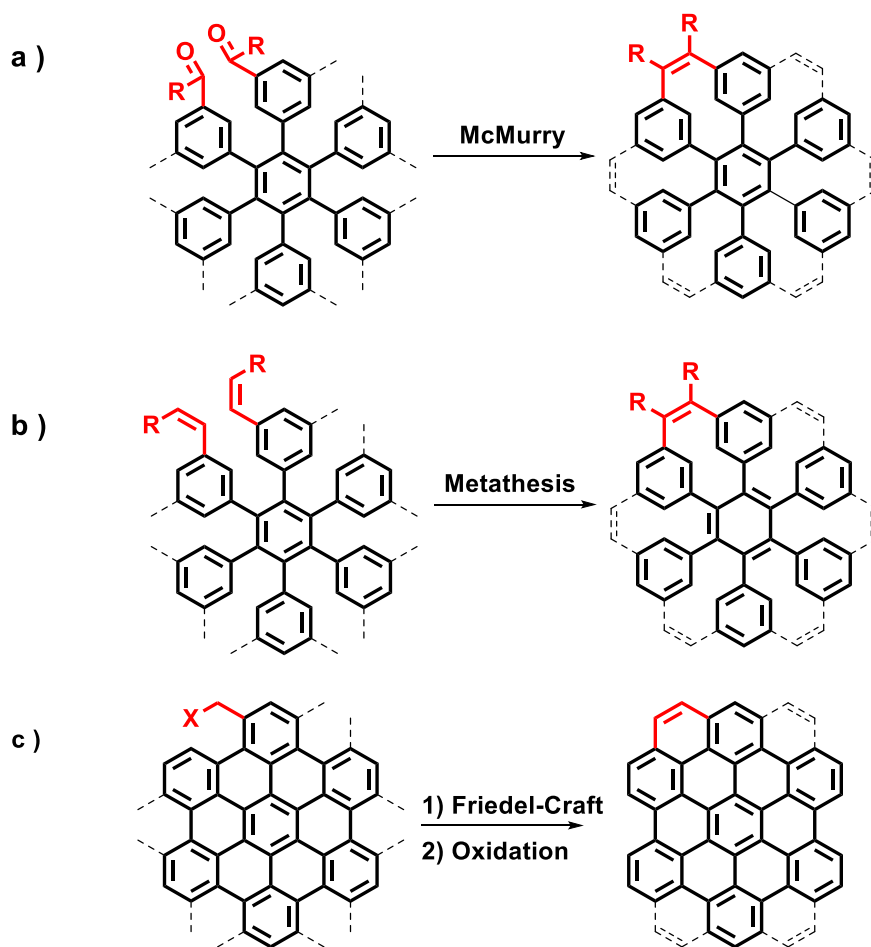


Figure 4-4. Possible chemical methods used to fuse C-C double bond on the armchair edge of HBC aromatic core, a) *McMurry* coupling; b) Metathesis; c) Friedel-Craft reaction.

4.2.1 Design and synthetic attempt toward full-zigzag HBC (4-5)

According to the above-mentioned synthetic strategy, we firstly tried the synthesis of “full-zigzag HBC” **4-5** via *McMurry* coupling and Metathesis methods. The HBC aromatic core with D_{6h} symmetry can generally be obtained by the cyclotrimerization of substituted 1,2-diphenylethyne to afford HPB precursor, followed by the cyclodehydrogenation (Fig. 4-5).¹⁵ By introducing C-C double bonds or carbonyl groups, the Metathesis and the *McMurry* chemistry can be applied, respectively. It should be noted that the formation of double bonds between neighboring two phenyl groups should be performed ahead of the cyclodehydrogenation, since the planarization of HPB precursors with substituted group like double bonds and electron-withdrawing groups are often unsuccessful. If the compound with six new double bonds could be synthesized successfully, it would be further converted to full-zigzag HBC **4-5** via UV irradiation.

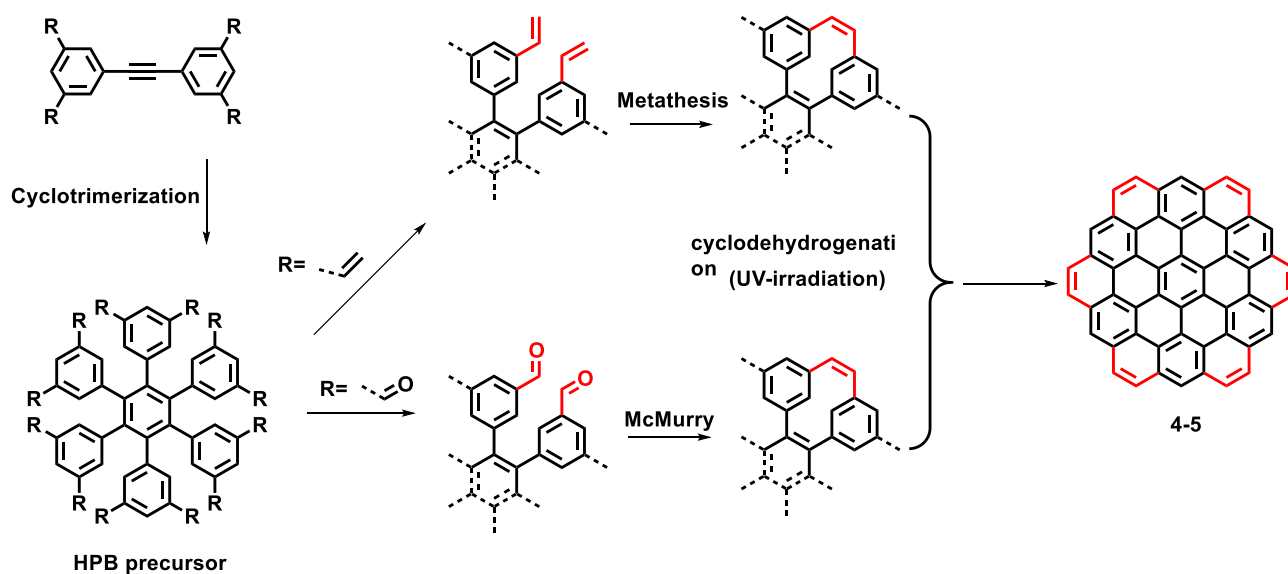


Figure 4-5. General synthetic route toward “full zigzag HBC” **4-5**

Based on the above-mentioned general ideas, we first used the *McMurry* chemistry. Thus we designed the synthetic route as shown in Fig 4-6.

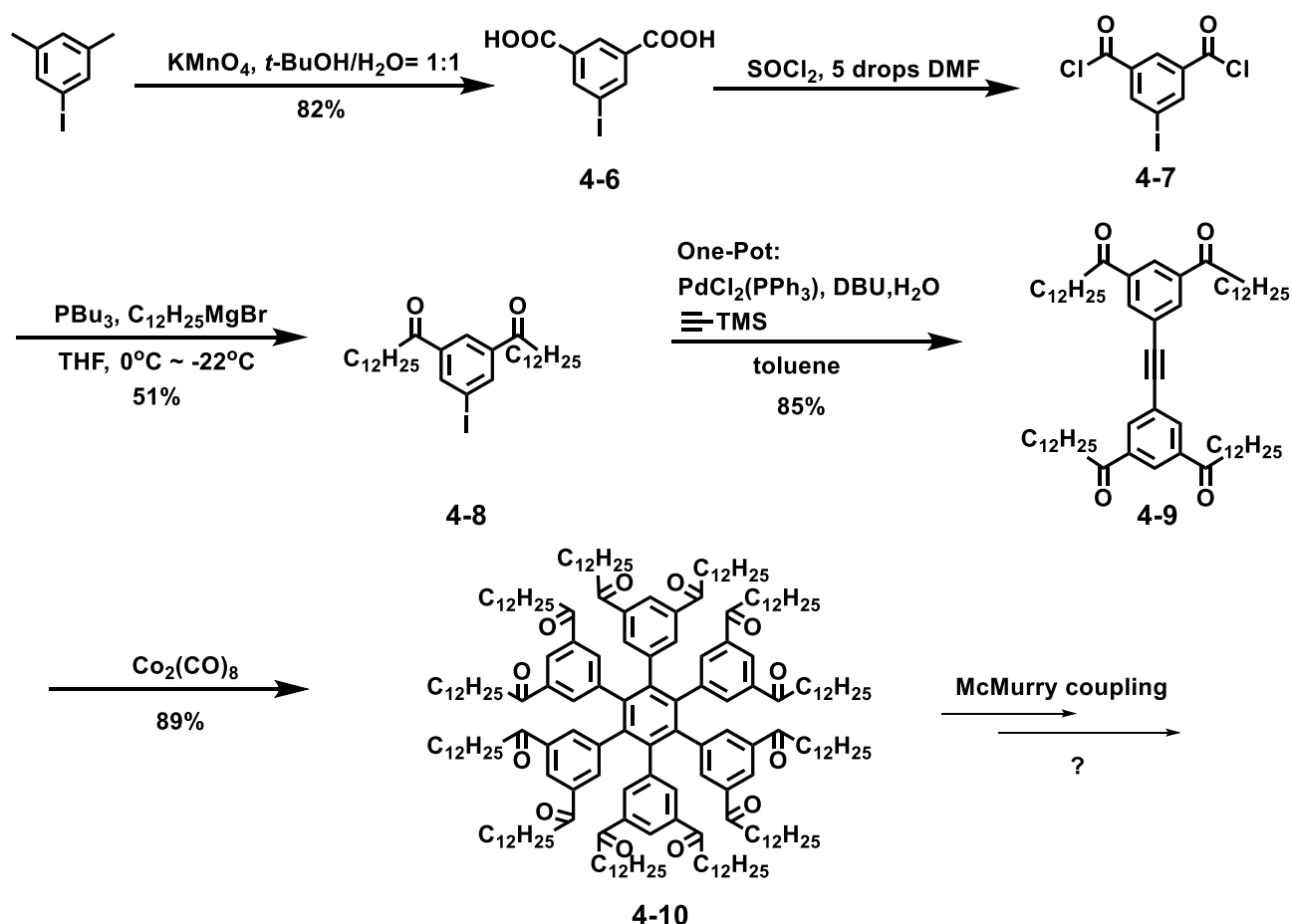


Figure 4-6. Synthetic route toward full zigzag HBC through *McMurry* coupling

Starting from 1-iodo-3,5-dimethylbenzene, the oxidation by potassium permanganate (KMnO_4) under a base condition afforded corresponding 5-iodoisophthalic acid **4-6** in 82% yield.¹⁶ Then, compound **4-6** was converted to 5-iodoisophthaloyl dichloride **4-7** by adding excess thionyl chloride (SOCl_2) and catalytic amount of DMF (5 drops). The resulting crude product of **4-7** was used for the next step without further purification after the workup, and compound **4-8** was obtained in 51% yield for two steps after a reaction with Grignard reagent, dodecylmagnesium bromide ($\text{C}_{12}\text{H}_{25}\text{MgBr}$), catalyzed by tributylphosphine (PBu_3).¹⁷ Next, a one-pot *Sonogashira* coupling of compound **4-8** and ethynyltrimethylsilane was performed to afford compound **4-9** in 85% yield.¹⁸ At last, compound **4-9** was subjected to the cyclotrimerization reaction catalyzed by dicobalt octacarbonyl ($\text{Co}_2(\text{CO})_8$) to give substituted HPB **4-10**. Compounds from **4-8** and **4-9** to **4-10** were identified by ^1H NMR analysis and MALDI-TOF MS (Fig. 4-7).

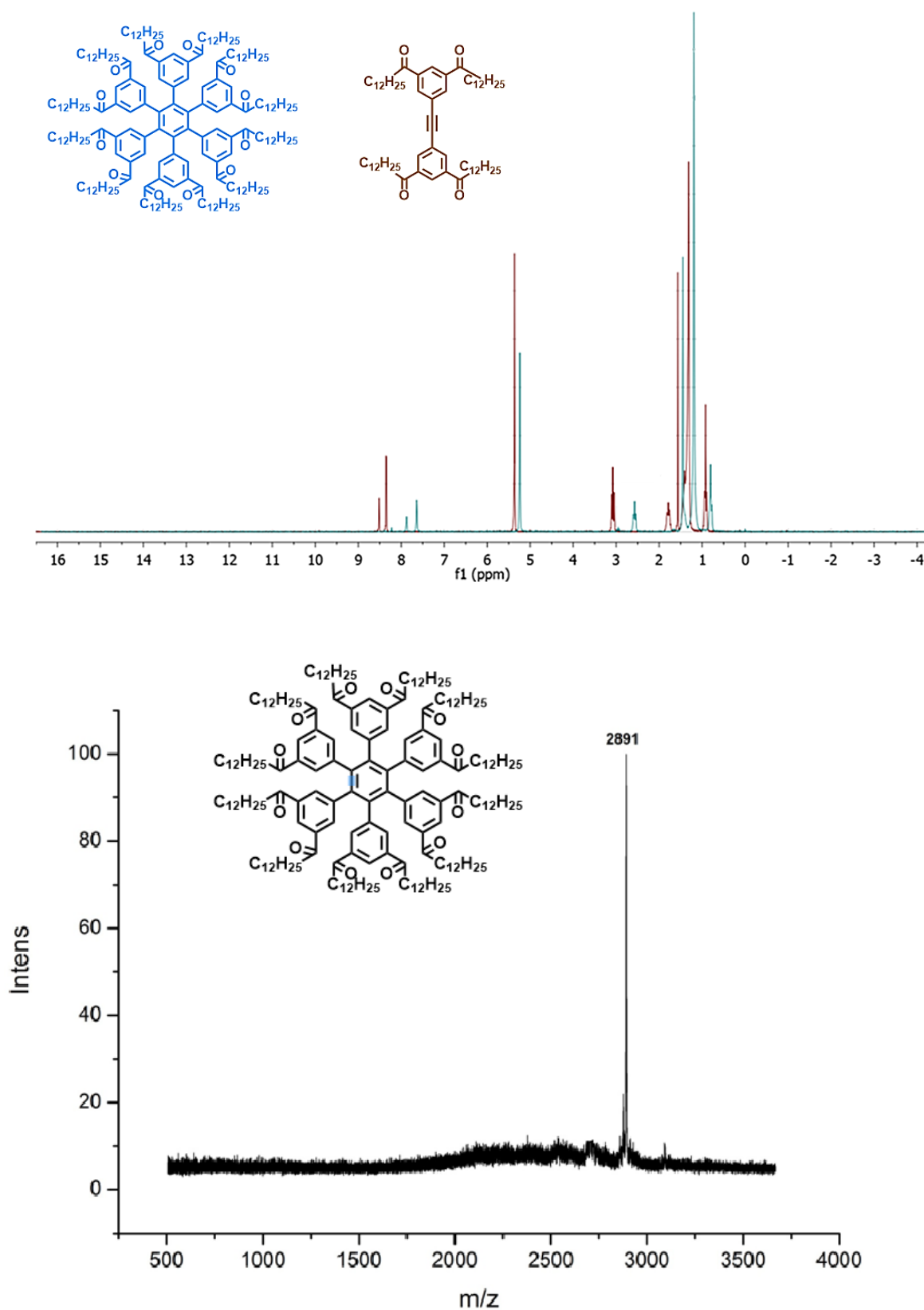


Figure 4-7. Top) proton NMR of compound 4-9 and 4-10; down) MALDI-TOF spectra of compound 4-10

Once compound **4-10** was obtained, the next crucial step is *McMurry* coupling reaction. Firstly, the condition reported in Ref. ¹⁹ was tested: To a stirred suspension of zinc powder in dry tetrahydrofuran was added titanium tetrachloride drop by drop at 0 °C under argon atmosphere, and the mixture was refluxed to generate a black slurry. Afterwards, the solution of **4-10** was added slowly by a syringe. After heating at 80 °C for 6 hours, the resulting brownish solution was cooled and quenched (Fig. 4-8). After standard work-up procedure, the resulting residue was subjected to MALDI-TOF MS measurement. However, the mass spectra showed no signal for the desired product **4-11**.

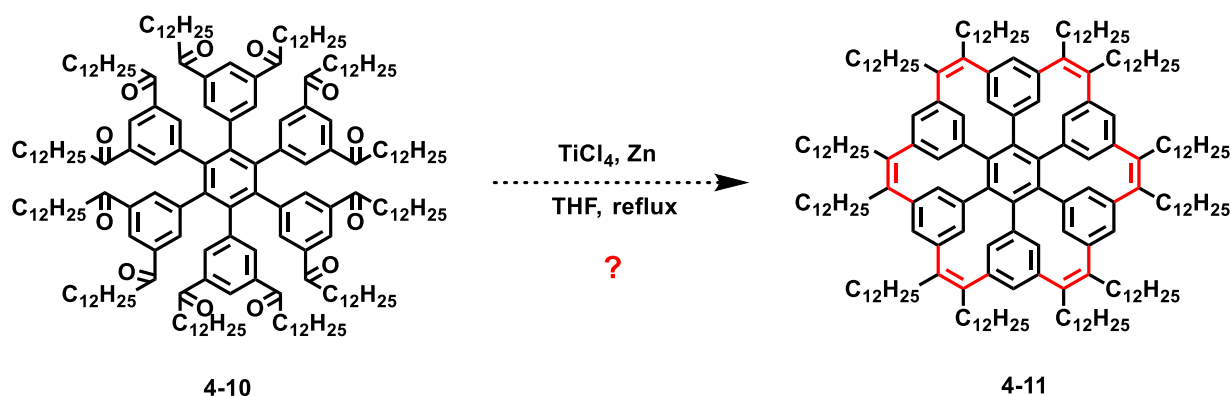


Figure 4-8. Classic reaction condition of *McMurry* reaction

In the previously reported reaction conditions, the intramolecular *McMurry* coupling required a low concentration of carbonyl reactant and long reaction time.^{9,20} In our case, considering the highly twisted HPB structures of reactant and that a six-fold intramolecular coupling need to be performed, a large excess of titanium reagent as well as reducing reagent (Zn, Zn-Cu couple or LiAlH₄) might be needed. A solvent with higher boiling point could be necessary as well for overcoming possible steric hindrance during the carbonyl coupling. Thus, a series of other reaction conditions using combination of TiCl₃/Zn-Cu, TiCl₃/LiAlH₄ and various solvent such as dimethoxyethane (DME) and *o*-dichlorobenzene were subsequently tested.^{10,21} The reactions were carried out basically with the same procedure as the classical condition except that carbonyl reactant **4-10** was added gradually over 30 h using a syringe pump to minimize the concentration of the carbonyl reactant. After refluxing for another 24 hours, the reaction was quenched with water and subjected to a standard workup procedure. The obtained residue was firstly subjected to thin-layer chromatography (TLC) analysis. The TLC plate indicated that the starting material **4-10** was totally converted. A series of new spots with different polarity were formed (Ethyl acetate/ petroleum ether= 1:50). There were

one weak polar spot (spot 1) on the top and a series of stronger polar spots (spot 2) at the bottom of TLC plate (Fig. 4-9).

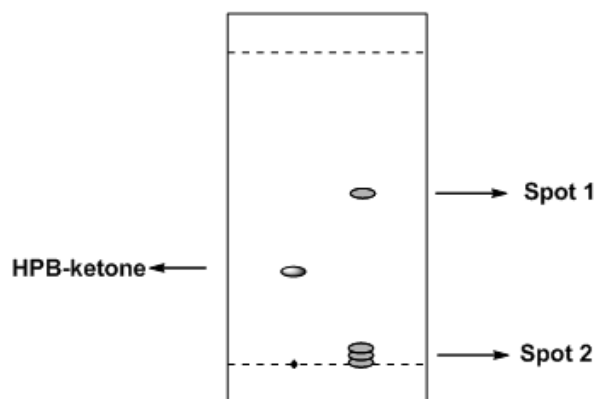


Figure 4-9. TLC results of optimized *McMurry* coupling reaction. (Ethyl acetate/ petroleum ether= 1:50)

The spot 1 was then separated by column chromatography on silica gel, and subjected to proton NMR and MALDI-TOF MS measurement. From the proton NMR spectrum, we can see that the signal belonging to aromatic protons shifted to higher field compared to precursor **4-9** and **4-10**, which indicated that carbonyl groups were reduced or reductively coupled. However, the spectrum obviously indicated that it was not a pure compound but more like a mixture of different compounds. Same conclusion was also drawn from the MALDI-TOF MS spectrum, which displayed a series of peaks with m/z values spanning from 2095 to 2723 (Fig. 4-10). These peaks could not be assigned to any products with partially coupled double bonds with expected m/z of 2858.4, 2826.4, 2794.5, 2762.5, and 2730.5 or desired product **4-11** (expected $m/z = 2698.5$).

Regarding the spot 2, these compounds cannot be our desired product since desired fully intramolecularly coupled product **4-11** should have smaller polarity compared with that of its HPB precursor, considering the elimination of strong-polar carbonyl groups during the *McMurry* coupling.

These results thus indicated that the *McMurry* coupling of **4-10** did not enable the synthesis of **4-11**, resulting in the formation of a series of side products, which could not be identified. One possible reason could be due to the high steric hindrance during the six-fold intramolecular coupling.

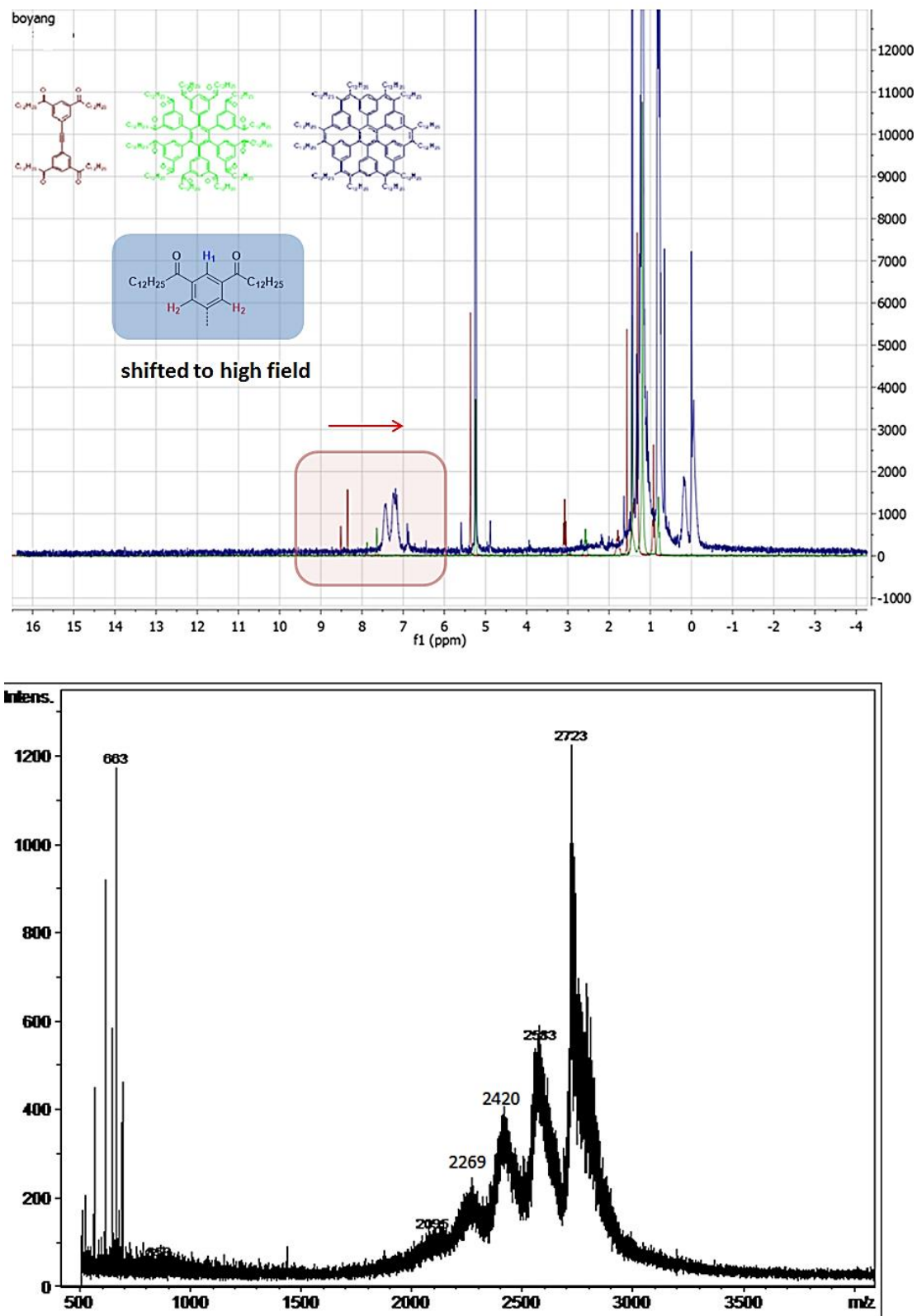


Figure 4-10. Proton NMR spectrum (top) and MALDI-TOF MS spectrum (bottom) of spot 1.

As mentioned above, another route is conversion of the carbonyl groups to carbon-carbon double bonds and the use of the Metathesis reaction. As shown in Fig. 4-11, the carbonyl groups can be transformed to C-C double bonds by *Wittig* reaction. However, the same problem with the high steric hindrance needs to be overcome even if the twelve-fold *Wittig* reaction can be successfully performed.

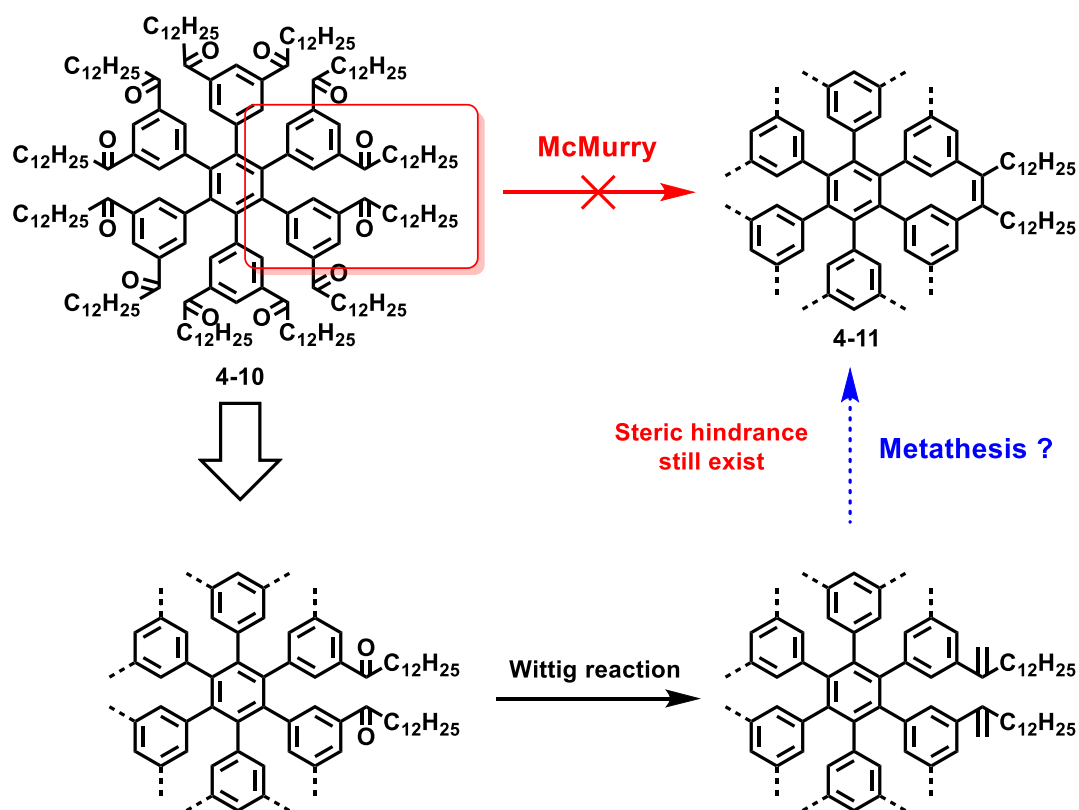


Figure 4-11. Possible Metathesis route toward compound 4-11

Considering this steric hindrance problem, fabrication of full zigzag HBC 4-5 from tetra zigzag HBC 4-4 via two fold Diels-Alder cycloaddition reaction seems a more feasible and promising way to realize our target (Fig. 4-12). Therefore, we decided to set aside the aforementioned methods for the direct preparation of full-zigzag HBC 4-5, and to first focus on the synthesis of tetra-zigzag HBC 4-4.

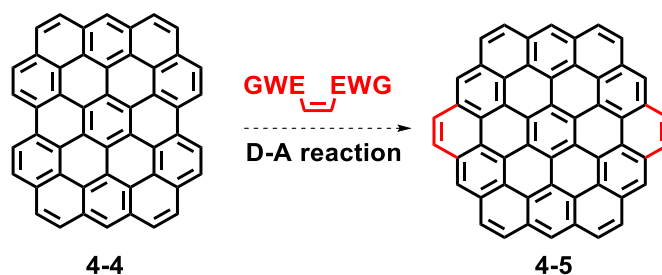


Figure 4-12. Possible transformation from compound 4-4 to 4-5

4.2.2 Design and synthesis of tetra zigzag molecule (4-4)

As mentioned in the synthetic strategy, our plan is to fabricate tetra zigzag HBC 4-4 through a Friedel-Craft (F-C) type reaction.^{12,14} The critical step is the introduction of the functional groups on the HPB precursor at specific positions shown in Fig. 4-13, which can eventually lead to the target tetra-zigzag HBC with D_{2h} symmetry. Here, the functionalized HPB precursor with the desired substitution pattern can be obtained by two-fold *Suzuki* coupling reaction between 2,3,5,6-tetraphenyl-1,4-dihalogenbenzene and di-functionalized phenylboronic acid.

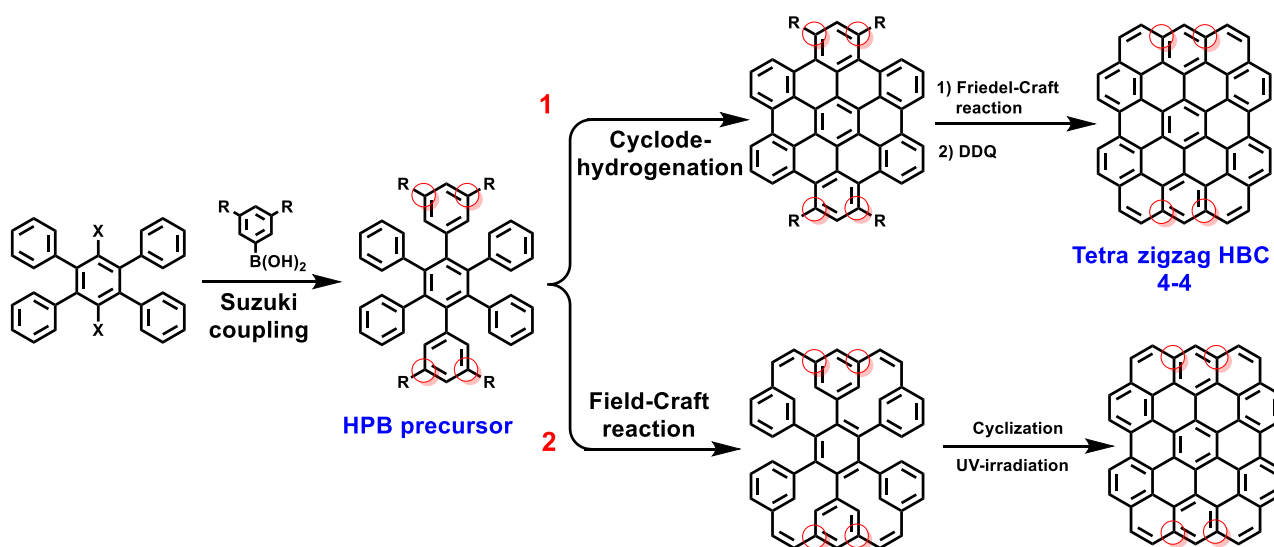


Figure 4-13. Possible synthetic routes toward tetra zigzag HBC 4-4

Once the desired HPB precursor is obtained with functional groups suitable for the subsequent F-C reaction, the next step will be to choose a proper synthetic pathway to prepare target molecule 4-4.

Here, there are two possible routes (Fig. 4-13): 1) perform the cyclodehydrogenation firstly, and then fuse four carbon-carbon double bonds into a π -conjugated system to provide **4-4** via the F-C reaction; 2) perform the F-C reaction firstly, and afterward cyclize the resulting compound via UV irradiation to give compound **4-4**. Comparing these two routes, the former one is more promising because the initial cyclodehydrogenation will form a planar HBC core, which could make the subsequent F-C reaction easier. The latter route 2 will possibly be hampered by the steric hindrance during the F-C reaction on the highly twisted HPB precursor.

Therefore, we firstly designed synthetic route as shown in Fig. 4-14. Our idea was to test if compound **4-14** could be obtained in this way, and the functional groups could be further introduced afterward using the bromine substituents.

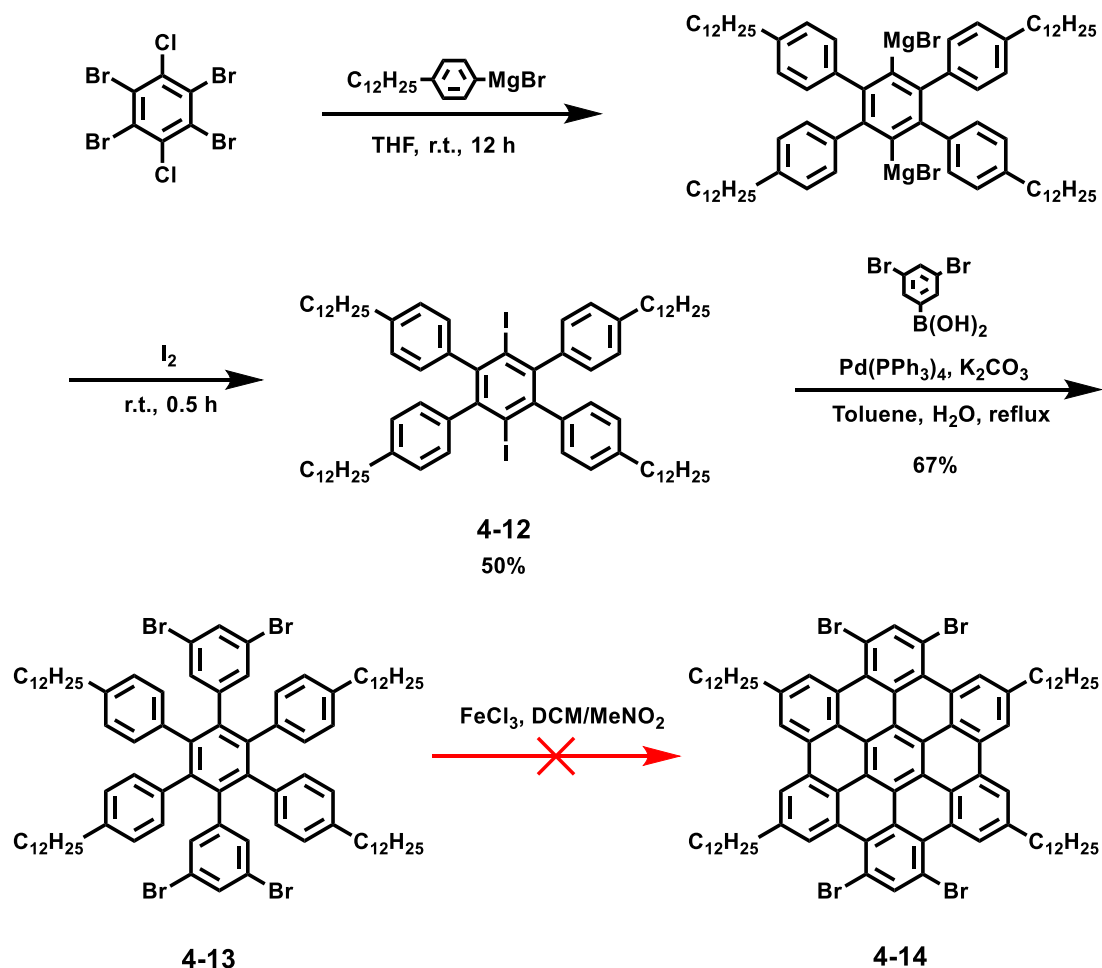


Figure 4-14. Synthetic route toward compound **4-14**

Treatment of commercially available 1,2,4,5-tetrabromo-3,6-dichlorobenzene with dodecylphenylmagnesium bromide in tetrahydrofuran (THF) at room temperature for 12 h led to the formation of dimagnesium intermediate, which was reacted with iodine to directly provide diiodobenzene **4-12** in 50% yield.²² Next, a twofold *Suzuki* coupling of compound **4-12** and 3,5-dibromophenylboronic acid was performed to give compound **4-13** in 67% yield. Then, cyclodehydrogenation of compound **4-13** was tested using iron(III) chloride, which however, did not provide the expected product **4-14**. The possible explanations were steric hindrance as well as electron-withdrawing effect caused by the bromine atoms.

Based on this unsuccessful result, we re-designed the synthetic route (Fig. 4-15), where the functional groups are introduced during the *Suzuki* coupling step. Here, we introduced benzyl ester groups, which could be converted to acyl chloride or halogenated alkyl chain for the intra-molecular F-C acylation or alkylation. As shown in Fig. 4-15, arylacetic acid ester **4-15** was prepared by a palladium-catalyzed arylation of acetoacetate esters and (3,5-dibromophenyl)trimethylsilane in 63% yield.²³ Next, trimethylsilane group was replaced by treatment with iodine monochloride to yield compound **4-16** in 85% yield.^{24,25}

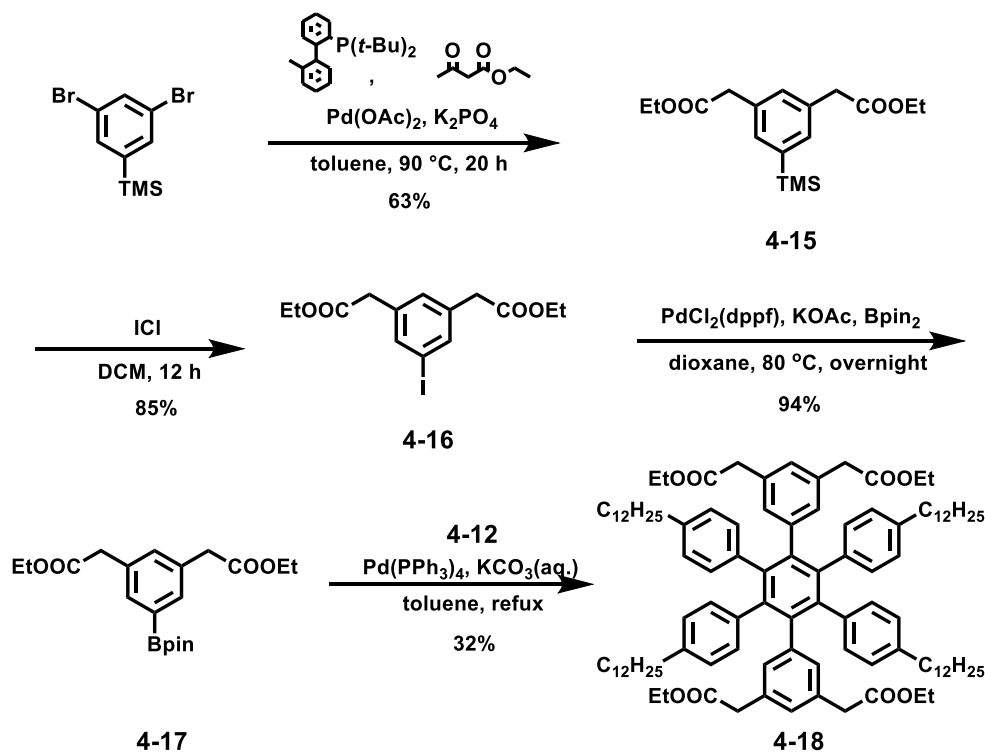


Figure 4-15. New synthetic route toward compound **4-18**

Next, a borylation of compound **4-16** was performed to give boronic ester **4-17** in 94% yield.²⁶ Then, a twofold *Suzuki* coupling of compounds **4-17** and **4-12** was performed to afford target molecule **4-18** in 32% yield.²⁷

With compound **4-18** in hand, we tested the feasibility of the intra-molecular F-C reaction. As displayed in Fig. 4-16, ethyl ester groups on compound **4-18** could be converted to acyl chloride and 2-chloroethyl groups, which enabled the F-C acylation and alkylation, respectively. The F-C acylation route was tested firstly as shown in Fig 4-16a. Acyl chloride **4-20** was prepared from compound **4-18** in two steps with 85% yield. F-C acylation catalyzed by Lewis acid aluminum chloride (AlCl₃) was then tested with compound **4-20**. However, the desired product **4-21** could not be generated, probably due to the high steric hindrance of the twisted HPB structure of **4-20**. In this case, hydrogenation could not be performed prior to the F-C reaction due to the instability of the acyl chloride.

Subsequently, another route (Fig. 4-16b) was tried as well. Compound **4-18** can be reduced to corresponding alcohol **4-22** in 79% yield, followed by the conversion of the hydroxyl groups to chlorine atoms to provide compound **4-23** in 81% yield.²⁷ Then, a dehydrogenation reaction of **4-23** was carried out using FeCl₃.

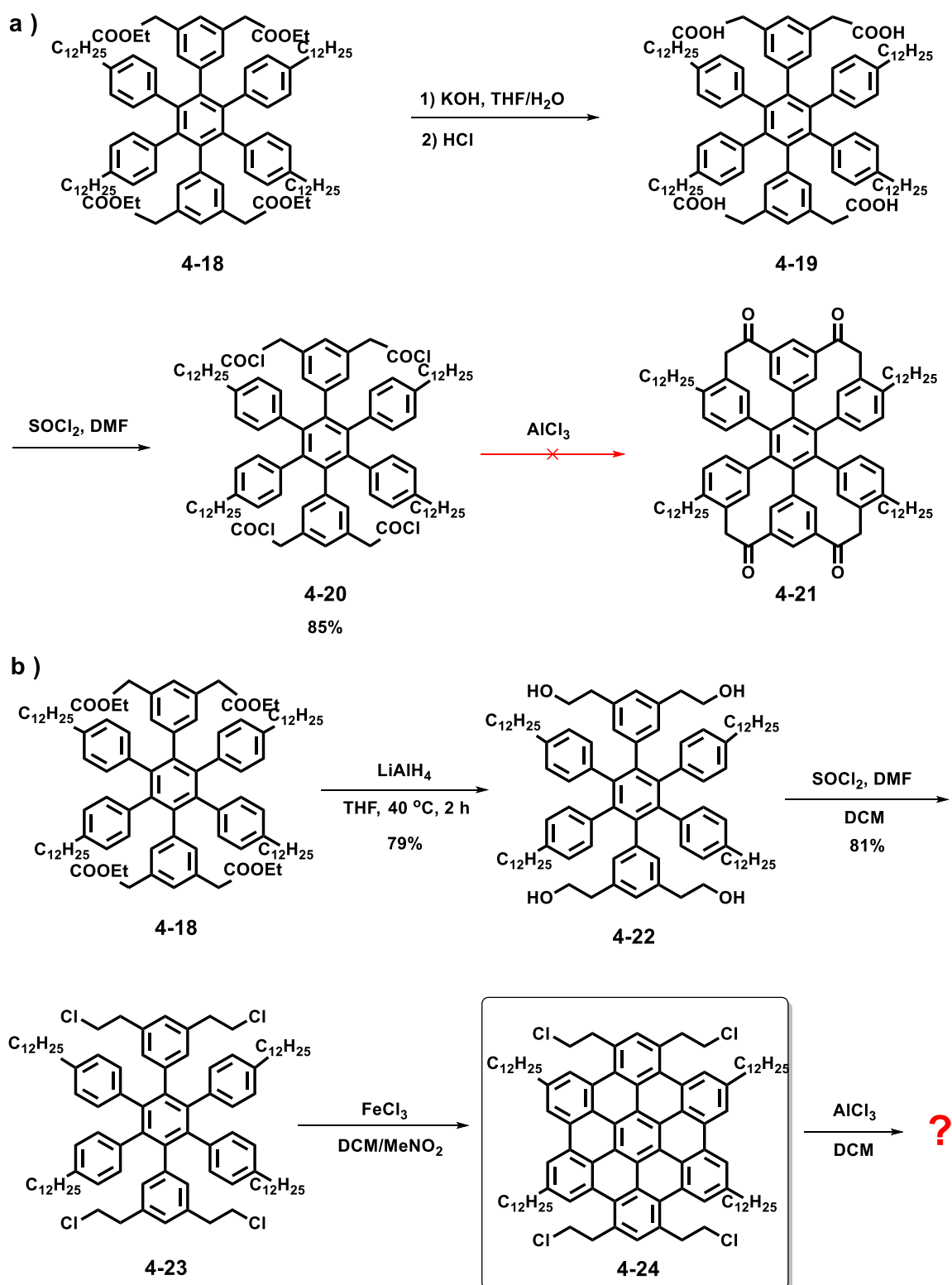


Figure 4-16. Synthetic routes toward tetra zigzag HBC via: a) Field-Craft acylation; b) F-C alkylation

As showed in Fig. 4-17, the MALDI-TOF mass analysis of the resulting crude product indicated that the cyclodehydrogenation of **4-23** proceeded, but resulted in a mixture with the largest signals

derived from di-chlorinated compounds such as **4-25**. A signal from non-chlorinated compound **4-24** (expected $m/z = 1442.86$) and other signals corresponded to further chlorinated compounds were detected. Interestingly, products after partial intra-molecular F-C alkylation were also observed, which could be explained by the use of the FeCl_3 that acted as Lewis acid like AlCl_3 .

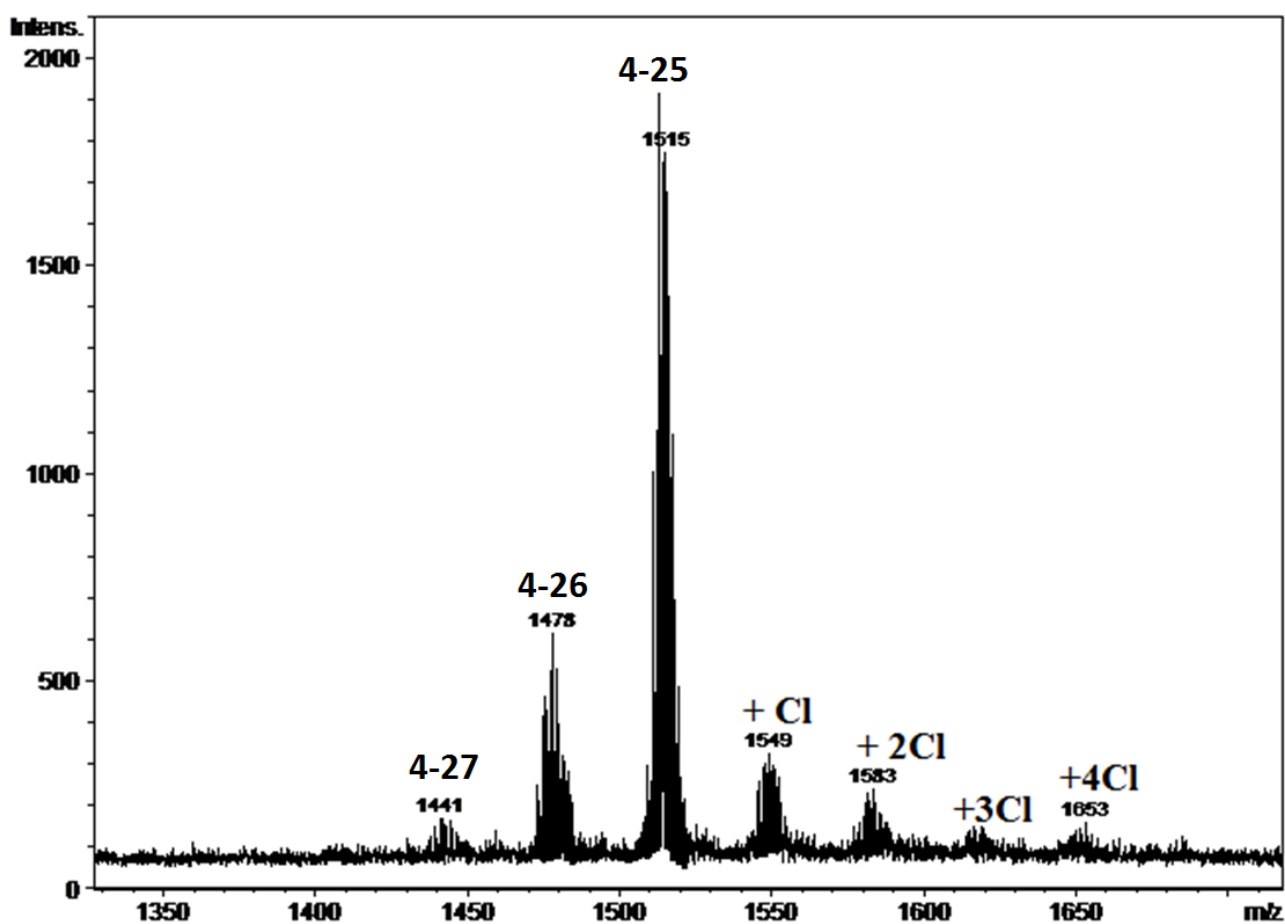
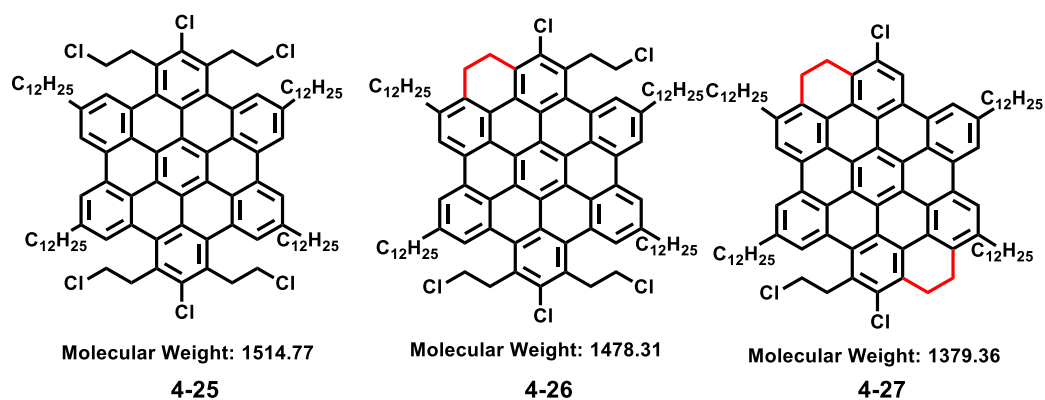
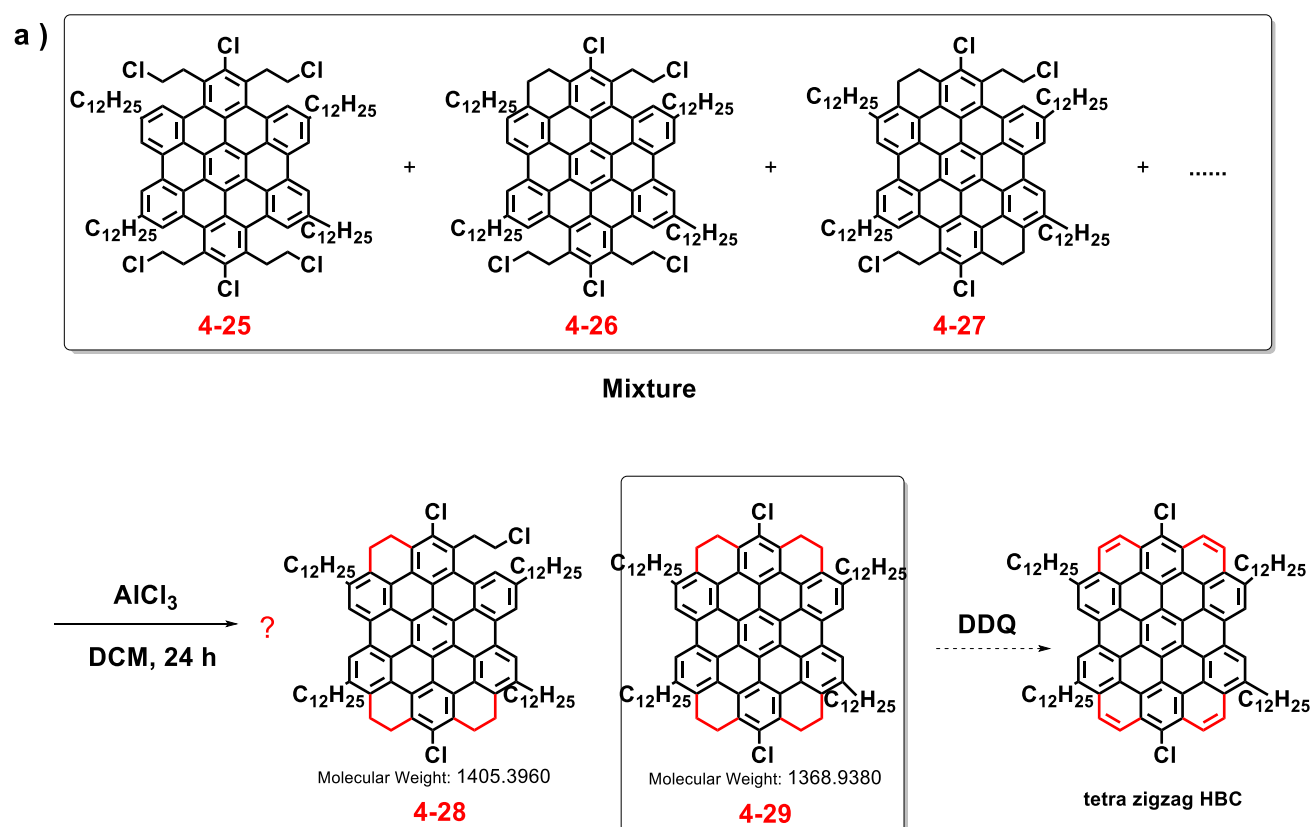


Figure 4-17. MALDI-TOF MS spectra and possible chemical structures of the products.

Since compounds **4-25~27** could still be converted to tetra-zigzag HBC via the intra-molecular F-C reaction and aromatization, we used the obtained mixture directly for the next step (Fig. 4-18a) to check if compound **4-29** could be generated. Using the mixture mentioned above as starting material and AlCl_3 as Lewis acid, the reaction was performed in dry dichloromethane under room temperature for 24 h. After standard workup, the resulting residue was subjected to MALDI-TOF mass characterization. As displayed in Fig. 4-18b, the mass spectrum indicated that three- and four-fold intra-molecular F-C alkylation had indeed occurred. The peaks in spectra can be assigned as compound **4-25**, **4-26**, **4-27**, **4-28** and **4-29**.



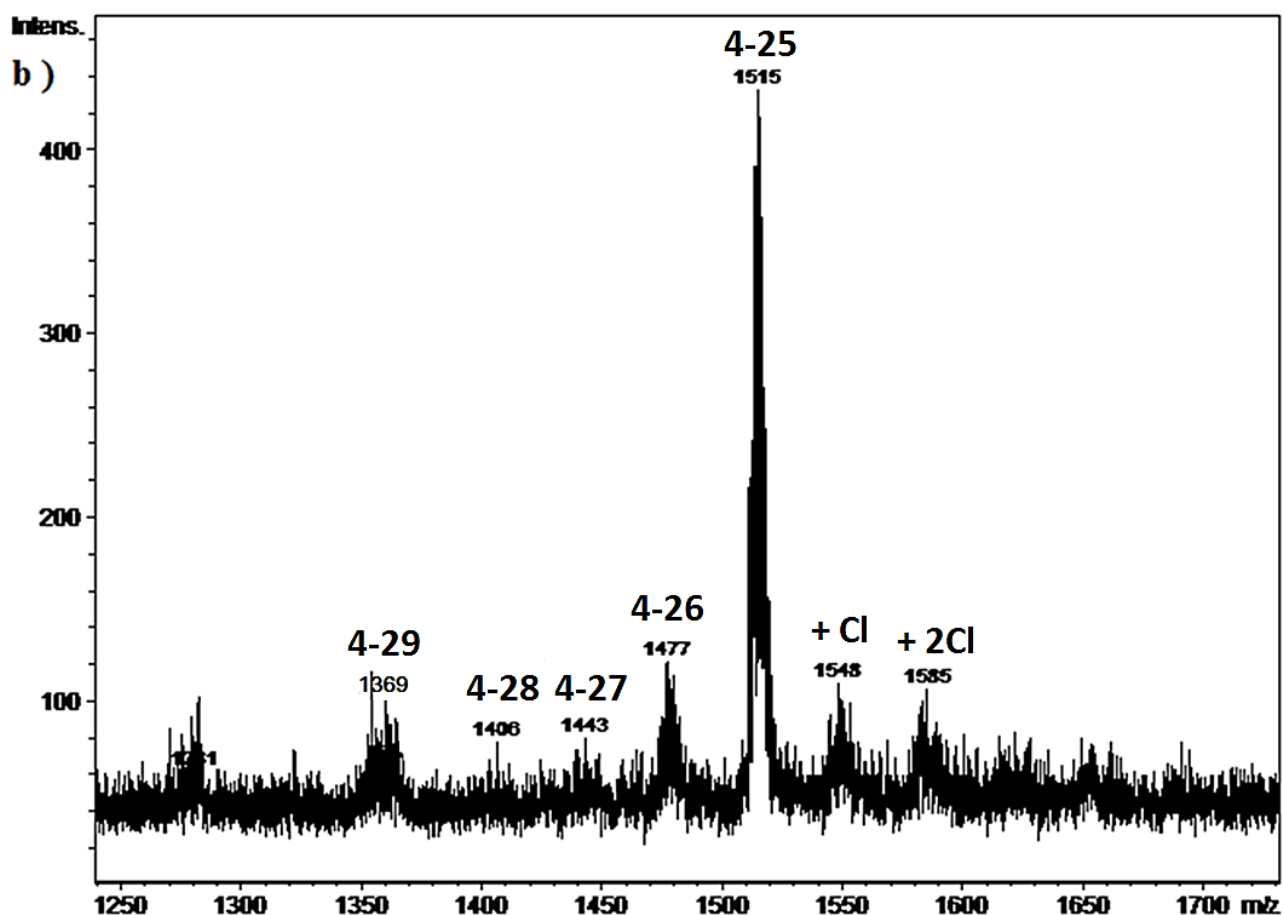


Figure 4-18. a) Synthetic scheme of F-C alkylation; b) MALDI-TOF MS of resulting residue

Judging from the mass spectrum, the desired compound **4-29** was indeed formed after F-C alkylation, which could be used for next oxidation reaction to afford final target tetra zigzag HBC molecule (Fig. 4-18a). However, the spectrum suggested that the main product was still precursor **4-25**, even after prolonged reaction time and increased reaction temperature to reflux. The F-C alkylation is a reversible reaction, and so it is understandable that there was a mixture of various products and the starting material still remained. If desired product **4-29** could be formed in an acceptable yield and isolated from other products, we could scale up the reactions to obtain sufficient amounts. However, the yield of **4-29** was seemingly very low, based on the relatively weak signal from the mass spectra of **4-29**, and the separation of **4-29** from other partially cyclized products was also difficult.

Based on the above-mentioned results, we concluded that the synthetic strategy through the F-C alkylation seemingly generated four-fold cyclized compound **4-29**, which was desired for the

target tetra-zigzag HBC. However, the existing problems of the low yield and the separation issue disabled this strategy as a feasible method in fabricating tetra zigzag HBC molecule.

4.3. Summary

In this chapter, we designed different synthetic routes and attempted the synthesis of full-zigzag HBC **4-5** and tetra-zigzag HBC **4-4** including *McMurry* coupling, metathesis, and F-C alkylation. However, all these methods turned out not to be as successful. Synthesis of NGs with zigzag edges like compounds **4-4** and **4-5** thus still remains a challenging work to be pursued.

Moreover, a series of novel molecules including **4-9**, **4-10**, **4-14**, **4-18**, **4-19**, **4-23**, and **4-24** were synthesized for the first time. Although these novel molecules were intermediates for synthesizing full-zigzag or tetra-zigzag HBC molecules, they still were interesting chemical molecules to be investigated and potentially used for other purpose.

4.4 References

- (1) Wang, Z. H.; Tomovic, E.; Kastler, M.; Pretsch, R.; Negri, F.; Enkelmann, V.; Mullen, K. *J Am Chem Soc* **2004**, *126*, 7794.
- (2) Kastler, M.; Schmidt, J.; Pisula, W.; Sebastiani, D.; Mullen, K. *J Am Chem Soc* **2006**, *128*, 9526.
- (3) Collins, S. K.; Grandbois, A.; Vachon, M. P.; Cote, J. *Angew Chem Int Edit* **2006**, *45*, 2923.
- (4) Iuliano, A.; Piccioli, P.; Fabbri, D. *Org Lett* **2004**, *6*, 3711.
- (5) Pelly, S. C.; Parkinson, C. J.; van Otterlo, W. A. L.; de Koning, C. B. *J Org Chem* **2005**, *70*, 10474.
- (6) Blaszcza.Lc; McMurry, J. E. *J Org Chem* **1974**, *39*, 258.
- (7) Eddy, R. L.; Gillilan.Pf; Ibarra, J. D.; McMurry, J. F.; Thompson, J. Q. *Am J Med* **1974**, *56*, 179.
- (8) Furstner, A.; Hupperts, A. *J Am Chem Soc* **1995**, *117*, 4468.
- (9) McMurry, J. E. *Chemical Reviews* **1989**, *89*, 1513.
- (10) McMurry, J. E.; Fleming, M. P. *J Am Chem Soc* **1974**, *96*, 4708.
- (11) Chang, C. Y.; Cheng, Y. J.; Hung, S. H.; Wu, J. S.; Kao, W. S.; Lee, C. H.; Hsu, C. S. *Adv Mater* **2012**, *24*, 549.
- (12) Hylarides, M. D.; Daub, G. H.; Vanderjagt, D. L.; Silverman, I. R. *J Labelled Compd Rad* **1983**, *20*, 1121.
- (13) Sartori, G.; Maggi, R. *Chemical Reviews* **2006**, *106*, 1077.
- (14) Yoshida, M.; Minabe, M.; Suzuki, K. *B Chem Soc Jpn* **1983**, *56*, 2179.
- (15) Muller, M.; Kubel, C.; Mullen, K. *Chem-Eur J* **1998**, *4*, 2099.
- (16) Blunt, M. O.; Russell, J. C.; Gimenez-Lopez, M. D.; Taleb, N.; Lin, X. L.; Schroder, M.; Champness, N. R.; Beton, P. H. *Nat Chem* **2011**, *3*, 74.

- (17) Maeda, H.; Okamoto, J.; Ohmori, H. *Tetrahedron Lett* **1996**, *37*, 5381.
- (18) Mio, M. J.; Kopel, L. C.; Braun, J. B.; Gadzikwa, T. L.; Hull, K. L.; Brisbois, R. G.; Markworth, C. J.; Grieco, P. A. *Org Lett* **2002**, *4*, 3199.
- (19) Rieger, R.; Kastler, M.; Enkelmann, V.; Mullen, K. *Chem-Eur J* **2008**, *14*, 6322.
- (20) McMurry, J. E.; Lectka, T.; Rico, J. G. *J Org Chem* **1989**, *54*, 3748.
- (21) McMurry, J. E.; Rico, J. G. *Tetrahedron Lett* **1989**, *30*, 1169.
- (22) Yang, X. Y.; Don, X.; Muellen, K. *Chem-Asian J* **2008**, *3*, 759.
- (23) Zeevaart, J. G.; Parkinson, C. J.; de Koning, C. B. *Tetrahedron Lett* **2004**, *45*, 4261.
- (24) Kissel, P.; Breitler, S.; Reinmuller, V.; Lanz, P.; Federer, L.; Schluter, A. D.; Sakamoto, J. *Eur J Org Chem* **2009**, 2953.
- (25) Bo, Z. S.; Schluter, A. D. *J Org Chem* **2002**, *67*, 5327.
- (26) Ishiyama, T.; Murata, M.; Miyaura, N. *J Org Chem* **1995**, *60*, 7508.
- (27) Zeng, Z. B.; Guan, Z. P.; Xu, Q. H.; Wu, J. S. *Chem-Eur J* **2011**, *17*, 3837.

Chapter 5. Chemical functionalization of nanographene molecules

In this chapter, a series of large polycyclic aromatic hydrocarbon molecules (PAHs) or nanographene molecules (NGs), such as HBC, C60 (triangle), C78, C96, C132, and C222 as well as few of their derivatives with alky chains were synthesized following reported procedures. After obtaining these NG molecules, functionalization of them via different chemical approaches such as Pd/C catalyzed hydrogenation and edge chlorination reaction were attempted, aiming at the synthesis of defined functional derivatives. Further, the optoelectronic properties and self-assembling behavior of resulting chlorinated NGs were investigated.

5.1 Introduction

As demonstrated in chapter 1, two-dimensional (2D), all benzenoid, shape-persistent PAHs have gained increasing importance in material science. Such 2D nanostructures exhibit interesting properties such as 2D crystallinity on surfaces, liquid crystallinity, intriguing photophysical features, and potential application in electronics and hydrogen storage.¹⁻⁷

Carbon-rich materials including fullerene-like structures, single-walled carbon nanotubes (SWNTs), and graphite nanofibers or graphene materials are the most promising materials as hydrogen sorbents. These materials can absorb hydrogen in the amount exceeding to the values required for hydrogen storage mobiles systems. They are promising candidates for applications as the hydrogen storage systems⁸. The hydrogenated products of carbon nanomaterials also have potentially useful applications, for example as batteries, catalysts and OLED materials⁹. Smaller nanostructures such as hydrogenated NGs are also promising H₂ storage materials. Therefore, we conceived chemical reduction of the small NGs for the purposes of yielding hydrogen storage materials as well as novel functional NGs with defined molecular structures. Besides, parent NGs without side substituents suffer from a relatively low solubility, which can be ascribed to their planarity, causing strong aggregation effect in solution. One solution is to employ side substituents at the NGs' periphery from the very beginning of the whole synthesis. An alternative solution is chemical functionalization after the synthesis, including two general strategies: functionalization 1) at the edge via the replacement of peripheral hydrogen atoms with functional groups; 2) on the basal plane of NGs via covalent addition to C=C bonds. Moreover, the electronic properties of NGs can be modified after the functionalization.

Regarding the former strategy, precise edge functionalization is a long-sought and appealing strategy towards controllable manipulation of the physical properties of graphene¹⁰⁻¹³. Moreover, the precise edge functionalization is also feasible in small NGs. One typical example is perchlorocoronene, which was first synthesized in 1988,¹⁴ by complete edge chlorination of coronene precursor. The obtained fully edge chlorinated coronene had been proven as a non-planar molecule. Notably, the perchlorocoronene can be further functionalized via nucleophilic substitution reaction. For example, the further thiolation of perchlorocoronene led to new class of molecules, which were considered as members of a new prospective host series.

Among many methods of the latter strategy (such as *Friedel-Crafts* reaction, diazonium salt addition^{15,16}), the hydrogenation reactions, namely addition of hydrogen atoms to carbon-carbon double bonds, are classical and feasible ones. The saturated periphery even helped the assembling to highly order columnar structures via π - π stacking by some interlocking effect.

Here, we introduced to apply these methods to other bigger conjugated NGs such as C₆₀, C₉₆, which may provide novel defined molecules or functional materials through reactions including chemical reduction and edge chlorination.

5.2 Edge chlorination of NGs

As aforementioned in last section, edge chlorination is a promising chemical functionalization protocol for NGs. We chose a series of unique well-defined NG molecules, namely nanographenes for atomically precise edge chlorination. These nanographene molecules were synthesized by cyclodehydrogenation of dendritic polyphenylene precursors following the reported procedures.¹⁷

5.2.1 Synthetic strategy

The synthetic strategy is quite straightforward. In collaboration with [REDACTED], chlorination was accomplished in CCl₄ at 80 °C with excess iodine monochloride and catalyzed by AlCl₃. (Fig. 5-1a; e.g. C₄₂H₁₈ to C₄₂Cl₁₈) After quenching the reaction with ethanol, the precipitate was filtered and washed, providing chlorinated nanographenes C₄₂Cl₁₈ (**5-1**). Chlorination of other NG molecules was performed in the same synthetic procedure, affording corresponding chlorinated products: C₄₈Cl₁₈ (**5-2**), C₆₀Cl₂₂ (**5-3**), C₆₀Cl₂₄ (**5-4**), C₉₆Cl₂₇H₃ (**5-5**), C₁₃₂C₁₃₀H₂ (**5-6**), and C₂₂₂Cl₄₂ (**5-7**) (Figure 5-1b) in a yield of 83–97%.

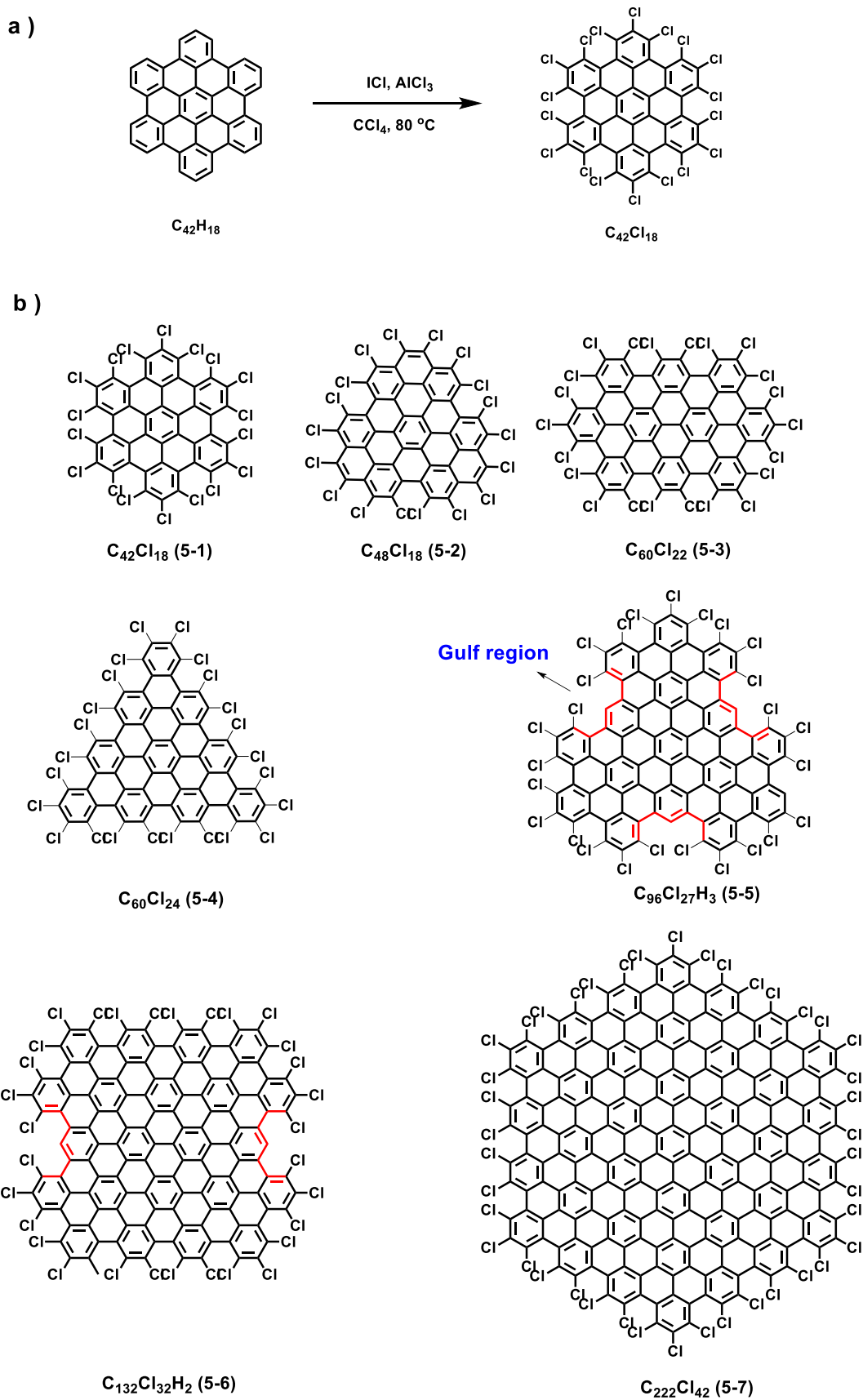


Figure 5-1. a) General synthetic route of edge chlorination b) Edge chlorinated products from 5-1 ~ 5-7

5.2.2 Characterization and analysis of chlorinated nanographenes

Once the chlorinated nanographene molecules were synthesized, the elemental composition of chlorinated products **5-1**~**5-7** was characterized and confirmed by MALDI-TOF MS. As shown in Figure 5-2a, there was a pattern of many peaks due to the isotopic distribution in the respective mass spectra of **5-1**~**5-7**. The isotopic distribution pattern of the mass peak was in good agreement with the calculated patterns (Fig. 5-2b), confirming the molecular formulae of **5-1** ~**5-7**, revealing their defined molecular composition.

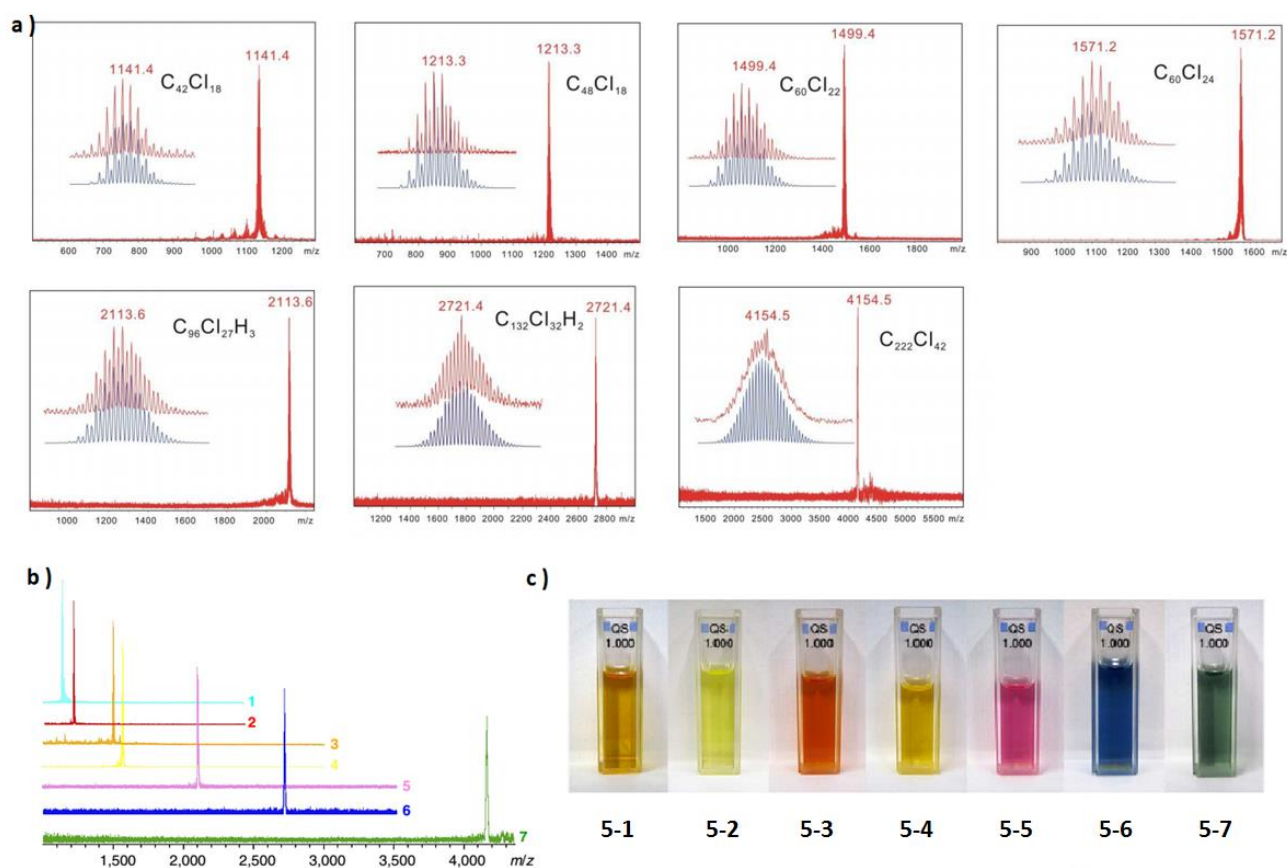


Figure 5-2. a) Mass spectra of chlorinated nanographenes (**5-1**~**5-7**), the calculated and experimental isotopic distribution patterns of mass peak are represented in blue and red, respectively; b) comparing the mass spectra of **5-1**~**5-7**; c) photos of the toluene solution of **5-1**~**5-7**.

A longer reaction time or higher reaction temperature did not lead to further chlorination or destruction of the products. Thus, the chlorination appears to occur selectively at the nanographene edges by electrophilic substitution, whereas chlorine substitution did not affect the sp^2 framework of nanographene under the reaction conditions. Interestingly, in contrast to the complete edge

chlorination in the case of **5-1**~**5-4** and **5-7**, three and two hydrogen atoms remained in **5-5** and **5-6**, respectively, after the chlorination reaction (Figure 5-1b). The number of unreacted hydrogens was exactly the same as that in the gulf regions in **5-5** and **5-6** (as show in Figure 5-1b). Remarkably, we were able to record the ^1H NMR spectrum of **5-5** in 1,1,2,2-tetrachloroethane- d_2 at 120 °C, which is the largest nanographene measured by ^1H NMR to date (Figure 5-3). We assume that the hydrogen atoms in the gulf region cannot be replaced due to the steric hindrance induced by the neighboring substituted chlorines.

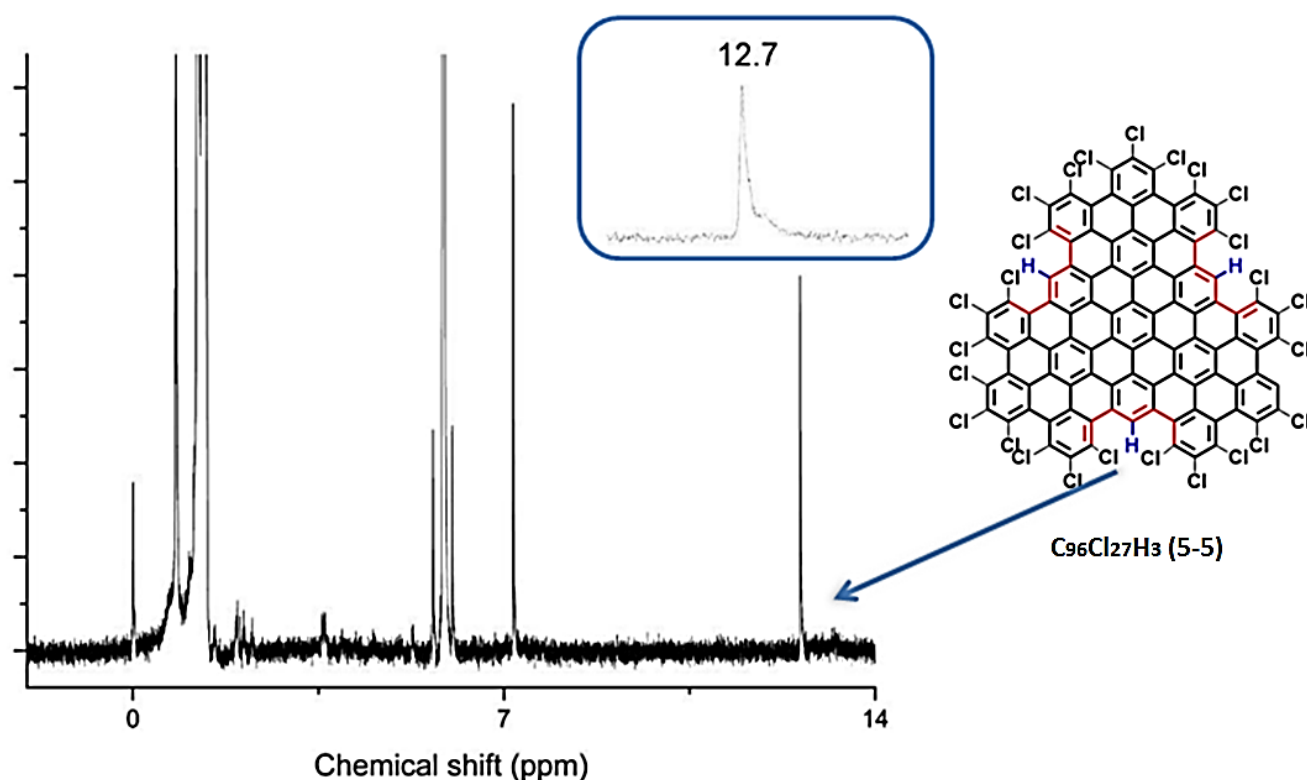


Figure 5-3. ^1H NMR spectrum of **5-5**. The data were acquired in tetrachloroethane- d_2 at 120 °C. The ^1H NMR signal of **5-5** appears at 12.7 ppm. The inset image shows the singlet characteristic of ^1H NMR peak of **5-5**, which confirms the equivalent chemical environment of three hydrogen atoms in **5-5**.

In comparison with the insoluble nature of parent nanographenes with hydrogen termination (Figure 1-10), chlorinated molecules **5-1**~**5-7** can be readily dissolved to form homogeneous solutions in common organic solvents such as toluene, chloroform, and carbon disulphide (Figure 5-2c; typical concentrations of saturated carbon disulphide solutions of **5-1**~**5-7** range from 4.0 to 0.2 mg ml^{-1}).

Therefore, taking advantage of the increased solubility and the well-defined chemical structures, our colleague [REDACTED] succeeded in growth single crystals of **5-1**~ **5-5** by solvent evaporation. The structures of **5-1** ~ **5-5** were unequivocally characterized by X-ray diffraction, as depicted in Fig. 5-4. Notably, compound **5-5** with a molecular size of 2.0 nm is the largest nanographene so far characterized crystallographically.

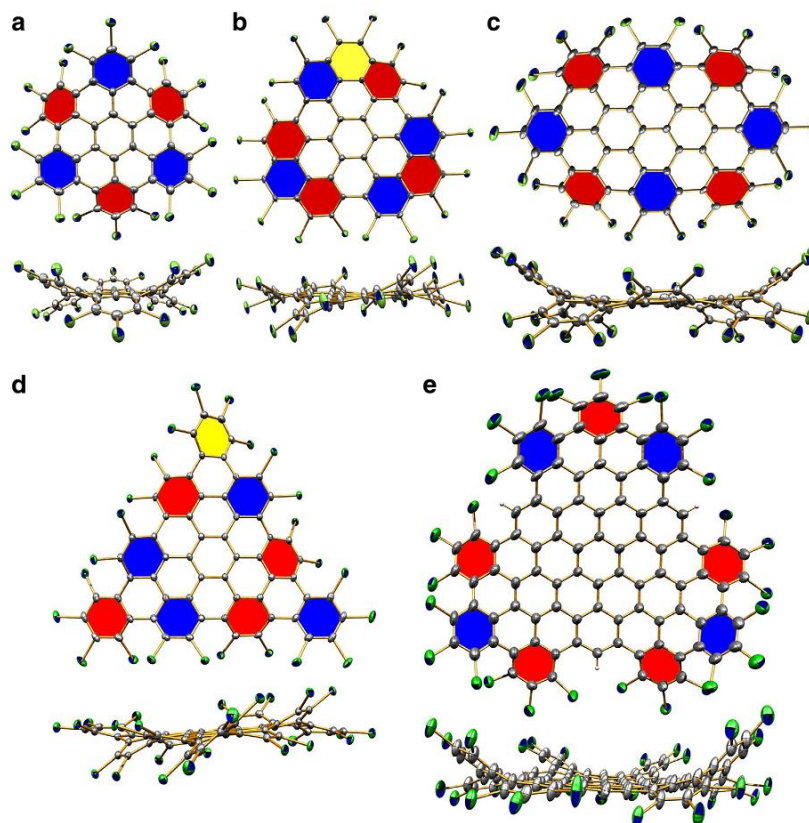


Figure 5-4. Crystal structures of chlorinated nanographene (**5-1** ~**5-5**). (a) $C_{42}Cl_{18}$ (**5-1**); (b) $C_{48}Cl_{18}$ (**5-2**); (c) $C_{60}Cl_{22}$ (**5-3**); (d) $C_{60}Cl_{24}$ (**5-4**); (e) $C_{96}Cl_{27}H_3$ (**5-5**). Front- and side- view representations of the structures of **5-1** ~ **5-5** are shown. The carbon and chlorine atoms are represented as grey and green balls, respectively. The peripheral hexagons flip up and down with respect to the inner rings, which are highlighted in blue and red, respectively. The hexagons in **5-2** and **5-4**, which adopt the twisted configuration, are highlighted in yellow.

The crystal structural data (Table 5-1) of compounds **5-1** ~ **5-5** provide information that is relevant for understanding the bond length and structure evolution of two-dimensional infinite graphene¹⁸. Although the mean bond length of **5-1**~ **5-5** is comparable to the fully equalized C-C bond value in infinite graphene (1.415 \AA)¹⁹, two classes of C-C bonds can be distinguished for **5-1** and **5-3** ~ **5-5**. One C-C bond located in the benzenoid rings has a shorter mean length, whereas the longer bond connecting the benzenoid rings has more of a single-bond character. This is consistent

with the fully benzenoid description in terms of Clar's sextet model²⁰. With the increase of the π -system, however, there is a clear tendency towards equalization of the bond lengths in the interior of **5-5** (1.411-1.429 Å). Compound **5-2** with a partial zigzag edge is unique in that the bond lengths are more equalized and no sextet benzenoid rings can be assigned based on the distinction of bond lengths. This clearly exemplifies the influence of the periphery structure on the whole molecule. The olefinic bonds at edges of **5-1** ~ **5-5** are obviously shorter than those in their interior, indicating a large polarization of the charge distribution at the periphery²¹ (Table 5-1).

Compared with the hydrogen termination of parent nanographenes, the chlorine atoms of **5-1** ~ **5-5** induce severe steric hindrance and force the outer benzene rings of the carbon framework to flip up and down in an alternating manner (Fig. 5-4). The curvature of the non-planar discs **5-1** ~ **5-5** can be quantified by the dihedral angles between the inner rings and the outside distorted ring (β -angle), which are as large as 48° (Table 5-1). This value is much larger than that (23.6°) of the bowl-shaped fullerene segment corannulene²².

Table 5-1. Geometric parameters of molecular structures of **5-1**~**5-5**.

Formula	C-C Bond length (Mean bond length) (Å)	C-C Bond length (Mean bond length) of benzenoid rings (Å)	C-C Bond length (Mean Bond length) of bonds which connect benzenoid rings (Å)	C-C Bond length (Mean Bond length) of bond at edge (Å)
C ₄₂ Cl ₁₈ (5-1)	1.373-1.487 (1.420)	1.373-1.437 (1.408)	1.433-1.487 (1.461)	1.373-1.412 (1.391)
C ₄₈ Cl ₁₈ (5-2)	1.365-1.440 (1.413)	/ ^a	/	1.365-1.380 (1.372)
C ₆₀ Cl ₂₂ (5-3)	1.366-1.493 (1.421)	1.366-1.438 (1.409)	1.430-1.493 (1.457)	1.366-1.414 (1.394)

$C_{60}Cl_{24}$ (5-4)	1.374-1.466 (1.416)	1.374-1.429 (1.407)	1.428-1.466 (1.445)	1.374-1.415 (1.386)
$C_{96}Cl_{27}H_3$ (5-5)	1.356-1.482 (1.415)	1.356-1.438 (1.404)	1.416-1.482 (1.445)	1.356-1.411 (1.386)

^a $C_{48}Cl_{18}$ (5-2) cannot be described as benzenoid polycyclic aromatic hydrocarbon by the distinction of bond length.

5.2.3 Optical and electronic properties of chlorinated nanographene

The ultraviolet-visible-near-infrared (UV-Vis-NIR) optical absorption spectra of 5-1~5-7 were measured by collaborating with [REDACTED]. The absorption bands of compounds 5-1 ~ 5-7 (Fig. 5-5a) are sharper and exhibit more abundant fine structures than those of alkyl-substituted counterparts²³, suggesting less aggregation in solution. Time-dependent density functional theory (DFT) calculations indicate strong configurational mixing associated with near degeneracy of the frontier molecular orbitals. More interestingly, the absorption bands of 5-1 ~ 5-7 show a bathochromic shift of 40-50 nm with respect to the hydrogen-terminated compounds²³. Thus, edge chlorination appears to be a powerful way for decreasing the optical HOMO-LUMO energy gap of nanographenes (Fig. 5-5b). In fact, a decrease in the optical gap is a consequence of asymmetric stabilization of the frontier molecular orbitals when substituting hydrogens with electron-withdrawing chlorines (the effect is smaller for the highest occupied molecular orbital, where it is partly compensated by a mesomeric electron-donating effect).

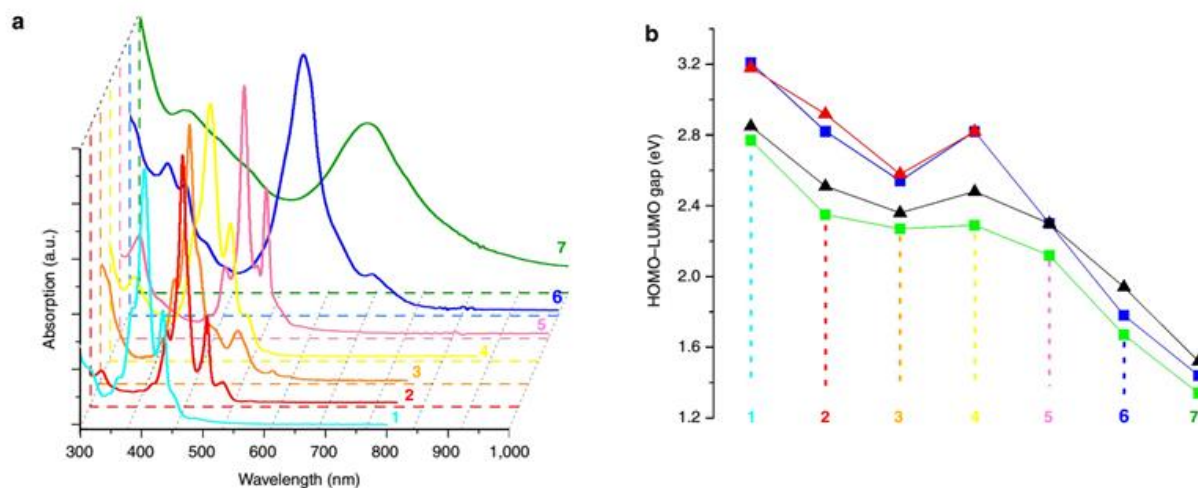


Figure 5-5. Optical and electronic properties of chlorinated nanographenes (**5-1** ~ **5-7** were represented by Arabic numbers **1** ~ **7** in figure) a) UV-Vis-NIR spectra of **5-1** ~ **5-7** were acquired in toluene. The respective spectra are indicated by the corresponding Arabic numeral of the chlorinated nanographenes. b) The calculated and experimental highest occupied molecular orbital-lowest unoccupied molecular orbital (HOMO-LUMO) gaps of **5-1** ~ **5-7** are represented by green squares and black triangles, and those of their hydrogen-terminated counterparts are represented by blue squares and red triangles, respectively.

The electron-withdrawing effect of chlorines lowers the energetic position of the frontier molecular orbitals for all chlorinated nanographenes (**5-1** ~ **5-7**) by around 1.0 eV, in comparison with the respective hydrogen-terminated analogues. The calculated energy position of the lowest unoccupied molecular orbital in **5-1** ~ **5-7** spans from -3.37 to -4.01 eV (Fig. 5-6), which is in the range of energy levels suited for electron injection in *n*-channel semiconductors²⁴. This result indicates the potential use of chlorinated nanographenes as electronic acceptors in devices. With helps of our colleague ██████████ in MPIP, a FET transistor device was fabricated using the vacuum-deposited film of compound **5-4** (40 nm in thickness). Indeed, we found the film, despite the amorphous morphology on the surface, shows an obvious *n*-type transport behavior, with a mobility of $1.0 \times 10^{-4} \text{ cm}^2\text{V}^{-1}\text{s}^{-1}$ and on/off ratio of 10^3 (Fig. 5-6). In contrast, the typical alkyl chain substituted NGs display *p*-type transport features¹⁷.

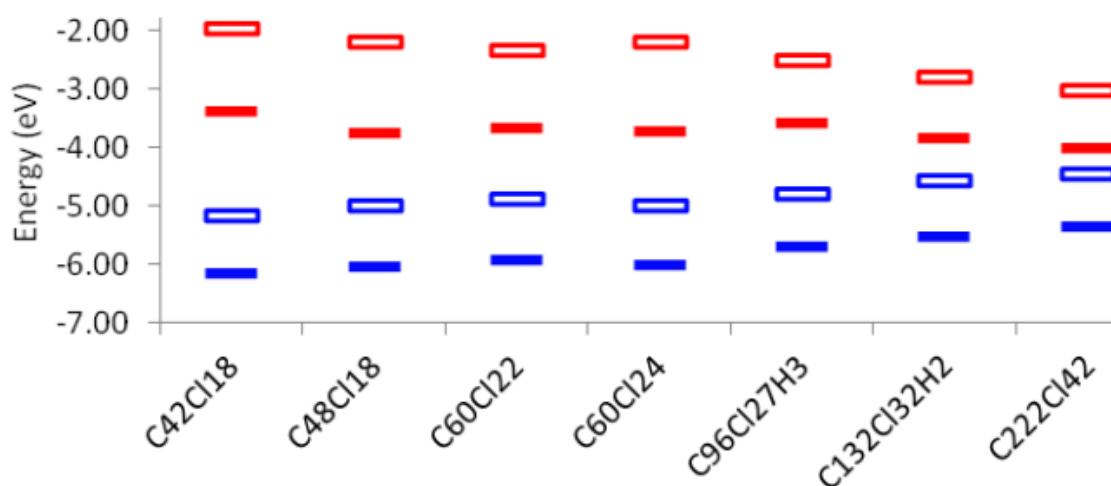


Figure 5-6. HOMO-LUMO alignment of chlorinated nanographenes (**5-1** ~ **5-7**) and their parent molecules. The HOMO and LUMO energy levels are represented as blue and red bars (full color bars for the chlorinated nanographenes and open color bars for the hydrogen terminated nanographenes).(Calculated by ██████████ ██████████, Mons, Belgium. All theoretical calculations of **5-1**~**5-7** were carried out at the DFT level, with the Heyd-Scuseria-Ernzerhof (HSE) functional.)

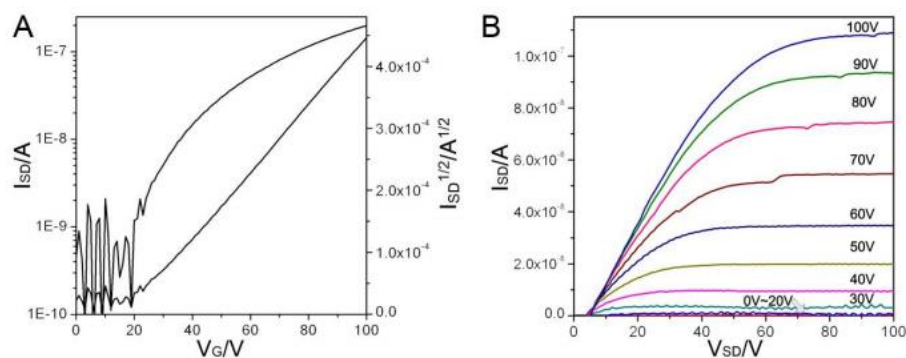


Figure 5-7. A) Typical transfer curve ($V_{DS} = 100$ V) and B) output curve of OFET transistors of compound **5-4**.

5.3 Attempts on hydrogenation (Pd/C catalyzed hydrogenation)

As presented in Figure 5-8, a series of NGs were first synthesized following reported procedures¹⁷. Afterward, Pd/C catalyzed hydrogenations on these NGs were tested.

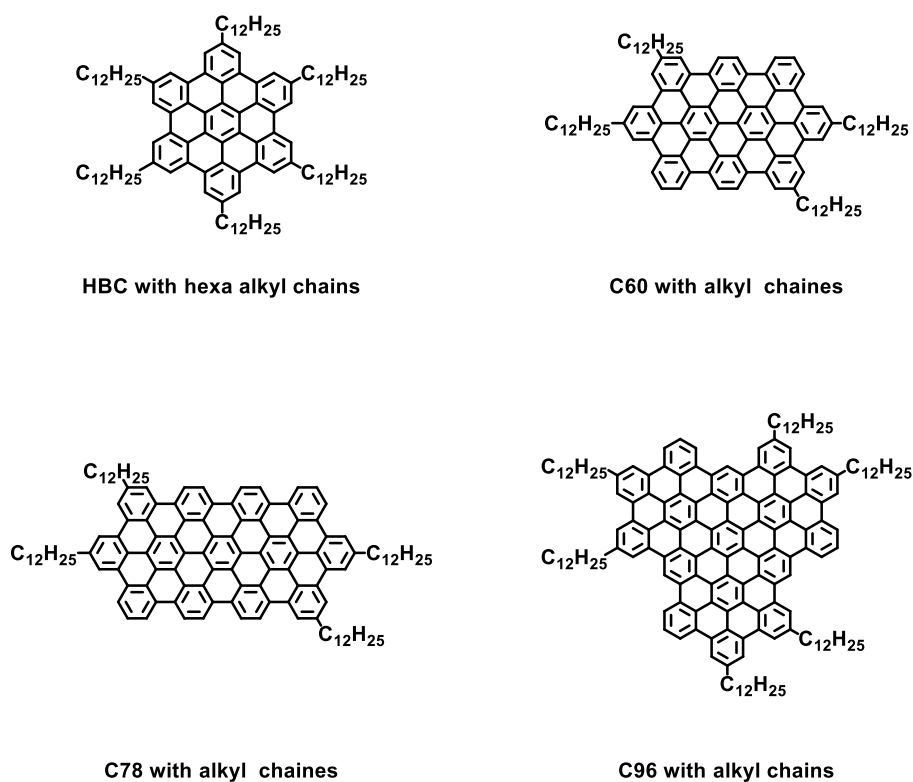


Figure 5-8. Structures of NGs for reduction.

As demonstrated in chapter 1, the protocol developed by Mark Watson showed the selective hydrogenation on HBC with alkyl chains, yielding defined peralkylated coronene²⁵. Initially, we followed this reported procedure. The reaction was performed in an autoclave which was charged with 100 mg of hexa-*n*-dodecyl-HBC and 10%Wt. Pd/C catalyst dissolved in dry THF. Then, the autoclave was sealed and charged with 65 bar hydrogen gas, and heated to 60 °C for 12 h. Subsequently, MALDI-TOF MS measurement of the resulting product indicated the successful formation of the target compound **5-8** as shown in Figure 5-9.

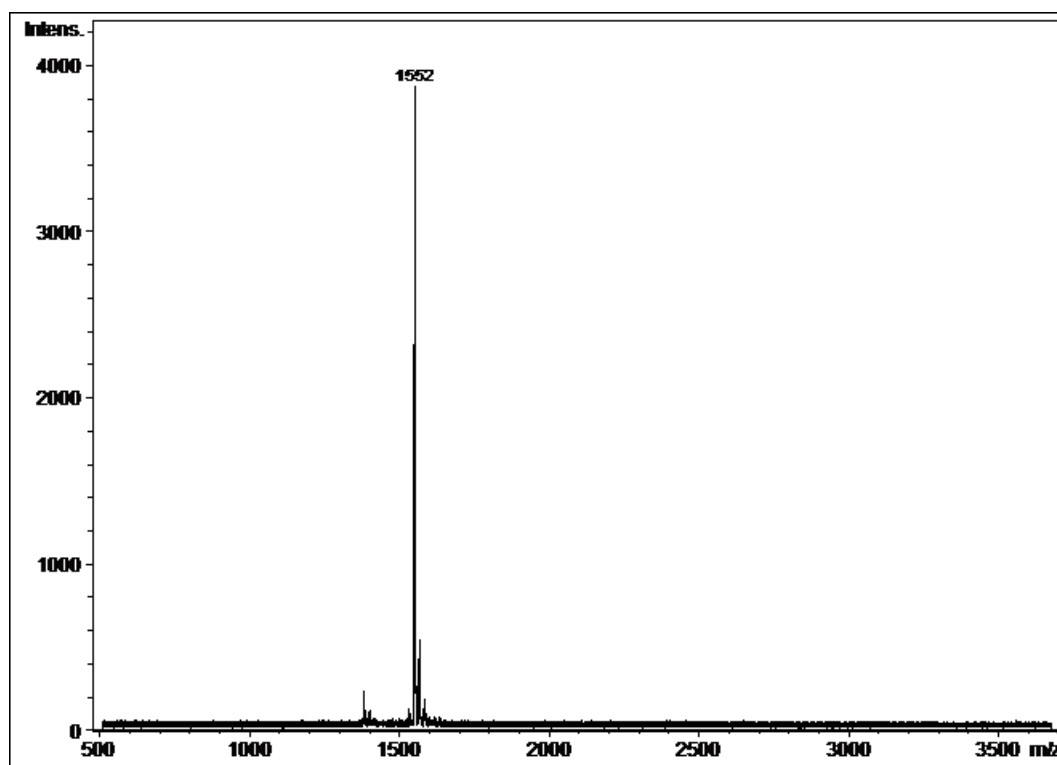
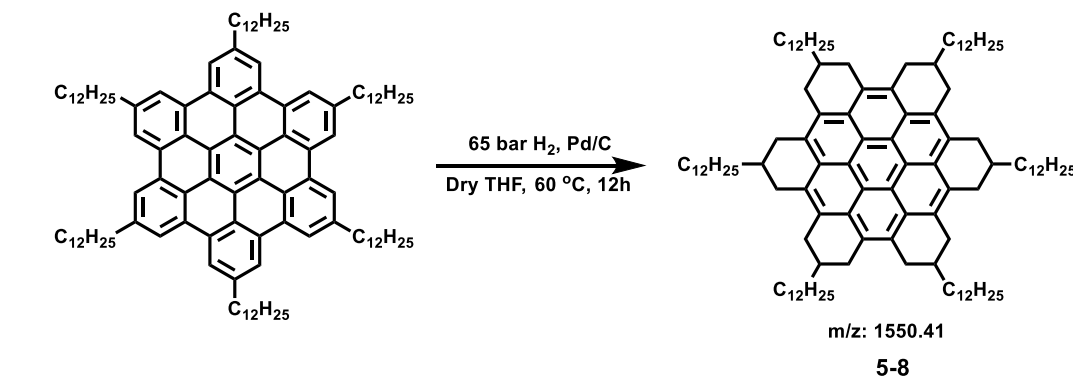


Figure 5-9. top) Synthetic scheme of compound **5-8**; down) MALDI-TOF MS of compound **5-8**

Based on the assumption that further hydrogenation (of the peripheral benzene rings) of the NGs including peralkylated coronene, C60, C78, and C96 showed in Figure 5-10, could lead to selectively hydrogenated products. The Pd/C catalyzed hydrogenations were performed under varying conditions including reaction temperature, time, as well as the pressure of hydrogen.

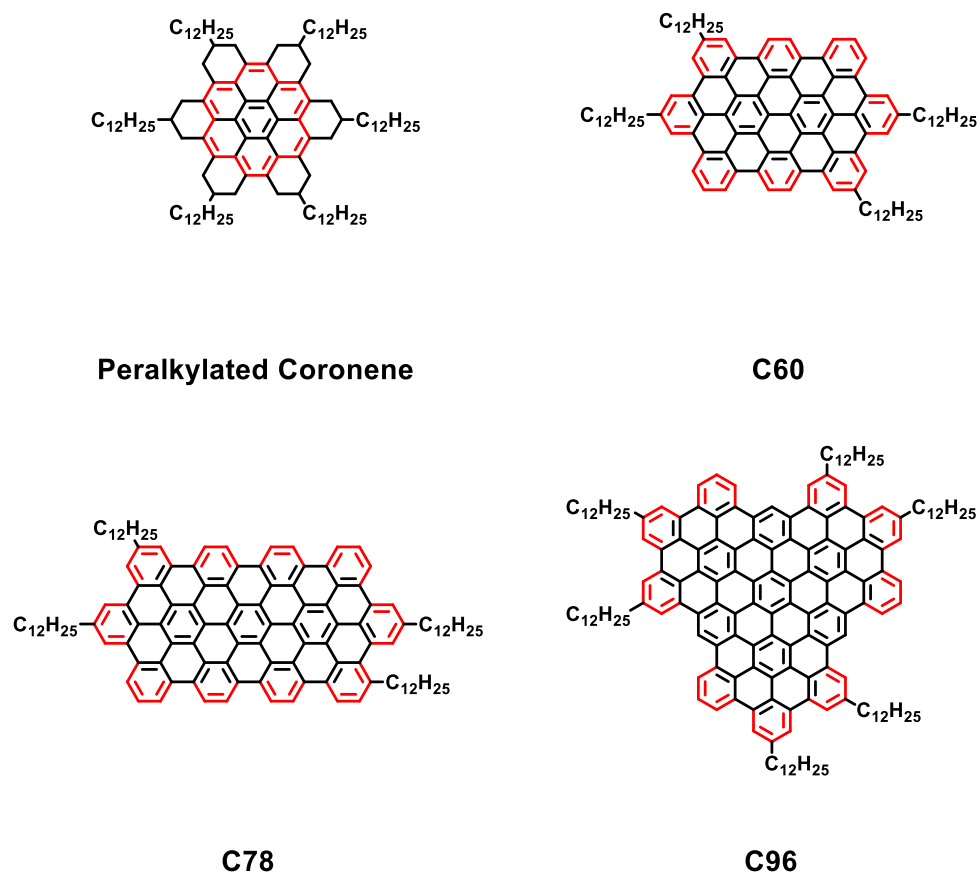


Figure 5-10. Chemical structures of NGs for catalytic hydrogenation (carbon-carbon double bonds that proposed to be hydrogenated are marked with red color).

The hydrogenation of peralkylated coronene **5-8** was tested firstly by increasing the reaction temperature from 60 to 100 °C and reaction pressure of hydrogen from 65 to 120 bar. However, the MALDI-TOF MS spectra indicated that the reaction did not work at all (Table 5-2). Based on unsuccessful attempt of hydrogenation of **5-8**, which might be ascribed to higher energy barrier as well as increased steric hindrance compared to hydrogenation of hexa-*n*-dodecyl-HBC, planar NGs with extended conjugation system including C60, C78, and C96 were further subjected to the catalytic hydrogenation. As shown in Table 5-2, from the MALDI-TOF MS measurement results, basically there occurred no hydrogenation except for C60 with four dodecyl chains. This result might

be because these reaction conditions were not drastic enough to overcome the energy barrier of hydrogenation on the interior plane of the π -systems.

Table 5-2. Catalytic hydrogenation results of PAHs

Substances (m/z)	Reaction conditions	time	MALDI-TOF (m/z)
Peralkylated coronene (1550 ^a)	Pd/C, THF, H ₂ : 120 bar, 100 °C	24 h	1551 ^b
C60 (1415 ^a)	Pd/C, THF, H ₂ : 80 bar, 100 °C	96 h	1419-1429 ^b
C60 (1415 ^a)	Pd/C, THF, H ₂ : 120 bar, 120 °C	2 week	1438 ^b
C78 (1635 ^a)	Pd/C, THF, H ₂ : 65 bar, 60 °C	24 h	1636 ^b
C96 (2192 ^a)	Pd/C, THF, H ₂ : 60 bar, 60 °C	72 h	2193 ^b
C96 (2192 ^a)	Pd/C, THF, H ₂ : 100 bar, 100 °C	96 h	2193 ^b
C96 (2192 ^a)	Pd/C, THF, H ₂ : 130 bar, 130 °C	72 h	2193 ^b

a) The molecular weight of starting material; b) the m/z value after hydrogenation.

Regarding the hydrogenation of C60 (with six dodecyl substituents to improve solubility), the reaction was carried out under conditions of heating at 60 °C for 96 h with hydrogen pressure of 80 bar and 10% Wt. Pd/C as catalyst. After removal of the solvent, the residue was subjected to MALDI-TOF MS measurement (Figure 5-11, b). The results exhibited a broad peak (Table 5-2, marked as blue, m/z : 1419-1429), which indicated the occurrence of further hydrogenation. However, the mass of our expected target molecule, which can be named as “peralkylated ovalene” following the same principle as **5-8**, should be 1438 (Fig 5-11, b). Thus, the mass peak at 1429 possibly indicated an incompletely hydrogenated molecule (Fig. 5-11, a).

In fact, the peralkylated ovalene (with alkyl chains substitution) was claimed to be obtained before^{17,26}. Thus, partial hydrogenation of C60 observed above indicated that a higher energy barrier needed to be overcome by using harsher conditions such as higher H₂ pressure and reaction temperature to afford desired hydrogenated target product (Table 5-2, hydrogenation of C60, blue

color). Thus, we increased the reaction pressure from 80 to 120 bar as well as temperature from 60 to 120 °C. The reaction time was prolonged from 96 hours to 2 weeks as well. The resulting mixture was then subjected to MALDI-TOF MS analysis. The final MALDI-TOF MS spectrum indicated that desired product with molecular weight of 1438.27 was seemingly obtained (Fig. 5-11, b).

Notably, the mass spectrum was not sufficient to validate the chemical structures of the resulting product as expected compound **5-8**. Further investigations, such as UV-Vis absorption, NMR characterization, and high resolution mass spectra, need to be performed in future based on scale-up synthesis.

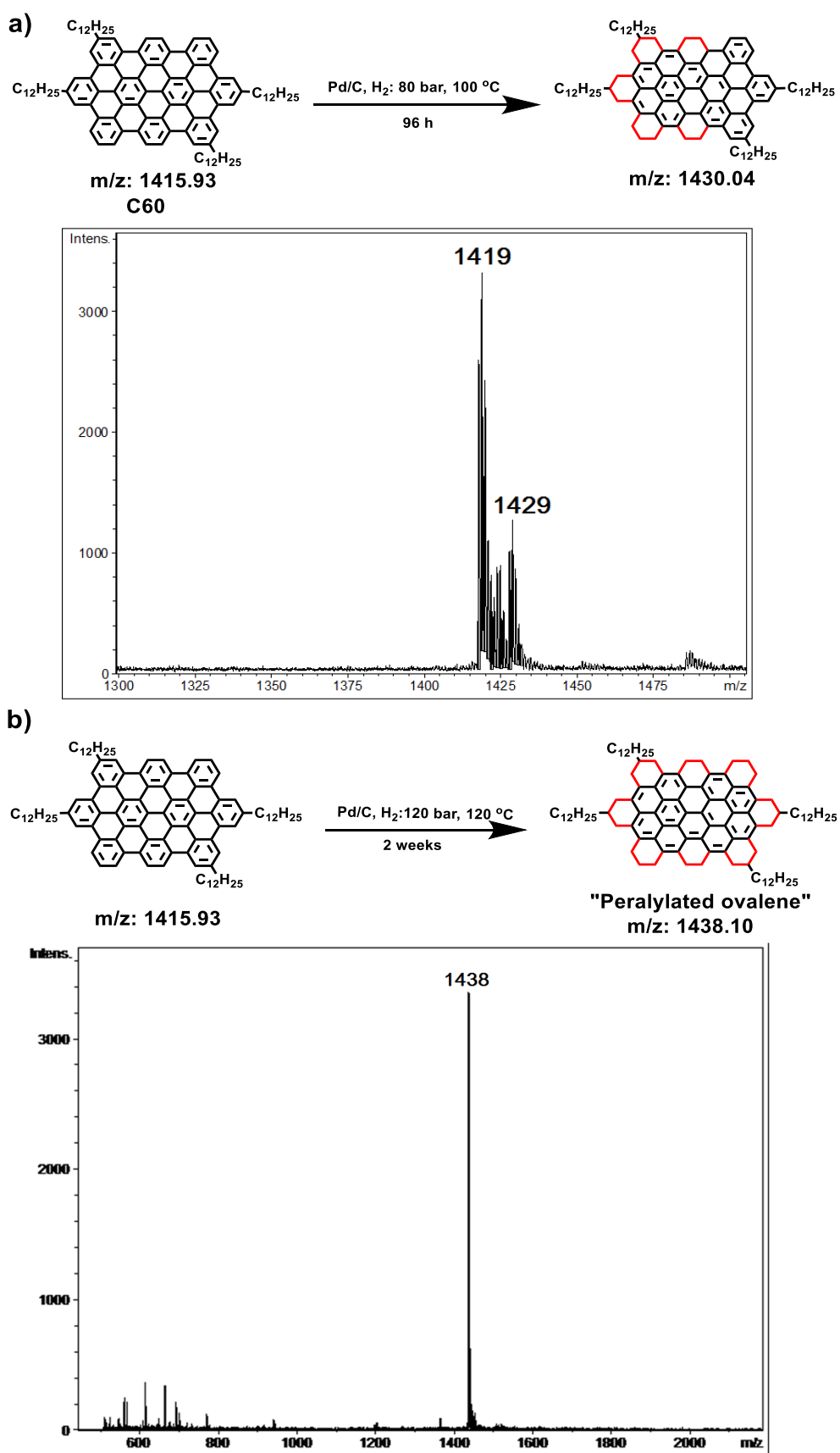


Figure 5-11. Possible reaction scheme and MALDI-TOF MS spectra of hydrogenation of C60 under condition 1 (a) and 2 (b)

5.4 Summary

In this chapter, three different functionalization protocols for NGs have been performed: 1) edge chlorination; 2) catalytic hydrogenation. The latter method was barely successful in obtaining novel structurally defined hydrogenated NG molecules except for the case of C₆₀. The MALDI-TOF MS spectra of the hydrogenated product of C₆₀ suggested that the desired “peralkylated ovalene” was obtained. The further investigation such as by UV-Vis absorption, NMR characterization, and single crystal structure needs to be performed in future after scaling up the reaction. On the contrary, the former edge chlorination protocol enables atomically precise edge functionalization of nanographenes, providing well-defined chemically functionalized graphene materials, as an important step towards controlled property modulation. The unambiguous crystallographic characterization of chlorinated nanographenes reveals the structural similarity between nanographenes and infinite graphene, and provides an atomic model for edge-functionalized graphene materials. Here we demonstrate that precise edge chlorination serves as an efficient approach to modulate the properties of nanographenes, for example, solubility, HOMO-LUMO energy gap, energetic position of the frontier molecular orbital, and charge transport. This strategy in combination with defined graphene synthesis can lead to designable and uniform graphene materials required by most practical technologies.

5.5 References

- (1) Hendel, W.; Khan, Z. H.; Schmidt, W. *Tetrahedron* **1986**, *42*, 1127.
- (2) Iyer, V. S.; Wehmeier, M.; Brand, J. D.; Keegstra, M. A.; Mullen, K. *Angewandte Chemie-International Edition In English* **1997**, *36*, 1604.
- (3) Palermo, V.; Morelli, S.; Simpson, C.; Mullen, K.; Samori, P. *J Mater Chem* **2006**, *16*, 266.
- (4) Tomovic, Z.; Watson, M. D.; Mullen, K. *Angew Chem Int Edit* **2004**, *43*, 755.
- (5) Bushby, R. J.; Lozman, O. R. *Curr Opin Solid St M* **2002**, *6*, 569.
- (6) Laschat, S.; Baro, A.; Steinke, N.; Giesselmann, F.; Hagele, C.; Scalia, G.; Judele, R.; Kapatsina, E.; Sauer, S.; Schreivogel, A.; Tosoni, M. *Angew Chem Int Edit* **2007**, *46*, 4832.
- (7) Chandrasekhar, S.; Sadashiva, B. K.; Suresh, K. A. *Pramana* **1977**, *9*, 471.
- (8) Schur, D. V.; Tarasov, B. P.; Zaginaichenko, S. Y.; Pishuk, V. K.; Veziroglu, T. N.; Shul'ga, Y. M.; Dubovoi, A. G.; Anikina, N. S.; Pomytkin, A. P.; Zolotareenko, A. D. *Int J Hydrogen Energ* **2002**, *27*, 1063.
- (9) Nossal, J.; Saini, R. K.; Alemany, L. B.; Meier, M.; Billups, W. E. *Eur J Org Chem* **2001**, 4167.
- (10) Cervantes-Sodi, F.; Csanyi, G.; Piscanec, S.; Ferrari, A. C. *Phys Rev B* **2008**, *77*.
- (11) Hod, O.; Barone, V.; Peralta, J. E.; Scuseria, G. E. *Nano Lett* **2007**, *7*, 2295.
- (12) Rosenkranz, N.; Till, C.; Thomsen, C.; Maultzsch, J. *Phys Rev B* **2011**, *84*.
- (13) Yan, Q. M.; Huang, B.; Yu, J.; Zheng, F. W.; Zang, J.; Wu, J.; Gu, B. L.; Liu, F.; Duan, W. H. *Nano Lett* **2007**, *7*, 1469.
- (14) Baird, T.; Gall, J. H.; Macnicol, D. D.; Mallinson, P. R.; Michie, C. R. *J Chem Soc Chem Comm* **1988**, 1471.
- (15) Jeon, I. Y.; Yu, D. S.; Bae, S. Y.; Choi, H. J.; Chang, D. W.; Dai, L. M.; Baek, J. B. *Chem Mater* **2011**, *23*, 3987.
- (16) Wang, X. R.; Li, X. L.; Zhang, L.; Yoon, Y.; Weber, P. K.; Wang, H. L.; Guo, J.; Dai, H. J. *Science* **2009**, *324*, 768.
- (17) Wu, J.; Pisula, W.; Müllen, K. *Chemical Reviews* **2007**, *107*, 718.
- (18) Moran, D.; Stahl, F.; Bettinger, H. F.; Schaefer, H. F.; Schleyer, P. V. *J Am Chem Soc* **2003**, *125*, 6746.
- (19) Weinert, M.; Wimmer, E.; Freeman, A. J. *Phys Rev B* **1982**, *26*, 4571.
- (20) Randic, M. *Chemical Reviews* **2003**, *103*, 3449.

- (21) Philpott, M. R.; Kawazoe, Y. *Chem Phys* **2009**, 358, 85.
- (22) Marcinow, Z.; Sygula, A.; Ellern, A.; Rabideau, P. W. *Org Lett* **2001**, 3, 3527.
- (23) Rieger, R.; Mullen, K. *J Phys Org Chem* **2010**, 23, 315.
- (24) Newman, C. R.; Frisbie, C. D.; da Silva, D. A.; Bredas, J. L.; Ewbank, P. C.; Mann, K. R. *Chem Mater* **2004**, 16, 4436.
- (25) Watson, M. D.; Debije, M. G.; Warman, J. M.; Mullen, K. *J Am Chem Soc* **2004**, 126, 766.
- (26) Simpson, C. D. P. D. *Ph.D. Thesis, University of Mainz* **2003**.

Chapter 6. Conclusion and Outlook

6.1 Conclusion

In this PhD work, we mainly focused on three aspects including bottom-up synthesis of novel structurally defined GNRs with zigzag edges, attempts for synthesis of nanographene molecules (NGs) with zigzag edges, and edge functionalization of NGs, which were demonstrated in chapter 2/3, 4, and 5, respectively. The results of above works could be concluded as follows:

1. The bottom-up surface-assisted synthesis of atomically precise GNRs with four types of edge structures, i.e. a hybrid of zigzag and gulf-type, a hybrid of zigzag and cove-type, zigzag with fluoranthrene-type subunits, full-zigzag, has been achieved with help of [REDACTED] firstly.

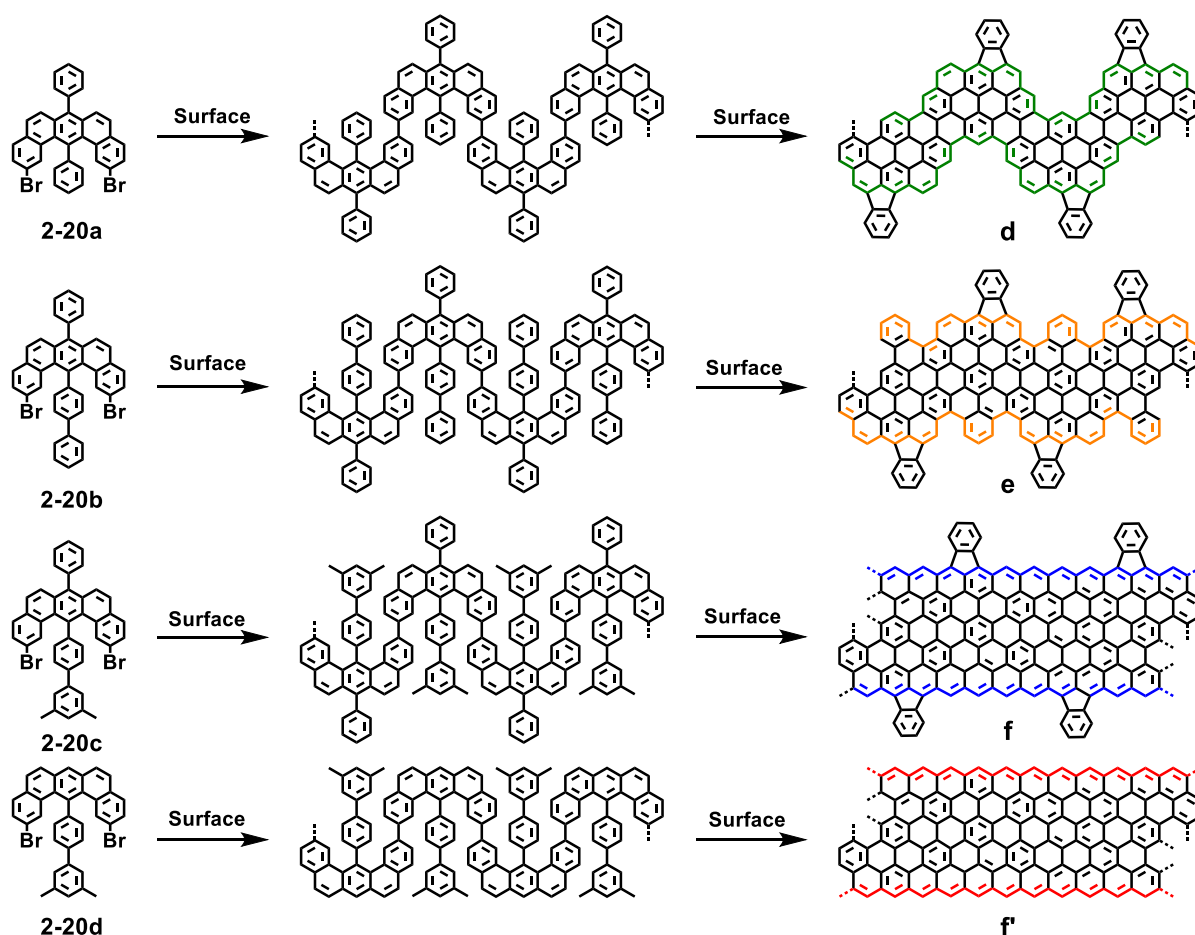


Figure 6-1. Synthesis of four types of GNRs with zigzag edge structures from monomer 2-20.

The synthesis was based on surface-assisted fabrication approach from “U-shaped” monomeric precursors from 2-20a to 2-20d. During the synthetic procedure, a thermally induced aryl-aryl coupling rendered the polymerization, which led to a snake-like polymer. Afterward thermally

induced oxidative ring closure further led to the formation of corresponding novel GNRs **d-f'** (Fig. 6-1). Particularly, GNR (**f**) and (**f'**) demonstrated spin-polarized edge states, which had been predicted before by several theoretical calculations. This work was believed to be a significant breakthrough, because for the first time ZGNRs with atomically precise edge structures could be experimentally investigated into their fundamental electronic and magnetic properties.

In parallel with the surface-assisted synthesis, the bottom-up solution synthesis of GNR with hybrid of zigzag and gulf edge structures was carried out from monomer **3-1c**, by applying the AA-type *Yamamoto* polymerization and the subsequent oxidative cyclodehydrogenation (Fig. 6-2). Moreover, three model PAH molecules **3-15**, **3-17**, and **3-19** were synthesized as the short segments corresponding to longitudinal extended GNR **3-3c** (estimated length: >100 nm). GNR **3-3c** demonstrated a relatively low optical bandgap of 1.54 eV for its narrow structure (~ 1nm), which was clearly induced by the partial zigzag edge.

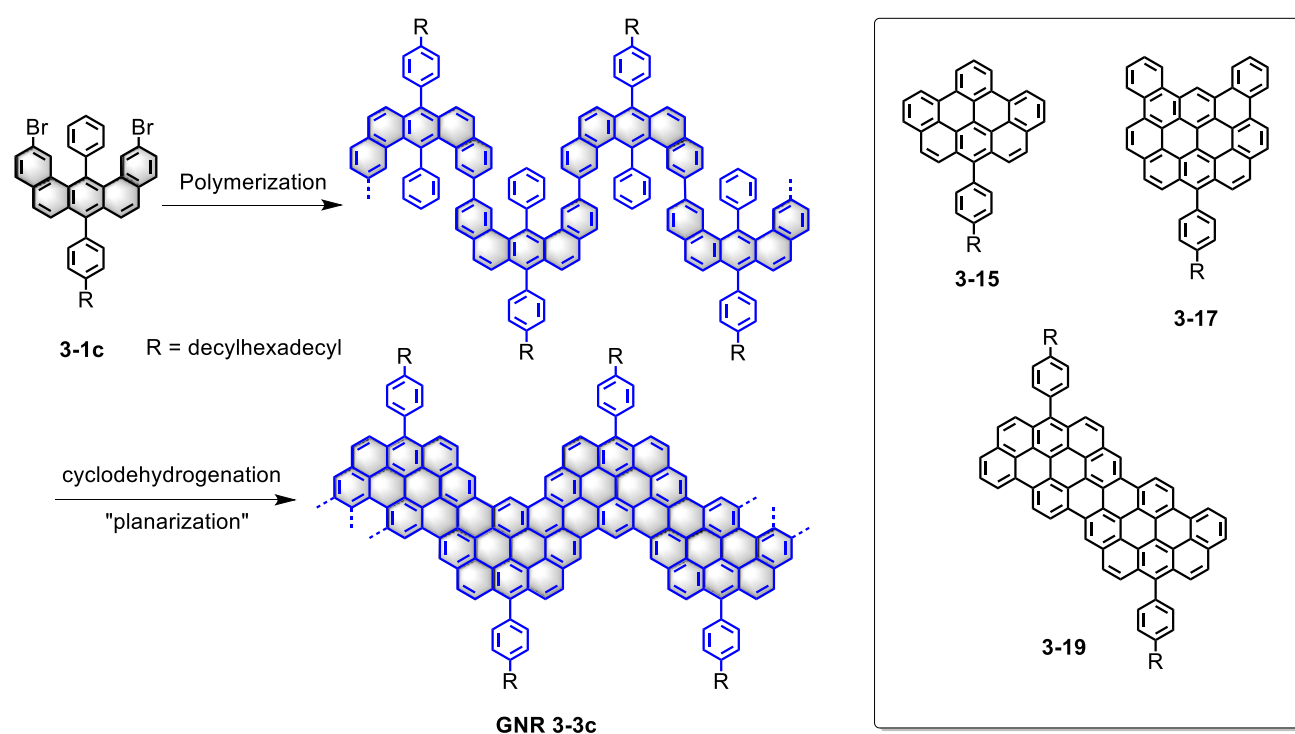


Figure 6-2. Synthetic scheme of GNR **3-3c** from monomer **3-1c** and three model PAH molecules.

2. In chapter 4, attempts for synthesis of tetra-zigzag HBC **4-4** and full-zigzag HBC **4-5** molecules were tried. Although target molecules were not obtained after employing several synthetic methods including *McMurry* coupling and *Friedel-Craft* reaction, a series of novel molecules, i.e. functionalized hexa-phenyl benzene **4-10**, **4-13**, **4-18~4-20**, were successfully synthesized and comprehensively characterized.

3. As the last part of this thesis, the chemical functionalization of 2D disk-like nanographene molecules was explored and investigated. Firstly, the edge chlorination successfully yielded a series of atomically precise edge functionalized NGs including **5-1~5-7**. The solubility of chlorinated NGs was dramatically increased, allowing to grow single crystals of **5-1~5-5** by solvent evaporation. The crystal structures of chlorinated NGs revealed the non-planar structures of these NGs. Further characterizations by UV-Vis absorption and DFT calculations proved that the edge chlorination played an important role in lowering the HOMO-LUMO energy gap of chlorinated NGs.

On the other hand, the Pd/C catalyzed hydrogenation of a series of NGs including C60, C70, and C96 were carried out to examine the feasibility of obtaining new structural defined molecules *via* reducing large conjugated π -systems. Apart from C60 system, the hydrogenation did not work well in other π -systems.

6.2 Outlook

Previously, it has been reported that the electronic properties of ZGNR can be modified through the incorporation of impurities *via* first principle calculations.^{1,2} In their work, ZGNRs doped with nitrogen atom at different sites with hydrogen passivated zigzag edges were investigated. The results indicated that hetero-atom doping was an efficient way to control the electronic property of ZGNRs. Following studies by Kan, E, Huang et al. further proved the electronic properties of GNR can be controlled *via* doping of nitrogen or boron atoms into GNR structures.

Based on our successful synthesis of the novel GNRs on Au (111) surface (Fig.6-1), we can expect that a new class of heteroatom doped GNRs can be fabricated *via* the same procedure and the electronic properties of these doped GNRs can be manipulated as well. The most promising case is nitrogen doped GNR structures shown in Fig. 6-3. Synthesis of the nitrogen doped monomers and their corresponding GNRs will be our next direction.

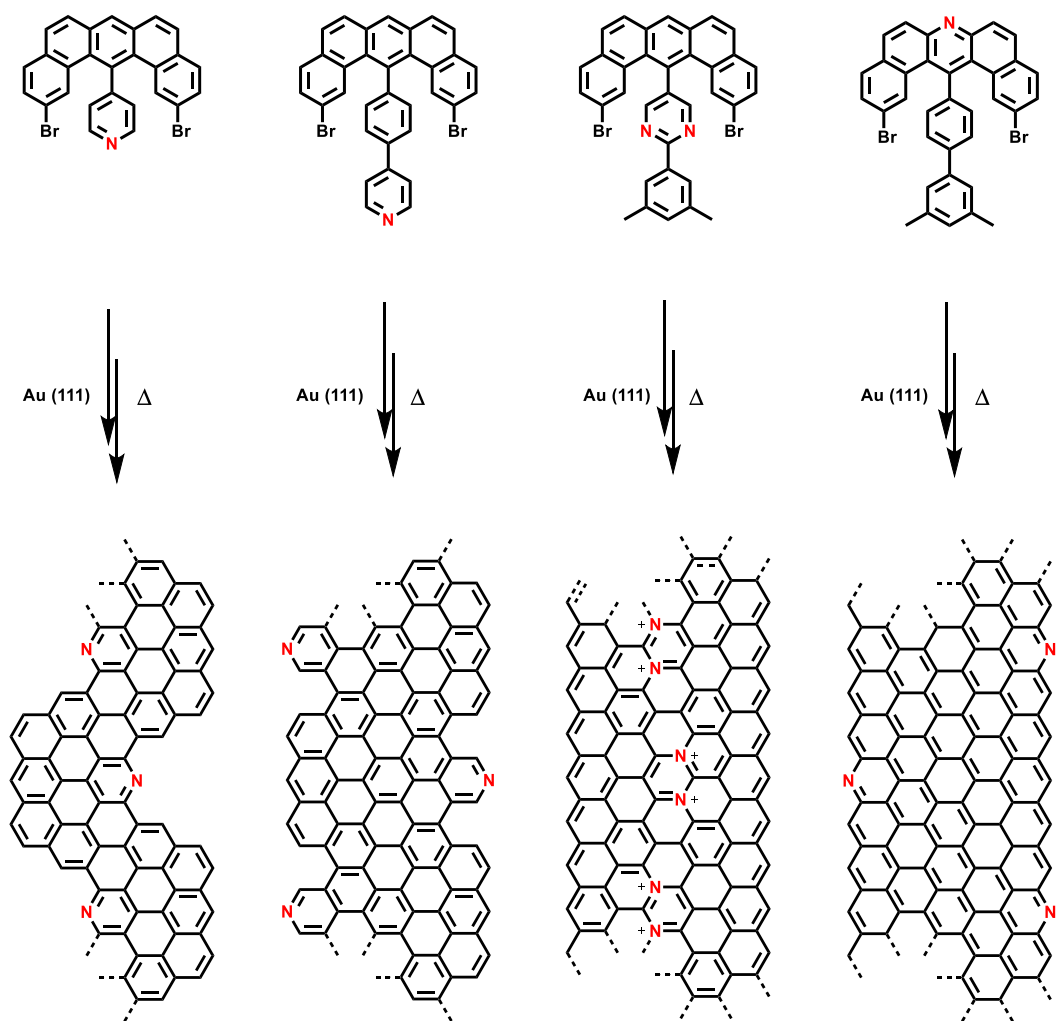


Figure 6-3. Possible N-doped monomers and their corresponding GNRs' structures

For solution synthesis of novel GNRs, according to the successful synthesis of GNR **3-3c**, a promising research direction in the near future emerges, which is fabrication of GNRs with hybrid of zigzag and cove edge structure (see Fig. 6-4). Compared to GNR **3-3c**, the cove edges along the periphery might lead to a GNR with the chiral and non-planar structure as well as different electronic property.

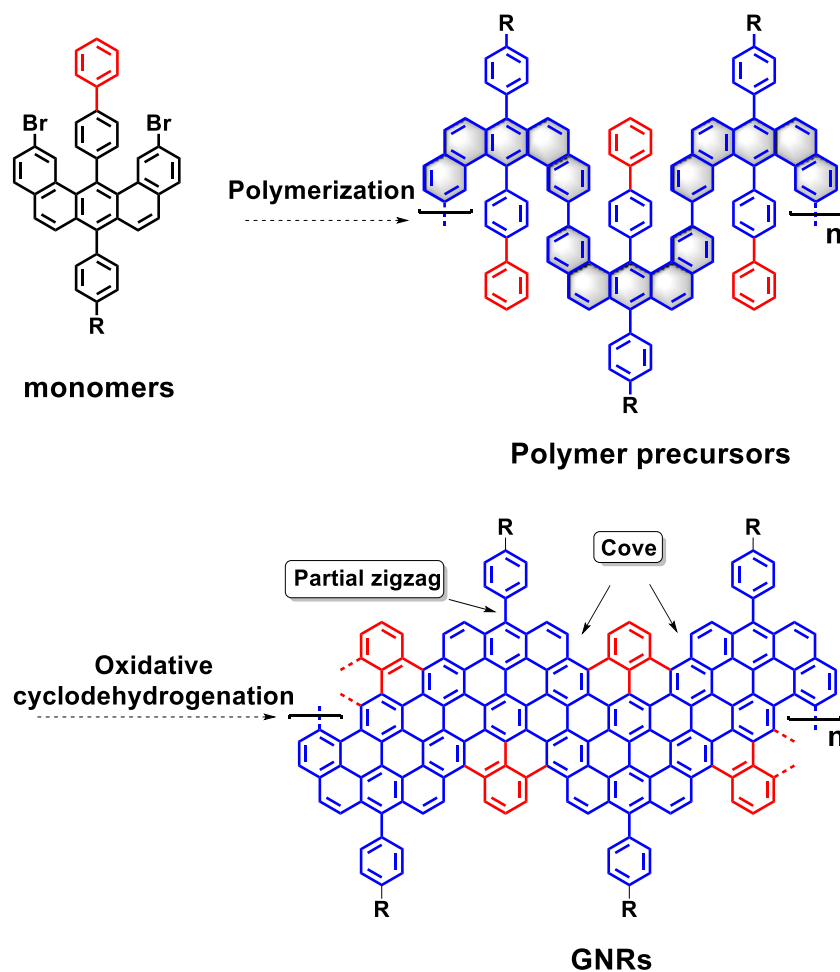


Figure 6-4. Proposed scheme for synthesizing new GNRs with hybrid of zigzag and cove edge structures.

Regarding to the synthesis of tetra-zigzag HBC **4-4**, an alternative synthetic strategy is needed according to unsuccessful attempts of using *McMurry* coupling and F-C alkylation. Inspired by my later work of fabricating GNRs with zigzag edge structure, novel synthetic routes shown in Fig. 6-5 are conceived, based on pyrylium chemistry and Pt-catalyzed cyclization, which might be the feasible solutions.

At last, as demonstrated in chapter 5, the MALDI-TOF mass spectra of Pd/C catalyzed hydrogenation of C₆₀ suggested the formation of peralkylated ovalene **5-8** product. However, the mass spectrum was not sufficient to validate the chemical structures of resulted product as expected compound **5-8**. The further investigation such as by UV-Vis absorption, NMR characterization, and single crystal structure needs to be performed in future after scaling up the reaction.

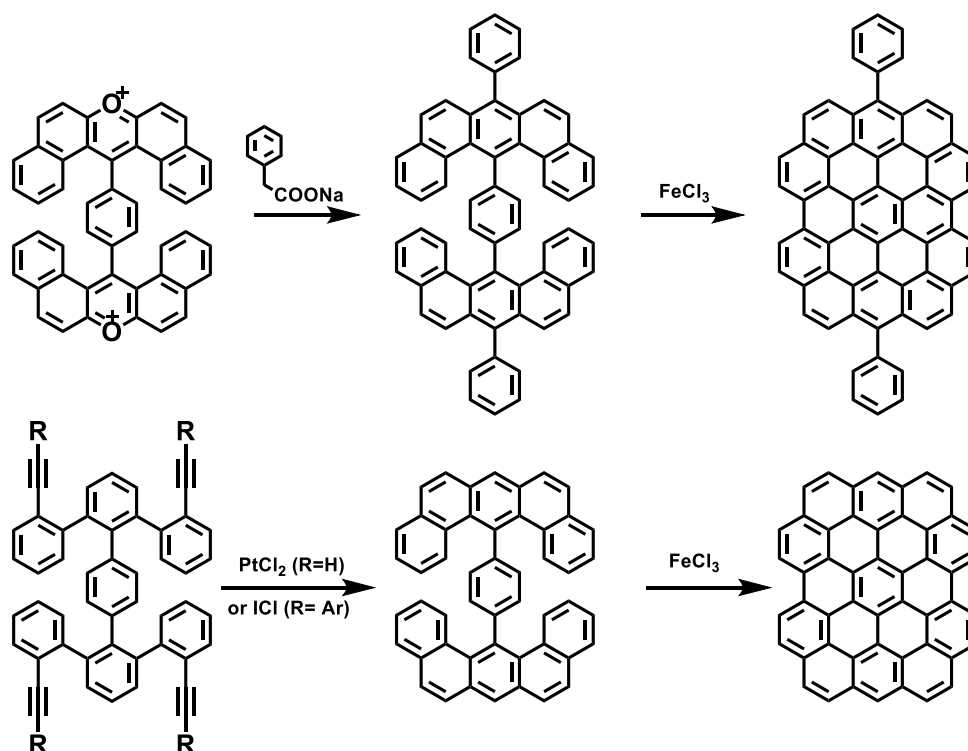


Figure 6-5. Another two possible synthetic routes toward tetra-zigzag HBC 4-4 based on pyrylium chemistry and Pt catalyzed cyclization.

6.3 References

- (1) Yu, S. S.; Zheng, W. T.; Wen, Q. B.; Jiang, Q. *Carbon* **2008**, *46*, 537.
- (2) Kan, E. J.; Li, Z. Y.; Yang, J. L.; Hou, J. G. *J Am Chem Soc* **2008**, *130*, 4224.

Chapter 7. Experiment part

7.1 General information

7.1.1 Materials

Materials in all aforementioned work were purchased from Fluka, Sigma-Aldrich, Acros, ABCR, TCI, and other commercial suppliers and used as received unless otherwise specified. The NGs used chapter 4 including HBC,¹ C60,² C78,³ C96,⁴ and C222⁵ were prepared following the reported procedures.

7.1.2 Methods

All reactions dealing with air- or moisture-sensitive compounds were carried out in a dry reaction vessel under argon. Microwave-assisted reactions were performed using a CEM microwave reactor Discover-S-Class. Preparative column chromatography was performed on silica gel from Merck with a grain size of 0.063–0.200 mm (silica gel) or 0.04–0.063 mm (flash silica gel, Geduran Si 60). Both analytical and preparative thin layer chromatography (TLC) was performed on silica gel coated substrates “60 F254” from Merck.

7.2 Analytical techniques

7.2.1 NMR spectroscopy

Solution-state ¹H and ¹³C NMR spectra were measured on Bruker DPX 250, AMX 300, and DRX500 spectrometers, and referenced to residual signals of the deuterated solvent. Abbreviations: s = singlet, d = doublet, dd = double doublet, t = triplet, m = multiplet. The solid-state NMR characterization of GNR **3-3c-I'** was performed by our collaborator [REDACTED] and [REDACTED] at Aarhus University, Denmark. All solid-state ¹H and ¹³C spectra were acquired on

a 16.4 T (700 MHz for ^1H) spectrometer using a 1.3 mm Bruker probe operating in double-resonance mode. The magic-angle-spinning (MAS) frequency was set to 59524 Hz giving a rotor period of 16.8 μs . For both ^1H and ^{13}C , all experiments used $\pi/2$ and π pulses lasting 1.8 μs and 3.6 μs , respectively. Referencing of ^1H and ^{13}C has been done relative to tetramethylsilane (TMS) using adamantane as a secondary reference.^{6,7} In general, the 2D ^1H - ^1H double quantum-single quantum (DQ-SQ)^{8,9} experiments were acquired with the carrier at 5 ppm. In the recoupled polarization heteronuclear single quantum correlation (^{13}C ¹⁰ REPT-HSQC) experiments,¹¹ the ^1H and ^{13}C carrier was set at 5 ppm and 80 ppm, respectively. In all experiments, the recycling delay was set to 2 s. Low power SW_F -TPPM decoupling¹² in combination with high MAS was employed during detection of ^{13}C . Processing was done in Topspin. Phase correction was done manually and windowing functions were imposed. In case of ^1H - ^1H DQ-SQ spectra and the corresponding 1D ^1H spectra, a Gaussian multiplication using a line broadening parameter of -10 and a fraction parameter of 0.01 was applied. In the $^{13}\text{C}\{^1\text{H}\}$ REPT-HSQC experiments, an exponential multiplication using a line broadening parameters of 40 was applied.

7.2.2 Mass spectrometry

Field desorption mass spectra (FD-MS) were obtained with a VG Instruments ZAB 2-SE-FDP using 8 kV accelerating voltage. Matrix-assisted laser desorption/ionization time-of-flight (MALDI-TOF) mass spectra were recorded using a Bruker Reflex II utilizing a 337 nm nitrogen laser, calibrated against poly(ethylene glycol) (3000 g/mol). Unless otherwise specified all the NGs, polymer precursors, and GNR samples were measured by solid-state sample preparation with tetracyanoquinodimethane (TCNQ) as matrix. The high-resolution electrospray ionization mass spectrometry (HR-ESI-MS) was performed on an ESI-Q-TOF system (maXis, BrukerDaltonics, Germany), where the instrument was operated in wide pass quadrupole mode for MS experiments, with the TOF data being collected between m/z 100–5000. The high-resolution time-of-flight mass spectrometry (APPI-TOF and MALDI-TOF) measurements were performed on a SYNAPT G2 Si high resolution time-of-flight mass spectrometer (Waters Corp., Manchester, UK) with matrix-assisted laser desorption/ionization (MALDI) or atmospheric pressure photoionization (APPI) source. For MALDI-ToF MS measurement, the samples were mixed with DCTB({(2E)-2-methyl-3-[4-(2-methyl-2-propanyl)phenyl]-2-propen-1-ylidene}malononitrile) and dropped on a MALDI sample plate. For APPI ToF MS measurement, the samples were diluted in toluene to 5 ppm and then being infused into the ionization source directly by a Legato 185 syringe pump (KD

Scientific, MA, USA) at a flow rate of 5 $\mu\text{L}/\text{min}$. The mass spectrometer was calibrated against red phosphors under MALDI mode previously and the spectra were recorded using C60 as lockmass.

7.2.3 UV-vis absorption spectroscopy

UV-vis absorption spectra were recorded at room temperature on a Perkin-Elmer Lambda 900 spectrophotometer. The optical bandgap was calculated based on the onset of p-band for NGs and from the absorption edge for the GNRs. For the measurements GNR samples were dispersed in organic solvents by sonication (>30 min) in a Branson-1510 ultrasonicator followed by centrifugation (1–5 min at 13.4 krpm).

7.2.4 Photoluminescence spectroscopy

Photoluminescence (PL) spectroscopic analysis of model compounds **6-15**, **6-17** and **6-19** were recorded on a SPEX-Fluorolog II (212) spectrometer. The measurement was performed on a dispersion in tetrahydrofuran (THF).

7.2.5 FTIR spectroscopy

Infrared spectra were measured on a Nicolet 730 FT-IR spectrometer equipped with an attenuated total reflection (ATR) setup. The samples were deposited as pristine material on the diamond crystal and pressed on it with a stamp. Measurements with a scan number of 128 were recorded for each sample and the background was subtracted. The FTIR of GNRs and their precursors was also measured by our collaborator [REDACTED] and [REDACTED] at Politecnico di Milano using Nicolet Nexus equipment coupled with a Thermo-Nicolet Continuum infrared microscope and a cooled MCT detector (77 K). The spectra of the samples (as powders) were

acquired by using the diamond anvil cell technique with a 15× infrared objective (256 scans, 2 cm⁻¹ resolution, 650 – 4000 cm⁻¹ spectral range).

7.2.6 Raman spectroscopy

Raman spectra of model compounds **3-15**, **3-17**, **3-19** and GNRs **3-3c** were measured by [REDACTED] (MPIP, Mainz) with Nicolet NEXUS NXR 9650 (Nd-YAG laser excitation at 1064 nm, InGaAs detector) and [REDACTED] and [REDACTED] at Politecnico di Milano with a Jobin-Yvon Labram HR800UV spectrometer equipped with the 514.5 nm excitation of an Ar⁺ laser. The laser power at the sample was always of the order of a few mW to prevent (or reduce as possible) laser-induced effects on the samples; care has been adopted to verify the reproducibility of the spectra. The sample was analyzed in a back-scattering geometry on a glass slide by using the microscope with the 50 × objective, respectively.

7.2.7 Size-exclusion chromatography analysis

Analytical size exclusion chromatography (SEC) was performed on SDV PSS GPC columns using THF as eluent at a temperature of 303 K. Absorbance was determined on a UV S-3702 detector (SOMA) at a fixed wavelength of 270 nm. The samples were referenced with respect to standard polystyrene (PS) as well as poly(p-phenylene) (PPP) calibration curves.

7.2.8 STM visualization

STM visualizations of model compound **6-19** were performed by the group of [REDACTED] [REDACTED] (Katholieke Universiteit Leuven, Belgium) at room temperature using PicoLE (Agilent) operating in constant-current mode. STM tips were prepared by mechanical cutting from Pt/Ir wire (80%/20%, diameter 0.2 mm). A molecular model was constructed using HyperChem 7.0 program (HyperChem(TM) Professional 7.5, Hypercube, Inc., 1115 NW 4th Street, Gainesville, Florida 32601, USA). The images were processed using SPIPTM (Image Metrology A/S, Denmark)

software, and calibrated using the graphite lattice as reference for obtaining correct lateral dimensions. The measurements were performed both at the TCB/substrate (HOPG and Au) interface.

7.2.9 AFM visualizaion

AFM measurements were performed by the group of [REDACTED] (Katholieke Universiteit Leuven, Belgium) with a Multimode AFM with a Nanoscope IV controller (Veeco/Digital Instruments, Santa Barbara, USA). For the AFM measurements of GNR **6-3c**, GNR powders were dispersed in TCB followed by heat and sonication cycles to ensure dissolution of GNRs. The AFM samples were then prepared by applying a drop of hot TCB dispersion on HOPG followed by evaporation of TCB at higher temperatures (~100 °C). For the deposition of GNR **6-3c**, the GNR powders were sonicated in TCB for 1 h and then heated at 120 °C for 20~30 min. The hot dispersion was then applied to a hot HOPG surface preheated at 120 °C. After the hot deposition, the HOPG sample was heated for another 15 min, and then washed with 2 mL of pure TCB and heated again to completely remove the solvent. Images were recorded at room temperature and processed using SPIPTM (Image Metrology A/S, Denmark) software.

7.2.10 DFT calculation

Density functional theory (DFT)¹³ calculations were performed by [REDACTED] (MPIP) and [REDACTED] (EMPA, Switzerland), applying the screened exchange hybrid density functional according to Heyd-Scuseria-Ernzerhof (HSE).¹³⁻¹⁵ All stationary points were optimized and characterized with the 6-31G(d) Gaussian basis set.¹⁶ A k-point sampling of 27 (30) k points that are uniformly positioned along the 1D Brillouin zone is employed for GNRs with armchair (zigzag) shaped edges. Calculations have been carried out using the GAUSSIAN09 program.¹⁷

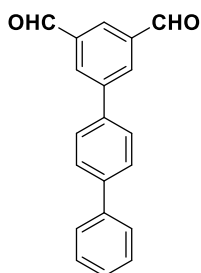
The computational Raman and FTIR calculation of model compounds **3-15** and **3-17** as well as GNR **3-3c** have been carried out within Density Functional Theory. The selected method, B3LYP/6-31G(d,p), is a good compromise between accuracy and computational costs when simulating the vibrational properties of sizeable π -conjugated compounds such as those examined in this work. Gaussian09 rev. D.01¹⁸ was employed to carry out all calculations here reported on molecular

species. The calculation of the IR spectrum of the polymer within 1D periodic boundary conditions has been carried out with the CRYSTAL14 code^{19,20} at B3LYP/6-31G(d,p) level. To limit the computational cost the model of the polymer considers shorter alkyl substituents. Custom computer codes (developed in-house) have been used to analyze the output from calculations and provide a graphical representation of normal modes.

7.3 Synthetic procedures

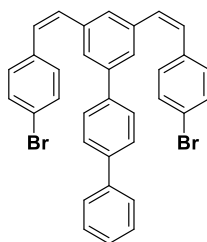
7.3.1 Synthesis of monomer precursors for fabricating GNRs on surface

7.3.1.1 [1,1':4',1''-terphenyl]-3,5-dicarbaldehyde (2-1)

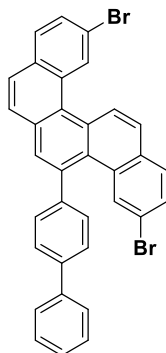


A 100 mL round flask has been filled with 5-bromoisophthalaldehyde (5 g, 23.5 mmol), 4-biphenylboronic acid (7 g, 35.2 mmol) in 50 ml toluene and 10 mL potassium carbonate (16 g, 117.4 mmol) water solution. After degassed by argon bubbling for 10 min, the tetrakis(triphenylphosphino)palladium(0) (1.36 g, 1.2 mmol) has been added. The reaction mixture has been then refluxed overnight, and stopped after thin-layer chromatography indicated that the starting material is totally converted. After cooling down to room temperature, the mixture has been extracted with dichloromethane for three times (10 mL \times 3), and then the combined organic layer has been washed three times with water and dried over magnesium sulfate, then evaporated. The residue has been purified by silica gel column chromatography (eluent: 20% ethyl acetate/hexane) yielding compound **2-1** (5.7 g, 86% yield). ¹H NMR (300 MHz, CD₂Cl₂) δ 7.39 (s, 2H), 7.49 (tt, J = 6.7, 0.9 Hz, 2H), 7.64 – 7.72 (m, 2H), 7.79 (d, J = 2.3 Hz, 3H), 8.34 (t, J = 1.5 Hz, 1H), 8.42 (d, J = 1.5 Hz, 2H), 10.18 (s, 2H); ¹³C NMR (75 MHz, CD₂Cl₂) δ 127.54, 128.10, 128.34, 129.47, 129.93, 133.18, 137.78, 138.29, 140.64, 141.96, 143.17, 191.65; FD-MS (8 kV): m/z : calcd:286.1; found: 286.4.

7.3.1.2 3,5-Bis((Z)-4-bromostyryl)-1,1':4',1''-terphenyl (2-2)



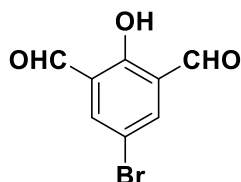
In a round-bottomed flask protected with argon, the phosphonium salt (3.2 g, 6.3 mmol) was dissolved in anhydrous THF (100 mL). The mixture was cooled to $-78\text{ }^{\circ}\text{C}$ and stirred while *tert*-BuOK (705 mg, 6.3 mmol) was added. The orange-red solution obtained was allowed to warm to room temperature and stirred for an additional 45 min. At this point, aldehyde **2-1** (34.1 mmol) was added as a solution in anhydrous THF. After stirring for 12 h the reaction mixture turned light-yellow. THF was removed and the resulting material was passed through a short silica gel plug using DCM as the eluent. A white solid of the title compound as a mixture of *cis/trans* isomers was obtained in a yield of 96 %. The resulting stilbene was used in the next step without additional purification. FD-MS (8 kV): *m/z*: calcd: 592.02; found: 592.8.

7.3.1.3 13-([1,1'-Biphenyl]-4-yl)-5,11-dibromobenzo[*c*]chrysene (2-4)

The corresponding benzo-stilbene **2-2** (5 mmol) as a *cis/trans* mixture was dissolved in toluene (200 mL). The resulting solution was placed in a quartz photochemical reactor and iodine (11 mmol) was then added. Argon was bubbled through the stirred solution for 15~20 min before an excess of propylene oxide (10 mL) was added. After irradiation for 10 h the colour of iodine had disappeared. The mixture was washed with aqueous $\text{Na}_2\text{S}_2\text{O}_3$ to remove residual traces of iodine, concentrated *in vacuo* and then purified by flash chromatography on silica gel. A mixture of light petroleum (PE) and dichloromethane (PE/DCM = 1:1) was used as eluent. The targeted compound **2-4** was obtained

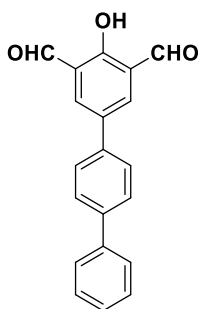
with 31 % yield as a white solid. ^1H NMR (300 MHz, CD_2Cl_2) δ 7.56-7.33 (m, 6H), 7.60 (dd, $J = 8.5$, 1.9Hz, 1H), 7.88-7.70 (m, 6H), 8.01 – 7.90 (m, 5H), 8.95 (d, $J = 9.1$ Hz, 1H), 9.13 (d, $J = 1.5$ Hz, 1H); FD-MS: m/z : calcd: 587.99; found: 587.4.

7.3.1.4 4-Bromo-2,6-diformylphenol (2-5)



p-Bromophenol (6.8 g, 37.3 mmol) and hexamethylenetetramine (11.2 g, 79.6 mmol) were dissolved in anhydrous trifluoroacetic acid (TFA) (60 mL) under Ar, and the resulting yellow solution was refluxed for 24 h (color change to orange). The mixture was poured into 4 M HCl (300 mL), and left to crystallize overnight. The resulting yellow crystals were collected by filtration, dried and recrystallized (EtOH/ H_2O). The resulting yellow needles were filtered off, and dried in a vacuum oven at 80 °C to give pure **2-5** (3.7 g, 41% yield). Mp: 136 °C. ^1H NMR (300MHz, CDCl_3): δ 11.52 (s, 1H, -OH), 10.16 (s, 2H, -CHO), 8.03 (s, 2H, Ar-H). ^{13}C NMR (75MHz, CDCl_3): δ 190.81 (-CHO), 162.25 (arom. C-1), 141.92 (arom. C-3,5), 139.75 (arom. C-2,6), 124.60 (arom. C-4). MS (EI): m/z (%) = 228 (M^+ , 45).

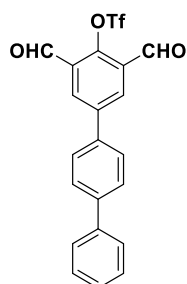
7.3.1.5 4-Hydroxy-[1,1':4',1''-terphenyl]-3,5-dicarbaldehyde (2-6)



$\text{Pd}(\text{PPh}_3)_4$ (378 mg, 10 mol%) was added to a stirred solution of 4-Bromo-2,6-diformylphenol (1.5 g, 6.55 mmol), phenylboronic acid (1.95 g, 9.82 mmol), K_2CO_3 (3.60 g, 26.2 mmol) in dry toluene (50 mL) and ethanol (10 mL) at room temperature under Ar. atmosphere and the contents were stirred at the same temperature for 20 min. The reaction mixture was slowly heated to 75–80 °C

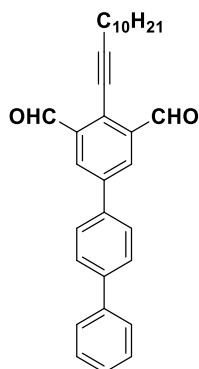
for 2 h. After completion of the reaction (TLC), the solvents were removed under reduced pressure, the reaction mixture was extracted with ethyl acetate (2×20 mL) and washed with water, the organic layer was separated, dried over sodium sulfate, solvent removed under reduced pressure and the obtained crude product was purified by flash chromatography using silica gel (70–230) with DCM as eluent to give final product **2-6** as yellow powder (1.03 g, 52% yield). ^1H NMR (300 MHz, CD_2Cl_2) δ 7.35 – 7.42 (m, 1H), 7.48 (ddt, $J = 7.7, 6.1, 1.4$ Hz, 2H), 7.61 – 7.79 (m, 6H), 8.25 (s, 2H), 10.31 (s, 2H), 11.67 (s, 1H); ^{13}C NMR (75 MHz, CD_2Cl_2) δ 124.03, 127.47, 128.17, 128.24, 129.44, 133.36, 136.08, 137.54, 140.72, 141.21, 163.38.

7.3.1.6 3,5-Diformyl-[1,1':4',1''-terphenyl]-4-yl trifluoromethanesulfonate (2-7)



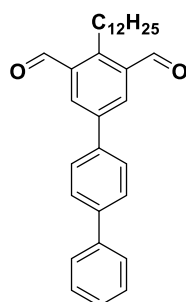
To a solution of **2-6** (2 g, 6.6 mmol) and Et_3N (2.5 mL, 17.8 mmol) in 20 mL of CH_2Cl_2 was added trifluoromethanesulfonic anhydride (9.9 mL, 9.9 mmol) dropwise at 0°C over 10 min. The reaction mixture was warmed to room temperature and stirred for 2 h. The solution was cooled to 0°C and quenched with 20 mL of 1.5 M HCl. After separation, the aqueous phase was extracted twice with CH_2Cl_2 (15 mL) and the combined extract was dried over Na_2SO_4 . The organic phase was passed through a short plug of silica gel, which was then washed with CH_2Cl_2 (50 mL). The filtrates were concentrated under reduced pressure and the resulting crude solid was recrystallized from hexane to give the title compound as a yellow solid (2.2 g, 75% yield). ^1H NMR (300 MHz, CD_2Cl_2) δ 7.34 – 7.45 (m, 1H), 7.45 – 7.59 (m, 2H), 7.60 – 7.74 (m, 2H), 7.77 (d, $J = 2.9$ Hz, 4H), 8.48 (s, 2H), 10.34 (s, 2H); ^{13}C NMR (75 MHz, CD_2Cl_2) δ 127.56, 128.15, 128.46, 129.51, 130.82, 134.18, 136.25, 140.39, 142.55, 142.80, 148.44, 186.29; FD-MS (8 kV): m/z : calcd: 434.04; found: 434.3.

7.3.1.7 4-(Dodec-1-yn-1-yl)-[1,1':4',1''-terphenyl]-3,5-dicarbaldehyde (2-8)



To a mixture of dialdehyde **2-7** (967 mg, 2.2 mmol), PdCl₂(PPh₃)₂ (78 mg, 0.11 mmol) and CuI (21 mg, 0.11 mmol) in 50 ml of triethylamine solution, 1-dodecyne (1.43 ml, 6.7 mmol) was added. After 12 h of stirring at 85 °C, 20 ml of a saturated aqueous ammonium chloride solution and 20 ml of diethyl ether were added. The organic layer was separated, and the aqueous layer was back extracted with diethyl ether. The combined organic layers were washed with brine and water, dried over sodium sulfate, and concentrated. Purification of the residue by flash column chromatography afforded final product **2-8** (0.63g, 63% yield). ¹H NMR (300 MHz, CD₂Cl₂) δ 0.88 (t, *J* = 6.4 Hz, 3H), 1.00 – 1.46 (m, 14H), 1.63 – 1.93 (m, 2H), 2.61 (t, *J* = 7.1 Hz, 2H), 7.40 (dd, *J* = 5.9, 2.6 Hz, 1H), 7.48 (ddt, *J* = 7.8, 6.1, 3.2 Hz, 2H), 7.61 – 7.72 (m, 2H), 7.72 – 7.89 (m, 4H), 8.41 (s, 2H), 10.67 (s, 2H); ¹³C NMR (75 MHz, CD₂Cl₂) δ 14.45, 23.27, 28.95, 29.68, 29.90, 30.09, 30.16, 30.27, 32.49, 39.76, 76.40, 98.50, 117.85, 127.47, 127.53, 127.82, 127.94, 128.27, 129.46, 130.51, 137.96, 191.47; FD-MS (8 kV): *m/z*: calcd: 450.3; found: 451.2

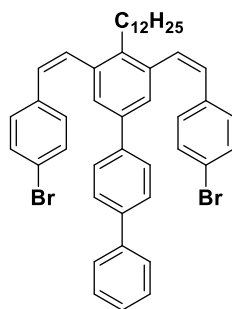
7.3.1.8 4-Dodecyl-[1,1':4',1''-terphenyl]-3,5-dicarbaldehyde (2-9)



To a 100 mL autoclave vessel charged with a stir bar, a solution of compound **2-8** (100 mg, 0.22 mmol) dissolved in 20 mL anhydrous tetrahydrofuran was added. Then, the solution was degassed by argon bubbling for 20 min and an active palladium on active carbon for hydrogenation (10 mg, 10 wt. %) was added subsequently. Next, the autoclave was sealed and the atmosphere

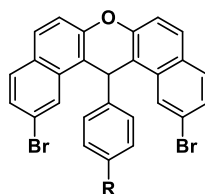
inside were replaced *via* a hydrogen steel cylinder from air to hydrogen with a pressure of 5 bar. Afterward the autoclave was let to keep stirring at room temperature for one hour until the hydrogenation reaction was completed. The hydrogenated solution was then passed through a short pad of silica gel to remove platinum catalyst. Finally, the resulting organic solution was evaporated to afford **2-9** as a bright white solid (~ 100 mg, 99% yield). ^1H NMR (300 MHz, CD_2Cl_2) δ 0.81 – 0.96 (m, 3H), 1.28 (s, 18H), 1.49 (q, $J = 7.4$ Hz, 2H), 3.41 – 3.55 (m, 2H), 7.39 (d, $J = 7.3$ Hz, 1H), 7.43 – 7.54 (m, 2H), 7.68 (dt, 2H), 7.77 (d, $J = 3.4$ Hz, 4H), 8.37 (s, 2H), 10.49 (s, 2H); ^{13}C NMR (75 MHz, CD_2Cl_2) δ 14.47, 23.28, 26.45, 29.94, 29.99, 30.17, 30.22, 30.25, 30.36, 32.51, 34.10, 127.52, 127.79, 128.25, 129.45, 134.11, 136.04, 137.83, 139.59, 140.75, 141.59, 147.26, 191.59; FD-MS (8 kV): m/z : calcd: 454.3; found: 454.6.

7.3.1.9 3,5-Bis((Z)-4-bromostyryl)-4-dodecyl-1,1':4',1''-terphenyl (2-10)



A 100 mL round bottom flask was charged under an Ar. atmosphere with phosphonium salt (676 mg, 1.3 mmol) in dry THF (30 mL) and cooled to 0 °C. *t*-BuOK (148 mg, 1.3 mmol) was added in small portions and the mixture was stirred for 90 min at 24 °C. Benzaldehyde **2-9** (200 mg, 0.44 mmol) in dry THF (15 mL) was added dropwise at 0 °C. The resulting mixture was stirred for 12 h at r.t., quenched with 1N HCl (100 mL), and extracted with diethyl ether (2 × 10 mL). The combined organic phases were dried (MgSO_4), and concentrated on a rotary evaporator. The title compound **2-10** as a mixture of *cis/trans* isomers was obtained after purified by chromatography as yellow solid (284.4 mg, 85 % yield). The **2-10** was used directly for the next step without additional isolation of isomers. FD-MS (8 kV): m/z : calcd: 758.2; found: 758.6.

7.3.1.10 Dibenzo[*a,j*]xanthene (2-17a, b and c)



- 2-17a** R =H;
2-17b R =phenyl;
2-17c R = 3,5-dimethylphenyl;

To a mixture of aromatic aldehyde (R=H, benzaldehyde; R=phenyl, [1,1'-biphenyl]-4-carbaldehyde; R=3,5-dimethylphenyl, 3',5'-dimethyl-[1,1'-biphenyl]-4-carbaldehyde)(1 mmol) and 7-bromo-naphthol (2 mmol), *p*-toluensulfonic acid monohydrate (*p*-TSA) (0.02 mmol) was added. The mixture was stirred at 125 °C for 24 h, and the reaction was monitored by thin-layer chromatography (TLC) plate. When the reaction was completed, the mixed solvent (20 mL) of ethanol and deionized water (EtOH/H₂O = 1/3) was added. Then, the mixture was kept stirring for another 2 h and then a pale white solid was filtered off and washed with above mixed solvent. Finally, the crude products were purified by recrystallization from ethanol to afford target compound **2-17** (White needles).

2,12-Dibromo-14-phenyl-14H-dibenzo[*a,j*]xanthene (2-17a):

Yield = 86%; Mp: 220.5-221.5 °C; ¹H NMR (300 MHz, CD₂Cl₂) δ 6.31 (s, 1H) 7.06 (t, *J* = 7.5 Hz, 1H) 7.21 (t, *J* = 7.5 Hz, 2H) 7.57–7.43 (m, 6H) 7.76 (dd, *J* = 17.8, 8.8 Hz, 4H) 8.54 (s, 2H); ¹³C NMR (75 MHz, CD₂Cl₂) δ 38.50, 116.75, 118.97, 122.00, 125.70, 127.38, 128.30, 128.52, 129.31, 129.56, 130.12, 131.01, 133.08, 144.94, 149.68; HRMS (APPI-TOF, positive) *m/z* calcd for C₂₇H₁₆Br₂O [M]⁺ 514.9601, found 514.9611.

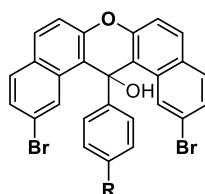
14-([1,1'-Biphenyl]-4-yl)-2,12-dibromo-14H-dibenzo[*a,j*]xanthene (2-17b):

Yield = 83%; Mp: 310.9-311.5 °C; ¹H NMR (300 MHz, CD₂Cl₂) δ 6.34 (s, 1H) 7.38 – 7.19 (m, 3H) 7.43 (dd, *J* = 8.4, 1.8 Hz, 4H) 7.60 – 7.48 (m, 6H) 7.77 (dd, *J* = 22.9, 8.8 Hz, 4H) 8.57 (d, *J* = 1.9 Hz, 2H); ¹³C NMR (75 MHz, CD₂Cl₂) δ 38.10, 116.64, 118.99, 122.06, 125.67, 127.41, 127.81, 127.96, 128.34, 128.88, 129.20, 129.60, 130.12, 131.04, 133.05, 140.21, 140.79, 143.96, 149.70; HRMS (APPI-TOF, positive) *m/z* calcd for C₃₃H₂₀Br₂O[M]⁺ 590.9914, found 590.9918.

2,12-Dibromo-14-(3',5'-dimethyl-[1,1'-biphenyl]-4-yl)-14H-dibenzo[*a,j*]xanthene (2-17c):

Yield = 73%; Mp: < 319 °C; ^1H NMR (500 MHz, $\text{C}_2\text{D}_2\text{Cl}_4$) δ 6.28 (s, 1H), 6.93 (s, 1H), 7.05 (s, 2H), 7.43 (d, $J = 7.4$ Hz, 2H), 7.53 (m, 6H), 7.77 (dd, $J = 35.5, 8.7$ Hz, 4H), 8.54 (s, 2H); ^{13}C NMR (125 MHz, $\text{C}_2\text{D}_2\text{Cl}_4$) δ 21.27, 37.51, 37.51, 115.91, 118.46, 121.47, 124.82, 125.01, 127.42, 127.72, 128.21, 128.88, 128.95, 129.30, 130.36, 132.33, 138.08, 139.53, 139.91, 142.84, 148.98; HRMS (MALDI-TOF, positive) m/z calcd for 620.0173, found 620.0178.

7.3.1.11 Dibenzo[*a,j*]xanthen-14-ol (2-18a, b and c)



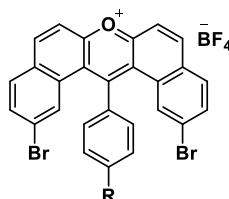
2-18a R = H;

2-18b R = phenyl;

2-18c R = 3,5-dimethylphenyl;

Compound **2-17** (5 mmol) and lead dioxide (PbO_2 , 7.5 mmol) in glacial acetic acid (50 ml) were stirred while heating on an oil bath at 120 °C for 12 h. The cooled mixture was poured onto crushed ice and the solid residue **2-18** (crud compound **2-18a**, **2-18b** and **2-18c**) was filtered off, dried under vacuum at 80 °C and used directly for the next step.

7.3.1.12 Dibenzo[*a,j*]xanthylium tetrafluoroborate (2-19a, b and c)



2-19a R = H;

2-19b R = phenyl;

2-19c R = 3,5-dimethylphenyl;

Compound **2-18** (5 mmol) in acetic anhydride (15 ml) and toluene (10 ml) were cooled to 0 °C and treated with tetrafluoroboric acid solution (48 wt. % in water)(ca. 25 mmol) until no further precipitation occurred. The cooled solution was filtered and washed with anhydrous ether to yield **2-19** as an orange red powder.

2,12-Dibromo-14-phenyldibenzo[*a,j*]xanthenylium tetrafluoroborate (2-19a):

Yield=90%; ¹H NMR (300 MHz, CD₂Cl₂) δ 7.38 (s, 2H), 7.58 (dd, *J* = 8.1, 1.5 Hz, 2H), 7.93 (dd, *J* = 8.4, 1.8 Hz, 2H), 8.02 – 8.10 (m, 5H), 8.34 (d, *J* = 9.1 Hz, 2H), 8.81 (d, *J* = 9.1 Hz, 2H); ¹³C NMR (75 MHz, DMSO) δ 71.41, 117.96, 118.35, 119.71, 126.19, 126.30, 126.99, 127.45, 129.22, 129.90, 130.57, 130.67, 132.00, 146.07, 147.65; HRMS (APPI-TOF, positive) *m/z* calcd for C₂₇H₁₅Br₂O[M]⁺ 514.9557, found 514.9512.

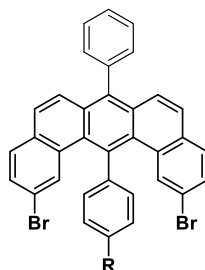
14-([1,1'-Biphenyl]-4-yl)-2,12-dibromodibenzo[*a,j*]xanthenylium tetrafluoroborate (2-19b):

Yield=92%; ¹H NMR (300 MHz, CD₂Cl₂) δ 7.49 – 7.70 (m, 7H), 7.81 – 7.98 (m, 4H), 8.09 (d, *J* = 8.5 Hz, 2H), 8.16 – 8.25 (m, 2H), 8.35 (d, *J* = 9.1 Hz, 2H), 8.76 – 8.92 (m, 2H); ¹³C NMR (75 MHz, DMSO) δ 71.41, 118.01, 118.26, 119.82, 125.62, 126.43, 126.75, 127.06, 127.42, 128.79, 129.21, 129.94, 130.62, 130.72, 132.02, 137.84, 138.98, 146.13, 146.86; HRMS (APPI-TOF, positive) *m/z* calcd for C₃₃H₁₉Br₂O[M]⁺ 590.9870, found 590.9804.

2,12-Dibromo-14-(3',5'-dimethyl-[1,1'-biphenyl]-4-yl)-14-dibenzo[*a,j*]xanthenylium tetrafluoroborate (2-19c)

Yield=88%; ¹H NMR (500 MHz, C₂D₂Cl₄) δ 2.50 (s, 6H), 7.20 (s, 1H), 7.46 (s, 2H), 7.52 (s, 2H), 7.61 (d, *J* = 7.8 Hz, 2H), 7.95 (d, *J* = 8.3 Hz, 2H), 8.08 (d, *J* = 8.4 Hz, 2H), 8.20 (d, *J* = 7.8 Hz, 2H), 8.32 (d, *J* = 9.0 Hz, 2H), 8.81 (d, *J* = 9.1 Hz, 2H); ¹³C NMR (125 MHz, C₂D₂Cl₄) δ 21.47, 117.54, 121.13, 125.45, 126.18, 126.58, 129.74, 130.42, 130.93, 131.30, 131.45, 132.59, 133.07, 135.37, 138.92, 139.37, 146.37, 146.90, 159.45, 167.67; HRMS (MALDI-TOF, positive) *m/z* calcd for C₃₅H₂₃Br₂O⁺[M]⁺ 617.0116, found 617.0127.

7.3.1.13 Diphenylbenzo[*m*]tetraphene (2-20a, b and c)



2-20a R =H;
2-20b R =phenyl;
2-20c R = 3,5-dimethylphenyl;

A mixture of the pyrylium salt **2-19** (3 mmol) and sodium 2-phenylacetate (9 mmol) in acetic anhydride (Ac₂O, 50 ml) was stirred at 150 °C for 12 h under argon atmosphere. After cooling to the room temperature, the precipitate was filtered off and washed with Ac₂O, then methanol. The crud product was re-precipitated from chloroform and hexane to give umbrella monomer **2-20** as brown powder.

2,12-Dibromo-7,14-diphenylbenzo[m]tetraphene (2-20a):

Yield = 34%; Mp: > 400 °C; ¹H NMR (500 MHz, C₂D₂Cl₄, 353K) δ 7.34 – 7.43 (m, 12H), 7.47 – 7.55 (m, 5H), 7.60 (t, *J* = 7.4 Hz, 2H), 7.65 (t, *J* = 7.2 Hz, 1H); ¹³C NMR (126 MHz, C₂D₂Cl₄, 353K) δ 118.68, 125.87, 127.03, 127.17, 127.86, 128.59, 128.93, 129.10, 129.25, 130.57, 130.79, 131.26, 131.86, 132.38, 132.70, 137.58, 138.40, 139.23, 144.01; HRMS (APPI-TOF, positive) *m/z* calcd for C₃₄H₂₀Br₂ [M]⁺ 585.9932, found 585.9934.

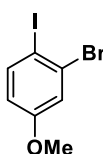
14-([1,1'-Biphenyl]-4-yl)-2,12-dibromo-7-phenylbenzo[m]tetraphene (2-20b)

Yield = 32%; Mp: > 400 °C; ¹H NMR (500 MHz, C₂D₂Cl₄, 353K) δ 7.39 – 7.58 (m, 14H), 7.58 – 7.66 (m, 6H) 7.82 (t, *J* = 14.2 Hz, 2H) 7.89 (t, *J* = 15.2 Hz, 2H); ¹³C NMR (126 MHz, C₂D₂Cl₄, 353K) δ 118.85, 125.92, 127.08, 127.20, 127.46, 127.80, 127.89, 128.61, 128.81, 129.17, 129.24, 129.88, 130.62, 131.53, 131.85, 132.34, 132.39, 132.82, 137.66, 138.04, 139.22, 141.57, 142.67, 143.07; HRMS (APPI-TOF, positive) *m/z* calcd for C₄₀H₂₄Br₂[M]⁺ 662.0245, found 662.0262.

2,12-Dibromo-14-(3',5'-dimethyl-[1,1'-biphenyl]-4-yl)-7-phenylbenzo[m]tetraphene (2-20c):

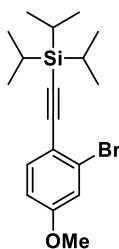
Yield= 38%; Mp: > 400 °C; ^1H NMR (500 MHz, $\text{C}_2\text{D}_2\text{Cl}_4$) δ 2.48 (s, 6H), 7.12 (s, 1H), 7.48 (d, J = 7.3 Hz, 6H), 7.56 – 7.50 (m, 6H), 7.57 (s, 2H), 7.70 – 7.60 (m, 5H), 7.91 (d, J = 8.0 Hz, 2H); ^{13}C NMR (125 MHz, $\text{C}_2\text{D}_2\text{Cl}_4$) δ 21.48, 118.57, 120.18, 125.62, 125.80, 126.85, 126.97, 127.79, 128.53, 129.04, 129.11, 129.73, 130.30, 131.19, 131.71, 132.00, 132.10, 132.60, 137.39, 137.77, 138.33, 138.83, 141.17, 142.30, 142.67; HRMS (MALDI-TOF, positive) m/z calcd for $\text{C}_{42}\text{H}_{28}\text{Br}_2[\text{M}]^+$ 690.0558, found 690.0561.

7.3.1.14 3-Bromo-4-iodoanisole (2-22)



A stirred solution of 3-bromoanisole (10 g, 53.5 mmol), mercury (II) oxide (8.8 g, 40.6 mmol), and acetic anhydride (1 mL) in dichloromethane (100 mL) has been refluxed for 30 min. Then, the iodine (17.6 g, 69.5 mmol) has been added by six portions every 30 min. After refluxing for 12 h and filtration over a pad of celite, the filtrate has been washed with a saturated sodium thiosulfate solution. The aqueous layer has been extracted with dichloromethane (3 x 10 mL), the combined organic layers have been dried over sodium sulfate, and evaporated to remove solvent. Then, purification by flash chromatography (eluent: cyclohexane) has afforded the titled compound **2-22**. Colorless oil (Yield = 94%). ^1H NMR (300 MHz, CD_2Cl_2) δ 3.77 (s, 3H), 6.62 (dd, J = 8.8, 2.9 Hz, 1H), 7.21 (d, J = 2.9 Hz, 1H), 7.71 (d, J = 8.8 Hz, 1H); ^{13}C NMR (75 MHz, CD_2Cl_2) δ 56.19, 89.80, 115.84, 118.96, 130.31, 140.79, 160.85.

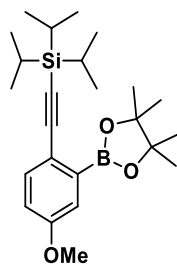
7.3.1.15 ((2-Bromo-4-methoxyphenyl)ethynyl)triisopropylsilane (2-23)



To a mixture of aryl iodide compound **2-22** (10 g, 32 mmol), bis-(triphenylphosphine)palladium (II) dichloride (448 mg, 0.64 mmol), copper(I) iodide (243.4 mg, 1.28 mmol), triethylamine (14 mL)

in tetrahydrofuran (100 mL) has been added drop wise under an argon atmosphere. Next, the liquid compound (triisopropylsilyl) acetylene (8.74 g, 48 mmol) has been added *via* a syringe as well. After the mixture has been stirred at room temperature overnight, diethyl ether (20 mL) has been added to the crude mixture. Then the mixture has been filtered over a short pad of celite to remove catalyst. The organic layer has been washed with brine (5 mL) for three times, and the organic layer has been collected and dried over magnesium sulfate and evaporated. Purification by flash chromatography (eluent: 1% diethyl ether/hexane) has afforded the compound **2-23**. Colorless oil (Yield = 93%); ^1H NMR (300 MHz, CD_2Cl_2) δ 1.16 (s, 21H), 3.80 (s, 3H), 6.82 (dd, $J = 8.7, 2.6$ Hz, 1H), 7.14 (d, $J = 2.5$ Hz, 1H), 7.44 (d, $J = 8.6$ Hz, 1H); ^{13}C NMR (75 MHz, CD_2Cl_2) δ 11.98, 19.07, 56.24, 94.56, 105.40, 113.98, 118.33, 118.37, 126.89, 135.07, 160.61; HRMS (MALDI-TOF, positive) m/z calcd for $\text{C}_{18}\text{H}_{27}\text{BrOSi}[\text{M}]^+$ 366.1015, found 366.1078.

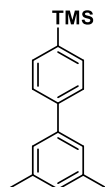
7.3.1.16 Triisopropyl((4-methoxy-2-(4,4,5,5-tetramethyl-1,3,2-dioxaborolan-2-yl)phenyl)ethynyl)silane (2-24)



A 250 mL round flask has been charged with compound **2-23** (19.5 g, 53.1 mmol), bis(pinacolato)diboron (14.8 g, 58.4 mmol), potassium acetate (15.6 g, 159 mmol) and [1,1'-bis(diphenylphosphino)ferrocene]dichloropalladium(II) (1.2 g, 1.6 mmol). Then the stirring mixture has been degassed by argon bubbling for 20 min. Afterwards, the mixture has been stirred overnight at 80 °C under an argon atmosphere. After cooling to room temperature, the mixture has been washed with water and extracted with ethyl acetate (20 mL X 3). The combined organic layer has been washed with brine, dried over magnesium sulfate, and evaporated. At last, the crud residue **2-24** has been purified by passing through a shot pad of silica gel (eluent: 10% ethyl acetate/hexane) to remove the catalyst and used directly for the next step. Brown yellow oil (Yield = 85%). ^1H NMR (300 MHz, CD_2Cl_2) δ 1.15 (d, $J = 1.2$ Hz, 23H), 1.33 (s, 12H), 3.81 (s, 3H), 6.89 (dd, $J = 8.6, 2.9$ Hz, 1H), 7.23 (d, $J = 2.8$ Hz, 1H), 7.45 (d, $J = 8.5$ Hz, 1H); ^{13}C NMR (75 MHz, CD_2Cl_2) δ 11.86, 18.97,

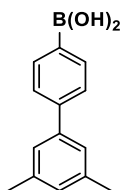
25.00, 55.63, 84.28, 90.90, 108.06, 116.72, 120.34, 120.80, 135.85, 159.17; HRMS (ESI, positive) m/z calcd for $C_{24}H_{40}BO_3Si[M+H]^+$ 415.2840, found 415.2845.

7.3.1.17 (3', 5'-Dimethyl-[1,1'-biphenyl]-4-yl)trimethylsilane (2-25)



A 250 mL round flask has been charged with 1-bromo-3,5-dimethylbenzene (6 g, 32.4 mmol), (4-(trimethylsilyl)phenyl)boronic acid (9.44 g, 48.6 mmol), potassium carbonate solution (18 g in 10 mL water), ethanol 10 mL, and toluene 50 mL. The mixture has been degassed by argon bubbling for 10 min. Then tetrakis(triphenylphosphino)palladium(0) (1.87 g, 1.62 mmol) has been added. The resulting mixture has been further degassed by argon bubbling for 10 min, and treated with liquid nitrogen bath. After three times freeze-pump-thaw procedure, the mixture has been refluxed overnight. The reaction has been monitored by thin-layer chromatography plate. Once the reaction is completed, the mixture has been washed with deionized water and the aqueous layer has been extracted with ethyl acetate for three times (10 mL x 3). The combined organic layer has been washed with brine, dried over sodium sulfate, and evaporated. The crud product has been purified by silica gel column chromatography (eluent: 5% dichloromethane/hexane) to afford compound **2-25**. Colorless oil (Yield = 95%). 1H NMR (300 MHz, CD_2Cl_2) δ 0.32 (s, 9H), 2.39 (s, 6H), 7.02 (m, 1H), 7.24 (ddd, $J = 1.9, 1.3, 0.7$ Hz, 2H), 7.60 (t, $J = 1.3$ Hz, 4H); ^{13}C NMR (75 MHz, CD_2Cl_2) δ -0.83, 21.72, 125.47, 126.87, 129.55, 134.34, 138.90, 139.65, 141.48, 142.27.

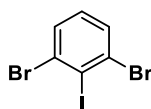
7.3.1.18 (3',5'-dimethyl-[1,1'-biphenyl]-4-yl)boronic acid (2-26)



Compound **2-25** (8 g, 31.4 mmol) has been directly treated with neat boron tribromide (12.6 g, 50.3mmol) under argon atmosphere. A condenser charged with argon has been attached, and the

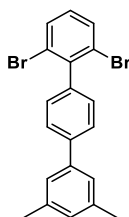
mixture has been heated to 100 °C for 4 h. Once cooled, excess boron tribromide has been distilled off under vacuum at room temperature. The resulting gray-purple solid has been dissolved in dry hexane (50 mL) and cooled to 0 °C with an ice bath. Water has been slowly added drop wise while stirring vigorously until the reaction had been fully quenched. The resulting mixture has been filtered and the white solid has been washed with deionized water and hexane. The white powder has been dried at 80 °C under vacuum overnight, yielding boronic acid **2-26**, which has been used directly for the next step. White powder.

7.3.1.19 1,3-Dibromo-2-iodobenzene (2-27)



At -75 °C, butyllithium (42.4 mmol) in hexane (50 mL) and diisopropylamine (42.4 mmol) have been added successively to tetrahydrofuran (20 mL). After 15 min, 1, 3-dibromobenzene (5.12 mL, 10 g, 42.4 mmol) has been added. The mixture has been kept at -75 °C for 2 h before a solution of iodine (10.76 g, 42.4 mmol) in tetrahydrofuran (50 mL) is added. After addition of a 10% aqueous solution (0.10 L) of sodium thiosulfate, the mixture has been extracted with diethyl ether for three times (10 mL x 3). The combined organic layer has been washed with water and brine once, and then dried over sodium sulfate before being evaporated to dryness. Upon crystallization from ethanol (100 mL), the colorless platelets have been obtained. Colorless platelets (Yield = 91%). ¹H NMR (300 MHz, CD₂Cl₂) δ 7.10 (t, *J* = 8.0 Hz, 1H), 7.58 (d, *J* = 8.1 Hz, 2H); ¹³C NMR (75 MHz, CD₂Cl₂) δ 109.67, 131.09, 131.73.

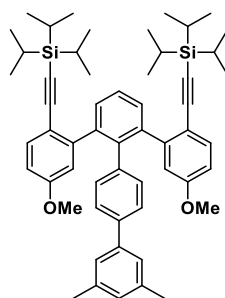
7.3.1.20 2,6-Dibromo-3',5'-dimethyl-1,1':4',1''-terphenyl (2-28)



In a glove box, tris(dibenzylideneacetone)dipalladium(0) (1.02 g, 1.11 mmol), tricyclohexylphosphine (1.25 g, 4.45 mmol), compound **2-27** (8.04 g, 22.23 mmol), and boronic acid

2-26 (5.03 g, 22.23 mmol) have been added to a reaction vessel that is equipped with a stir bar. The degassed tripotassium phosphate (14.16 g, 66.7 mmol) water solution has been then added, followed by 100 mL anhydrous tetrahydrofuran. The reaction mixture has been then stirred at 60 °C for 3 days. Once the reaction is finished, the reaction mixture has been diluted with ethyl acetate, and then extracted by ethyl acetate for three times. The combined organic layer have been washed three times with water and once with brine, then dried over magnesium sulfate and evaporated. The final product **2-28** has been obtained after purification by silica gel column chromatography (eluent: 10% dichloromethane/hexane). Colorless oil (Yield = 48%). Mp: 104.2-104.9 °C; ¹H NMR (300 MHz, CD₂Cl₂) δ 2.40 (s, 6H), 7.04 (tt, *J* = 1.6, 0.8 Hz, 1H), 7.12 (t, *J* = 8.0 Hz, 1H), 7.23 – 7.35 (m, 4H), 7.64 – 7.73 (m, 4H); ¹³C NMR (75 MHz, CD₂Cl₂) δ 21.72, 125.08, 125.52, 127.31, 129.70, 130.19, 130.56, 132.50, 138.96, 140.58, 140.89, 141.62, 143.25; HRMS (APPI-TOF, positive) *m/z* calcd for C₂₀H₁₆Br₂ [M]⁺ 413.9619, found 413.9619.

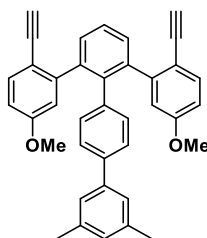
7.3.1.21 2,6-di[5-methoxy-2-((triisopropylsilyl)ethynyl)phenyl]-3',5''-dimethyl-1,1':4',1''-terphenyl (**2-29**)



A 100 mL round flask has been filled with compound **2-28** (1.16 g, 2.79 mmol), boronic ester **2-24** (3.47 g, 8.36 mmol) in 50 ml toluene and 5 mL potassium carbonate (2.31 g, 16.72 mmol) water solution. After degassed by argon bubbling for 10 min, the tetrakis(triphenylphosphino)palladium(0) (322 mg, 0.28 mmol) has been added. The reaction mixture has been then refluxed overnight, and stopped after thin-layer chromatography indicated that the starting material is totally converted. After cooling down to room temperature, the mixture has been extracted with ethyl acetate for three times (10 mL x 3), and then the combined organic layer has been washed three times with water and dried over magnesium sulfate, then evaporated. The residue has been purified by silica gel column chromatography (eluent: 10% ethyl acetate/hexane) yielding compound **2-29**. Yellow solid (Yield = 81%). Mp: 180.8-181.2 °C; ¹H NMR (300 MHz, CD₂Cl₂) δ 1.02 (s, 42H), 2.30 (s, 6H), 3.50 (s, 6H), 6.30 (d, *J* = 2.6 Hz, 2H), 6.63 (dd, *J* = 8.6, 2.7 Hz, 2H), 7.05 – 7.17 (m, 4H), 7.17 – 7.25 (m, 2H),

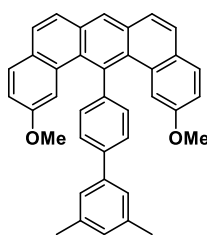
7.38 (q, $J = 1.9$ Hz, 4H), 7.42 (s, 1H); ^{13}C NMR (75 MHz, CD_2Cl_2) δ 11.92, 19.04, 21.64, 55.64, 92.66, 107.35, 113.62, 115.91, 116.48, 125.05, 125.93, 126.87, 129.25, 130.72, 131.26, 133.81, 138.72, 139.11, 139.42, 139.46, 140.87, 141.09, 147.54, 159.20; HRMS (ESI, positive) m/z calcd for $\text{C}_{56}\text{H}_{71}\text{O}_2\text{Si}_2[\text{M}+\text{H}]^+$ 831.4993, found 831.4979.

7.3.1.22 2,6-Di[5-methoxy-2-ethynyl-phenyl]-3',5'-dimethyl-1,1':4',1''-terphenyl (2-30)



To a solution of compound **2-29** (1.5 g, 1.8 mmol) in 50 mL of dry tetrahydrofuran, a solution of tetra-*n*-butylammonium fluoride (5.69 g, 18 mmol) in tetrahydrofuran (10 mL) has been added. After stirring at room temperature for 2 h, water has been added to the reaction mixture and tetrahydrofuran has been removed in *vacuo* at 40 °C. The resulting suspension has been extracted three times with ethyl acetate, and the combined organic layers have been washed five times with water, dried over magnesium sulfate, and evaporated. The yielding white solid has been used directly for the next step without further purification.

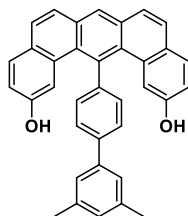
7.3.1.23 14-(3',5'-Dimethyl-[1,1'-biphenyl]-4-yl)-2,12-dimethoxy-dibenzo[*a,j*] anthracene (2-31)



A 100 mL round flask has been charged with compound **2-30** (1.1 g, 2.12 mmol) and platinum (II) chloride (56.4 mg, 0.21 mmol). Then the mixture has been kept under vacuum conditions for 20 min and refilled with argon. 60 ml of anhydrous toluene has been added by syringe afterwards. The mixture has been heated at 80 °C for 24 h after reaction is completed, as judged by thin-layer chromatography (TLC) plate. The toluene has been then removed under vacuum conditions and the

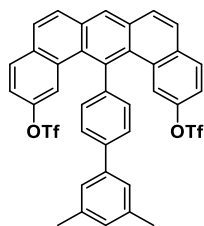
residue has been purified by silica gel column chromatography (eluent: 5% dichloromethane/hexane) yielding the compound **2-31**. White solid (Yield = 63%). Mp: 234.4-235.2 °C; ^1H NMR (300 MHz, CD_2Cl_2) δ 2.44 (s, 6H), 3.27 (s, 6H), 7.00 (s, 3H), 7.04 (d, $J = 2.5$ Hz, 1H), 7.10 (s, 1H), 7.31 (dt, $J = 1.5, 0.8$ Hz, 2H), 7.61 – 7.77 (m, 8H), 7.87 – 7.95 (m, 2H), 8.36 (s, 1H); ^{13}C NMR (75 MHz, CD_2Cl_2) δ 21.77, 55.13, 111.74, 117.12, 125.18, 125.37, 128.33, 129.18, 129.92, 130.09, 130.23, 132.45, 132.86, 133.15, 139.34, 144.96, 156.99 ; HRMS (ESI, positive) m/z calcd for $\text{C}_{38}\text{H}_{31}\text{O}_2[\text{M}+\text{H}]^+$ 519.2324, found 519.2302.

7.3.1.24 14-(3',5'-Dimethyl-[1,1'-biphenyl]-4-yl)-dibenzo[*a,j*]anthracene-2,12-diol (2-32)



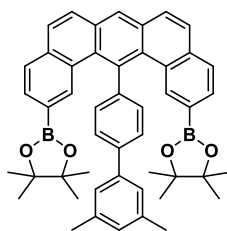
Compound **2-31** (250 mg, 0.48 mmol) has been dissolved in 40 mL dry dichloromethane under argon atmosphere. Then, 5.8 mL 1M BBr_3 (1.45 g, 5.78 mmol in dichloromethane) have been added drop wise to the solution at 0 °C. The solution has been then allowed to warm to room temperature and stirred for 6 h. The reaction has been monitored by thin-layer chromatography plate. Once the reaction is completed, 10 mL water has been slowly added at 0 °C. The mixture has been washed with water and extracted with dichloromethane for three times. Then, the organic layer has been dried over magnesium sulfate, and evaporated. The residue has been re-precipitated as a pale green powder from dichloromethane/hexane (1:50) and used directly for the next step without further purification.

7.3.1.25 14-(3',5'-Dimethyl-[1,1'-biphenyl]-4-yl)-dibenzo[*a,j*]anthracene-2,12-bis(trifluoromethanesulfonate) (2-33)

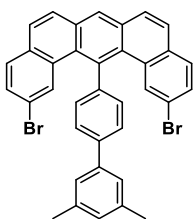


Crude compound **2-32** (236 mg, 0.48 mmol) has been dissolved in 20 mL dichloromethane and cooled to 0 °C. Then 0.36 mL triethylamine (2.6 mmol) have been added drop wise. Afterwards, 1 M Tf₂O (1.44 mL) solution has been added by syringe. The mixture solution has been allowed to warm to room temperature and stirred for 4 h. Once thin-layer chromatography plate shows the complete of the reaction, the dichloromethane has been removed and the residue has been purified by silica gel column chromatography (eluent: 10% ethyl acetate/hexane) yielding compound **2-33**. White solid (Yield = 78%). Mp: 305.9-306.7 °C; ¹H NMR (300 MHz, CD₂Cl₂) δ 2.45 (s, 6H), 7.11 (s, 1H), 7.30 (d, *J* = 2.5 Hz, 2H), 7.38 (dd, *J* = 8.7, 2.5 Hz, 2H), 7.43 (s, 2H), 7.53 (d, *J* = 8.2 Hz, 2H), 7.79 (s, 1H), 7.82 (s, 1H), 7.92 (d, *J* = 2.8 Hz, 2H), 7.94 – 7.98 (m, 3H), 8.00 (s, 1H), 8.51 (s, 1H); ¹³C NMR (75 MHz, CD₂Cl₂) δ 21.49, 116.39, 119.74, 122.06, 125.89, 127.94, 128.04, 128.83, 129.15, 129.64, 130.65, 130.87, 131.01, 132.46, 132.78, 134.23, 138.64, 139.91, 140.83, 142.22, 143.72, 146.60; HRMS (ESI, positive) *m/z* calcd for C₃₈H₂₅F₆O₆S₂[M+H]⁺ 755.0997, found 755.0993.

7.3.1.26 14-(3',5'-Dimethyl-[1,1'-biphenyl]-4-yl)-dibenzo[*a,j*]anthracene-2,12-diyl -bis(4,4,5,5-tetramethyl-1,3,2-dioxaborolane) (2-34)

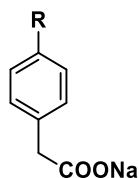


A Schlenk tube has been charged with compound **2-33** (110 mg, 0.145 mmol), [1,1'-bis(diphenylphosphino)ferrocene]dichloropalladium(II) (6 mg, 0.007 mmol), 5mL dry dioxane and triethylamine (0.12 mL, 0.87 mmol). The solution has been degassed by argon bubbling for 10 min and pinacolborane (0.08 mL, 0.58 mmol) has been added. The mixture has been then heated at refluxing temperature for 12 h. Then the solvent has been removed under vacuum and the residue purified by silica gel chromatography (eluent: 5 % ethyl acetate/hexane) to afford compound **2-34**. Light yellow solid (Yield = 71%). Mp: 282.6-283.2 °C; ¹H NMR (300 MHz, CD₂Cl₂) δ 1.02 (24H, d, *J* = 7.3 Hz), 2.40 (6H, d, *J* = 10.1 Hz), 7.01 (1H, s), 7.48 – 7.54 (4H, m), 7.69 – 7.73 (4H, m), 7.78 – 7.81 (2H, m), 7.85 – 7.88 (2H, d, *J* = 8.8 Hz), 7.96 – 7.99 (4H, m), 8.35 (1H, s); ¹³C NMR (75 MHz, CD₂Cl₂) δ 21.70, 24.79, 83.97, 125.41, 128.02, 128.05, 128.50, 128.54, 128.96, 129.20, 129.36, 129.84, 131.21, 131.83, 132.06, 136.60, 136.78, 138.48, 140.45, 140.83, 142.87, 143.00, 143.22, 144.08; HRMS (APPI-TOF, positive) *m/z* calcd for C₄₈H₄₈B₂O₄[M]⁺ 710.3739, found 710.3778.

7.3.1.27 2,12-Dibromo-14-(3',5'-dimethyl-[1,1'-biphenyl]-4-yl)-dibenzo[*a,j*]-anthracene (2-20d)

A 12 mL sealtube has been charged with compound **2-34** (50 mg, 0.07 mmol), copper (II) bromide (95 mg, 0.42 mmol), 2 mL tetrahydrofuran, 6 mL methanol and 4 mL water. The tube has been degassed by argon bubbling for 10 min, then sealed and heated at 120 °C overnight. After cooling to the room temperature, the mixture has been extracted with dichloromethane for three times (5 mL x 3). The combined organic layers have been dried over magnesium sulfate, and then evaporated. The residue has been purified by silica gel chromatography (eluent: 10 % dichloromethane/hexane) and re-precipitated from dichloromethane/methanol (1:10) to yield final product **2-20d**. Colorless solid (Yield = 60%). Mp: 267.9-268.5 °C; ^1H NMR (300 MHz, CD_2Cl_2) δ 2.45 (s, 6H), 7.10 (s, 1H), 7.47 – 7.55 (m, 8H), 7.69 – 7.73 (m, 4H), 7.88 – 7.97 (m, 4H), 8.43 (s, 1H); ^{13}C NMR (75 MHz, CD_2Cl_2) δ 21.79, 119.77, 125.96, 127.76, 128.03, 128.39, 128.70, 129.62, 129.80, 130.33, 130.48, 131.26, 132.02, 132.56, 132.71, 133.07, 133.37, 136.04, 139.05, 141.59, 143.46; HRMS (APPI-TOF, positive) m/z calcd for $\text{C}_{36}\text{H}_{24}\text{Br}_2[\text{M}]^+$ 614.0245, found 614.0246.

7.3.2 Synthesis of monomer precursor 3-1 for solution-mediated fabrication of GNR 3-3c in solution**7.3.2.1 Sodium 2-phenylacetate (3-5)**



3-5a; R=H
 3-5b; R=*t*-Bu
 3-5c; R=I

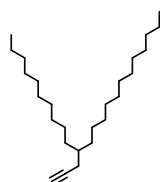
The sodium phenylacetate **3-5** was prepared from 4-substituted phenylacetic acid and one equivalent of sodium methylate (0.5 M methanol solution) through simple mixing and subsequent evaporation of the solvent in almost quantitative yields (~99%).

Sodium 2-phenylacetate (3-5a): White solid; ^1H NMR (300 MHz, D_2O) δ 3.51 (s, 2H), 7.28 (d, $J = 7.4$ Hz, 3H), 7.32 – 7.41 (m, 2H); ^{13}C NMR (75 MHz, D_2O) δ 44.44, 126.40, 128.61, 129.11, 137.26, 181.06.

Sodium 2-(4-(*tert*-butyl)phenyl)acetate (3-5b): White solid; ^1H NMR (300 MHz, D_2O) δ 1.28 (s, 9H), 3.48 (s, 2H), 7.22 (s, 1H), 7.25 (s, 1H), 7.42 (s, 1H), 7.45 (s, 1H); ^{13}C NMR (75 MHz, D_2O) δ 30.55, 33.74, 43.94, 125.52, 128.95, 134.40, 149.79, 181.08.

Sodium 2-(4-iodophenyl)acetate (3-5c): White solid; ^1H NMR (300 MHz, D_2O) δ 3.45 (s, 2H), 7.02 (s, 1H), 7.05 (s, 1H), 7.67 (s, 1H), 7.70 (s, 1H); ^{13}C NMR (75 MHz, D_2O) δ 43.93, 90.99, 131.27, 136.99, 137.44, 180.40.

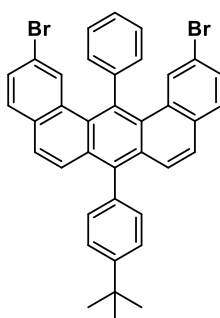
7.3.2.2 11-(prop-2-yn-1-yl)tricosane (3-7)



To a suspension of lithium acetylide-ethylenediamine complex (22.1g, 240 mmol) in methyl sulfoxide (DMSO) (10 mL) was added 2-decyltetradecyl bromide **3-6** (10.0 g, 23.9 mmol) at 0 °C. The reaction mixture was stirred for 12 h at the room temperature. After the completion of the reaction, saturated aqueous solution of ammonium chloride (10 mL) was added to the mixture. The mixture was then extracted with ether, washed with brine, dried over magnesium sulfate, and

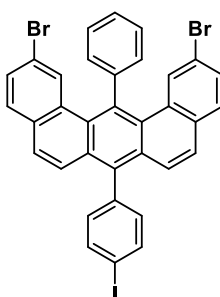
concentrated in vacuo. The residue was purified by silica gel column chromatography (eluent: hexane) to afford compound **3-7** as a colorless oil (8.3 g, 95% yield): ^1H NMR (300 MHz, CD_2Cl_2); ^1H NMR (250 MHz, CD_2Cl_2) δ 0.77 – 0.98 (m, 6H), 1.27 (s, 4H), 1.94 – 2.02 (m, 1H), 2.16 (dd, J = 5.6, 2.6 Hz, 1H), 4.67 (s, 1H); ^{13}C NMR (75 MHz, CD_2Cl_2) δ 14.71, 23.29, 23.52, 27.55, 30.22, 30.52, 30.74, 32.77, 34.14, 37.66, 69.48, 83.84.

7.3.2.3 2,12-dibromo-7-(4-(*tert*-butyl)phenyl)-14-phenylbenzo[*m*]tetraphene (**3-1b**)



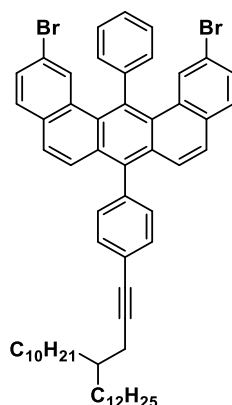
A mixture of pyrylium salt **3-9** (**2-17a**) (1.8 g, 2.99 mmol) and Sodium 2-(4-(*tert*-butyl)phenyl)acetate (**3-5b**) (1.7 g, 8.97 mmol) in acetic anhydride (Ac_2O , 50 mL) was stirred at 150 °C for 12 h under argon atmosphere. After cooling to the room temperature, the precipitate was filtered off and washed with Ac_2O , and then methanol. The crude product was re-precipitated from chloroform and hexane to give U-shaped monomer **3-1b** as brown powder (29% yield): Mp: > 400 °C; ^1H NMR (500 MHz, $\text{C}_2\text{D}_2\text{Cl}_4$, 353 K) δ 1.49 (s, 9H), 7.36 (s, 1H), 7.38 (s, 1H), 7.42 (d, J = 1.8 Hz, 2H), 7.46 – 7.53 (m, 8H), 7.62 (t, J = 8.5 Hz, 4H), 7.67 – 7.76 (m, 3H); ^{13}C NMR (126 MHz, $\text{C}_2\text{D}_2\text{Cl}_4$, 353 K) δ 31.83, 35.00, 118.72, 120.59, 125.73, 126.45, 127.15, 127.21, 129.15, 129.43, 130.84, 131.12, 131.38, 131.76, 132.46, 132.57, 132.88, 135.89, 138.00, 138.25, 144.15, 151.03. HRMS (MALDI-TOF, positive) m/z calcd for $\text{C}_{38}\text{H}_{28}\text{Br}_2$ $[\text{M}]^+$ 644.0537, found 644.0547.

7.3.2.4 2,12-dibromo-7-(4-iodophenyl)-14-phenylbenzo[*m*]tetraphene (**3-12**)



Compound **3-12** was prepared following same procedure as **3-1b** to afford a brown powder (31% yield): ^1H NMR (500 MHz, $\text{C}_2\text{D}_2\text{Cl}_4$, 353 K) δ 7.28 (d, $J = 7.5$ Hz, 2H), 7.43 – 7.61 (m, 10H), 7.65 (d, $J = 8.1$ Hz, 2H), 7.77 (dt, $J = 27.0, 7.1$ Hz, 3H), 8.03 (d, $J = 7.5$ Hz, 2H); ^{13}C NMR (126 MHz, $\text{C}_2\text{D}_2\text{Cl}_4$, 353 K) δ 93.87, 119.09, 125.56, 127.49, 127.58, 129.20, 129.31, 129.58, 130.61, 130.98, 131.47, 132.56, 132.60, 132.91, 133.97, 136.30, 138.12, 139.01, 139.15, 144.12; HRMS (APPI-TOF, positive) m/z calcd for $\text{C}_{34}\text{H}_{19}\text{Br}_2\text{I} [\text{M}]^+$ 713.8878, found 713.8882.

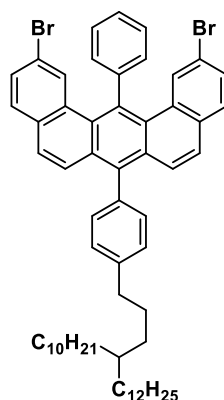
7.3.2.5 2,12-dibromo-7-(4-(4-decyloctadec-1-yn-1-yl)phenyl)-14-phenylbenzo- [m]tetraphene (3-13)



To a 50 mL Schlenk tube was charged with compound **3-12** (100 mg, 0.14 mmol), bis-(triphenylphosphine)palladium (II) dichloride (5 mg, 0.007 mmol), and copper(I) iodide (2.7 mg, 0.014 mmol), and then triethylamine (42.5 mg, 0.42 mmol) in tetrahydrofuran (10 mL) was added drop wise under an argon atmosphere. Subsequently, compound **3-7** (152 mg, 0.42 mmol) in 10 mL tetrahydrofuran was added *via* a syringe. After stirring at room temperature overnight, the reaction mixture was diluted with toluene (10 mL) and filtered over a short pad of celite to remove the catalyst. Afterward the resulting organic solution was washed with deionized water (10 mL) twice and then with brine (5 mL). The combined organic layers were dried over magnesium sulfate and evaporated. Purification by flash chromatography with silica gel (eluent: 10% dichloromethane/hexane) afforded compound **3-13** as a grey solid (114 mg, 86% yield): ^1H NMR (250 MHz, CD_2Cl_2) δ 0.78 – 0.94 (m, 7H), 1.31 (d, $J = 16.5$ Hz, 42H), 2.48 (d, $J = 5.7$ Hz, 2H), 7.28 – 7.57 (m, 11H), 7.63 (dd, $J = 8.3, 3.8$ Hz, 4H), 7.73 (dd, $J = 9.5, 7.3$ Hz, 2H); ^{13}C NMR (75 MHz, CD_2Cl_2) δ 14.46, 23.27, 24.24, 27.40, 29.95, 30.26, 30.54, 32.51, 34.24, 37.90, 81.61, 90.94, 119.01, 124.54, 126.19, 127.55, 127.65, 129.44, 129.75, 130.92, 131.33, 131.78, 132.22, 132.36, 132.74,

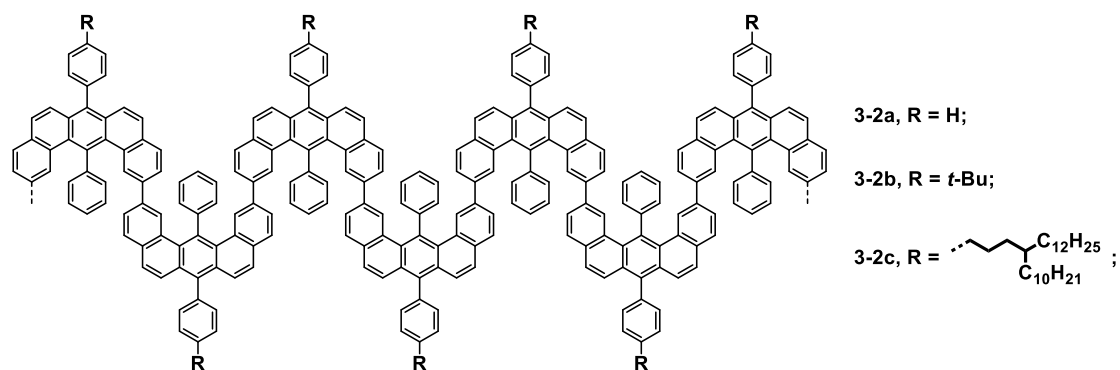
132.94, 133.04, 137.49, 138.82, 138.93, 144.61; HRMS (APPI-TOF, positive) m/z calcd for $C_{60}H_{68}Br_2 [M]^+$ 948.3667, found 948.3686.

7.3.2.5 2,12-dibromo-7-(4-(4-decylhexadecyl)phenyl)-14-phenylbenzo[*m*] tetraphene (3-1c)



To a 100 mL autoclave vessel charged with a stir bar, a solution of compound **3-13** (100 mg, 0.11 mmol) dissolved in 20 mL of anhydrous tetrahydrofuran was added. Then, the solution was degassed by argon bubbling for 20 min and an active platinum(IV) dioxide catalyst (PtO_2 , surface area $\geq 75 \text{ m}^2/\text{g}$) for hydrogenation (1.3 mg, 0.0055 mmol) was added. Next, the autoclave was sealed and the atmosphere inside was replaced *via* a hydrogen steel cylinder from air to hydrogen with a pressure of 5 bar. Afterward the autoclave was let to keep stirring at room temperature for one hour until the hydrogenation reaction was completed. The resulting reaction mixture was then passed through a short pad of silica gel to remove platinum catalyst. Finally, the resulting solution was evaporated to afford “U-shape” monomer **3-1c** as a bright yellow solid (103.7 mg, 99% yield): 1H NMR (300 MHz, CD_2Cl_2) δ 0.81 – 0.92 (m, 6H), 1.27 (d, $J = 12.1$ Hz, 44H), 1.75 (s, 2H), 2.78 (t, $J = 7.7$ Hz, 2H), 7.31 (s, 1H), 7.34 (s, 1H), 7.37 – 7.57 (m, 12H), 7.62 (s, 1H), 7.66 (d, $J = 1.8$ Hz, 1H), 7.70 (d, $J = 1.5$ Hz, 1H), 7.74 (dd, $J = 3.6, 2.0$ Hz, 1H); ^{13}C NMR (75 MHz, CD_2Cl_2) δ 14.45, 23.26, 27.27, 29.16, 29.95, 30.26, 30.31, 30.74, 32.50, 33.84, 34.24, 36.77, 37.85, 118.89, 126.50, 127.37, 127.53, 129.18, 129.38, 129.69, 131.17, 131.30, 131.83, 132.18, 132.78, 132.98, 133.06, 136.65, 138.30, 138.60, 143.48, 144.70; HRMS (APPI-TOF, positive) m/z calcd for $C_{60}H_{72}Br_2 [M]^+$ 952.3980, found 952.3985.

7.3.3 Synthesis of polymer precursor 3-2(a, b, and c) in solution



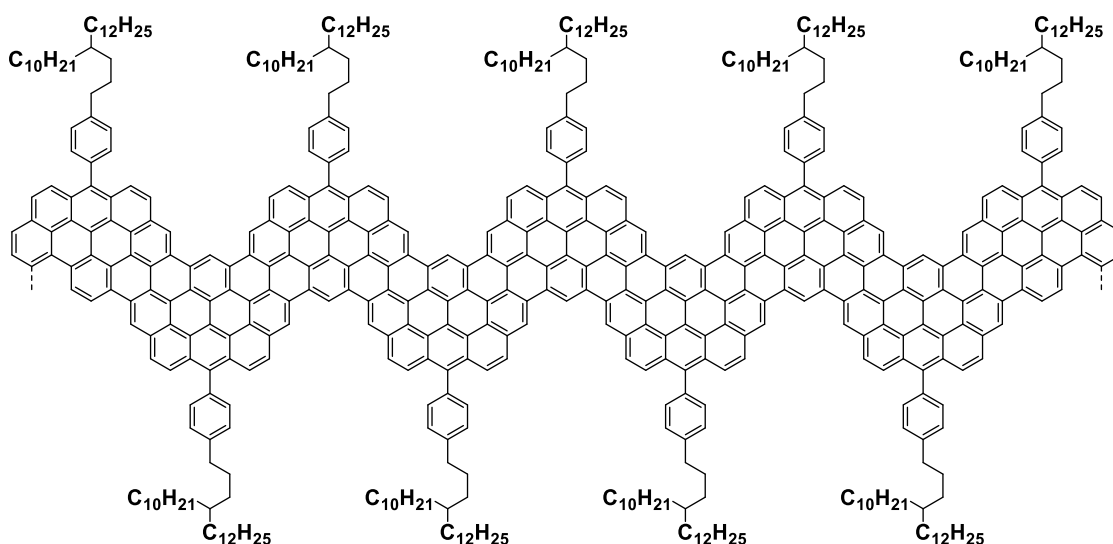
The catalyst solution was prepared inside the glove box by adding 1 mL of dry DMF and 2 mL of dry toluene to a mixture of bis(cyclooctadiene)nickel(0) (2 eq. of **3-1**), 2,2'-bipyridine (2 eq. of **3-1**), and cyclooctadiene (2 eq. of **3-1**). The resulting solution was stirred for 30 min at 60 °C. Then, a solution of monomer **3-1** (**3-1a**:100 mg, 0.17 mmol; **3-1b**:100 mg, 0.155 mmol; **3-1c**:100 mg, 0.105 mmol) was dispersed or dissolved in 2 mL of toluene and 1 mL of DMF was added. The reaction mixture was i) stirred for 24 h at 120 °C in a microwave reactor or ii) for 3 days at 80 °C in an oil bath under the exclusion of light. After cooling, the reaction mixture was slowly dropped into dilute methanolic hydrochloric acid. The yellow precipitate that formed was collected by filtration and washed repeatedly by methanol and dilute hydrochloric acid to completely remove the catalyst. Polymer precursors **3-2a** and **3-2b** were barely soluble in common organic solvent such as THF, chloroform, and toluene. The polymer precursor **3-2c** could be dissolved perfectly in the solvent mentioned above, and thus could be further fractionated by using recycling preparative SEC (Waters Ultrastyrigel 103 Å, 19 × 300 mm, eluent: chloroform, 3.0 mL/min) to obtain large-molecular-weight fraction **3-2c-I** (microwave condition) with M_w of 92000 g/mol, M_n of 23000 g/mol and PDI of 4.0, as well as **3-2c-II** (normal heating condition) with M_w of 184000 g/mol, M_n of 97000 g/mol and PDI of 1.9.

3-2a: FTIR (powder) 3050, 3026, 2928, 1947, 1900, 1744, 1599, 1506, 1495, 1473, 1439, 1393, 1200, 1176, 1154, 1071, 1026, 1001, 890, 832, 821, 778, 755, 729, 698 cm^{-1} .

3-2b: FTIR (powder) 3049, 3026, 2958, 2901, 2864, 1907, 1736, 1605, 1508, 1474, 1460, 1441, 1392, 1361, 1267, 1199, 1113, 1070, 1022, 1000, 961, 903, 834, 779, 752, 729, 700, 604 cm^{-1} .

3-2c: FTIR (powder) 3089, 3049, 3024, 2922, 2850, 2360, 1903, 1783, 1740, 1708, 1600, 1511, 1461, 1441, 1395, 1376, 1258, 1201, 1180, 1071, 1021, 1000, 963, 887, 833, 778, 751, 725, 699, 601 cm^{-1} .

7.3.4 Synthesis of GNR 3-3c in solution



Method 1 (FeCl_3) for the synthesis of GNR **3-3c (Fe)**: In a typical experiment, a solution of polymer precursor **3-2c-I** (10 mg) in unstabilized dichloromethane (40 mL) was degassed by argon bubbling for 10 min. To the degassed solution was added a suspension of iron(III) chloride (201 mg, 1.24 mmol, 7 eq. for one hydrogen to be removed) in nitromethane (3 mL). After stirring at room temperature for 72 h under continuous bubbling with argon, the reaction was quenched by the addition of methanol to form dark black precipitates. Filtration by suction using a membrane filter and washing intensively with methanol and THF gave GNR **3-3c-I (Fe)** as a dark purple powder (9.6 mg, 98% yield)

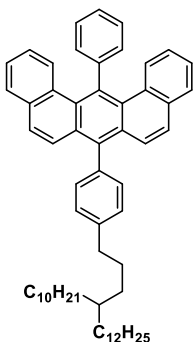
Method 2 ($\text{Cu}(\text{OTf})_2/\text{AlCl}_3$) for the synthesis of GNR **3-3c (Cu)**: In a typical experiment, copper (II) triflate (105 mg, 0.29 mmol, 3 eq. for one hydrogen to be removed) was dried completely under vacuum at 80 °C. After cooling, aluminium (III) chloride (39 mg, 0.29 mmol) and dry CS_2 (100 mL) were added under an argon atmosphere. The mixture was suspended by intense stirring for 15 min, warmed to 30 °C and then polymer precursor **3-2c-I** (10 mg) dissolved in CS_2 (4 mL) was added *via* a syringe. After stirring for 3 days at 30 °C, the reaction was quenched by adding methanol (50 mL).

The residue was collected by filtration with a membrane film, washed successively with ammonium hydroxide solution, HCl, water, ethanol, CS₂, and dichloromethane, and then subsequently dried in *vacuo* to afford GNR **3-3c-I (Cu)** as a black powder (9.1 mg, 93% yield).

3-3c-I (Fe) and (Cu): FTIR (powder) 3048, 3027, 2921, 2851, 1714, 1588, 1457, 1210, 1157, 1078, 882, 839, 720, 701 cm⁻¹; Raman (powder, 514.5 nm) 3196, 2897, 2655, 1598, 1325 cm⁻¹.

7.3.5 Synthesis of model compounds 3-15, 3-17, and 3-19

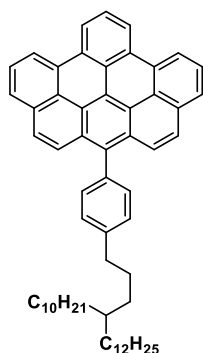
7.3.5.1 7-(4-(4-decylhexadecyl)phenyl)-14-phenylbenzo[*m*]tetraphene (3-14)



To a 50 mL Schlenk tube equipped with a stir bar, monomer **3-1c** (100 mg, 0.105 mmol) dissolved in 10 mL tetrahydrofuran was added. After the solution was cooled to -78 °C, a *n*-butyllithium (0.34 mL, 0.21 mmol, 1.6 M in hexane) was added drop wise *via* a syringe. The mixture was stirred for 30 min, and then quenched by adding 5 mL methanol. After the solvent was evaporated under vacuum, the residue was washed with deionized water for three times, and then with brine. The organic layer was dried over magnesium sulfate and evaporated. The residue was purified by silica gel column chromatography (eluent: 10% dichloromethane/hexane) to afford the title compound **3-14** as a white solid (81.8 mg, 98% yield): ¹H NMR (300 MHz, CD₂Cl₂) δ 0.87 (t, *J* = 6.6 Hz, 6H), 1.29 (d, *J* = 13.4 Hz, 44H), 1.77 (s, 2H), 2.70 – 2.84 (m, 2H), 6.94 (ddd, *J* = 8.6, 7.0, 1.5 Hz, 2H), 7.28 (d, *J* = 8.7 Hz, 2H), 7.32 – 7.49 (m, 10H), 7.51 (s, 1H), 7.53 – 7.64 (m, 3H), 7.75 (d, *J* = 7.8 Hz, 2H); ¹³C NMR (75 MHz, CD₂Cl₂) δ 34.66, 43.47, 47.50, 49.41, 50.15, 50.16, 50.45, 50.47, 50.53, 50.95, 52.72, 54.11, 54.47, 57.01, 58.09, 144.68, 146.16, 146.71, 147.94, 148.50,

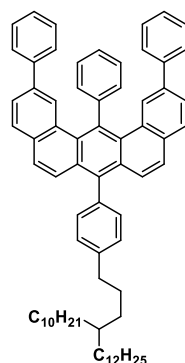
148.76, 149.30, 150.35, 150.88, 151.09, 151.71, 152.54, 152.70, 154.66, 157.27, 158.08, 158.30, 163.47, 166.18; HRMS (APPI-TOF, positive) m/z calcd for $C_{60}H_{74} [M]^+$ 794.5791, found 794.5800.

7.3.5.2 14-(4-(4-decylhexadecyl)phenyl)phenanthro[2,3,4,5-pqrab]perylene (3-15)



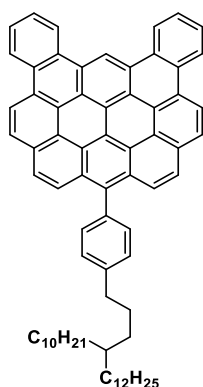
To a solution of compounds **3-14** (100 mg, 0.13 mmol) in dichloromethane (DCM) (10 mL) cooled to 0 °C were added 2,3-dichloro-5,6-dicyano-*p*-benzoquinone (DDQ) (86 mg, 0.38 mmol, 1.5 eq. / carbon-carbon bond) and trifluoroacetic acid (TFA) (0.53 mL, DCM/TFA = 9.5/0.5). The mixture was stirred at 0 °C for 1 h, and then 10% $NaHCO_3$ aq. (20 mL) solution was added and stirred for 30 min. The organic phase was washed with water (20 mL \times 2), dried over magnesium sulfate, and evaporated. The residue was purified by silica gel column chromatography (eluent: 5% dichloromethane/hexane) to give the title compound (84.6 mg, 85% yield) as sticky white solid: 1H NMR (300 MHz, CD_2Cl_2) δ 0.86 (s, 6H), 1.09 – 1.53 (m, 44H), 1.83 (p, $J = 8.8$ Hz, 2H), 2.76 – 2.94 (m, 2H), 7.52 (d, $J = 1.9$ Hz, 4H), 7.91 – 8.10 (m, 7H), 8.14 – 8.23 (m, 2H), 8.96 – 9.09 (m, 4H); MALDI-TOF-MS: calcd for $C_{60}H_{70} [M]^+$ 790.54, found: 790.25; FTIR (powder) 3074, 3042, 2920, 2950, 2362, 2162, 2035, 1593, 1514, 1463, 1421, 1382, 1300, 1199, 1004, 894, 829, 795, 754, 724 cm^{-1} .

7.3.5.3 7-(4-(4-decylhexadecyl)phenyl)-2,12,14-triphenylbenzo[*m*]tetraphene (3-16)



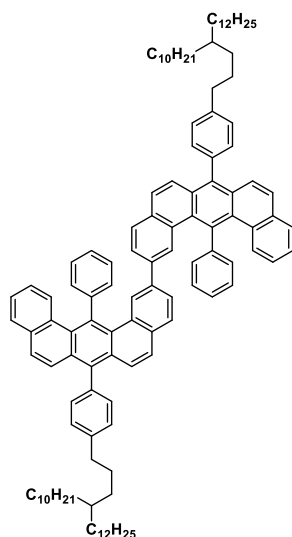
To a solution of compound **3-1c** (100 mg, 0.105 mmol) and phenylboronic acid (25.6 mg, 0.21 mmol) in 10 ml toluene in a 100 mL round flask was added 2 mL of potassium carbonate (86.8 mg, 0.63 mmol) aqueous solution. After degassing with argon bubbling for 10 min, tetrakis(triphenylphosphino)palladium(0) (24.3 mg, 0.021 mmol) was added, and The reaction mixture was then refluxed overnight. After cooling to the room temperature, toluene was removed in *vacuo* at 50 °C. The resulting suspension was extracted three times with dichloromethane, and the combined organic layers were washed with deionized water, dried over magnesium sulfate, and evaporated. The residue was purified by silica gel column chromatography (eluent: 5% dichloromethane/hexane) to provide compound **3-16** as a bright yellow solid (70.6 mg, 71% yield): ^1H NMR (300 MHz, CD_2Cl_2) δ 0.86 (t, $J = 6.5$ Hz, 6H), 1.28 (d, $J = 13.0$ Hz, 57H), 1.76 (q, $J = 11.9, 9.5$ Hz, 2H), 2.78 (t, $J = 7.6$ Hz, 2H), 7.15 – 7.21 (m, 3H), 7.27 – 7.38 (m, 7H), 7.41 – 7.49 (m, 5H), 7.53 – 7.74 (m, 11H), 7.84 (d, $J = 8.2$ Hz, 2H); ^{13}C NMR (75 MHz, CD_2Cl_2) δ 14.47, 23.28, 27.30, 29.21, 29.97, 30.28, 30.34, 30.76, 32.52, 33.90, 34.26, 36.81, 37.89, 125.63, 126.07, 127.38, 127.55, 127.94, 128.86, 129.01, 129.11, 131.02, 131.59, 131.74, 132.39, 132.82, 133.71, 136.90, 136.97, 137.92, 138.14, 141.36, 143.34, 146.40; HRMS (APPI-TOF, positive) m/z calcd for $\text{C}_{72}\text{H}_{82}$ $[\text{M}]^+$ 946.6417, found 946.6428.

7.3.5.4 9-(4-(4-decylhexadecyl)phenyl)dibenzo[*a,r*]ovalene (3-17)



Compound **3-17** was prepared following the same procedure as compound **3-15** except for the purification method: A crude product of **3-17** was quickly passed through a pad of silica gel with hot THF as eluent. The titled compound **3-17** was then re-precipitated by adding methanol and obtained as a red solid (81% yield): $^1\text{H NMR}$ (500 MHz, $\text{C}_2\text{D}_2\text{Cl}_4$, 393 K) δ 0.89 – 1.04 (m, 6H), 1.47 (dd, $J = 49.3, 13.2$ Hz, 45H), 2.07 (p, $J = 7.7$ Hz, 2H), 3.07 (t, $J = 7.5$ Hz, 2H), 7.73 (d, $J = 7.6$ Hz, 2H), 7.83 (d, $J = 7.5$ Hz, 2H), 7.91 (d, $J = 3.7$ Hz, 4H), 8.47 – 8.65 (m, 3H), 8.78 (d, $J = 8.2$ Hz, 2H), 9.12 (dd, $J = 38.2, 6.0$ Hz, 4H), 9.41 (d, $J = 8.3$ Hz, 2H), 10.39 (s, 1H); MALDI-TOF-MS: calcd for $\text{C}_{72}\text{H}_{74}$ $[\text{M}]^+$ 938.58, found: 938.66; FTIR (powder) 3066, 3051, 3029, 2921, 2851, 2359, 2160, 2037, 1898, 1679, 1608, 1511, 1459, 1460, 1408, 1377, 1357, 1237, 1206, 1179, 1069, 1024, 1005, 908, 837, 814, 785, 759, 744, 727 cm^{-1} .

7.3.5.5 7,7'-bis(4-(4-decylhexadecyl)phenyl)-14,14'-diphenyl-2,2'-bibenzo[*m*] tetraphene (3-18)

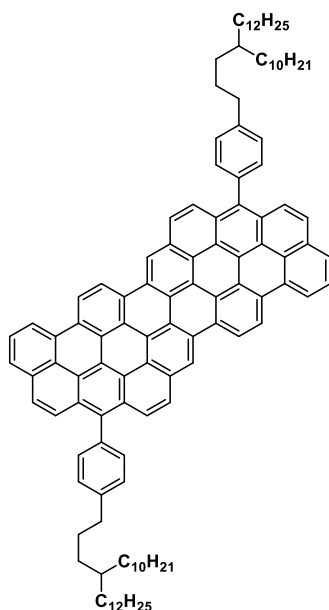


To a 50 mL Schlenk tube equipped with a stir bar, monomer **3-1c** (200 mg, 0.21 mmol) dissolved in 10 mL tetrahydrofuran was added. After the solution was cooled to -78 $^{\circ}\text{C}$, a solution of *n*-butyllithium (0.34 mL, 0.21 mmol, 1.6 M in hexane) was added drop wise *via* a syringe. The mixture was kept stirring for 30 min, and then quenched by adding 5 mL methanol. After the solvent was evaporated under vacuum, the residue was washed with deionized water for three times, and then with brine. The organic layer was dried over magnesium sulfate and evaporated. The residue was purified by silica gel column chromatography (eluent: 10% dichloromethane/hexane) to afford a mixture of mono- and di-brominated compounds and compound **3-14** as a pale yellow solid.

Next, the obtained mixture was subjected to *Yamamoto* polymerization following the procedure described in the synthesis of polymer precursor **3-2c**. After stirring for 1 h at 80 $^{\circ}\text{C}$, the

reaction mixture was cooled to the room temperature, and then slowly dropped into dilute methanolic hydrochloric acid. The yellow precipitate that formed was collected by filtration and washed repeatedly by methanol and dilute hydrochloric acid to completely remove the catalyst. Afterward the resulting oligomers were roughly separated by flash column chromatography with silica gel and then further purified by recycling preparative SEC (Waters Ultrastaygel 103 Å, 19 × 300 mm, eluent: chloroform, 3.0 mL/min) to afford compound **3-18** in 16% yield: ^1H NMR (300 MHz, CD_2Cl_2) δ 0.86 (t, $J = 5.7$ Hz, 12H), 1.28 (d, $J = 12.6$ Hz, 88H), 1.62 – 1.90 (m, 4H), 2.78 (t, $J = 7.6$ Hz, 4H), 6.84 (dd, $J = 8.3, 1.5$ Hz, 2H), 6.89 – 6.96 (m, 2H), 7.08 (d, $J = 8.5$ Hz, 2H), 7.34 (d, $J = 8.0$ Hz, 5H), 7.37 – 7.48 (m, 8H), 7.48 – 7.59 (m, 8H), 7.68 (td, $J = 16.4, 15.4, 7.6$ Hz, 9H), 7.82 (s, 2H); ^{13}C NMR (75 MHz, CD_2Cl_2) δ 14.45, 23.26, 27.28, 29.21, 29.95, 30.24, 30.26, 30.31, 30.74, 32.50, 33.89, 34.25, 36.80, 37.88, 124.44, 125.95, 126.18, 126.48, 127.31, 127.73, 128.25, 128.36, 128.63, 128.85, 129.09, 129.30, 130.04, 130.75, 130.84, 131.29, 131.45, 132.33, 132.64, 133.48, 134.46, 136.66, 137.02, 137.93, 137.96, 143.29, 146.29; HRMS (APPI-TOF, positive) m/z calcd for $\text{C}_{120}\text{H}_{146} [\text{M}]^+$ 1588.1458, found 1588.1476.

7.3.5.6 Model compound (3-19)

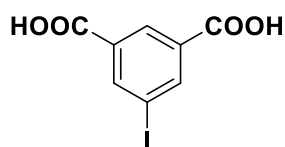


Compound **3-19** was prepared following the same procedure as compound **3-15** except for the purification method: A crude product of **3-19** was quickly passed through a pad of silica gel with hot toluene as eluent. The titled compound **3-19** was then re-precipitated by adding methanol and obtained as a red solid (47% yield): ^1H NMR (500 MHz, $\text{C}_2\text{D}_2\text{Cl}_4$, 393 K) δ 0.96 (d, $J = 6.5$ Hz, 13H), 1.37 – 1.50 (m, 87H), 2.00 (d, $J = 7.6$ Hz, 4H), 2.90 – 3.05 (m, 4H), 7.52 – 7.57 (m, 1H), 7.62 – 7.72 (m, 6H), 7.86 (d, $J = 20.9$ Hz, 2H), 7.98 – 8.08 (m, 3H), 8.11 (t, $J = 8.4$ Hz, 2H), 8.15 – 8.29 (m, 4H),

8.32 (d, $J = 8.3$ Hz, 1H), 8.53 (d, $J = 4.0$ Hz, 2H), 8.69 (d, $J = 8.5$ Hz, 1H), 8.82 (d, $J = 9.5$ Hz, 1H), 8.91 (d, $J = 9.5$ Hz, 1H), 9.65 (dd, $J = 29.2, 8.7$ Hz, 2H); MALDI-TOF-MS: calcd for $C_{120}H_{134} [M]^+$ 1575.05, found: 1575.03.; FTIR (powder) 3081, 3051, 3025, 2922, 2851, 2160, 2037, 1980, 1916, 1788, 1738, 1608, 1593, 1509, 1457, 1411, 1356, 1186, 1157, 1072, 1019, 963, 881, 823, 807, 786, 740, 699 cm^{-1} .

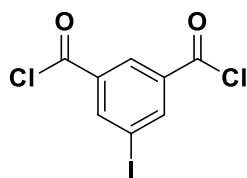
7.3.6 Synthesis of NGs with zigzag edges

7.3.6.1 5-Iodoisophthalic acid (4-6)



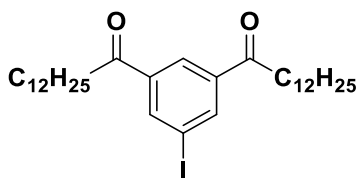
$KMnO_4$ (21.67 g, 0.137 mol) was added to a suspension of 5-iodo-xylene (12 g, 0.0648 mol, 8.82 mL) in *tert*-butanol/ H_2O (120 mL, 1:1). After heating the suspension for 1 h at 100 °C, another portion of $KMnO_4$ (21.67 g, 0.137 mol) was added. The suspension was heated at 100 °C for another 20 h and then cooled to r.t. After filtration over a pad of Celite and washing with water, the filtrate was concentrated to one-third in vacuo and acidified with concentrated HCl. The resulting white precipitate was dissolved in concentrated $NaHCO_3$ solution and washed three times with diisopropyl ether (100 mL). After further acidification with concentrated HCl the white precipitate was collected and dried at 80 °C overnight. Yield: 12.8 g (85%). 1H NMR (300 MHz, $DMSO-d_6$): δ 13.54 (br s, 2H, COOH), 8.40 (s, 3H). ^{13}C NMR (75 MHz, $DMSO-d_6$): δ 165.2 (2C), 141.4 (2C), 133.1 (2C), 129.1 (1C), 94.8 (1C). EA: calculated for $C_8H_5O_4I$ (292.03): C 32.90, H 1.73; found: C 33.05, H 1.86.

7.3.6.2 5-Iodo-isophthaloyl dichloride (4-7)



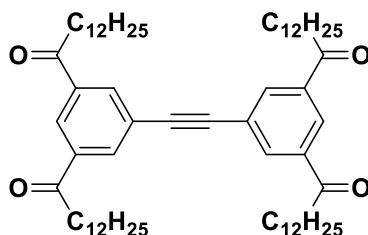
A solution of 5-iodo-isophthalic acid **4-6** (1.5 g, 5.1 mmol) in thionyl chloride (30 mL) and *N,N'*-dimethylformamide (five drops) was refluxed for 6 h under dry conditions with subsequent removal of the excess of the thionyl chloride in vacuo. The residue was dried under high vacuum and yielded a red-brownish oil. Yield: 1.68 g (100%). ^1H NMR (300 MHz, $\text{DMSO-}d_6$): δ 8.38 (s, 3H). ^{13}C NMR (75 MHz, $\text{DMSO-}d_6$): δ 165.2 (2C), 141.4 (2C), 133.0 (2C), 129.1 (1C), 94.8 (1C).

7.3.6.3 1,1'-(5-Iodo-1,3-phenylene)bis(tridecan-1-one) (**4-8**)



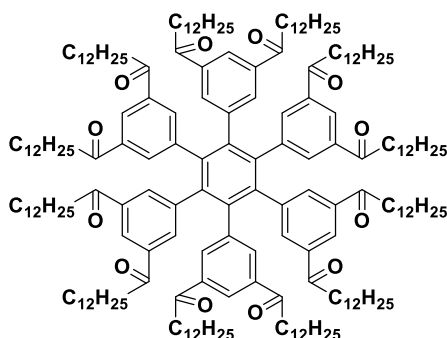
To a THF solution of **4-7** (1.69 g, 5.14 mmol) cooled to $-22\text{ }^\circ\text{C}$ in dry ice- CCl_4 bath, Bu_3P (2.8 mL, 11.3 mmol) was added under argon atmosphere and the resulting mixture was stirred for 20 min. To the well-stirred mixture, a THF solution of dodecylmagnesium bromide (1.0 M, 10.3 mL, 10.3 mmol) was added rapidly by a syringe. After stirring for 10 min at the same temperature, the reaction was quenched by the addition of 1 M HCl (10 mL). The whole mixture was poured into 1 M HCl (100 mL) and extracted with ether (60 mL x 3). The combined organic layers were washed with 1% NaHCO_3 and brine (200 mL each), and dried over MgSO_4 . After removal of the solvent, the residue was subjected to column chromatography (*n*-hexane/EtOAc = 10: 1) to afford a pure product as a white solid (1.56 g, 51% yield). ^1H NMR (300 MHz, CD_2Cl_2) δ 0.89 (q, $J = 6.9, 5.4$ Hz, 6H), 1.14 – 1.50 (m, 36H), 1.63 – 1.82 (m, 4H), 2.99 (dt, $J = 10.5, 7.1$ Hz, 4H), 8.43 (s, 2H), 8.47 (s, 1H); ^{13}C NMR (75 MHz, CD_2Cl_2) δ 14.47, 23.29, 24.58, 29.78, 29.95, 30.04, 30.10, 30.22, 30.23, 30.26, 32.52, 39.29, 95.08, 127.03, 139.63, 141.20, 198.77; FD-MS (8 kV): m/z : calcd: 596.31; found: 597.5.

7.3.6.4 1,1',1'',1'''-(Ethyne-1,2-diylbis(benzene-5,1,3-triyl))tetrakis(tridecan-1-one) (**4-9**)



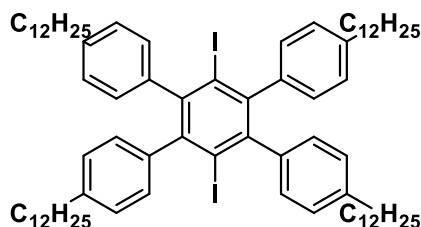
A 25 mL round bottom flask with teflon-coated magnetic stir bar was fitted with a rubber septum and flame dried under vacuum. The flask was purged with dry argon, and charged with $\text{PdCl}_2(\text{PPh}_3)_2$ (353 mg, 6 mol%), CuI (160 mg, 10 mol%) and starting material **4-8** (5 g, 8.4 mmol). Septum was parafilmmed after solids were added. While stirring, dry benzene (20.0 mL, starting material is 0.20 M in dry benzene) purged with dry argon was added by syringe. Argon-purged DBU (7.5 mL, 6 equiv) was then added by syringe, followed by a purge of the reaction flask with argon. Ice-chilled trimethylsilylethynylene (592 μL , 0.50 equiv) was then added by syringe, followed immediately by distilled water (60 μL , 40 mol%). The reaction flask was covered in aluminum foil and left stirring at a high rate of speed for 18 h, at the end of which the reaction mixture is partitioned in ethyl ether and distilled water (50 mL each). The organic layer was washed with 10% HCl (3×75 mL), saturated aqueous NaCl (1×75 mL), dried over MgSO_4 , gravity-filtered and the solvent removed in *vacuo*. The crude product was purified by silica gel column chromatography (*n*-hexane/EtOAc = 5: 1) to yield a white solid (3.4 g, 85% yield). ^1H NMR (300 MHz, CD_2Cl_2) δ 0.84 – 0.90 (m, 6H), 1.17 – 1.47 (m, 78H), 1.67 – 1.82 (m, 8H), 3.03 (t, $J = 7.3$ Hz, 8H), 8.30 (d, $J = 1.6$ Hz, 4H), 8.48 (q, $J = 2.5$, 1.8 Hz, 2H); ^{13}C NMR (75 MHz, CD_2Cl_2) δ 14.25, 23.07, 24.44, 29.63, 29.73, 29.86, 29.91, 30.02, 30.06, 32.30, 39.20, 89.59, 124.11, 127.58, 135.04, 138.23, 199.18; FD-MS (8 kV): m/z : calcd 962.81; found: 962.7.

7.3.6.5 1,2,3,4,5,6-Hexakis(3,5-di(tridecan-1-one)phen-1-yl)benzene (4-10)



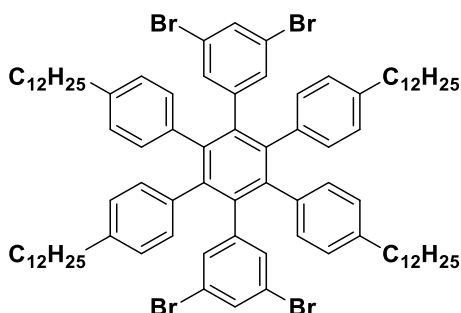
In a 100 mL round flask, **4-9** (1.2 g, 1.19 mmol), $\text{Co}_2(\text{CO})_8$ (20.4 mg, 59.7 μmol , 5.0 mol%), and dry 1,4-dioxane (60 mL) were placed under nitrogen atmosphere. The mixture was degassed and heated at 120 °C for 24 h. The resulting dark brown mixture was filtered off and the solvent was removed under reduced pressure. The residue was purified by column chromatography (silica gel, *n*-hexane/EtOAc = 2:1) to afford **4-10** (1.02 g, 89%). ^1H NMR (300 MHz, CD_2Cl_2) δ 0.88 (t, J = 6.3 Hz, 36H), 1.28 (d, J = 5.2 Hz, 216H), 1.45 – 1.59 (m, 24H), 2.66 (t, J = 7.2 Hz, 24H), 7.72 (s, 12H), 7.96 (s, 6H); ^{13}C NMR (75 MHz, CD_2Cl_2) δ 14.26, 23.09, 24.27, 29.63, 29.79, 29.94, 30.01, 30.09, 30.12, 30.14, 32.34, 38.99, 125.71, 134.45, 137.09, 140.00, 140.42, 198.75; MALDI-TOF-MS (M_w = 2888.4): m/z : 2888.1.

7.3.6.6 4,4''-Didodecyl-4',5'-bis(4-dodecylphenyl)-3',6'-diiodo-1,1':2',1''-terphenyl (**4-12**)



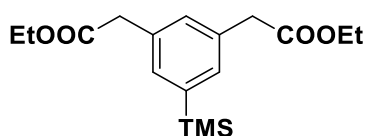
A suspension of 1,4-dichloro-2,3,5,6-tetrabromobenzene (1.00 g, 2.16 mmol) in dry THF (20 mL) was added to a solution of (4-dodecylphenyl)magnesium bromide (32 mmol) in dry THF (32 mL) under argon, and the resulting mixture was stirred at room temperature for 12 h. I_2 (13.72 g, 54 mmol) was added directly to the reaction mixture at 0 °C, and the reaction was stirred at room temperature for 2 h. The reaction was quenched with water, and the resulting mixture was extracted with CHCl_3 (3 \times 100 mL). The combined organic layers were washed with 2 M aqueous NaHSO_3 solution (2 \times 200 mL), brine (50 mL), and water (50 mL) and dried with MgSO_4 . After filtration of the MgSO_4 , the solvent was removed in vacuo, and the resulting mixture was filtered. The solid was washed with a little bit of benzene and hexane, then purified by chromatography (eluent *n*-hexane/benzene = 30:1) to give **4-12** (1.4 g, 50%). ^1H NMR (250 MHz, CD_2Cl_2): δ 6.81 (d, J = 7.7 Hz, 8 H), 6.75 (d, J = 7.6 Hz, 8H), 2.43 (t, J = 7.2 Hz, 8H), 1.24 (m, 80 H), 0.72 (t, J = 6.6 Hz, 12H). ^{13}C NMR (75 MHz, CD_2Cl_2): δ 146.9, 143.7, 142.0, 130.2, 127.7, 109.0, 35.9, 32.4, 31.7, 30.2, 30.1, 29.9, 29.8, 29.6, 23.1, 14.3. FD-MS (8 kV): m/z : calcd: 1307.6; found: 1307.4; HRMS (ESI): calcd for $\text{C}_{78}\text{H}_{116}\text{I}_2$: 1306.7166 $[\text{M}]^+$; found: 1306.7169.

7.3.6.7 3,5-Dibromo-4'-(3,5-dibromophenyl)-4''-dodecyl-3',5',6'-tris(4-dodecylphenyl)-1,1':2',1''-terphenyl (4-13)



An oven-dried 100 mL Schlenk tube equipped with a magnetic stirrer bar and a septum was charged with a suspension of 1,4-diiodo-2,3,5,6-tetraarylbenzene (**4-12**) (500 mg, 0.38 mmol, 1.0 equiv), (3,5-dibromophenyl)boronic acid (321mg, 1.15 mmol, 3.0 equiv), K_2CO_3 (1.1g, 7.65 mmol, 20 equiv), and aliquat 336 (0.01 mmol, 0.02 equiv) in toluene (15 mL). The mixture was degassed by three “freeze–pump–thaw” cycles, and then $Pd(PPh_3)_4$ (22 mg, 0.02 mmol, 0.05 equiv) was added. The resulting mixture was degassed again by three “freeze–pump–thaw” cycles. The mixture was warmed to the 100 °C and stirred for the 24 h under argon. The reaction mixture was quenched with water and extracted with $CHCl_3$. The organic extract was washed with brine, dried over $MgSO_4$, and concentrated in vacuo. Flash chromatographic purification on silica gel furnished the desired product **4-13** as a white solid (389 mg, 67% yield). 1H NMR (300 MHz, CD_2Cl_2) δ 0.89 (s, 12H), 1.26 (d, $J = 8.4$ Hz, 72H), 1.38 – 1.56 (m, 8H), 2.41 (s, 8H), 6.76 (qd, $J = 8.9, 8.1, 3.7$ Hz, 12H), 6.90 (t, $J = 2.0$ Hz, 8H), 7.16 (dt, $J = 5.7, 1.8$ Hz, 2H); ^{13}C NMR (75 MHz, CD_2Cl_2) δ 14.51, 23.32, 29.48, 30.00, 30.13, 30.29, 30.35, 31.89, 32.56, 35.93, 121.41, 127.61, 131.14, 131.57, 133.76, 137.51, 139.11, 140.92, 141.12, 145.05. MALDI-TOF-MS ($M_w = 1518.6$): m/z : 1517.5.

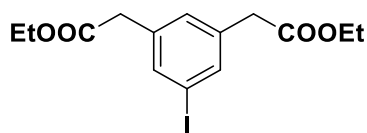
7.3.6.7 Diethyl 2'-(5-(trimethylsilyl)-1,3-phenylene)diacetate (4-15)



Firstly, the catalyst solution was prepared inside the glove box by adding 5 mL of dry toluene to a mixture of $Pd(OAc)_2$ (145.7 mg, 0.65 mmol), di-*tert*-butyl(2'-methyl-[1,1'-biphenyl]-2-yl)phosphane

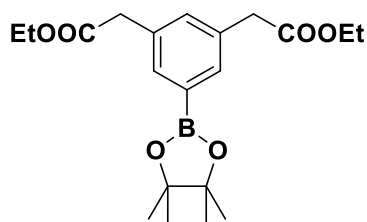
(406 mg, 89 mmol). The resulting solution was stirred for 30 min at room temperature. Then, potassium phosphate (K_3PO_4) (19 g, 89 mmol), a solution of (3,5-dibromophenyl)trimethylsilane (5 g, 16.2 mmol) and ethyl 3-oxobutanoate (4.5 mL, 35.7 mmol) dissolved in 20 mL of toluene were added. The reaction mixture was stirred for 16 h at 90 °C. After cooling, the reaction mixture was quenched with water and extracted with ethyl acetate. The organic extract was washed with brine, dried over $MgSO_4$, and concentrated *in vacuo*. Flash chromatographic purification on silica gel furnished the desired product **4-15** as yellow oil (3.3 g, 63% yield). 1H NMR (300 MHz, CD_2Cl_2) δ 0.26 (s, 9H), 1.25 (t, $J = 7.1$ Hz, 6H), 3.59 (s, 4H), 4.13 (q, $J = 7.1$ Hz, 4H), 7.17 (s, 1H), 7.31 (d, $J = 1.8$ Hz, 2H); ^{13}C NMR (75 MHz, CD_2Cl_2) δ 3.15, 14.21, 40.57, 61.30, 132.31, 133.64, 134.57, 140.86, 171.27; FD-MS (8 kV): m/z : calcd:322.2; found: 321.7.

7.3.6.8 Diethyl 2,2'-(5-iodo-1,3-phenylene)diacetate (**4-16**)



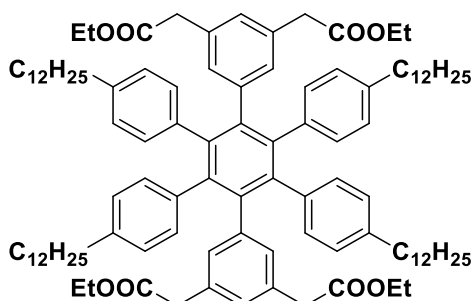
Compound **4-15** (1.1 g, 3.4 mmol) was dissolved in dichloromethane (50 mL) and cooled in ice bath. To this solution was added a solution of iodine monochloride (5.12 mL, 5.12 mmol) in dichloromethane (10 mL) dropwise over 20 min. After the ice bath was removed, the reaction mixture was stirred under r.t. overnight, followed by quenching with an aqueous solution of sodium thiosulfate pentahydrate (2.5 g, 9.9 mmol) and sodium hydroxide (0.5 g, 12.4 mmol) in water (100 mL). The organic phase was separated, washed with brine (50 mL \times 2) and dried over $MgSO_4$. After removal of the solvent under reduced pressure, the residue was dried *in vacuo* to give **4-16** as brownish oil (1.1 g, 95 % yield). 1H NMR (300 MHz, CD_2Cl_2) δ 1.17 – 1.36 (t, 6H), 3.46 – 3.64 (s, 4H), 4.14 (q, $J = 7.1$ Hz, 4H), 7.18 (dt, $J = 3.2, 1.5$ Hz, 1H), 7.57 (dd, $J = 4.2, 1.6$ Hz, 2H); ^{13}C NMR (75 MHz, CD_2Cl_2) δ 14.34, 40.87, 61.44, 94.31, 130.31, 137.04, 137.29, 171.17; FD-MS (8 kV): m/z : calcd:376.02; found: 376.3.

7.3.6.9 Diethyl 2,2'-(5-(4,4,5,5-tetramethyl-1,3,2-dioxaborolan-2-yl)-1,3-phenylene)diacetate (**4-17**)



A 250 mL round flask has been charged with compound **4-16** (1.4 g, 3.7 mmol), bis(pinacolato)diboron (1.04 g, 4.1 mmol), potassium acetate (1.10 g, 11.2 mmol) and [1,1'-bis(diphenylphosphino)ferrocene]dichloropalladium(II) (87 mg, 0.12 mmol). Then 50 mL dry 1,4-dioxane was added and the stirring mixture has been degassed by argon bubbling for 20 min. Afterwards, the mixture has been stirred overnight at 80 °C under an argon atmosphere. After cooling to room temperature, the mixture has been washed with water and extracted with ethyl acetate (20 mL × 3). The combined organic layer has been washed with brine, dried over magnesium sulfate, and evaporated. At last, the crud residue **4-17** has been purified by passing through a shot pad of silica gel (eluent: 10% ethyl acetate/hexane) to remove the catalyst and used directly for the next step. Brownish-yellow oil (1.32 g, 94%). ¹H NMR (300 MHz, CD₂Cl₂) δ 1.28 (t, *J* = 7.1 Hz, 6H), 1.37 (s, 12H), 3.65 (s, 4H), 4.17 (q, *J* = 7.3 Hz, 4H), 7.34 (d, *J* = 1.9 Hz, 1H), 7.63 (t, *J* = 1.7 Hz, 2H); ¹³C NMR (75 MHz, CD₂Cl₂) δ 14.60, 25.29, 41.49, 61.33, 84.46, 133.73, 134.64, 134.86, 171.91; FD-MS (8 kV): *m/z*: calcd:376.21; found: 376.8.

7.3.6.10 Tetraethyl 2,2',2'',2'''-(2',3',5',6'-tetrakis(4-dodecylphenyl)-[1,1':4',1''-terphenyl]-3,3'',5,5''-tetrayl)tetraacetate (**4-18**)



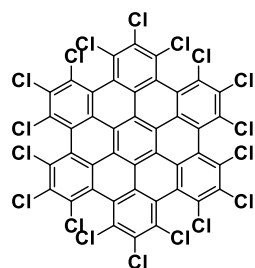
An oven-dried 100 mL Schlenk tube equipped with a magnetic stirrer bar and a septum was charged with a suspension of 1,4-diiodo-2,3,5,6-tetraarylbenzene (**4-12**) (200 mg, 0.15 mmol, 1.0 equiv), **4-17** (126 mg, 0.34 mmol, 2.2 equiv), K₂CO₃ (106 mg, 0.76 mmol, 5 equiv), and aliquat 336 (0.01

mmol, 0.02 equiv) in toluene (15 mL). The mixture was degassed by three “freeze–pump–thaw” cycles, and then Pd(PPh₃)₄ (9 mg, 0.008 mmol, 0.05 equiv) was added. The resulting mixture was degassed again by three “freeze–pump–thaw” cycles. The mixture was warmed to reflux and stirred for the 24 h under argon. The reaction mixture was quenched with water and extracted with CHCl₃. The organic extract was washed with brine, dried over MgSO₄, and concentrated in *vacuo*. Flash chromatographic purification on silica gel furnished the desired product **4-18** as a yellow solid (76 mg, 32% yield). ¹H NMR (300 MHz, CD₂Cl₂) δ 0.92 (t, 12H), 1.00 – 1.52 (m, 84H), 2.36 (dt, *J* = 15.6, 7.5 Hz, 8H), 3.24 (d, *J* = 3.1 Hz, 8H), 3.63 (s, 8H), 4.16 (q, *J* = 7.1 Hz, 8H), 6.70 (t, *J* = 4.6 Hz, 8H), 7.22 (s, 8H), 7.46 (q, *J* = 1.7, 1.1 Hz, 2H), 7.58 – 7.69 (m, 4H); ¹³C NMR (75 MHz, CD₂Cl₂) δ 14.53, 23.34, 29.63, 30.03, 30.16, 30.33, 32.59, 35.93, 41.70, 61.40, 127.07, 128.57, 129.18, 130.89, 131.85, 133.28, 135.31, 171.62, 171.92; MALDI-TOF-MS (*M*_w = 1551.1): *m/z*: 1551.9.

7.3.7 Chemical functionalization of NGs

7.3.7.1 Edge chlorination of NGs

7.3.7.1.1 Synthesis of edge chlorinated HBC (C₄₂Cl₁₈, 5-1)

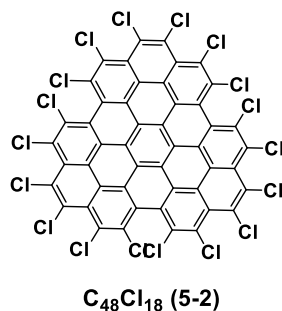


C₄₂Cl₁₈ (5-1)

A 50-ml flask was charged with 0.1 mmol (52 mg) of C₄₂H₁₈, 0.2 mmol (26 mg) of AlCl₃, 30 mmol (5 g) ICl and 35 ml of CCl₄, and then the reactants were stirred and refluxed at 80 °C for 48 h. After reaction, the products were poured into 30 ml ethanol to quench the reaction and precipitate the products. Next, the suspension was filtered and the precipitate was washed by ethanol, hydrochloric acid (1.0 mol/L), ion-free water and acetone, sequentially. After dried in vacuum, about 107 mg

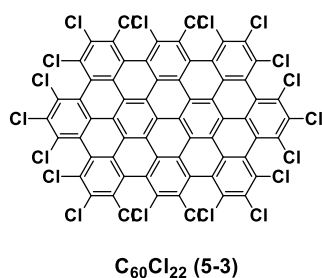
(0.097 mmol) yellow powder was obtained. The yield of **5-1** is about 97%. MALDI-TOF-MS ($M_w = 1141.4$): m/z : 1141.4.

7.3.7.1.2 Synthesis of edge chlorinated $C_{48}H_{18}$ ($C_{48}Cl_{18}$, **5-2**)



A 50-ml flask was charged with 0.05 mmol (30 mg) of $C_{48}H_{18}$, 0.1 mmol (13 mg) of $AlCl_3$, 15 mmol (2.5 g) ICl and 35 ml of CCl_4 , and then the reactants were stirred and refluxed at 80 °C for 48 h. The products were poured into 30 ml ethanol to quench the reaction and precipitate the products. Next, the suspension was filtered. The precipitate was collected and washed by ethanol, hydrochloric acid (1.0 mol/L), ion-free water and acetone, sequentially. After dried in vacuum, about 52 mg (0.043 mmol) orange powder was obtained. The yield of **5-2** is about 86%. MALDI-TOF-MS ($M_w = 1213.4$): m/z : 1213.3.

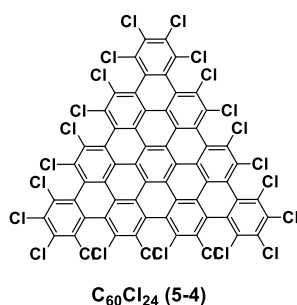
7.3.7.1.3 Synthesis of edge chlorinated $C_{60}H_{22}$ ($C_{60}Cl_{22}$, **5-3**)



A 50-ml flask was charged with 0.1 mmol (75 mg) of $C_{60}H_{22}$, 0.25 mmol (34 mg) of $AlCl_3$, 30 mmol (5 g) ICl and 35 ml of CCl_4 , and then the reactants were stirred and refluxed at 80 °C for 48 h. Next, the reaction was quenched by ethanol. After that, the excess ICl and CCl_4 were removed by rotary evaporator at 45 °C. The residual solid was washed with ethanol. The product was purified by column chromatography using chloroform as eluent. Compound **5-3** was collected as the first

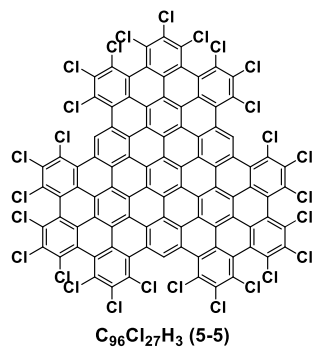
component at solvent front. After evaporating the solvent, the product was dried in vacuum. About 143 mg (0.095 mmol) dark-red powder was obtained. The yield of **5-3** is about 95%. MALDI-TOF-MS ($M_w = 1499.3$): m/z : 1499.4.

7.3.7.1.4 Synthesis of edge chlorinated $C_{60}H_{24}$ ($C_{60}Cl_{24}$, **5-4**)



A 50-ml flask was charged with 0.1 mmol (75 mg) of $C_{60}H_{24}$, 0.25 mmol (34 mg) of $AlCl_3$, 30 mmol (5 g) ICl and 35 ml of CCl_4 . The reactants were stirred and refluxed at 80 °C for 48 h, then quenched by ethanol. After that, the excess ICl and CCl_4 were removed by rotary evaporator at 45 °C. The residual solid was washed by ethanol. Next, the product was purified by column chromatography using chloroform as eluent. Compound **5-4** was collected as the first component at solvent front. After evaporating the solvent, the product was dried in vacuum. About 145 mg (0.093 mmol) red powder was obtained. The yield of **5-4** is about 93%. MALDI-TOF-MS ($M_w = 1571.2$): m/z : 1571.2.

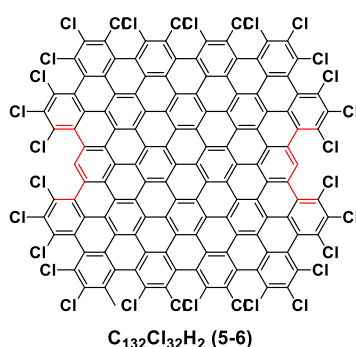
7.3.7.1.5 Synthesis of edge chlorinated $C_{96}H_{30}$ ($C_{96}Cl_{27}H_3$, **5-5**)



A 50-ml flask was charged with 0.05 mmol (60 mg) of $C_{96}H_{30}$, 0.20 mmol (28 mg) of $AlCl_3$, 30 mmol (5 g) ICl and 35 ml of CCl_4 . The reactants were stirred and refluxed at 80 °C for 48 h, then

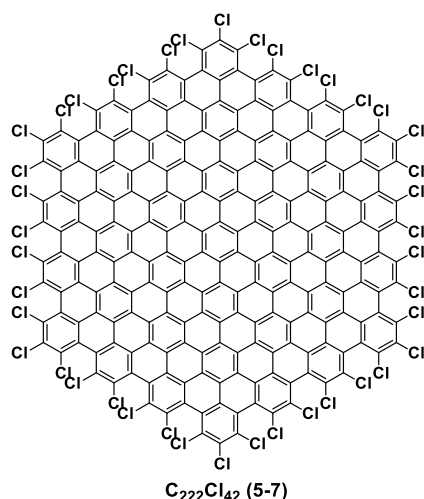
quenched by ethanol. After that, the excess ICl and CCl₄ were removed by rotary evaporator at 45 °C. The product was washed by ethanol and then purified by column chromatography using chloroform as eluent. Compound **5-5** was collected as the first component at solvent front. After evaporating the solvent and dried in vacuum, 100 mg (0.047 mmol) dark violet powder was obtained. The yield of **5-5** is about 95%. MALDI-TOF-MS ($M_w = 2112.2$): m/z : 2113.6.

7.3.7.1.6 Synthesis of edge chlorinated C₁₃₂H₃₄ (C₁₃₂Cl₃₂H₂, **5-6**)



A 50-ml flask was charged with 0.015 mmol (25 mg) of C₁₃₂H₃₄, 0.20 mmol (28 mg) of AlCl₃, 30 mmol (5 g) ICl and 35 ml of CCl₄. The reactants were stirred and refluxed at 80 °C for 5 days, and then the reaction was quenched by ethanol. After reaction, the excess ICl and CCl₄ were removed by rotary evaporator at 45 °C. The product was washed with ethanol. Next, the product was purified by column chromatography using chloroform/carbon disulphide (1:1) as eluent. Compound **5-6** was collected as the first component at solvent front. After evaporating the solvent and dried in vacuum, 34 mg black powder was obtained. The yield of **5-6** is about 83%. MALDI-TOF-MS ($M_w = 2721.9$): m/z : 2721.4.

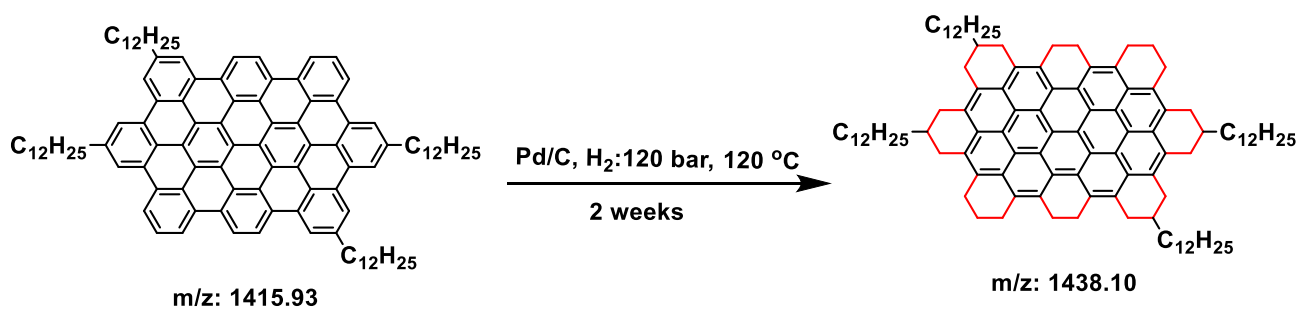
7.3.7.1.7 Synthesis of edge chlorinated C₂₂₂H₄₂ (C₂₂₂Cl₄₂, **5-7**)



A 50-ml flask was charged with 0.01 mmol (27 mg) of $C_{222}H_{42}$, 0.20 mmol (26 mg) of $AlCl_3$, 30 mmol (5.0 g) ICl and 35 ml of CCl_4 . The reactants were stirred and refluxed at 80 °C for 72 h, and then the reaction was quenched by ethanol. After that, the excess ICl and CCl_4 were removed by rotary evaporator at 45 °C. Next, 30 ml ethanol was added. After sonication for 5 min, the suspension was filtered and the precipitate was washed by ethanol. Next, the product was purified by column chromatography using chloroform/carbon disulfide (1:2) as eluent. Compound **5-7** was collected as the first component at solvent front. After evaporating the solvent and dried in vacuum, 38 mg black powder was obtained. The yield of **5-7** is about 90%. MALDI-TOF-MS ($M_w = 4154.6$): m/z : 4154.5.

7.3.7.2 Hydrogenation of NGs

Typical experimental procedure of Pd/C catalyzed hydrogenation of nanographene molecules including HBC, C_{60} with dodecyl chains and C_{96} with dodecyl chains was same as showed below:



All reactions conducted in the same fashion. NG precursor C₆₀ with dodecyl chains (100-500mg) was placed in a 300 ml, glass-lined autoclave along with an equivalent mass of Pd/C (10%). The autoclave was sealed and degassed via passage of an argon stream through a rubber septum. Dry THF was transferred via cannula under argon, the reaction vessel was sealed, pressurized to 120 bar, and heated to 120 °C for 2 weeks. After cooling to room temperature, the pressure was released to the atmosphere; the solution was passed through a 0.45m filter and then concentrated under reduced pressure. Hydrogenated C₆₀ showed in above scheme required further purification. MALDI-TOF-MS ($M_w = 1438.10$): m/z : 1438.0.

7.4 References

- (1) Stabel, A.; Herwig, P.; Mullen, K.; Rabe, J. P. *Angewandte Chemie-International Edition In English* **1995**, *34*, 1609.
- (2) Iyer, V. S.; Yoshimura, K.; Enkelmann, V.; Epsch, R.; Rabe, J. P.; Mullen, K. *Angew Chem Int Edit* **1998**, *37*, 2696.
- (3) Muller, M.; Iyer, V. S.; Kubel, C.; Enkelmann, V.; Mullen, K. *Angewandte Chemie-International Edition In English* **1997**, *36*, 1607.
- (4) Iyer, V. S.; Wehmeier, M.; Brand, J. D.; Keegstra, M. A.; Mullen, K. *Angewandte Chemie-International Edition In English* **1997**, *36*, 1604.
- (5) Simpson, C. D.; Brand, J. D.; Berresheim, A. J.; Przybilla, L.; Rader, H. J.; Mullen, K. *Chem-Eur J* **2002**, *8*, 1424.
- (6) Hayashi, S.; Hayamizu, K. *B Chem Soc Jpn* **1991**, *64*, 685.
- (7) Morcombe, C. R.; Zilm, K. W. *J Magn Reson* **2003**, *162*, 479.
- (8) Feike, M.; Demco, D. E.; Graf, R.; Gottwald, J.; Hafner, S.; Spiess, H. W. *J Magn Reson Ser A* **1996**, *122*, 214.
- (9) Saalwachter, K.; Lange, F.; Matyjaszewski, K.; Huang, C. F.; Graf, R. *J Magn Reson* **2011**, *212*, 204.
- (10) Beecher, P.; Servati, P.; Rozhin, A.; Colli, A.; Scardaci, V.; Pisana, S.; Hasan, T.; Flewitt, A. J.; Robertson, J.; Hsieh, G. W.; Li, F. M.; Nathan, A.; Ferrari, A. C.; Milne, W. I. *J Appl Phys* **2007**, *102*.
- (11) Saalwachter, K.; Schnell, I. *Solid State Nucl Mag* **2002**, *22*, 154.
- (12) Thakur, R. S.; Kurur, N. D.; Madhu, P. K. *Chem Phys Lett* **2006**, *426*, 459.
- (13) Parr, R. G. Y., W. *Oxford University Press: New York* **1989**.
- (14) Heyd, J.; Scuseria, G. E.; Ernzerhof, M. *J Chem Phys* **2003**, *118*, 8207.
- (15) Heyd, J.; Scuseria, G. E.; Ernzerhof, M. *J Chem Phys* **2006**, *124*.
- (16) Rassolov, V. A.; Ratner, M. A.; Pople, J. A.; Redfern, P. C.; Curtiss, L. A. *J Comput Chem* **2001**, *22*, 976.
- (17) Frisch, M. J. *Gaussian 09, Revision A. 1; Gaussian, Inc., Wallingford* **2009**.
- (18) M. J. Frisch, G. W. T., H. B. Schlegel, G. E.; Scuseria, M. A. R., J. R. Cheeseman, G. Scalmani, V. Barone, B. Mennucci, G. A.; Petersson, H. N., M. Caricato, X. Li, H. P. Hratchian, A. F. Izmaylov, J.; Bloino, G. Z., J. L. Sonnenberg, M. Hada, M. Ehara, K. Toyota, R. Fukuda, J.; Hasegawa, M. I., T. Nakajima, Y. Honda, O. Kitao, H. Nakai, T. Vreven, J. A.; Montgomery, J., J. E. Peralta, F. Ogliaro, M. Bearpark, J. J. Heyd, E. Brothers, K. N.; Kudin, V. N. S., R. Kobayashi, J.

Normand, K. Raghavachari, A. Rendell, J.; C. Burant, S. S. I., J. Tomasi, M. Cossi, N. Rega, J. M. Millam, M. Klene, J. E.; Knox, J. B. C., V. Bakken, C. Adamo, J. Jaramillo, R. Gomperts, R. E. Stratmann,; O. Yazyev, A. J. A., R. Cammi, C. Pomelli, J. W. Ochterski, R. L. Martin, K.; Morokuma, V. G. Z., G. A. Voth, P. Salvador, J. J. Dannenberg, S.; Dapprich, A. D. D., Ö. Farkas, J. B. Foresman, J. V. Ortiz, J. Cioslowski, and D.; Fox, J. *Gaussian 09, Revision D.01.*, Gaussian, Inc., Wallingford CT **2009**.

(19) Dovesi, R.; Orlando, R.; Erba, A.; Zicovich-Wilson, C. M.; Civalleri, B.; Casassa, S.; Maschio, L.; Ferrabone, M.; De La Pierre, M.; D'Arco, P.; Noel, Y.; Causa, M.; Rerat, M.; Kirtman, B. *Int J Quantum Chem* **2014**, *114*, 1287.

(20) R. Dovesi, V. R. S., C. Roetti, R. Orlando, C. M. Zicovich-Wilson, F.; Pascale, B. C., K. Doll, N. M. Harrison, I. J. Bush, P. D'Arco, M. Llunell, M.; Noël, C. a. Y. *University of Torino, Torino* **2014**.

List of Publications

1. Pascal Ruffieux, Shiyong Wang, **Bo Yang**, Carlos Sanchez, Jia Liu, Thomas Dienel, Leopold Talirz, Prashant Shinde, Carlo Pignedoli, Daniele Passerone, Tim Dumslaff, Xinliang Feng, Klaus Müllen, Roman Fasel. “On-surface synthesis of graphene nanoribbons with zigzag edge topology” *Nature*. **2015**, *531*, 489-492.
Accepted
2. **Bo Yang**, Akimitsu Narita, Joan Teyssandier, Hans van Gorp, Kunal S Mali, Ali Maghsoumi, Lasse Arnt Straasø, Michael Ryan Hansen, Pascal Ruffieux, Roman Fasel, Chiara Castiglioni, Alberto Milani, Matteo Tommasini, Steven De Feyter, Xinliang Feng, Klaus Müllen. “Bottom-up Approach Toward Graphene Nanoribbons with Zigzag Edge Structures: Solution-Mediated Synthesis and Characterization” *J. Am. Chem. Soc.*, **2016**.
Preparing
3. Yuan-Zhi Tan, **Bo Yang**, Khaled Parvez, Akimitsu Narita, Silvio Osella, David Beljonne, Xinliang Feng, Klaus Müllen. “Atomically precise edge chlorination of nanographenes and its application in graphene nanoribbons” *Nature Communication*, **2013**, *4*.
4. Ahmad N. Abbas, Bilu Liu, Akimitsu Narita, Lukas F. Dössel, **Bo Yang**, Wen Zhang, Jianshi Tang, Kang L. Wang, Hans Joachim Rader, Xinliang Feng, Klaus Müllen, and Chongwu Zhou. “Vapor-Phase Transport Deposition, Characterization, and Applications of Large Nanographenes” *J. Am. Chem. Soc.*, **2015**, *137*(13), pp 4453-4459.

Curriculum Vitae

Personal Details

Name: Bo Yang

Place of birth: Ningxia, China

Nationality: Chinese

Marital status: Single

University Education:

April 2011 – Present

PhD candidate in Max Planck Institute for Polymer Research, Mainz

Research adviser: [REDACTED]

July 2008 – April 2011

Master degree in Shanghai Jiao Tong University (SJTU), Shanghai

Research adviser: [REDACTED]

Sept. 2003 – July 2007

Bachelor degree in Shanghai Jiao Tong University (SJTU), Shanghai

Research work:

July 2009 – April 2011

Master thesis, School of Chemistry and Chemical Engineering in SJTU

Thesis title: “*The Synthesis of Axially Chiral Dibringed Phosphoramidite Ligands and Their Applications to γ -aryl- β , γ -unsaturated α -Ketoesters in Copper(I)-catalyzed Asymmetric 1,4-Conjugate*”

Curriculum Vitae

Addition

March 2008 – July 2009

Application Project, collaborate with Shanghai Pharmaceuticals Holding CO., Ltd Shanghai

Research title: “*Development of Novel synthetic Routes Toward the Carbapenem Antimicrobial: Faropenem Sodium with High Yield from Basic Medical Intermediate: 4AA*”

July 2006 – July 2007

Bachelor thesis, School of Chemistry and Chemical Engineering in **SJTU**

Thesis title: “*The Design and Synthesis of New Chiral Catalyst with 2,2',6,6'-Tetrasubstituted Biphenyl Backbone*”

Tutorial Jobs:

Oct. 2013 – July 2014

Assistant tutor in supervising undergraduate students in organic chemistry experimental courses in Johannes Gutenberg University of Mainz,

Faculty of Chemistry

March 2008 – July 2010

Assistant tutor in training lab skills of undergraduate students in organic chemistry experimental courses in **SJTU**, Shanghai,

School of chemistry and chemical Engineering

School Education:

Sept. 2000 – July 2003

The third Seior High School of Shizuishan City, Ningxia, China

Sept.1997 – July 2000

Erchang Junior High school of Dawuko City, Ningxia, China

Sept.1991 – July 1997

Erchang Elementary school of Dawuko City, Ningxia, China

Awards and Fellowships:

May 2011 – April 2014

Early-Stage Researcher (ESR), Marie Curie Initial Training Network (ITN) “GENIUS”

(Graphene-organic hybrid architectures for organic electronics: a multisite training action)

Sept. 8th – 13th 2013

Invited oral presentation, EUROMAT (European Congress and Exhibition on Advanced Materials and Processes) in Sevilla, 2013

Acknowledgements

First of all, I would like to thank Prof. Dr. [REDACTED] for giving me the opportunity to work in his research group on this exciting and challenging topic. I sincerely appreciate his continuous and kind support, helpful suggestions and guidance, and his trust in study and research work during last four years.

I would also like to thank Prof. Dr. [REDACTED] for the constant scientific discussions and excellent advices on the possibilities and problems of my research projects, which really enlighten my research field. In particular, I thank him for making significant effort for the proper corrections and suggestions on my work reports, manuscripts and thesis dissertation.

I would like to extend my thanks to Dr. [REDACTED] for his great help for scientific discussion, proper corrections, as well as inspiring comments and suggestions on my manuscripts and thesis dissertation. Reviewing and polishing scientific articles is always not an easy task, thanks to him again for paying valuable time and great patience.

I would also like to acknowledge all the colleagues in the Max-Planck Institute for Polymer Research, inside and outside our research group for their great support and exciting collaboration results, which could never been done without their involvements:

Dr. [REDACTED] for the successful collaboration on the edge chlorination of nanographene molecules.

Dr. [REDACTED] and Dr. [REDACTED] for cooperation on measurements of Raman spectra of the GNR powder samples.

Acknowledgements

Dr. [REDACTED] and [REDACTED] for measurements of proton and carbon NMR, two-dimensional H-H COSY NMR, as well as high temperature NMR.

[REDACTED] and [REDACTED] for measurements of the MALDI-TOF MS spectra.

Dr. [REDACTED] and [REDACTED] for measurements of the high-resolution MALDI-TOF MS spectra.

I would also like to cordially appreciate the Marie Curie Initial Training Network (ITN) “GENIUS” for the funding, various workshop training opportunities, and all the collaborations and networking. Sincere thanks to all partners within the GENIUS ITN for the valuable and significant questions, discussions, and comments during the GENIUS meetings. Particularly, I would like to acknowledge the coordinator, project managers and cooperation partners:

Prof. Dr. [REDACTED] (CNR., Bologna, Italy) for coordinating the project, all the helpful comments and suggestions.

Dr. [REDACTED] (CNR., Bologna, Italy) for managing the project, organizing meetings, events, and paper works about GNIUS project.

Prof. Dr. [REDACTED] (I.S.I.S., Strasbourg, France) for his accept and kindly help of my secondment in I.S.I.S.

Dr. [REDACTED] (I.S.I.S., Strasbourg, France) for working together during my secondment in Strasbourg, showing me how to preparing films by spin-coating and help me to perform STM analysis of my model compounds and GNR samples. I appreciate all the members of the group of prof. Dr. [REDACTED] as well as people in I.S.I.S. for taking care of me.

Acknowledgements

Dr. [REDACTED] and other collaborators (UM., Mons, Belgium) for all the theoretical studies on my GNRs and model compounds.

Dr. [REDACTED] (BASF., Germany), Dr. [REDACTED] (UCAM., United Kingdom), Prof. Dr. [REDACTED] (UCL., London, United Kingdom), and Prof. Dr. [REDACTED] (UBER, Berlin, Germany) for organizing the GENIUS meetings and training events, and for all the kind helps and advices.

[REDACTED] for his great help and assistance as our project manager in MPIP.

My sincere thanks also go to cooperation partners outside the MPIP and GENIUS ITN for the fruitful collaboration works and support:

Prof. [REDACTED] and Prof. [REDACTED] (Politecnico di Milano, Italy) for detailed Raman and FTIR investigations of model compounds and GNRs including simulated and experimental results, which dramatically improved the characterization of GNRs.

[REDACTED] and Prof. [REDACTED] (Aarhus University, Denmark) for their solid-state NMR investigations of the GNRs and their precursors to corroborate the efficient “graphitization”.

Prof. Dr. [REDACTED] and Dr. [REDACTED], Dr. [REDACTED], Dr. [REDACTED] (EMPA, Dübendorf, Switzerland) for their fruitful works for the surface-assisted synthesis of GNRs through AA-type polymerization.

Great thanks belong to all the members of groups of Prof. Dr. [REDACTED], especially colleagues of synthesis section as well as in my office and laboratory for discussions, kindly helps, encouragements, inspirations, and best working environment: Dr. [REDACTED], Dr. [REDACTED]

